Modelling and Experimental Investigation of Magnetic Flux Leakage Distribution for Hairline Crack Detection and Characterization

Chukwunonso. K.W. Okolo
Wolfson Centre for Magnetics
School of Engineering
Cardiff University

A thesis submitted for the degree of
Doctor of Philosophy
February 2018.

Declaration

This work has not previously been accepted in substance for any degree and is not concurrently submitted in candidature for any other degree.

Signed: (candidate) Date: 22/02/2018

Statement 1

This thesis is being submitted in partial fulfilment of the requirements for the degree of PhD.

Signed: (candidate) Date: 22/02/2018

Statement 2

This thesis is the result of my own independent work/investigation, except where otherwise stated. Other sources are acknowledged by explicit references.

Signed: (candidate) Date: 22/02/2018

Statement 3

I hereby give consent for my thesis, if accepted, to be available for photocopying and for inter-library loan, and for the title and summary to be made available to outside organizations.

Signed: (candidate) Date: 22/02/2018

Acknowledgements

I would like to express my gratitude to everyone who have assisted me during the period of my PhD study at Cardiff University.

Also I would like to express my heartfelt appreciation to my supervisor Dr Turgut Meydan for giving me the opportunity to pursue this research at Cardiff University and for his consistent advice, supervision, support and encouragement. Also, special thanks to my second supervisor Dr Fatih Anayi for his helpful support and contribution from the start of this research.

I would like to thank Dr. Paul Williams, my friends and work colleagues from Wolfson Centre for Magnetics for the many intelligent ideas, conversations and the remarkable time spent.

My deepest thanks goes to my family, for their constant support and encouragement.

Finally, I dedicate this thesis to my parents and siblings for standing by me throughout my education at Cardiff University.

Abstract

The Magnetic Flux Leakage (MFL) method is a well-established branch of electromagnetic Non-Destructive Evaluation (NDE) extensively used to assess the physical condition of ferromagnetic structures. The main research objective of this research work presented in this thesis is the detection and characterization of the MFL distribution caused by rectangular surface and far-surface hairline cracks. It looks at the use of the direct current and pulsed current techniques to investigate the presence of hairline cracks in ferromagnetic steel pipelines, by comparing the Finite Element Modelling (FEM) technique with practical experiments. First, the expected response of an MFL probe scanned across the area of a hairline crack was predicted using the 3D FEM numerical simulation technique. The axial magnetization technique is employed and the characteristics of the surface and far-surface leakage field profile ($\boldsymbol{B_x}, \boldsymbol{B_y}, \boldsymbol{B_z}$) was simulated. The optimization of the magnetization and sensing methodologies were crucial to ensuring accurate numerical results. The performance of the modelled MFL inspection system on detecting and characterizing both surface and far-surface hairline cracks was confirmed using real low carbon steel plates, with well-defined artificial hairline slots. The experimental findings showed that the MFL signals caused by a 0.2 mm deep surface and 0.4 mm deep far-surface hairline cracks, with a constant width and length of 0.2 mm and 10 mm respectively, is detectable. The transient responses in the time and frequency domains, yielded information relating to different cracks located at different depths within the test specimen. The MFL sensor used was able to detect the inspected hairline cracks at 9 mm lift-off, which makes the newly developed system effective and beneficial in applications where large lift-off distances are required. The pulsed current inspection approach significantly reduced the power consumption and thermal effects by 50 %, compared to the direct current approach. Also, the experimental results were within 10 % of the simulated results.

Nomenclature

Symbol	Quantity	Unit
B	Magnetic Flux Density	T
E	Electric Field Strength.	V/m
H	Magnetic Field Strength	A/m
I	Current	A
L	Length of Flux Path.	m
N	Number of Winding	$Turns$
R	Resistance	Ω
S	Magnetic Reluctance	$A\,Wb^{-1}$
μ_0	Permeability of free space ($4\pi \times 10^{-7}$).	H/m
μ_r	Relative Permeability	
μ	Permeability ($\mu_0 \times \mu_r$)	H/m
σ	Conductivity	S/m
$\omega = 2\pi f$	Angular Frequency ($2\pi f$)	rad/s
Φ	Magnetic Flux	$weber$
X_L	Inductive Reactance	Ω
Z	Impedance ($\sqrt{R^2 + X_L^2}$)	Ω

List of Abbreviations

AMR:	Anisotropic Magnetoresistive
EC:	Eddy Current.
EDM:	Electro-Discharge-Machining.
EMAT:	Electromagnetic Acoustic Transducer.
ENDE:	Electromagnetic Non-Destructive Evaluation.
FEM:	Finite Element Method.
IR:	Infrared.
MFL:	Magnetic Flux Leakage.
MFLNDE:	Magnetic Flux Leakage Non-Destructive Evaluation.
MFLT:	Magnetic Flux Leakage Testing.
MMF:	Magneto Motive Force.
MT:	Magnetic Particle Testing.
NDE:	Non-Destructive Evaluation.
PCB:	Printed Circuit Board.
PEC:	Pulsed Eddy Current.
PIG:	Pipeline Inspection Gauge.
PMFL:	Pulsed Magnetic Flux Leakage.
QNDE:	Quantitative Non-Destructive Evaluation.

Conference Presentations

This research work has been presented in the following conferences.

i) The 22nd Soft Magnetic Materials Conference-(SMM22)-ABM, 13th - 16th September 2015, Sao Paulo, Brazil.

ii) The 11th European Magnetic Sensors and Actuators Conference-(EMSA11), 12th - 15th July 2016, Torino, Italy.

iii) The 18th International Symposium on Applied Electromagnetics and Mechanics Conference-(ISEM18), 3rd - 6th September 2017, Chamonix Mont-Blanc, France.

iv) The 23rd Soft Magnetic Materials Conference-(SMM23), 10th - 13th September 2017, Seville, Spain.

v) The 13th IEEE Sensors Conference-(IEEE13), 30th October - 1st November 2017, Glasgow, United Kingdom.

List of Publications

The following publications have been accomplished during this research.

Journal Papers

[J.1] C.K. Okolo and T. Meydan, "Pulsed Magnetic Flux Leakage Method for Hairline Crack Detection and Characterization", *AIP Advances 8 (4) (2018): 047-207.*

[J.2] C.K. Okolo and T. Meydan, "Finite Element Method and Experimental Investigation for Hairline Crack Detection and Characterization", *International Journal of Applied Electromagnetics and Mechanics (IOS Press), (2018).*

Conference Papers

[C.1] C.K. Okolo and T. Meydan, "Finite Element Method and Experimental Investigation for Hairline Crack Detection and Characterization". *Proceedings of the 18th International Symposium on Applied Electromagnetics and Mechanics (ISEM) (2017).*

[C.2] C.K. Okolo and T. Meydan, "Axial Magnetic Field Sensing for Pulsed Magnetic Flux Leakage Hairline Crack Detection and Quantification". *Proceedings of the IEEE Sensors, 1-3 (2017).*

Table of Contents

List of Figures

List of Tables

Chapter 1: Introduction

1.1) Introduction

This chapter provides an outline of the research work, the thesis aims, objectives and achievements.

1.2) Research Background

Non-Destructive Evaluation (NDE) refers to the various techniques used for examining and evaluating materials, structures and assemblies for presence of defects or variation in characteristics without causing any adverse effects to the future re-use of such components. In contrast, other inspection techniques are destructive in nature. Hence, they are only applied on a controlled number of test samples, rather than on the actual material or structure that is being put into use. The NDE system of testing generally uses a probing mechanism to identify material properties or to demonstrate the presence of anomalies in a material (surface, far-surface or obscured). That is, the approach and procedure used computes the physical properties or the variation in the physical properties of the material. The technique can be utilized on a sampling basis for a particular inspection or could be employed for a complete assessment of a material or component in a production quality control system.

There are several established electromagnetic NDE techniques well-suited for the evaluation of metallic components and assemblies, in the petrochemical, oil, gas, nuclear, energy and aerospace industries. This includes; Magnetic Flux Leakage (MFL) method, Pulsed Magnetic Flux Leakage (PMFL) method, Eddy Current (EC) method, Pulsed Eddy Current (PEC) method, Magnetic Particle Testing (MPT) method, etc. These methods are governed by the interaction between the conductive samples under investigation and the electromagnetic fields. The Electromagnetic NDE (ENDE) techniques are effective in applications involving the measurement of

thickness, conductivity, flaw detection, proximity assessment, resistance, thermoelectric parameters, etc.

Also, different sensor types such as; the Giant Magnetoresistive (GMR) sensors, Anisotropic Magnetoresistive (AMR) sensors or Hall Effect sensors can be used for magnetic field measurements. However, a major disadvantage of these sensors is the inability to be used for sensing large areas of a specimen. Hence, this has led to the evolution of sensor arrays for magnetic field measurements and imaging [1, 2]. This new sensor configuration provides a concurrent measurement of magnetic field at different spatial positions and can be used to develop the magnetic field distribution images of the sample under test.

Presently, one of the major challenges of the NDE industry is the need to produce an accurate quantitative estimation of components and assemblies. This is referred to as Quantitative Non-Destructive Evaluation (QNDE). QNDE presents various approaches to detect, estimate and compute the extent of deterioration in terms of the length, width and depth of defects, characterize distinct discontinuities as well as monitoring the life expectancy of materials over a period of time. QNDE is vital when investigating defective materials and components, thus, every aspect of the measurement system and defect geometries that have a direct or significant effect on the inspection output should be taken into account for an accurate evaluation. Progress in the accuracy of NDE methods is required in various applications such as in pipeline investigation, where high accuracy in flaw detection and characterization can cut down needless high-priced pipe replacement.

Steel materials are manufactured more each year than any other industrial metal. In 2015 the world production of crude steel and iron recorded a total of 1599×10^6 tonnes and 59×10^6 tonnes respectively, with 66 countries accounting for approximately 99 % of the total world crude steel production and 14 countries accounting for approximately 90 % of the world total iron production [3, 4]. Thus, economically, steel is regarded as one of the most important industrial products. Moreover, steel is extensively utilized as a constructional commodity for large scale designs and projects such as for; storage tanks, rail lines, bridges and pipelines, at the same time being used for manufacturing of high strength structures and assemblies. Therefore, there is an increasing demand for the inspection of steel components and

for the estimation of defects and irregularities present, in order to improve its service lifetime.

1.3) Pipeline Inspection and Problem Statement

Pipelines are widely used in the petrochemical, oil, gas and power generation industries. They consist of cylindrical steel shapes with wall thickness ranging from 8 mm to 12 mm, and are manufactured with precise specifications and requirements, to make sure the users, public and environment are safe [5]. Over time, external forces can impair the pipeline to a state capable of causing a spill or rupture. A flaw is an irregularity or variance from the initial structure of the pipeline. This could be a modification in the wall thickness due to missing metals or as a result of the pipe wall being deformed. Metal loss flaws develop due to a reduction in the pipe wall caused by both external or internal corrosion and cracks. This is because the bulk part of the pipeline is covered under the ground resulting in corrosion or cracks being the main risk to the health of the pipeline.

A crack is a flaw type caused by the stress-induced separation of the pipeline material [6, 7]. Steel materials are made up of granules which are strongly bonded together, however, different factors can result in these strong granular bonds detaching from each other, resulting in a crack which grows over time. One such factor is cyclic fatigue. This refers to the pipe stress that develops from the rise and fall of the pipe's operating pressure, which causes a slight change in the shape of the pipe [8]. Subsequently, this can lead to a gradual weakening and cracking of the pipe. Sometimes, during manufacturing, cracks are accidentally created in pipelines, which are initially too minute and insignificant to cause a breakdown, but can grow into larger cracks over time, capable of threatening the integrity of the pipe [6, 8]. Pipelines also suffer multiple alternating stress loads such as twist, push, pull and bend during drilling, and become corroded by corrosive fluids like liquefied H_2S, $C0_2$ and 0_2 [9]. Subsequently, dents, corrosions and cracks gradually evolve in the pipe, impair its health, as well as result in fracture failures [10]. Therefore, to prevent

economic losses and hazards, standard pipelines should be examined rigorously, before use, using the NDE technologies [11].

Pipeline networks consist of transmission lines, gathering pipelines and distribution lines as shown in Fig. 1.1. Pipeline operators consistently make use of the in-line inspection technologies in order to guarantee the integrity and safe operation of this network. Despite the use of so many NDE techniques, the MFL method remains the most popular, frequently used and powerful NDE technique. It has been used for extremely productive detection and characterization of flaws in different types of ferromagnetic steel components [12-24], especially in very elongated structures such as steel pipes [25-30]. The MFL technology has been productively utilized in a variety of applications such as for; tubing and piping inspection in gas and oil pipelines, tank floor inspection and rail line examination. Also, the recent improvements in MFL technology have helped to prevent serious damages such as breaking of pipelines, breakdown of reactors and wrecking of trains. The MFL technique is very fast and easy to implement.

However, establishing the crack geometries from just the acquired leakage field signal is difficult. The inspection accuracy of the MFL technique is poor and in most situations, the crack identification approach is different from the crack characterization approach. Also, measurement errors are usually encountered while using the MFL technique, especially in situations where the crack exist both on the surface under inspection and on the reverse surface (far-surface region), as large cracks on the far-surface region could be mistaken to be surface cracks (similar and indistinguishable).

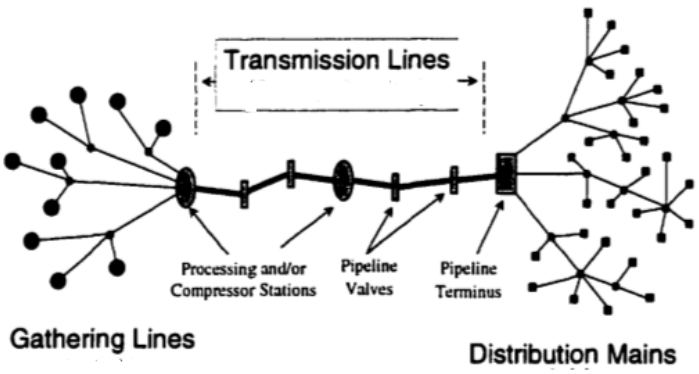

Figure 1.1. A schematic diagram of a gas pipeline system [29].

There are three different techniques for MFL inspection, these are; Direct Current (DCMFL) technique, Alternating Current (ACMFL) technique and Pulsed Current (PMFL) technique [32, 33]. The DCMFL approach employs the use of electromagnets or permanent magnets to produce a static magnetization current for the magnetization of the test sample. The electromagnet based DCMFL approach is well suited for hard-magnetization materials, like steel pipelines, since the supply current can be varied to provide the large currents required to generate a strong magnetization field. Depending on the excitation frequency selected, the ACMFL method is usually sensitive to surface and near surface flaws due to skin effect. This method is well-suited for detecting surface flaws, such as corrosions and cracks in pipeline structures. For the PMFL method, the probe is operated using a pulsed current, while the rich frequency components generate information from various depths due to skin effect. Also, with a good signal processing technique and data analysis, further information such as flaw position and profile can be ascertained.

The use of simulation models has aided in the study and analysis of electromagnetic NDE methods. It also allows NDE problems to be studied at several distinct levels and considerations. This helps for better understanding of the different actions and interactions of several high-level components of a system and hence, better furnished to handle the complexity of the entire system [34]. Simulation data are used in conjunction with experimental results, the latter being used to validate the former. Simulation models also provide guidance in the design and setup of experiments, such as; for the determination of the best material type and grade, best sensor type and location, suitable probe type and size, as well as the overall system configuration. These models can be grouped into two main categories, which are the analytical and numerical solutions that both make use of Maxwell's equations [35]. Analytical models are used for simulating, analyzing and generating predictions about components associated with complex physical processes (canonical geometries). They also have a closed form solution and easier to compute, which means that the equations used to define changes in the system can be given as mathematical analytic functions (either arithmetic, trigonometric or logarithmic functions). However, Numerical models make use of time-stepping operation to attain the model's performance over a period. It is only an approximation under certain circumstances and they are easy to change. Numerical models are not

restrained by material non-linearity or its geometry, which makes it best suited for complex crack characterization. Numerical analysis has aided greatly in the magnetic flux leakage investigation for crack location and characterization by predicting the output with great accuracy and efficiency, at a rate comparable with that of the experimental analysis [36, 37]. The numerical method is therefore preferred over the analytical method (closed form solution), because it provides accurate information on the underlying phenomenon surrounding the interaction between the induced magnetic field and the complex defect geometry, which gives rise to the resultant distribution pattern of the leakage field [36]. The numerical simulation technique also helps to provide a good understanding, description and analysis of the test result, which is necessary for an accurate defect characterization and quantification.

Much theoretical and experimental work has been carried out on the location and evaluation of near-surface and far-surface cracks that have a direct influence on the integrity of steel components [38-40]. However, little work and effort have been invested in the detection and quantitative evaluation of much smaller defect precursors and imperfections, such as very narrow rectangular hairline cracks, especially deep below the surface of pipeline structures (e.g. Stress Corrosion Cracking (SCC)). The oil, gas and petrochemical industries have a rapidly growing demand for a powerful and efficient NDE system to quantitatively assess the areas of metal loss caused by developing cracks on pipelines and storage tanks. Thereby, preventing such defects from growing into huge and dangerous ones capable of causing an overall system failure or explosion. Therefore, developing a well-optimized MFL measurement tool will help such industries and the NDE community as a whole in monitoring the health and life expectancy of steel materials. Moreover, detecting such anomalies would help tackle the inevitable problem of granular bond separation, which occurs during manufacturing, leaving steel structures with tiny cracks.

1.4) Research Aims and Objectives

Previously, many researchers have studied the theoretical (modelling) and experimental method of examination of ferromagnetic industrial components using the MFL technique of NDE separately. This is because prior models were not well equipped to handle the multiple and complicated industrial tasks. However, this work will provide a link between both techniques by first developing an optimized 3D FEM simulation model to predict the leakage field signal caused by surface and far-surface hairline cracks, followed by an experimental validation of the predicted results. The investigation will be conducted using both the DCMFL and PMFL approach.

This project will address the following:

1) An in-depth literature review on crack detection and characterization using the DCMFL and PMFL NDE methods.

2) Finite element computation of DCMFL and PMFL numerical models.

i) The magnetization and sensing methodologies of the MFL inspection system will be optimized, in order to significantly improve the detection sensitivity of the feeble leakage field from both surface and far-surface hairline cracks. The magnitude of the leakage flux needed to accurately detect, characterize and quantify both surface and far-surface hairline cracks will also be established.

ii) The characteristics and features (field profile) of various surface and far-surface hairline cracks with varying width and depth sizes will be studied using the 3D FEM simulation model, by acquiring the field response and distribution pattern of the leakage fields ($\boldsymbol{B_x}$, $\boldsymbol{B_y}, \boldsymbol{B_z}$) produced. Also, the effect of sample thickness, magnetizer lift-off and sensor lift-off, on the resultant MFL signal will be explored in order to identify the limit of detection of the various surface and far-surface hairline cracks inspected.

iii) The acquired information will be used to provide a quantitative assessment of the cracks, in terms of its size, orientation, shape and location within the specimen. This will be achieved by; (a) Measuring the strength of the axial, radial and tangential components of the leakage fields, emerging from both surface and far-surface hairline cracks. (b) Through an enhanced visualization and 3D fast imaging of the resultant leakage field distribution. (c) Using the information contained in the time and frequency domain spectrum to provide additional crack characterization.

3) Experimental investigation using both DCMFL and PMFL techniques.

i) The magnetic field response to artificially fabricated surface and far-surface hairline cracks (man-made cracks) with different sizes will be investigated, using the DCMFL and PMFL techniques.

ii) Using the PMFL method, the influence of excitation pulse period and pulse width variation on the magnetic field distribution, will be investigated and how this affects the detection capability for hairline cracks located at different depths within the specimen. Then, the features contained in the static and transient MFL signals will be used to reconstruct the crack profiles with respect to its shape, orientation, size (width and length) and location within the test plates.

iii) The effects of sensor lift-off and neighbouring cracks on the detection sensitivity, characterization and quantification of surface and far-surface hairline cracks will be investigated. The thermal effects (heating) caused by the newly developed DCMFL and PMFL inspection systems will also be compared.

iv) A quantitative approach based on DCMFL and PMFL techniques for detecting and mapping out features of various hairline cracks will be proposed for evaluation of ferromagnetic steel pipelines and for QNDE.

v) Validation of the finite element numerical predictions using experimental results will be performed.

1.5) Thesis layout

This thesis is grouped into 7 chapters, which includes the theoretical and experimental aspects of hairline crack detection and characterization, employing the magnetic flux leakage technique.

Chapter 1 presents the outline of the project background, the project's aims and objectives, the major improvements, achievements and the contributions of this research work to the MFL technology and the NDE society as a whole.

Chapter 2 presents a general review on NDE technology and a brief description of the most frequently used NDE methods in the oil, gas and petrochemical industries, with more emphasis on the magnetic flux leakage testing for crack detection and quantification. Also, a section is presented on the state-of-the-art in MFLNDE method, including the current trends in the MFLNDE technology for crack detection and characterization. A conclusion is presented at the end of the chapter, outlining the major challenges and problems recognized to be a major part of this research work.

Chapter 3 describes the theoretical background to MFLNDE including a brief introduction to Maxwell's equations. A general overview of the basic equations governing the MFLNDE phenomenon are described, in order to understand the basic theory in which the research methodology used in this project is established. Also, an overview of the direction taken in this project and the contributions of the method used in providing an enhanced crack detection and characterization capabilities, through modelling (3D imaging of the leakage field distribution due to cracks) and experimental validation of the predicted results is presented. Furthermore, a brief description of the FEM numerical simulation in solving MFLNDE problems are presented, as well as its benefits and superiority over the analytical approach with respect to cracks with non-uniform geometries. Finally, the research methodology adopted in this work is described, outlining the modelling approach employed in

tackling the forward problems as well as its implementation with respect to the experimental design for an extensive hairline crack examination.

Chapter 4 will present the FEM numerical examination employed in this project, in order to understand the MFLNDE technique for detecting and characterizing surface and far-surface hairline cracks. The manner in which the magnetization and sensing methodologies affect the inspection output is first investigated and optimized via FEM simulation, using the $\boldsymbol{B_x}$, $\boldsymbol{B_y}$ and $\boldsymbol{B_z}$ leakage field amplitude and distribution pattern. Then the research subsequently advances to the use of DCMFL method for detecting and characterizing surface and far-surface hairline cracks with different width sizes and depth locations within the test sample. This was accomplished through an enhanced visualization and 3D fast imaging of the resultant leakage field distribution. The feasibility of the FEM optimized DCMFL measurement probe system is then verified experimentally, using well defined artificially fabricated hairline slots in low carbon steel plates.

Chapter 5 will explore the use of PMFL inspection technique for the detection and characterization of surface and far-surface hairline cracks with different depth sizes. First, the FEM simulation approach will be used to investigate the influence of excitation pulse period variation, as well as the influence of pulse width variation on the detectability and characterization of the various surface and far-surface hairline cracks located at different depth within the test sample. Also, various surface and far-surface hairline cracks with different depth sizes will be inspected using the PMFL approach and the features contained in the time and frequency domain spectrum will be used to provide additional information needed for crack depth characterization. The practicality of the PMFL inspection system modelled in MagNet will be verified experimentally, using artificially fabricated hairline cracks.

Chapter 6 summarizes the present investigation and provides the conclusions to the simulation and experimental findings. Also, the contributions of the research to the MFL technology and the NDE society as a whole are presented. Finally, possible routes for future work are suggested based on the research findings, with the aim of developing the scope of the research.

1.6) Chapter Summary

This chapter gave an introduction to the current project work, which is based on the detection, characterization and quantification of surface and far-surface hairline cracks present in ferromagnetic pipeline structures, utilizing the visualization and 3D imaging techniques for QNDE. The present requirement and demands in the oil, gas and petrochemical industries for QNDE were presented as the foundation to the present study, which was preceded by the project aims and objectives. Also, the improvements and contributions of this work to the NDE society were presented.

1.7) References

1) H. M. Kim et al, "A Study on the Estimation of Defect Depth in MFL type NDT System". School of Electrical Engineering, *Pusan National University*, Busan, South Korea, gspark@pusan.ac.kr, (2014).
2) H. M. Kim, and G. S. Park, "A Study on the Estimation of the Shapes of Axially Oriented Cracks in CMFL Type NDT System". *IEEE Transactions on Magnetics* 50(2), 109-112, (2014).
3) World Steel Association, "Crude Steel Production Monthly Data 1990-2015". [Online]. Available at: https://www.worldsteel.org/statistics/statistics-archive/steel-archive.html. (2016). [Accessed 18 December 16].
4) World Steel Association, "Monthly Iron Production 1990 to 2015". [Online]. Available at: https://www.worldsteel.org/statistics/statistics-archive/iron-archive.html. (2016). [Accessed 18 December 16].
5) M. Boat, N. Pearson, R. Lieb, J. Davies, R. James and B. Woodhead, "Factors that Affect the Defect Sizing Capabilities of the Magnetic Flux Leakage Technique". *Silverwing (UK) Ltd*, (2012).
6) A. Mann "Cracks in Steel Structures". *Proceeding of the institute of Civil Engineering-Forensic Engineering* 164(1), 15-23 (2011). [Accessed 15 November 17].
7) M. Kemppainen and I. Virkkunen, "Crack Characteristics and Their Importance to NDE". *Journal of Non-destructive Evaluation* 30(3), 143-157, (2011). [Accessed 15 November 17].
8) U.S Department of Transportation, "Pipe Defects and Anomalies (pipeline & safety administration)". [Online]. Available at: http://primis.phmsa.dot.gov/comm/FactSheets/FSPipeDefects.htm?nocache=9047. [Accessed 18 November 16].
9) J. Wu, et al, "A Lift-Off-Tolerant Magnetic Flux Leakage Testing Method for Drill Pipes at Wellhead". *Sensors* 17(1), 201, (2017).
10) D. Brondel, R. Edwards, A. Hayman, D. Hill, S. Mehta and T. Semerad, "Corrosion in the Oil Industry". *Oilfield Rev* 6, 4–18, (1994).
11) API (American Petroleum Institute). "API Spec 5D-Specification for Drill Pipe". 5th ed.; *API: Washington, DC, USA*, (2002).
12) R. Shannon and L. Jackson, "Flux Leakage Testing Applied to Operational Pipelines" *Materials Evaluation*, vol. 46, 1516-1524, November (1988).
13) D. L. Atherton, "Magnetic Inspection is Key to Ensuring Safe Pipelines". *Oil and Gas Journal*, vol. 87, 52-61, August (1989).

14) D. L. Atherton, “Developments in magnetic inspection techniques for pipelines”. *CSNDT Journal*, vol. 2, 28-35, January (1990).

15) R. J. Eiber, T. A. Bubenik, J. B. Nestleroth, S. VV. Rust, VV. A. Maxey, and D. J. Jones, “GRI Non-Destructive Evaluation Program: Pipeline Simulation Facility Development (Annual Report: GRI-92/0140)”. Tech. rep, *Gas Research Institute*, Chicago, IL, (1991).

16) Y. Sun and Y. Kang, “Magnetic Mechanisms of Magnetic Flux Leakage Non-Destructive Testing”. *Appl. Phys*. Lett. 103, 184104, (2013).

17) P. Ramuhalli, L. Udpa and S.S. Udpa, “Neural Network-Based Inversion Algorithms in Magnetic Flux Leakage Non-destructive Evaluation”. *J. Appl. Phys*. 93, 8274–8276, (2003).

18) T. Nara, Y. Takanashi and M. Mizuide, “A Sensor Measuring the Fourier Coefficients of the Magnetic Flux Density for Pipe Crack Detection using the Magnetic Flux Leakage Method”. *J. Appl. Phys*. 109, (2011).

19) J. Wu, Y. Sun, Y. Kang and Y. Yang, “Theoretical Analyses of MFL Signal Affected by Discontinuity Orientation and Sensor-Scanning Direction”. *IEEE Trans. Magn*. 51, 1–7, (2015).

20) S. M. Dutta, F. H. Ghorbel and R. K. Stanley, “Dipole Modelling of Magnetic Flux Leakage”. *IEEE Trans. Magn*. 45, 1959–1965 (2009).

21) F. Forster, “New Findings in the Field of Non-Destructive Magnetic Leakage Field Inspection”. *NDT E Int*.19, 3–14, (1986).

22) J. Ding, Y. Kang and X. Wu, “Tubing Thread Inspection by Magnetic Flux Leakage”. *NDT E Int*. 39, 53–56 (2006).

23) Y. Sun, S. Liu, Z. Deng, R. Tang, W. Ma, X. Tian, Y. Kang and L. He, “Magnetic Flux Leakage Structural Health Monitoring of Concrete Rebar using an Open Electromagnetic Excitation Technique. *Structural. Health Monitoring: An International Journal*. 147592171668434, (2017).

24) S. Huang and W. Zhao, “Magnetic Flux Leakage: Theories and Imaging Technologies”. *Walter de Gruyter GmbH*: Berlin, Germany, (2016).

25) W. Jianbo, F. Hui, W. Jie and K. Yihua, “The Influence of Non-Uniform Wall Thickness on MFL Testing for a Steel Pipe”. *Insight*. 57, 703–708, (2015).

26) Y. Kang, J. Wu and Y. Sun, “The Use of Magnetic Flux Leakage Testing Method and Apparatus for Steel Pipe”. *Mater. Eval*. 70, 821–827, (2012).

27) Y. Sun and Y. Kang, “High-Speed Magnetic Flux Leakage Technique and Apparatus Based on Orthogonal Magnetization for Steel Pipe”. *Mater. Eval*. 68, 452–458 (2010).

28) T. A. Bubenik, J. B. Nestleroth, R. J. Eiber and B. F. Saffell, "Magnetic Flux Leakage (MFL) Technology for Natural Gas Pipeline Inspection". *Topical Report*; *Battelle Memorial Inst*.: Columbus, OH, USA, (1992).

29) M. Yilai, L. Li, G. Po and G. Xuan, "Improving SNR of MFL Detecting Defect Signal of Drill Pipe by Using Pole Piece". *Insight*. 54, 489–492, (2012).

30) Y. Ma, R. He and J. Chen, "A Method for Improving SNR of Drill Pipe Leakage Flux Testing Signals by Means of Magnetic Concentrating Effect". *IEEE Trans. Magn*. 51, 1–7, (2015).

31) K. Hwang, "3-D Defect Profile Reconstruction from Magnetic Flux Leakage Signatures Using Wavelet Basis Function Neural Networks". Electrical Engineering (Communications and Signal Processing*) PhD Thesis Lowa State University* (2000).

32) A. Sophian, G.Y. Tian, and S. Zairi. "Pulsed Magnetic Flux Leakage Techniques for Crack Detection and Characterisation". *Sensors and Actuators A: Physical* 125(2), 186-191, (2006).

33) G.Y. Tian, J. Wilson, M. Morozov, D. O. Thompson and D.E. Chimenti, "Complementary Electromagnetic Non-Destructive Evaluation". *AIP Conf. Proceedings* 1335(1), 1256-1263, (2011).

34) B. Rao, "Magnetic Flux Leakage Technique: Basics". *Journal of Non-destructive Testing & Evaluation*. 11(3), 7-17, December (2012). [Accessed 21 September 16].

35) J. C. Maxwell, "A Treatise on Electricity and Magnetism". London: Clarendon.

36) Electromagnetic Testing, "Non-destructive Testing Handbook". 3rd Edition, Vol. 5. ASNT Press, ISBN 1-57117-116-9, (2004).

37) M. Tanaka and H. Tsuboi, "Finite Element Model of Natural Crack in Eddy Current Testing Problem". *IEEE Transactions on Magnetics*. 37(5), 3125-3128 (2001).

38) W. S. Singh, B.P.C. Rao, S. Vaidyanathan, T. Jayakumar and B. Raj, "Detection of Leakage Magnetic Flux from Near-Side and Far-Side Defects in Carbon Steel Plates Using a Giant Magneto-Resistive Sensor". *IOP publishing Ltd*. Non-Destructive Evaluation Division, Indira Gandhi Centre for Atomic Research, 17 December (2007).

39) F.I. Al-Naemi, J.P. Hall and A.J. Moses, "FEM Modelling Techniques of Magnetic Flux Leakage-Type NDT for Ferromagnetic Plate Inspection". *Journal of Magnetism and Magnetic Materials.* 304, 790–793, Sept (2006).

40) W. Singh, S. Thirunavukkarasu, S. Mahadevan, B.P.C. Rao, C. K. Mukhopadhyay and T. Jayakumar, "Three-Dimensional Finite Element Modelling of Magnetic Flux Leakage Technique for Detection of Defects in Carbon Steel Plates", *Non Destructive Evaluation Division*, Indira Gandhi Centre for Atomic Research, Kalpakkam-603102, Tamil Nadu, (2010).

Chapter 2: Literature Review

2.1) Introduction

The NDE field is very large, thus, a high testing standard has been put forward to ensure the reliability of the NDE inspections and to avoid errors due to wrong application of the method used, skill and experience of the operator and misinterpretation of test results [1, 2]. Numerous steel structures need thorough and detailed inspection during manufacturing and operation, and various NDE methods are available for pipeline inspection and evaluation. The most frequently used inspection techniques include; magnetic flux leakage inspection, eddy current inspection, ultrasonic inspection, liquid penetration inspection and radiographic inspection. Each method has its own merits and drawbacks, so the choice of selection of each depends on the structure and properties of the material used, as well as the type of defect being considered. Due to the lengthy nature of pipelines, the test is usually carried out from the inside of the pipe. The magnetic flux leakage inspection, eddy current inspection and ultrasonic inspection are the most commonly used inspection techniques for estimating the integrity of pipelines. Magnetic flux leakage testing technique is one of the most reliable and widely used technique for crack detection and characterization, both on the circumferential and axial direction.

This chapter focuses on the literature review of the most commonly used and well established non-destructive testing methods, with more emphasis on the magnetic flux leakage technique. The principles, typical applications, merits and drawbacks of the different methods are also discussed.

2.2) Visual Testing

This is the oldest and simplest NDE method. It involves using the naked eye to search for defects and imperfections on a piece of material. It requires no special testing equipment, only the naked eyes of an experienced operator are needed. This

method can only be used for surface examination of a range of equipment, both internally and externally. It can be used for the inspection of pipelines, storage tank floors, rail lines and bridges for defects such as; welding flaws, cracking, dents and improper finishes. It is straightforward and not as technologically advanced when compared to other inspection techniques. Notwithstanding, it has so many advantages over the more technologically improved techniques. There are two frequently used visual testing techniques, which are the Liquid Penetrant Testing and the Magnetic Particle Testing.

2.2.1) Liquid Penetrant Testing

The Liquid Penetrant Testing (PT) is one of the most commonly used visual testing methods [3]. There are two common methods used here, which are the colour contrast and fluorescent dye methods [4]. These two methods make use of the same basic procedure. First, a penetrant solution is applied to the surface of an already cleaned test specimen, then an absorption time is allowed to enable suitable penetration of the solution into the surface defects. Second, excess penetrant is carefully extracted from the defect using a solvent or water. Third, a developer is used to pull the trapped penetrant remaining within the defect, and this provides a visual indication of the surface defect if present. The three procedures are followed by the analysis and interpretation of the test result. The detection technique is slightly different for the fluorescent dye and colour contrast. The colour contrast method relies on the clear variation between the red colour of the penetrant solution and the white colour of the developer shielding the surface of the specimen. The assessment of the result here is carried out with just a normal light. However, the fluorescent dye technique requires the extra use of an ultraviolet light to brighten the fluorescent dye which helps for proper analysis of the result [1]. Some advantages and disadvantages of liquid penetrant testing are listed in table 2.1, while Fig. 2.1 shows a diagram illustrating the principle of PT [1].

Table 2.1 Liquid Penetrant Testing (PT).

Method	Advantages	Disadvantages
Liquid Penetrant Testing (PT)	Suitable for ferrous and non-ferrous materials. Few equipment required. Easy and straightforward. Not expensive. Inspects large area of a material.	Limited to surface defects. Not suitable for porous and rough materials. Requires critical surface preparation before test. Requires post cleaning to remove chemicals. Environmental issues. Results cannot be recorded digitally.

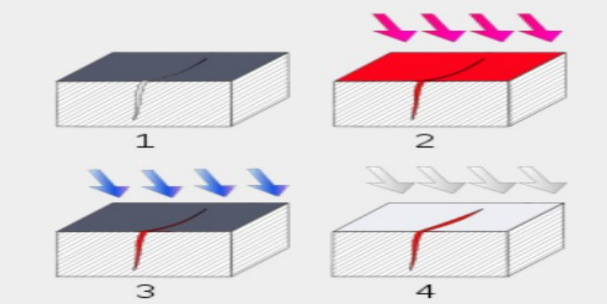

Figure 2.1. The Liquid Penetrant Testing (PT) [1].

2.2.2) Magnetic Particle Testing

The Magnetic Particle testing (MPT) is another commonly used visual inspection technique. This method is used for detecting discontinuities and defects such as; cracks, pits, voids, etc. at the surface or near-surface of ferromagnetic materials and components such as; iron, cobalt, nickel and steel [5]. It is mainly employed in the industrial sector to investigate metallic components such as oil and gas pipelines, storage tank floors and other ferromagnetic machineries, to avoid future breakdown and hazards. A few of the industries that make use of the magnetic particle testing include; structural steel, petrochemical, aerospace and automotive industries. The first step is the magnetization of the test sample, using a permanent magnet or an electromagnet; this generates magnetic field in the test sample. The presence of a

crack or any other discontinuity on the magnetized sample will change the initial direction of flux lines, due to an increased magnetic reluctance caused by a drop in the magnetic permeability at the defective region. Then ferrous iron particles are applied on the surface of the sample. The iron particles will be attracted to the defective region and form clusters, which is the area where the magnetic field lines are being interrupted, thus providing a visible indication of the defect. Since visual examination is a vital aspect of this method, there are a variety of magnetic particle testing techniques that could be employed, and the type used is highly dependent on the colour and shade of the metal sample being investigated [6]. The most frequently used iron particle is the yellow or red oxide particles or the black iron particles. When working with a very dark sample, a white paint is used to create a thin coat on the sample to give a clear and bright contrast. The test object is then examined with an ultraviolet light in a dark room to give a clear and bright indication of the defects. Some of the advantages and disadvantages of MPT are listed in table 2.2, while Fig. 2.2 shows a diagram illustrating the principle of MPT [1].

Table 2.2 Magnetic Particle Testing (MPT).

Method	Advantages	Disadvantages
Magnetic Particle Testing (MPT)	Detects surface and near surface defects. Few equipment required. Relatively inexpensive. Inspects complex and large area of a material. Surface preparation is less important.	Inspects ferromagnetic materials only. Large current is required for a large sample. Demagnetisation is crucial. Impurities like paint seriously influences sensitivity. Cannot quantify defects

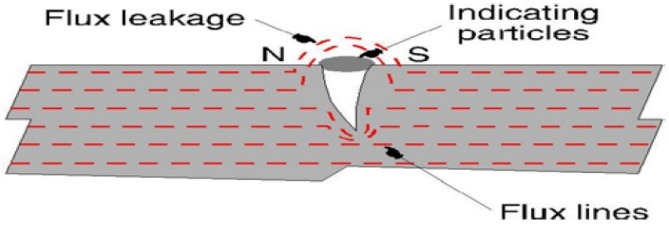

Figure 2.2. The Magnetic Particle Testing (MPT) [1].

2.3) Eddy Current Testing

Eddy Current Testing (ECT) is very beneficial for several different applications such as; for assessment of coating thickness, measuring the electrical conductivity of a material, evaluation of metal loss due to erosion and corrosion, detection of anomalies such as cracks, dents, and pits. It can also be used for material sorting in terms of their magnetic permeabilities and electrical conductivities. A few of the industries that make use of ECT are; aerospace, marine, automotive and manufacturing industries. This is a very attractive NDE technique for detecting surface and sub-surface defects, especially when its location and orientation has been established. The test setup required for ECT includes; a magnetizing coil connected to an alternating current source, a voltmeter to read the voltage variation across the coil and a conductive sample [7]. The first stage in ECT is the excitation of a conductive sample by passing an alternating current through a coil, which is in close proximity to the sample being investigated. This generates a varying magnetic field, which induces a current flow through the sample according to Faraday's Law of electromagnetic induction. These induced currents are known as eddy currents, and they travel in closed loops. The eddy current also produces its own secondary magnetic field, which opposes the initial field generated by the coil due to Lenz's law. The interaction between the two fields can be measured using an appropriate magnetic field sensor or a simple pick up coil. The information acquired from the sensor can now be processed to give an indication regarding the position and nature of any defect present, as well as any changes in the material property such as conductivity [8].

The signal measured by the pick-up coil is the coil impedance (Z), which depends on the difference between the initial and secondary fluxes (effective linking flux φl). The existence of a defect in the sample will alter the eddy currents conducting path, resulting in a distortion in its flow and variation in Z and φl. A common ECT technique is to adopt the differential probe system method, which involves using two similar coils but wound in opposite directions [9]. When both coils are brought in close proximity to a non-defective sample as shown in Fig. 2.3a, the signals emanating from both coils will cancel each other out, resulting to a zero output

($-\varphi l_1 = \varphi l_2$). However, if both coils are placed above a defective sample as shown in Fig. 2.3b, the defect will alter the eddy current flow and the linking fluxes ($-\varphi l_1 \neq \varphi l_2$) [10]. This change can then be seen in the form of a variation in the real and imaginary parts of the impedance as displayed in Figs. 2.3c and 2.3d. Since ECT makes use of an alternating current for its operation, the eddy current density will decrease exponentially with increasing depth down the sample. This is referred to as the skin effect [7]. The excitation frequency used for the coil can differ from a few Hz up to the MHz level. The level of frequency to be selected is dependent on the nature of the material used and the depth of the defect being considered. For surface defect detection, very high frequency levels are preferable to ensure an optimum resolution and best sensitivity. However, for sub-surface defects, lower frequency levels should be used to obtain the much needed penetration depth, but this lowers the sensitivity of detection for surface and near surface defects. Moreover, very high conductive ferromagnetic samples will require a much lower frequency to achieve the optimum penetration depth. Some of the advantages and disadvantages of ECT are listed in table 2.3, while Fig. 2.3 shows a diagram illustrating the principle of ECT [11].

Table 2.3 Eddy Current Testing (ECT).

Method	Advantages	Disadvantages
Eddy Current Testing (ECT)	Detects surface and sub-surface defects. Can be contactless. Used for more than defect detection. Fast and reliable. Suitable for coated samples. Wide range of frequency usage.	Inspects conductive samples only. Limited penetration depth. Requires skill and training. Impurities influences sensitivity. Suffers lift-off effects.

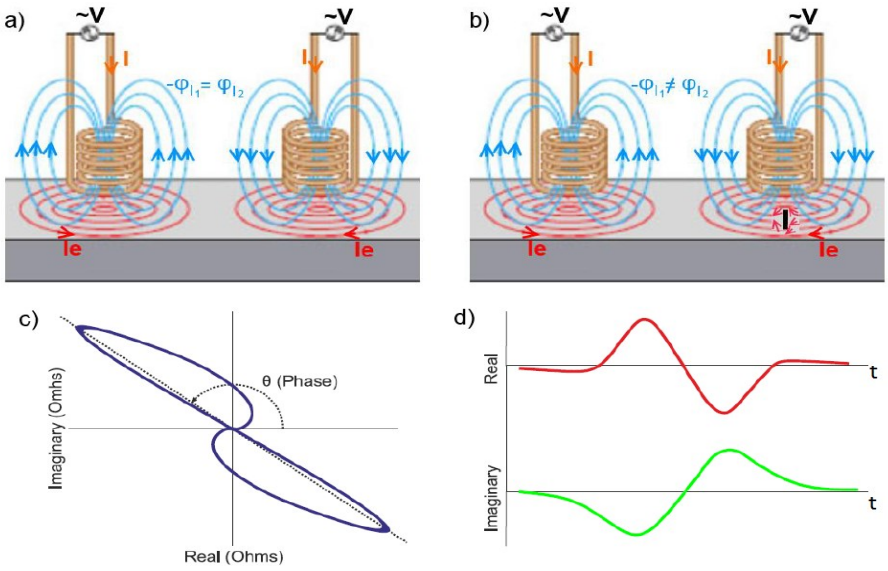

Figure 2.3. An Eddy Current differential probe placed directly above; a) non defective sample and b) defective sample displaying the EC flow distortion. A plot of the signal output emanating from an EC differential probe, illustrating the existence of a defect; c) loop on a complex plane and d) the impedance real and imaginary parts as a function of time [11].

2.4) Ultrasonic Testing

The Ultrasonic testing (UT) is a very attractive technique for characterizing the properties of materials in terms of attenuation and sound velocity. It is also used for locating surface and sub-surface defects in several different materials such as; woods, metals and plastics. It is mainly utilized in industries with product lines that are investigating stress corrosion cracking and other types of corrosion. The types of defects that can be detected while using this method includes; deformations, cracking, wall thickness variation, laminations (sloping), weld characteristics, internal and external metal loss, etc. The conventional UT method uses a piezoelectric transducer to convey high frequency ultrasonic sound pulses with short wave lengths to the sample being investigated. The transmitted pulses are then reflected by voids in the sample due to the presence of defects such as: welds, dents or cracks as displayed in Fig. 2.4a [3]. The reflections transmitted and received by the same transducer are then analyzed to differentiate between the reflections from the sample sides and edges and the reflections caused by the defects [3]. This method

requires the use of a coupling channel such as a gel or water to acoustically couple the pulses from the piezoelectric transducer to the sample under test. The need for a coupling liquid makes the UT inadequate in certain circumstances, because of the need for surface preparation and the risk of missing out flaws in areas where the coupling liquid is absent. Moreover, despite the ability of the UT method to detect defects all through the volume of the test sample, it is challenging to differentiate between reflections from the sample surfaces and reflections from the surface and sub-surface defects.

Presently, a lot of effort has been invested on the application and development of the Electromagnetic acoustic transducer (EMAT) method for an efficient NDE, by exploiting ultrasonic sound waves. EMAT is a type of transducer which is designed to use electromagnetic mechanisms to generate and receive sound, without being limited to electrically conductive samples [12, 13]. The major advantage of this technique is that it does not require contact or coupling medium to transmit ultrasonic sound waves to the test sample, since the sound generation is done directly within the sample and close to the transducer. This makes the EMAT method more effective and suitable for inspections in a wide variety of environments and conditions [14].

The EMAT process makes use of two components, a magnet (permanent or electromagnet) and an electric coil. The magnet is used to generate a static magnetic field, known as the initial magnetic field at the internal surface of the test piece. Then an alternating current with a frequency between 10 KHz and 20 KHz is passed through the coil [14]. This induces a current (eddy current) at the internal surface of the test piece, resulting in Lorentz forces. Ultrasound waves are then generated in the test piece when placed within close proximity to the EMAT, due to the interaction between the initial magnetic field and the magnetic field produced by the coil. The mode and type of ultrasound produced as well as its nature of propagation through the sample is dependent on the structure and type of transducer used [15]. EMAT is mainly useful in industries such as the oil and gas pipelines, pressure vessels, metal manufacturing and processing. Also, it is used in applications such as; characterization of material property, thickness measurements, weld inspection and flaw detection.

Some of the advantages and disadvantages of UT are listed in table 2.4, while Fig. 2.4a and 2.4b shows the diagrams illustrating the principle of UT and EMAT respectively.

Table 2.4 Ultrasonic Testing (UT).

Method	Advantages	Disadvantages
Ultrasonic Testing (UT)	Very reliable for defect sizing (high accuracy). Detects internal and external metal loss. Measures linear and direct wall thickness. Superior penetration depth than any other method. Can be used for material characterization.	Requires more skill than any other method. Roughness and poor surface finish can affect result. Often requires a reference sample. Surface need to be accessible to both probe and coupling liquid.

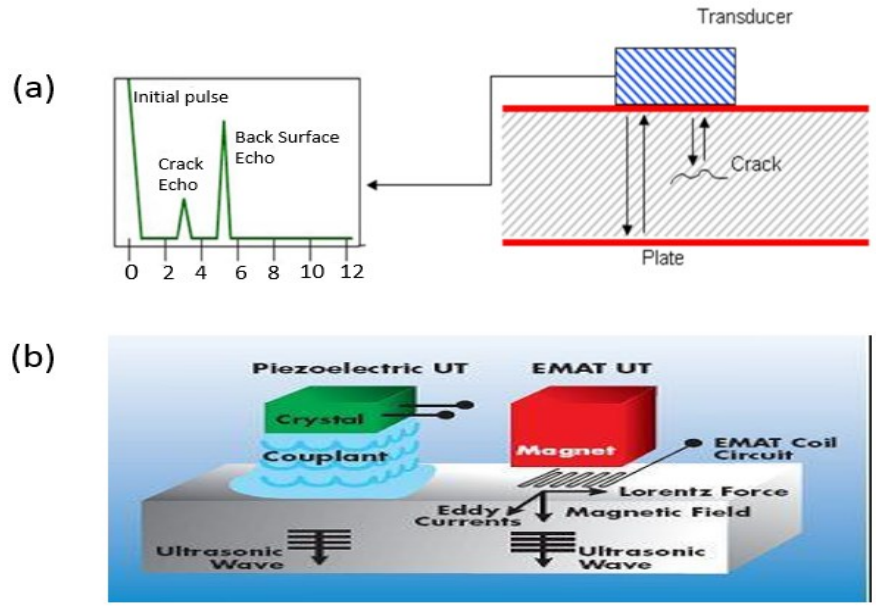

Figure 2.4. Showing a) the Ultrasonic Testing (UT) [3] and b) Electromagnetic acoustic transducer (EMAT) [14].

2.5) Radiographic Testing

Radiographic Testing (RT) is usually conducted in industries to evaluate the properties of a material without damaging it, and to make sure that the material is free of any errors and impurities. It also helps in identifying the nature and size of discontinuities, which are then evaluated according to acceptance criteria to determine their consideration as defects. This technique uses high frequency, short wavelength electromagnetic radiation generated by a radiation source to examine materials for embedded flaws. The radiation source could be either an x-ray generator or a radioactive source (industrial sources of gamma rays are, Co-60 Ir-192 or Cs-137). X-ray radiography is used to inspect a variety of non-metallic parts for porosity, water entrapment, cracks, etc. It can also be used to inspect other classes of metallic products such as; welds, casting and forging, as well as for locating discontinuities in fabricated structural assemblies like; inclusions, debris, loose fitting, corrosion, rivets, cracks and other variations. Gamma rays are the emissions from disintegrating nuclear of radioactive substances. Gamma-ray radiography has advantages of simplicity of operation, compactness of radioactive sources and independence from outside sources. It is used in engine components requiring high energy levels where access is difficult.

The main principle of RT is that it utilizes penetrating radiation that is guided towards a test specimen on to a photographic film (usually placed in a cassette), resulting in the image of the specimen's internal structure being recorded on the film. The specimen is positioned between the film (detecting device) and the radiation source. The specimen will absorb some of the radiation. The amount of energy absorbed by the specimen depends on its thickness and density, thus, greater proportion of the absorption will occur at the thicker and denser sections of the specimen [16]. The energy not absorbed by the object will cause exposure of the film. Since the magnitude of the radiation absorbed is dependent on the material thickness and density, discontinuities such as cracks, dents and welds present in the specimen will cause variations in the radiation intensity transmitted [17]. The variation in absorption is registered on film or electronically (computed radiography) [18, 19]. The shade of the film will differ with respect to the magnitude of radiation

reaching the film via the test object when developed. Lighter sections of the film demonstrate lower energy exposure, while darker sections demonstrate higher energy exposure. After processing, an image is obtained showing up as density changes in the film. These developed images provide information about the thickness variation of the specimen, including defect indication on or within the specimen (dark areas).

The accuracy of RT depends on the capability of the operator to interpret the radiographic images. The RT technique has sensitivity limitations for crack detection. The x-rays view a crack as a thickness deviation and the greater the deviation, the higher the chances of detecting a crack. A crack may not be visible if the pathway of the x-ray is not parallel to the crack, causing a reduced thickness deviation. The orientation of a crack must be ascertained prior to using the RT technique for inspection, since the angle between the crack and the radiation beam is so vital. RT is generally used to determine the integrity of welds, by locating internal defects such as inclusions and porosity, as well as gauging the thickness of objects. cracks must be at least 2 % of the section thickness for detection to occur [1]. For example, a sample with a thickness of 15 mm, the least defect that can be detected would be 0.3 mm in dimension, and for a sample with a thickness of 30 mm the least defect that can be detected would be 0.6 mm. Therefore, detection capability decreases with increasing sample thickness. Major benefits of using RT is that; it can effectively detect both surface and internal discontinuities, significant variations in composition can be checked, very few material limitations, hidden areas can easily be inspected, minimum preparation is required and a permanent test result is obtained. Its only major disadvantage is that radiations can be hazardous to the operator and nearby personnel. Some of the advantages and disadvantages of RT are listed in table 2.5, while Fig. 2.5 shows a diagram illustrating the principle of RT [20].

Table 2.5 Radiographic Testing (RT).

Method	Advantages	Disadvantages
Radiographic Testing (RT)	Detects surface and internal discontinuities. Permanent test result is obtained. Hidden areas can be inspected. Very few material limitations. Minimum preparation is required.	Radiations can be hazardous. Detection capability decreases as specimen thickness increases.

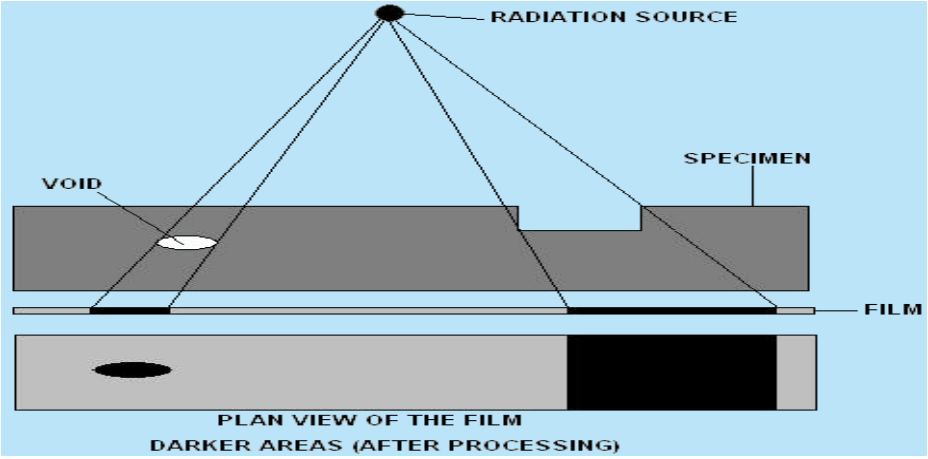

Figure 2.5. The Radiographic Testing (RT) [20].

2.6) Microwave Testing

The Microwave Testing (MT) is a non-contact NDE technique used for inspecting non-conductive samples such as; dielectrics and composites used in aircrafts, ships, cars, buildings and bridges [21]. The MT method has several unique attributes, which makes it more attractive over other NDE techniques. These attributes include; good penetration depth, relatively inexpensive, superior resolution, and the numerous features of the antenna used for the sensor system. The parameters measured by the MT technique are; loss factors, dielectric constants, reflection coefficients, transmission coefficients and the complex permeability, as a function of temperature and frequency [22]. The material parameters of concern (e.g. corrosion, cracks,

moisture content, dents, etc.) can then be associated to the parameters measured using relevant and acceptable calibration and modelling techniques.

The principle of MT involves transmitting high frequency electromagnetic waves into the sample being investigated. Then a receiver is used to map out the amplitude and phase characteristics of the transmitted and reflected wave, thereby producing an image of the sample under test [23]. In several applications, more modernized, much lighter, much stronger and more durable materials such as; dielectrics and composites are replacing metallic components. However, these new materials need a different inspection technique. The conventional electromagnetic NDE methods used for inspecting metallic components may not be well-suited to inspect such materials. This is usually as a result of the comparatively thicker nature, texture, attenuation, and reduced electrical conductivity of composites. In contrast, microwave NDE methods are more convenient for inspecting such materials. This is because, microwave signals can readily penetrate through low loss dielectric structures and can be used to inspect non-conductive specimens [24], as well as inspections under paintwork [25] such as; ceramics, plastics and glass, without undergoing any serious signal attenuation. Also, microwave testing method could be integrated with other NDE techniques, such as the eddy-current method to achieve the best result possible [26]. Some of the advantages and disadvantages of MT are listed in table 2.6, while Fig. 2.6 shows an image of a painted steel sample with a corrosion patch (dark section) obtained using the MT method [27].

Table 2.6 Microwave Testing (MT).

Method	Advantages	Disadvantages
Microwave Testing (RT)	Non- contact technique. Good penetration depth. Good resolution. Relatively inexpensive. Suitable for Inspecting non-conductive specimens. Suitable for inspections under paint work.	Microwave radiations can be hazardous.

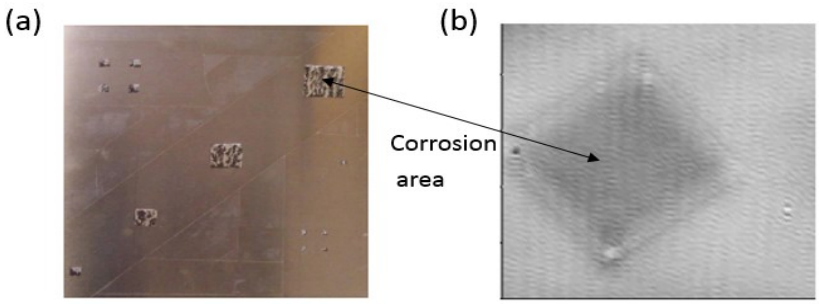

Figure 2.6. Showing; a) a picture of corroded steel and (b) intensity image of the corrosion patch on the painted steel obtained using Microwave Testing (MT) [27].

2.7) Thermography Testing

Thermography Testing (TT) is an NDE technique used for measuring and mapping out surface temperatures. The thermal and infrared measurement approach makes use of the thermal measurement of a specimen under investigation, as it undergoes a response to stimulus. Thermal imaging cameras are the most frequently used sensing technique. Thermography testing can be grouped into two methods, which are; the passive and the active measurement methods. Passive thermography is used to examine samples that are not at room temperature (usually higher). Passive imaging devices are used to capture hot spots suggestive of complications in an electrical or electronic circuit. The active thermography makes use of an external heat source, such as; eddy current or a lamp to heat the test sample, followed by the measurement of the temperature variation produced as a result of discontinuities present [28, 29]. For the eddy current type thermography, the sample is heated by means of heat induction, then the induced eddy currents are transformed to heat via ohmic heating according to Joule's law [30-32]. Any defect present in the sample will alter the current flow and modify the distribution pattern of the temperature. The results obtained can then be analyzed via thermal imaging, to show a sign of any serious imperfection. The imaging of the test sample after the heating stage can also be utilized for heat flow monitoring in the sample, as a function of the material properties and boundaries [1]. In composite materials, flash thermography has proven to be very profitable for imaging delamination and bond breakings.

A recent and vital improvement in the thermography NDE method is the use of mechanical energy to provide confined heating at the sub-surface flaw region, such as for; cracks and voids in metallic components [1]. This has created a new branch of implementation for the IR technique. The infrared thermography (a remote inspection technique) has been confirmed to be very reliable, efficient and cost-effective for the examination of concrete structures. Electromagnetic radiation is emitted from all materials with a wavelength proportional to the material temperature, and the material temperature is inversely proportional to the radiation frequency. Radiometers, which consist of an infrared detector, are used for the detection and measurement of such radiation. The infrared detector converts the radiation emitted into electrical signals, which are shown on the computer screen. The infrared thermography can effectively detect discontinuities in bridge decks, garage floors, building walls, highway pavements, parking lots, and for critical examination of aerospace structures [1, 33]. It can be used during the day or at night, depending on the type of result required and the surrounding condition. Variation in temperature distribution as minute as a few hundreds of a degree Celsius can be measured, via the infrared thermographic scanning system. Some of the advantages and disadvantages of TT are listed in table 2.7, while Fig. 2.7 shows a diagram illustrating the principle of TT [3].

Table 2.7 Thermography Testing (TT).

Method	Advantages	Disadvantages
Thermography Testing (TT)	Safe to use. Can examine large areas. Suitable for wide verities of materials. Reliable method. Temperature distribution can be imaged to show defect profile	Expensive IR cameras required.

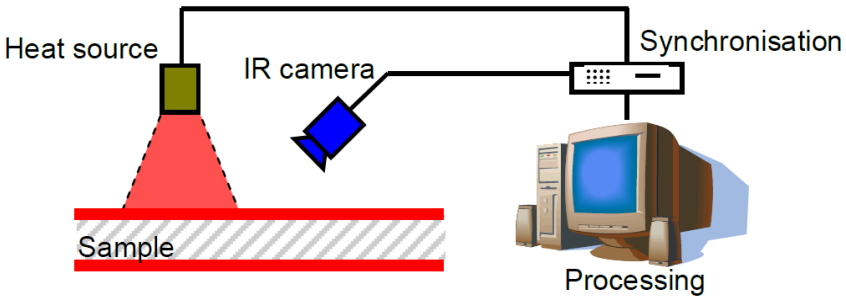

Figure 2.7. The active Thermography Testing (TT) [3].

2.8) Magnetic Flux Leakage Testing

Magnetic Flux Leakage Testing (MFLT) is a non-contact technique of NDE used for examining ferromagnetic steel structures for presence of defects such as; corrosion, cracks, welds, pits, etc. [34, 35]. It is the most reliable, efficient and widely used approach for detecting cracks present in both the circumferential and axial directions [36]. MFL method has been in existence as a notable technique for pipeline health monitoring since the 1960's [37, 38]. In the introductory phase, the sensing system used were magnetic powders, which outputs its test results by accumulating at the defective region. The technique is direct, easy, and highly sensitive. The MFLT has been extensively used in the petrochemical, oil and gas industries. Since the evolution of the semiconductor electronic industries, magnetic sensors have achieved enormous breakthrough in detecting the MFL signal with great accuracy. This eliminated the drawbacks of measuring devices like the coil sensor and magnetic powder. MFL inspection does not require pre-processing and the resulting leakage signal are simple to detect and distinguish. Online-based detection can be comfortably achieved and a high degree of automation can be realized. Furthermore, it can capture several types of anomalies such as; cracks, corrosion, cavities, shrinkage, voids, etc. MFL inspection is not limited to assessing the internal surfaces for flaws but can also assess external surfaces for far-surface flaws [39]. The required conditions for the detection environment are not many and they are not disturbed by the transportation medium. These numerous advantages confirm why the MFL testing method is regarded as the most popular and widely used NDE technique [36, 40].

As the Pipeline Inspection Gauge (PIG) is discharged through the underground pipe to implement the pipeline investigation process, vibrations could be felt at close proximity from the pipeline as the PIG moves along the pipeline during an MFL inspection [40-43]. This explains why the MFL detectors were termed intelligent PIGS [44, 45]. A typical MFL PIG system is shown in Fig 2.8. The PIG collects information about the pipeline, both internally and externally. The information that can be generated by the PIG include; the pipes diameter, temperature, curvature, bends, metal loss and corrosion. The PIG uses both magnetic flux leakage and ultrasound to generate information regarding the interior and exterior of the pipeline. The MFL technique inspects the pipeline system by magnetizing the pipe wall, followed by the detection of the leakage flux caused by corrosion, cracks or pits in the pipe wall. The ultrasonic technique measures the pipe wall thickness by measuring time delays in the reflection of high-frequency sound waves.

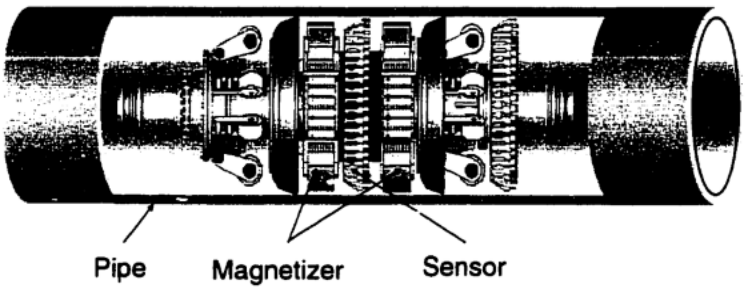

Figure 2.8. A schematic diagram of an MFL inspection system (PIG)[40].

MFL investigation became a popularly known and used NDE technique since the early 50s in the 20th century [36]. Since then, it has grown from the qualitative recognition of flaws in components and assemblies to the quantitative investigation stage [46]. Proper use of the MFL technique in inspecting pipeline structures would contribute immensely to their performance. It will also help significantly in guiding the decision making in the management of such facilities, as well as minimize the risk of complete damage [47].

In spite of some promising theoretical and experimental accomplishments based on MFL testing, the method is not completely accurate. Some of the major drawbacks of the MFL inspection are outlined as follows [48, 49]: a) Current inspection

techniques provide largely qualitative data and are unable to replicate the level of quantitative information achievable under laboratory conditions. b) The pipe wall must be near to magnetic saturation. c) It is very sensitive to the moving speed of the motor. d) Further study and analysis is required to develop a quantitative theory for flaw detection. Currently, no direct correlation exists between the MFL signal characteristics and the depth, shape and orientation of the flaw e) The probe is heavily influenced by the pipe wall topography, especially the presence of obstructions. f) Misinterpretation of data is possible due to the presence of pipeline impurities. g) The MFL technique can be applied to large areas, but at the same time is restrained to the material surface and near surface. Therefore, the method has difficulty in detecting long and narrow axial flaws located far beyond the sample surface.

The MFL inspection principle involves magnetizing the test structure (ferromagnetic steel pipe) with either a permanent magnet or an electromagnet to near or complete saturation. A magnetic field is generated, which is perpendicular to any existing defect (e.g. crack) within the pipe. The ferromagnetic material used for the pipeline manufacturing has a much higher permeability compared to the permeability of the surrounding air. Hence, there will be an increased magnetic flux lines flowing inside the pipe compared to those on the outside (flux is confined in the sample). If there is no defect in the magnetized pipe, a greater proportion of the flux will go through the inside region of the pipe material. However, a defect present in the pipe structure will cause a significant increase in the reluctance to the flow of flux lines, due to a decrease in magnetic permeability at the defective region [36]. This will result in a leakage of flux from the pipe wall, at the defective region [50, 51]. The leakage flux pattern (leakage field signature) is dependent on the orientation and geometry of the defect with respect to the magnetic flux in the pipe material. The leakage flux along the pipe axis is called the axial ($\boldsymbol{B_x}$) MFL component, the leakage flux normal to the pipe surface is referred to as the radial ($\boldsymbol{B_y}$) MFL component, while the leakage field along the circumferential axis of the pipe surface is called the tangential ($\boldsymbol{B_z}$) MFL component as shown in Fig. 2.9.

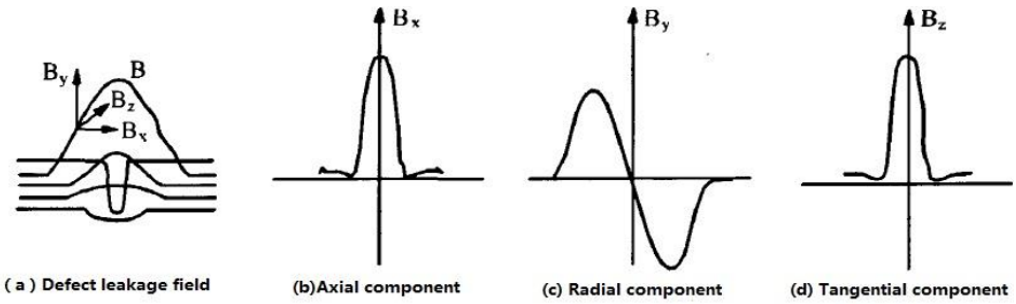

Figure 2.9. Showing; a) The leakage field from a defect and the vector components of the leakage field in; b) axial direction, c) radial direction and c) tangential direction [36].

The width of the defect is represented by the horizontal axis while the vertical axis represents the magnetic flux leakage intensity. The permeability of the ferromagnetic material used for the magnetic circuit plays a vital role in determining the magnitude of the magnetic flux flowing within the closed path of the circuit. It also determines the magnitude of the magnetic flux density and the leakage field that will occur. The higher the permeability of the ferromagnetic material used, the greater the flux intensity that will be developed within the circuit and the higher the leakage field magnitude that will occur. The induced magnetic field should be large enough to cause a sizable leakage field to occur, especially for the detection of miniature defects (e.g. hairline cracks) in pipeline structures [52]. If enough magnetic saturation of the test sample is not achieved, defects less than a few percent of the sample's cross-sectional area may not be identified, while using the MFL inspection technique. The magnetic saturation of the sample is dependent on the magnetization sources used (permanent or electromagnet) to magnetize the sample, as well as the gap between the magnetizer and the test sample (magnetizer lift-off). A single or multiple MFL sensors (sensor array) such as; GMR sensors, AMR sensors or Hall Effect sensors, which are sensitive to variation in flux density, is placed perpendicular to the defect orientation and within close proximity to the defect in order to pick up the signal produced by the leakage field, both from the internal and external surfaces of the pipe. The leakage signal magnitude is dependent on the distance between the MFL sensor and the test sample (sensor lift-off).

There are three different techniques for magnetizing the pipe wall, while employing the MFL inspection technique of NDE. These methods are; the Direct Current (DC), Alternating Current (AC) and Pulsed Current (PC) magnetization techniques.

The DC magnetization technique employs the use of an electromagnet or permanent magnet to produce a static magnetization current for the magnetization of the test pipeline. The electromagnet based DC magnetization is best applied for materials with hard-magnetization, such as; steel pipelines, storage tanks, rail lines and bridges. This is because a large supply current is needed to generate a strong magnetization field. This approach can detect a far-surface hairline crack located 9.6 mm away from the surface of the pipeline and the magnetization can easily be adjusted by simply controlling the magnitude of the supply current. However, demagnetization of the test sample is crucial every time this approach is used. The permanent magnet based magnetization utilizes a permanent with a large coercivity (coercive force ($\boldsymbol{H_c}$)) as the excitation source. It shares similar characteristics with the electromagnet-based magnetization, however, the ability to adjust and control the magnetization intensity is less convenient, compared to the electromagnet approach. Generally, the types of permanent magnets used are; ferrite, Neodymium-Iron-Boron (NdFeB), aluminum-nickel-cobalt, and rare-earth permanent magnets, especially the rare-earth permanent magnets, due to their high-energy nature and reduced size. The DCMFL inspection technique provides limited information about detected cracks, in terms of location and sizing. This is because the crack must exist on one side of the test sample to ensure accurate interpretation of the crack size, as the approach only relies on just one measurement feature (i.e. the leakage field amplitude/intensity) to detect and characterize defects. Another major drawback of the DCMFL technique is the continuous powering of the excitation yoke and coil leading to overheating and the need to cool down the system, especially for longer inspection periods. This approach is not suitable for inspecting long pipelines.

The AC magnetization technique employs the use of a sinusoidal waveform, with a single excitation frequency, to produce a varying magnetization current for the magnetization of the pipeline material. The AC magnetization technique can be used to inspect materials with non-uniform surfaces for the presence of cracks. However, the problem of skin-effect arises due to the eddy current phenomenon. Hence, the penetration depth of the induced magnetic field decreases with increasing excitation frequency. The ACMFL technique is usually sensitive to only one side of the test sample, depending on the excitation frequency selected. Selecting a high excitation

frequency results in magnetic field concentration at the surface layer of the sample, which is suitable for surface crack detection and characterization. However, using a low frequency excitation will provide deeper magnetic field penetration into the test sample, which is suitable for far-surface crack detection, while causing a decrease in sensitivity for surface and near surface crack measurements.

The PC magnetization technique employs the use of a square pulse to produce a varying magnetization current, for the magnetization of the pipeline material. The single excitation waveform (square pulse) contains a string of frequency components, with the sensitivity to surface and near surface measurements (i.e. high frequency components), as well as the required depth penetration of low frequency excitation, suitable for far-surface crack detection and characterization. Therefore, the PMFL technique allows for the detection and characterization of far-surface cracks in thicker samples, while still maintaining a good measurement sensitivity to surface and near surface cracks, using a relatively simple driver circuit.

After the inspection is completed, the recorded MFL signals are carefully analyzed and interpreted using methods that convert the measured signal into information regarding the pipeline integrity. The result from the analysis is used to obtain the nature and severity of the defect. Zatsepin and Shcherbinin presented an analytical illustration of a dipole model for the prediction of the leakage field pattern due to a rectangular defect [53]. The concept of this technique is shown in Fig. 2.10. Where $\boldsymbol{H_a}$ is the induced magnetic field in the test sample, $\boldsymbol{H_d}$ is the demagnetizing field produced by the magnetic charges at the end surfaces of the defect, 2a and b are the width and depth of the defect respectively.

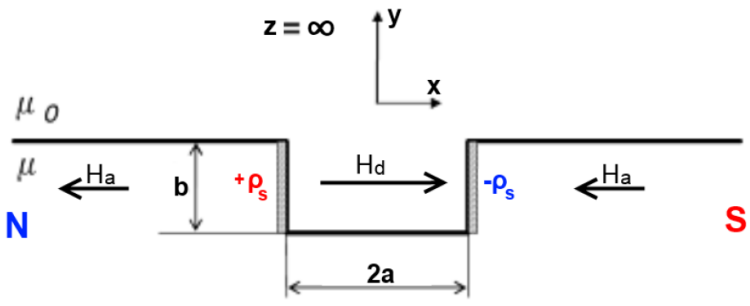

Figure 2.10. The dipole model of the leakage field principle as presented by Zatsepin and Shcherbinin for a rectangular defect [53].

Equations (2.1) and (2.2) show the tangential ($\boldsymbol{B_x}$) and normal ($\boldsymbol{B_y}$) components of the leakage flux density respectively, as presented by Zatsepin and Shcherbinin for the above scenario.

$$B_x = \frac{\mu_0 \rho_s}{2\pi}\left[tan^{-1}\left(\frac{b(x+a)}{(x+a)^2+y(y+b)}\right) - tan^{-1}\left(\frac{b(x-a)}{(x-a)^2+y(y+b)}\right)\right] \quad (2.1)$$

$$B_y = \frac{\mu_0 \rho_s}{4\pi} In\left[\frac{((x+a)^2+(y+b)^2)((x-a)^2+y^2)}{((x-a)^2+(y+b)^2)((x+a)^2+y^2)}\right] \quad (2.2)$$

The magnetic charge density at the end surface of the defect (i.e. at the dipole north and south poles) is denoted by ρ_s, and can be obtained from equation (2.3) as presented by Edwards and Palmer [54]. Where n is the ratio of the defect depth and the half-width, i.e. $n = b/a$.

$$\rho_s = \boldsymbol{H_a}\left(\frac{\pi n(\mu_r - 1)}{(n+\mu_r)tan^{-1}(n)}\right) \quad (2.3)$$

Abe et al. confirmed the leakage field distributions calculated using equations (2.1), (2.2) and (2.3), via practical experiments. The experimental results had a good correlation with the calculated results for the scenario of a rectangular defect present in a steel sample, as shown in Figs. 2.11a and 2.11b [55].

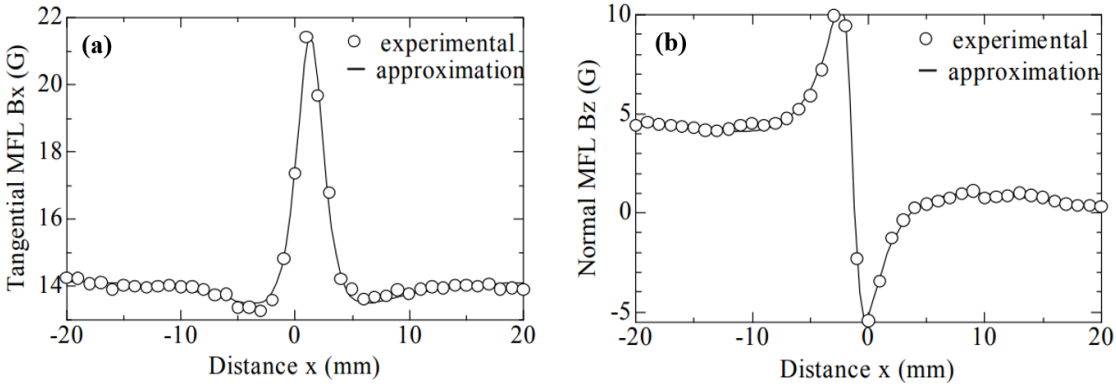

Figure 2.11. The MFL signals caused by a rectamgular defect present in a steel sample a) Tangential component and b) Normal component [55].

2.9) Major Issues of MFL Testing

Despite the fact that the MFL technique has a high probability of detecting cracks, the technique is not very sensitive to crack size and it requires accurate calibration measurements. Hence, the characterization of cracks is difficult, especially for far-surface cracks. The MFL technique also has a poor sensitivity to small cracks leading to misinterpretation of signals caused by permeability variation in the pipeline material. Moreover, the nature of the MFL signals means that an experienced operator is required to accurately interpret the signals, thereby increasing the inspection time and cost. Therefore, there is a need to develop new feature extraction techniques in order to automate the crack characterization process for estimating crack geometries, especially for hairline cracks.

The major factors affecting the MFL inspection results are the; scanning speed, spatial resolution of the signals obtained and the sensor lift-off. For traditional static MFL inspection systems (i.e. stationary probe relative to sample surface) with DC magnetization, eddy current will not be induced in the conductive sample. However, for dynamic MFL inspection systems (i.e. moving probe relative to sample surface), eddy currents are induced in the sample and concentrates around the sample surface, even though the magnetization current is DC. The induced eddy currents are due to the relative motion (scanning speed) between the induced magnetic field and the magnetized material [56, 57]. The induced eddy-current changes the magnetic field profile in the sample, and the change is linearly related to the scanning speed of the probe. Moreover, the eddy current profile is dependent on the scanning speed, hence, the skin effect also applies in dynamic MFL inspection. Fig. 2.12 shows the axial ($\boldsymbol{B_x}$) component of the MFL signal as a function of scanning distance, for different probe speeds. As can be seen, the trajectories of the leakage field in each dynamic case is asymmetric compared to that at 0 m/s. The two peaks of the leakage field signal occur at the ends/edges of the crack and can be quantitatively used to determine the width of a crack, especially for very wide cracks. The variation in magnitude of the two peaks demonstrates the probes moving direction. Also, as the scanning speed increases, the variation in magnitude between the two peaks increases. In addition, the eddy currents generated due to the probe speed decreases

the net induced field in the specimen [56]. This in-turn results in a decrease in the MFL signal amplitude as shown in Fig. 2.12.

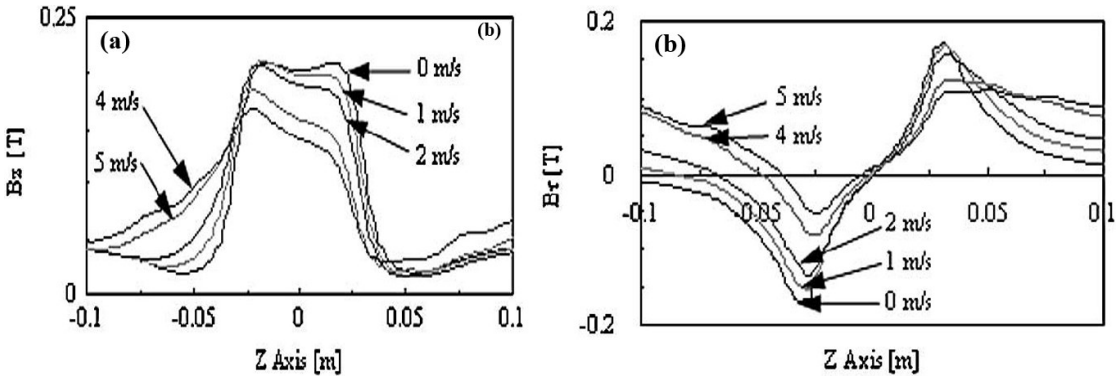

Figure 2.12. The MFL signal amplitude at different scanning speeds a) Axial component of the MFL signal and b) Radial Component of the MFL signal [57].

The decrease in the MFL signal amplitude due to the scanning speed can be up to 75% in the pipeline inspection industries, where the scanning speed is as high as 8 m/s [58]. The MFL signals are also distorted as the scanning speed increases [57]. The percentage decrease in the MFL signal amplitude due to the inspection speed can be calculated from equation (2.4). The percentage decrease in the MFL signal is denoted by $\%SigRd$, while the MFL_{ref} and MFL_{pp} are the peak to peak value of the defect signal at the lowest scanning speed obtainable (lowest speed of the translation stage) and the peak to peak value of the defect at a specified velocity respectively.

$$\%SigRd = \left[\left(\frac{MFL_{ref} - MFL_{pp}}{MFL_{ref}}\right)\right] \times 100 \quad (2.4)$$

During pipeline inspection, the MFL signal sampling is generally implemented at a fixed spatial resolution (relative to space) instead of at a temporal spatial resolution, since the scanning speed can change [59]. More data will be obtained while using a system with a high resolution, which consequently increases the defect characterization capability. However, the trade-off between the increased resolution and excessive data must be optimized during system design [60]. The spatial resolution of an MFL system can be obtained from equation (2.5). The spatial resolution is denoted by SR (samples/mm), while the scanning velocity (mm/s) and

sampling frequency of the data acquisition card (samples/s) are denoted by V_{scan} and f_{sample} respectively.

$$SR = \frac{f_{sample}}{V_{scan}} \tag{2.5}$$

The MFL signal amplitude decreases with increasing sensor distance relative to the sample surface, as shown in Fig. 2.13a by Singh et al [61] and Fig. 2.13b by Fei et al [62]. The reduction in the signal amplitude is due to the leakage field attenuation with increasing sensor distance from the defect. The signal attenuation becomes more severe at higher scanning speeds, where the rate of change of the induced magnetic field in the sample is significantly increased.

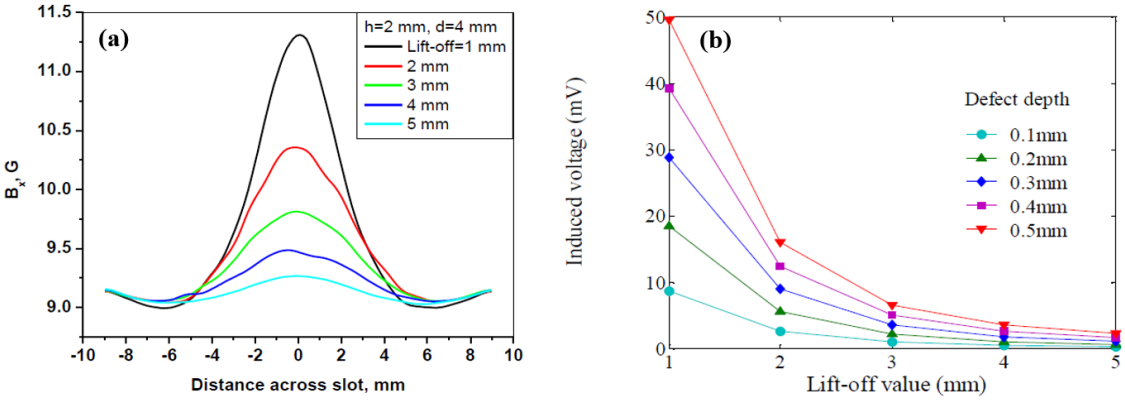

Figure 2.13. Showing a) The MFL signal amplitude at various sensor lift-offs for a 4mm deep sub-surface defect positioned at 2mm below the sample surface [61] and b) The MFL signal amplitude as a function of sensor lift-off for various surface defects with different depth sizes [62].

Another serious limitation of the MFL method is the reduced sensitivity in detecting defects positioned further away from the sample surface (far-surface defects). This is because of the low penetration depth of the induced magnetic field in the sample caused by skin effect (eddy current generation), thus making the detection of such defects difficult to achieve, as shown in Fig. 2.14.

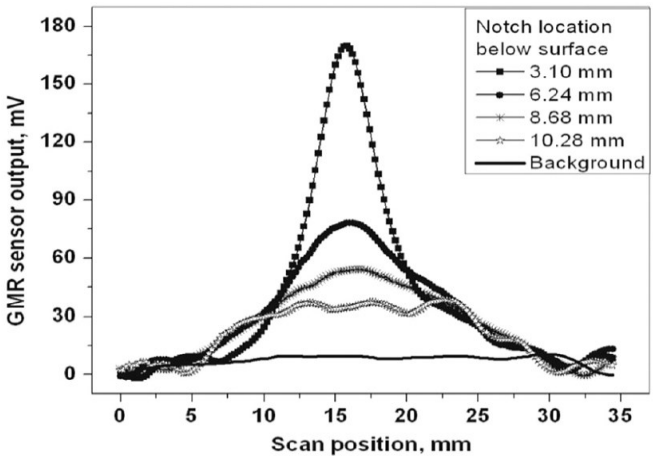

Figure 2.14. Showing a decrease in the sensitivity of MFL signal with increasing defect distance from the surface of a 12mm thick sample [63].

A lot of the MFL investigations are based on the speculation that the defect under scrutiny is a simple one, i.e straight slots or notches. However, defects could be complicated in shape and can cause a major challenge to the accurate characterization and quantification of such defects. For instance, defects could occur at an angle to the test sample surface, and the leakage field is highest in cases where the defect is perpendicular to the flux and decreases as the angle decreases. Minimum detection is achieved when the defect is postioned parallel to the flux lines, as shown Fig. 2.15.

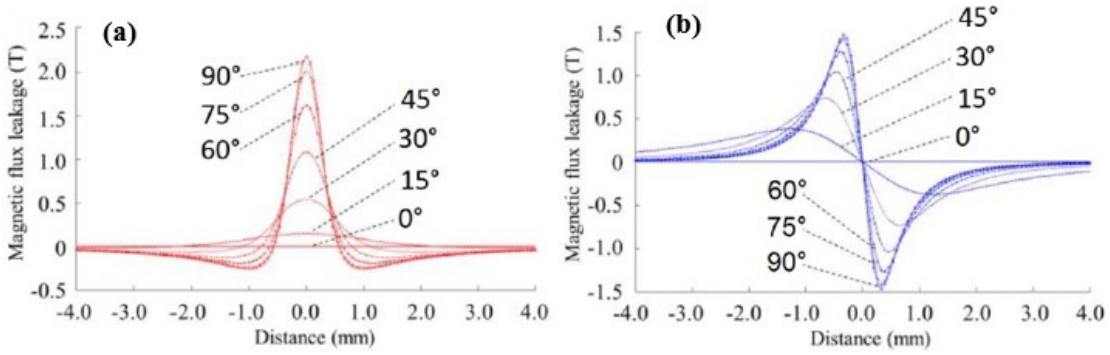

Figure 2.15. Showing an increase in the MFL signal amplitude with increasing angle between the defect and magnetic field direction a) Tangential component and b) Normal component [64].

A full MFL signal analysis plan is made up of three processes, as illustrated in the flowchart in Fig. 2.16. These processes are; identification stage, compensation stage and characterization stage [65]. As the MFL PIG system travels along the pipe, the

recorded data contains both the highly hazardous defect information and information for less hazardous defects (leakage field signals from fringes, valves, junctions, welds, etc.). The highly hazardous defect information (leakage field signals from cracks, corrosion, erosion, holes, pits etc.) are separated from the less hazardous ones using a signal identification procedure. The next stage is the compensation process. Here, the MFL signals are compensated for influence of operational variables [66] such as; sensor orientation, lift-off effects, pipe grade, scanning velocity, residual stress, etc. The shape and size of the leakage signal is modified by such variables to a significant extent, making defect characterization very challenging. However, the signal compensation processes are methods used to ensure that the leakage signal is insensitive to operational parameters, at the same time maintaining a good sensitivity to defect information. The last stage is the defect characterization; the reason for this stage is to ascertain the defects shape and size – an exercise that fall into a wide classification of problems in NDE termed inverse problems.

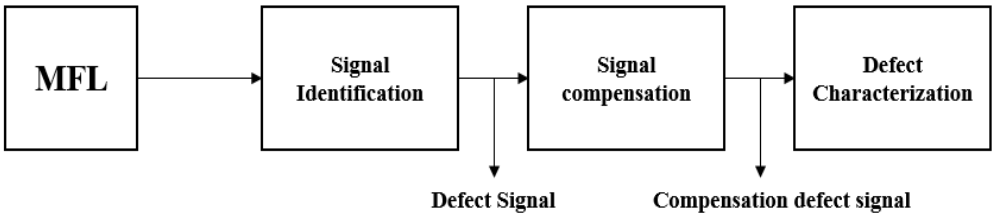

Figure 2.16. A magnetic flux leakage signal interpretation scheme.

The task of evaluating the orientation, size, shape and location of defects, based on the information embedded in the acquired signal is known as defect characterization. A signal measured in a physical operation could be evaluated for causes pointing to its source, in order to retrieve the input to the operation with unspecified parameters controlling its action, from a finite group of output examinations [40, 67]. That is deducing the previous state or condition of an object or event from their final data or result collected. This process is called an inverse problem.

Three different approaches could be used to tackle an inverse problem, these include: a database method, an iterative method, and a model based method. The database method employs a database to match the obtained result with a stored pattern. One of the benefits of this technique is that causes could be established immediately if their result matches the formerly stored patterns. The completeness of a database is hence,

a vital factor to be treated in this method. The iterative method involves establishing a forward model, followed by the modification of the predicted model till it corresponds with the measured response. The iterative method is very beneficial especially where closed form solution is absent. It is also capable of producing a correct estimate of defect parameters. The forward model could also be used to generate data sets for the database method. The disadvantage of this method is that it requires a thorough computation (large computational overhead). The efficiency of the iterative method relies on the original prediction and the initial information when an optimization scheme is used. The calibration technique is one of the most widely used characterization techniques used in industry, and it employs the use of various calibration techniques that can interpret the collected data in terms of corresponding lengths, depths and widths of defects. Here, the actual relationships between the MFL signal characteristics and the defect parameters are established based on the data gathered from a series of experiments. A modification of this method comprises of the recognition and use of the features obtained from the signal to evaluate the defect parameters. A technique involving this approach was proposed by Shcherbinin et al. [68] while using the algorithm proposed by Bulychev et al. [69], for evaluating the width of crack-like flaws. The technique made use of the magnetic permeability for the material used for the test piece with the defect, as well as the tangential component of the magnetic flux density. A general appraisal of the methodology for different pipe-wall defects is illustrated in [70]. The neural network method is another approach that is effective in estimating the entire profile of defects [71].

Analytical techniques to obtain the leakage field signals from defects exist [72, 73]. However, the best approach to tackling MFL problems is the finite element numerical methods, especially for non-uniform surfaces and for defects with complex geometries. Lord was the first to present work on the calculation of leakage field signals [74]. His effort was succeeded by the works of Forster [75], Brudar [76] and Atherton [77]. Only 2D problems with relatively small amount of elements were discussed. Moreover, because of the limitations of early computers, only a few situations and conditions could be modelled. Present works are tackled by solving the benchmark MFL problems [78]. This can be seen in the works of Zeng [79], Pignotti [80], Ruch [81] and Lunin [82]. These works were performed in 2D and 3D

environment. However, they were very specific to the requirements of the benchmark problems and did not include a discussion on the MFL signals acquired from defects of different types. Another present-day study using the 3D FEM technique and excitation yoke can be seen in works of Zuoying et al [83]. The work presented the leakage field amplitude as a function of defect length, width, depth and lift-off. However, there were no examination relating to surface and far-surface defects.

The MFL problems are usually considered a multi-parameter problem and the measurement system parameters can be grouped into; sample dependent (material, wall thickness and diameter), defect-type dependent (surface/far-surface, shape, depth, length and width), set-up dependent (excitation current, yoke and air gap), etc. The above listed studies covers only a few of the many leakage field influencing parameters, and still many questions are still unanswered. Some of the advantages and disadvantages of MFLT are listed in table 2.8, while Fig. 2.17 shows a diagram illustrating the principle of MFLT [84].

Table 2.8 Magnetic Flux Leakage Testing (MFLT).

Method	Advantages	Disadvantages
Magnetic Flux Leakage Testing (MFLT)	Fast and reliable. Relatively Cheap. Non-contact. Versatile. Safe to use. Detects both surface and far-surface defects.	Inspects only ferromagnetic materials. Suffers lift-off effects.

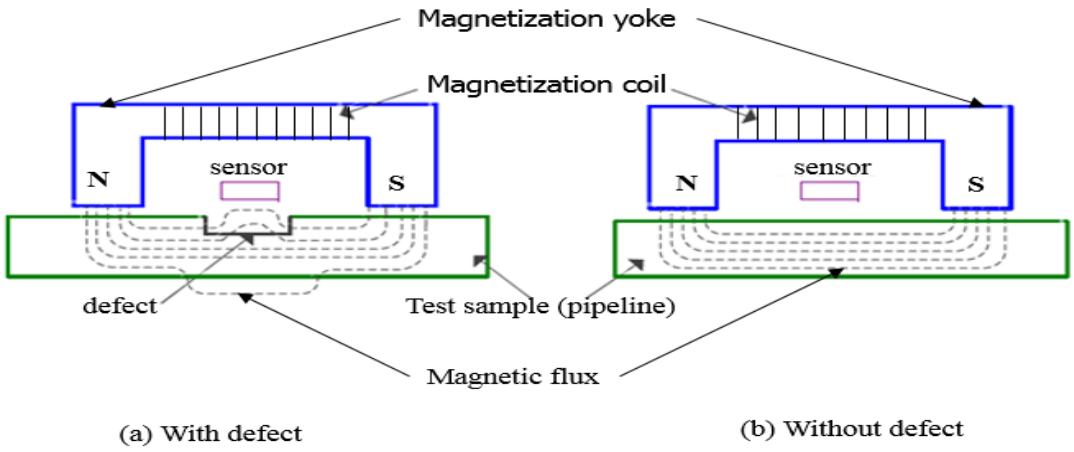

Figure 2.17. A schematic drawing of the Magnetic Flux Leakage Testing (MFLT); a) without a defect and b) without a defect [84].

2.10) State-of-the-art in Magnetic Flux Leakage Testing

The MFL inspection is an extensively used non-destructive evaluation technique for detecting defects both on the surface and far-surface of ferromagnetic components. However, the traditional MFL methods are not capable of estimating their approximate size and orientation, hence, an additional transducer is required to provide the extra information needed. The pulsed magnetic flux leakage technique is a state-of-the-art electromagnetic non-destructive evaluation method, which provides the advantage of using an excitation signal with a range of frequency components that delivers the deeper penetration depth of low-frequency excitation (50Hz) suitable for far-surface measurements and the sensitivity to surface and sub-surface measurements of high-frequency excitation (10 kHz) [85]. According to Y. Cheng and K. Rong, an alternating current with a very high frequency is suitable for surface and sub-surface crack detection, as illustrated in Fig. 2.18 [86]. However, for a coil wound around a ferromagnetic core, very high frequency will result to a higher impedance and higher losses, thus decreasing the excitation current. They also stated that an excitation current with a square pulse has a higher exciting efficiency compared to a sine wave. This is because the excitation coil and sample are likely to be overheated when operating with a powerful excitation current with a very high frequency. However, a periodic square pulse excitation current provides an

advantage of a reduced thermal effect (reduced working temperature) whilst still maintaining a satisfactory exciting efficiency.

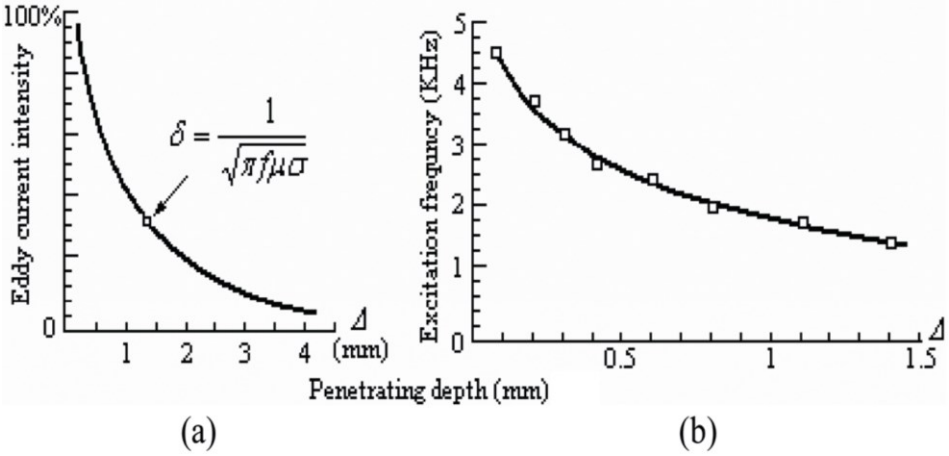

Figure 2.18. A graph showing the penetration depth of a ferromagnetic material (ferrite core) as a function of a) Eddy current and b) Excitation frequency [86].

One of the latest developments in the MFLNDE technology is the improvement from easy detection of flaws (qualitative assessment) to the evaluation of defect location and parameters (quantitative assessment) [85, 87]. So many researchers working in the QNDE of materials have presented different techniques, using the MFL method [85-91]. The PMFL method has been proven to outshine the potentials of other MFL methods in delivering useful quantitative data for estimating defect parameters. Asides providing a wide spectrum of frequency components, which delivers deeper penetration depth when compared to the traditional MFL technique, information relating to the defect location and parameters can be established from features contained in the transient signal. The principal features needed to evaluate the size and depth information of the defect from the transient signal are the time-to-peak and the magnitude of the differential PML signals [92]. Notwithstanding the remarkable developments, accurate characterization of surface and far-surface defects still remains a crucial problem.

One of the factors that is well known to pose a major problem for an efficient PMFL inspection is the lift-off effects, where the variation in the distance between the sensor and magnetizer reduces the sensitivity of detection. It is also capable of causing inaccurate measurements of the true magnitude of the MFL signal, which

could lead to defects being missed or undersized, especially for hairline cracks [93]. Such lift-off effects arise due to the presence of debris, welds, varying coating thicknesses, sensor tilt, non-uniform surface, shape and texture. A lot of effort has been channelled towards the reduction and elimination of the lift-off effects and some progress has been recorded through the use of an enhanced probe design, processing techniques, construction and use of sensor arrays [94-96].

Magnetic sensitive sensors such as GMR sensors, AMR sensors and Hall Effect sensors, has shown huge dominance over the conventional coil sensor system with the PMFL technique [85]. An optimum acquisition of information from the specimen has been achieved while using the very sensitive magnetic sensors, rather than the traditional coil sensors [85, 97]. It has been proven that the sensitivity of the MFL inspection, particularly the PMFL technique is improved while using the magnetic field sensors, compared to the coil sensor for detecting MFL signals. Also, the conventional coil sensor system is not very sensitive to low frequency fields, where the electromotive force developed around the loop is equivalent to the rate of change of the field, instead of the field magnitude. Hence, the coil performance reduces as frequency decreases. The use of magnetic sensor arrays for PMFL probes have been developed and have shown better prospect for acquiring more information regarding the orientation and position of defects, via mapping of the magnetic field distribution as well as producing a better depth information [98,99]. More information is attainable at a particular time with the sensor array topology; hence, the detection probability is enhanced. The PMFL technique is very profitable especially where space is at premium. For instance, investigations that are performed from the interior of the pipe, permanent magnets will not be able to fit into the bore. Also, DC-electromagnets will produce immense heat and at a faster rate too. However, using the PMFL technique were the saturation magnetization field is generated only for a short duration, pipe walls of about 5 mm thick have been successfully inspected with minimal heat generated [100]. This also means that more energy will be saved while using the PMFL method of NDE.

The PMFL technique has shown its dominance over the conventional MFL methods. However, there is still an urgent need to research further towards advancing in the detection and characterization of defects, so as to provide an efficient and superior

defect QNDE. This is not limited to evaluating the position of defects, but also providing vital information relating to the complete defect geometries. In the case of the reconstruction of 3D defects, a detailed and exact sizing technique is crucial. This is a serious problem in QNDE for MFLNDE, because naturally existing defects hardly possess a simple geometry. The complication of such geometries alters the resulting leakage signals obtained from the interaction between the applied field and defects. To completely understand the influence of defect geometry on the information obtained and to acquire an optimal defect information, it is necessary to understand the basic phenomena of the interaction as well as their influence on the final test result. Through the use of modelling methods in MFLNDE, the desired understanding can be provided. This simplifies and speeds up not just the forward problem but also the inverse problem, which is vital for an accurate experimental design, specification and setup. The modelling approach also helps in the extraction of features for an accurate 3D defect quantification and reconstruction.

The use of neural network methods to resolve the functional relationship between the geometrical parameters of defects and the leakage field signals is presently a fast growing research topic with a lot of progress made. The defect pattern recognition technique for NDE based on fuzzy subset theory was proposed by R. Gomez [101]. He used the radial basis function neural network method in the interpolation calculation, as well as the non-linear approximation of the leakage field. In addition, he developed a radial basis function network model and proposed the learning algorithm, in order to provide a practical means of sizing defects in pipeline structures. Also, a practical algorithm based on neural network and model feature extraction for automatic defect detection for MFL testing was proposed by R. Christen et al. [102]. The use of wavelet neural network technique to simulate the inter-relationships between defect parameters and leakage field signals caused by defects was proposed by H. Kyungtae [103], P. Ramuhalli et al. [104] and A. Joshi et al. [105]. They presented an inversion algorithm based on the neural network of the adaptive wavelet basis function that could appreciably restructure the defect profile in the presence of noise. With regards to domestic analysis on neural network of a defect present in a pipeline structure, T. Wang et al. used the entropy spectral analysis approach to characterize the leakage field signals and presented a reliable pipeline defect recognition and sizing technology, based on the neural network of

radial basis function [106, 107]. He also studied the technique of sizing the leakage field signals caused by defects in gas and oil pipelines. The wavelet neural network and radial basis neural network methods of predicting the non-linear relationships between defect size and the MFL signals was proposed by M. Wei et al. [108, 109]. Furthermore, the finite element analysis approach to investigate the relationships between the leakage field signal and defect size was presented by L. Yang et al. [110, 111]. They established a defect identification sizing technique for pipeline structures based on the neural network and data fusion.

Despite the great advancements in the theoretical and experimental aspect of MFL testing, there are still challenges and problems associated with MFL detection and characterization techniques; a) The sensitivity of MFL technique to small cracks (i.e. hairline cracks) is poor and the leakage signals caused by permeability variation in the pipeline material could be mistaken to be the leakage signals caused by small cracks, thereby, making crack characterization difficult [72]. b) The nature of the leakage field profile means that an experienced operator is needed to interpret the complicated signals correctly, thus increasing the inspection time and cost [47] c) The MFL technique requires rigorous calibration measurements. d) There is a need to develop a feature extraction technique to automate the crack characterization process, in order to evaluate the shape, location, size and orientation of cracks [47]. e) Moreover, the MFL detection sensitivity decreases with increasing probe speed, thus, reducing the detection sensitivity [57, 112]. Another serious limitation of the MFL method is the reduced sensitivity in detecting cracks positioned far-away from the pipe surface due to skin-effect, as well as the difficulty in characterizing cracks due to the reduced spatial resolution of the leakage field signal detected by the sensor, especially for cracks with complicated geometries [60]. Furthermore, the leakage field signal caused by a deep far-surface crack could be mistaken to be a signal caused by a shallow surface crack, especially for hairline cracks.

2.11) Chapter Summary

In this chapter, a detailed review is presented on various NDE methods used for detecting and characterizing cracks and other types of defects. The efficacy of magnetic field sensors for mapping out the resultant leakage field distribution through the sensor array or scanning methodology, alongside the capability of the PMFL mapping technique in providing a different means of characterizing and quantifying cracks in ferromagnetic pipelines is promising. It is evident from the survey that numerous problems exist in MFLNDE inspection, which requires urgent attention and solution, especially those associated with cracks with miniature sizes with respect to the sample wall thickness and those with complicated geometries:

Based on the survey conducted, the following problems have been identified, alongside their proposed possible solutions:

a) The need for characterization of hairline cracks based on their shapes and sizes: The effect of crack shapes and parameters on the inspection output, specifically the width and depth sizes with respect to the sample wall thickness need to be meticulously addressed. Previous research has focused on locating the presence of defects that have a direct influence on the integrity of pipelines (cracks with large width and depth sizes). However, only limited effort has been channelled to locating and evaluating tiny anomalies and imperfections such as very narrow hairline cracks, especially deep below the surface of pipeline structures, and how they affect the inspection output. Therefore, the integrity of the pipeline and other ferromagnetic steel structures are still at risk. For this reason, a thorough and systematic study on the influence of both surface and far-surface hairline cracks needs to be conducted, in order to provide the much-required solution in achieving a comprehensive and complete crack quantification for QNDE.

b) Ability to obtain useful crack information, as well as quick inspection output suitable for effective hairline crack characterization: Feature extraction via visualization and 3D imaging of the resultant leakage field distribution can solve the problem of false evaluation and interpretation of cracks, as a result of geometrical characteristics. A large area will be covered by the MFL data

collected via the 3D imaging technique. This would be sufficient for the effective characterization of hairline cracks, as well as for cracks with non-uniform geometries. The contours of the imaged signal can be related to the crack geometries via feature recognition and extraction of the crack features.

c) Understanding the basic phenomena surrounding the interaction between the crack geometry and the induced magnetic field, that gives rise to the resultant leakage field: By performing the MFL investigation using the FEM approach, easy visualization and imaging of the resultant leakage field distribution can give a good description of the investigation results and also help with the analysis of the interaction between the induced magnetic field and the various surface and far-surface hairline crack geometries, for a satisfactory QNDE. The MagNet FEM software package by Infolytica can be used to achieve the above requirements, by simulating the electromagnetic NDE problems associated with the DCMFL and PMFL techniques. Also, the solutions to the forward and inverse MFLNDE problems for evaluating the resultant leakage fields relating to the various hairline cracks, as well as the experimental conditions can be provided via the FEM simulation technique.

d) Establishing the much-desired link between the information obtained and crack characterization. An improved understanding and description of the physical phenomena resulting from practical experiments can be obtained by forming a sound relationship between the modelling and experimental techniques. This will also help in providing useful information regarding the shape, orientation, size and location of the crack, thus, simplifying both the forward and inverse problems. The simulation results can also be used for crack profile identification, hairline crack quantification and to facilitate the experimental probe design and set-up. Moreover, this would also help in bridging the gap between the modelling and experimental system of MFL investigation for an effective QNDE.

2.12) References

1) S. Kumar and D. Mahto, "Recent Trends in Industrial and Other Engineering Applications of Non Destructive Testing: A Review". *International Journal of Scientific & Engineering Research* 4(9), September (2013). [Online]. Available at: https://papers.ssrn.com/sol3/papers.cfm?abstract_id=2770922. [Accessed 11 Jan. 2017].
2) A. Sophian, G.Y Tian, D. Taylor and J. Rudlin, "Flaw Detection and Quantification for Ferromagnetic Steels Using Pulsed Eddy Current Techniques and Magnetization". *Transactions on Engineering Services* Vol 44, (2003). [Online]. Available at: https://www.witpress.com/elibrary/wit-transactions-on-engineering-sciences/44/13946. [Accessed 11 Jan. 2017].
3) I. M. Z. Abidin, "Modelling and Experimental Investigation of Eddy Current Distribution for Angular Defect Characterisation". In Electrical, Electronic and Computer Engineering. Volume, *PhD Newcastle upon Tyne: Newcastle University*, (2010).
4) M. Simsir and A. Ankara, "Comparison of Two Non-destructive Inspection Techniques on the Basis of Sensitivity and Reliability". *Materials and Design*, 28(5), 1433-1439, (2007).
5) A.J. Mcevily, "Failures in Inspection Procedures: Case Studies". *Engineering failure analysis*, 11(2), 167-176, (2004).
6) Non-Destructive Testing Blog, "Magnetic Particle Testing". (2017). [Online]. Available at: http://tspndt.com/non-destructive-testing-industrial-supplies-blog/what-is-magnetic-particle-testing. [Accessed 10 Jan. 2017].
7) Canadian General Standard Board, "Advanced Manual for Eddy Current Test Method". CAN/CGSB-48.14-M86.
8) G.Y. Tian and A. Sophian, "Study of Magnetic Sensors for Pulsed Eddy Current Techniques". *Insight*, 47(5), 277-279, (2005).
9) B. Raj, T. Jayakumar and M. Thavasimuthu, "Practical Non-destructive Testing". Second Edition, *Woodhead Publishing Ltd*, (2002).
10) L. Mierczak, "Evaluation of Structural Integrity of Steel Components by Non-Destructive Magnetic Methods". In Electrical and Electronic Engineering. Volume, *PhD Thesis: Cardiff University*, (2016).
11) J. G. Martin, J. Gomez-Gil and E. Vazquez-Sanchez, "Non-destructive Techniques Based on Eddy Current Testing". *Sensors*, vol. 11, 2525-2565, (2011).

12) R.S. Edwards, A. Sophian, S. Dixon, G.Y. Tian and X. Jian, "Dual EMAT and PEC Non-Contact Probe: Applications to Defect Testing". *NDT & E International* 39(1), 45-52, (2006).

13) R.S. Edwards, A. Sophian, S. Dixon and G.Y. Tian, "Data Fusion for Defect Characterisation using Dual Probe System". *Sensors and Actuators A: Physical* 144(1), 222-228, (2008).

14) Kemplon Engineering, "The Sound of True Welding: Electromagnetic Acoustic Transducer (EMAT): A Novel Method for Non Destructive Testing (NDT) of Welds". February (2016). [Online]. Available at: http://www.kemplon.com/the-sound-of-true-welding-electromagnetic-acoustic-transducer-emat-a-novel-method-for-non-destructive-testing-ndt-of-welds/. [Accessed 17 Jan. 2017].

15) R. Bickerstaff, M. Vaughn, G. Stoker, M. Hassard, and M. Garrett, "Review of Sensor Technologies for In-line Inspection of Natural Gas Pipelines". [Online]. Available at: http://docplayer.net/37157726-Review-of-sensor-technologies-for-in-line-inspection-of-natural-gas-pipelines.html. [Accessed 11 Jan. 2017].

16) H. Charles, "The ABC's of Non-destructive Weld Examination". *The Welding Journal of American Welding Society*, Vol.3, May (1997).

17) H. Charles, "The ABC's of Non-destructive Weld Examination", The Welding Journal of American Welding Society, Vol.3, May (1997).

18) F. Larry, "Welding: Principles and Applications". 5th Edition, *Thomson Delmar Learning*, (2002).

19) B.P.C. Rao, "Visual Techniques in Non-destructive Testing". *Encyclopaedia of Materials: Science and Technology*, Elsevier Science Ltd, 6043-6046, September (2001).

20) [Online].Available,at:http://14.139.172.204/nptel/CSE/Web/112101005/images/lec4-3.html. [Accessed 7 March. 2017].

21) A.K. Mohammed, W. Saleh and N. Qaddoumi, "Defect Imaging and Characterization in Composite Structures Using Near-Field Microwave Non-destructive Testing Techniques". *Composite Structures* 62(3-4), 223-259, (2003).

22) D. K. Ghodgaonkar and N. A. Ali, "Microwave Non-destructive Testing of Composite Materials using Free-Space Microwave Measurement Techniques". *15TH World Conference on Non-destructive Testing,* October (2000).

23) Ida N, *Microwave NDT*. Dordrecht / Boston / London: Kluwer academic publishers, (1992).

24) S. I. Ganchev, J. Bhattacharyya, S. Bakhtiari, N. Qaddoumi, D. Brandenburg, and R. Zoughi, "Microwave Diagnosis of Rubber Compounds". *IEEE Transactions on Microwave Theory and Techniques,* vol. 42, 18-24, (1994).

25) M. T. Ghasr, S. Kharkovsky, R. Zoughi, and R. Austin, "Comparison of Near-Field Millimeter-Wave Probes for Detecting Corrosion Precursor Pitting under Paint". *IEEE Transactions on Instrumentation and Measurement,* vol. 54, 1497-1504, (2005).

26) D. Beilken and J. Hinken, "Microwave Based Non-Destructive Testing using Modified Eddy Current Systems" *Fall Conference & Quality Testing show ECNDT,* 1.8.4, (2007).

27) M. T. Ghasr, S. Kharkovsky, R. Zoughi, M. O'Keefe, and D. Palmer, "Millimeter Wave Imaging of Corrosion under Paint: Comparison of Two Probes". *In Review of Quantitative Non-destructive Evaluation*, D. O. Thompson and D. E. Chimenti, Eds.: *American Institute of Physics*, 447-454, (2006).

28) J. M. Milne, and W. N. Reynolds, "The Non-destructive Evaluation of Composites and Other Materials by Thermal Pulse Video Thermography". SPIE, Vol. 520, 119-122, (1984).

29) W. N. Reynolds and G. M. Wells, "Video-Compatible Thermography", *British journal of NDT*, Vol. 26, 40-44, (1984).

30) J. Wilson, G. Y. Tian, I. Z. Abidin, S. Yang, and D. Almond, "Pulsed Eddy Current Thermography: *system development and evaluation*". *Insight,* vol. 52, 87-90, (2010).

31) G. Riegert, T. Zweschper and G. Busse, "Lock-in Thermography with Eddy-Current Excitation", *Quantitative Infra-Red Thermography Journal*, Vol. 1, 21-32, (2004).

32) B. Oswald-Tranta, "Thermo-inductive Crack Detection". *Non-destructive Testing and Evaluation*, Vol. 22, 137-153, Aug (2007).

33) G. Riegert, K. P. fleiderer, H. Gerhard, I. Solodov and G. Busse, "Modern Methods of NDT for Inspection of Aerospace Structures". *ECNDT*, Berlin, Germany, (2006).

34) M. Boat, N. Pearson, R. Lieb, J. Davies, R. James and B. Woodhead, "Factors that Affect the Defect Sizing Capabilities of the Magnetic Flux Leakage Technique". *Silverwing (UK) Ltd*, (2012).

35) G.S. Park. S.H. Park, M. K. Hui, W. J. Dong, H. I. Sang, H.P. Jeong and S.L. Jin, "A Study on the Estimation of Defect Depth in MFL type NDT System". *IEEE Transactions* 40(2), 663–666, (2004).

36) Y. Shi et al. "Theory and Application of Magnetic Flux Leakage Pipeline Detection". *Sensors* 15(12), 31036-31055, (2015).

37) H.M. Kim and G.S. Park, "A Study on the Estimation of the Shapes of Axially Oriented Cracks in CMFL Type NDT System*". IEEE Trans. Magn* 50(2), (2014).

38) P.J. Qing and J.A. Zhi, “Internal and External Defect Identification of Pipelines using the PSO-SVM Method”. *Insight Non-Destruct. Test. Cond. Monit* 57(2), 85–91, (2015).

39) Y.D. Wang, Y.T. Xu, B. Wang, S.B. Ding, J.L. Xu and M.L. Zheng, “Research on Metal Atmospheric Storage Tank Inspection Method for Standard in China. *In Proceedings of the ASME 2009 Pressure Vessels and Piping Division Conference*, Prague, Czech Republic, Vol. 1, 447–452, July (2009).

40) K. Hwang, “3-D Defect Profile Reconstruction from Magnetic Flux Leakage Signatures using Wavelet Basis Function Neural Networks”. Electrical Engineering (Communications and Signal Processing) *PhD Thesis Lowa State University*, (2000).

41) G. C. Short, “Conventional Pipeline Pigging Technology: part 1 - Challenges to the Industry”. *Pipes & Pipelines International*, vol. 37, 8-11, May (1992).

42) Anon Natural Gas Pipelines, “Greater use of Instrumented Inspection Technology can Improve Safety PB93-113447/GAR”. Tech. Rep, General Accounting OflBce, Washington, DC. (1992).

43) K. K. Tandon, “MFL Tool Hardware for Pipeline Inspection”. *Materials Performance*, 36(2), 75-79, (1997).

44) C. Liang, L. Xing, B.L. Xun and Y.H. Zuo, “Signal Extraction using Ensemble Empirical Mode Decomposition and Sparsity in Pipeline Magnetic Flux Leakage Non-destructive Evaluation”. *Rev. Sci. Instrum*. 80, (2009).

45) A. A. Doubov, V.G. Kouleev, “Inspection of Welding Defects with Metal Magnetic Memory Method. *Welded Pipe Tube* 31, 44–48, (2008).

46) Y. Li, G.Y. Tian and S. Ward, “Numerical Simulations on Electromagnetic NDT at High Speed”. *Insight Non-Destruct. Test. Cond. Monit* 48, 103–108, (2006).

47) J. Wilson and G.Y. Tian, “Pulsed Electromagnetic Methods for Defect Detection and Characterisation”. NDT&E *International* 40, 275–283, January (2007).

48) Z.Y. Du and J.J Ruan, “3-D FEM Simulation of Velocity Effects on Magnetic Flux Leakage Testing Signals”. *IEEE Trans. Magn*. 44, 1642–1645, (2008).

49) M.S. Safizadeha and T. Azizzadeh, “Corrosion Detection of Internal Pipeline using NDT Optical Inspection System”. *NDT&E Int*, 52, 144–148, (2012).

50) Y.Z. Yong, F. Zhong and W. Chong, “A Fast Method for Rectangular Crack Sizes Reconstruction in Magnetic Flux Leakage Testing”. *NDT&E Int* 42, 369–375, (2009).

51) A.N. Pechenkov, V.E. Shcherbinin and J.G. Smorodinskiy, “Analytical Model of a Pipe Magnetization by Two Parallel Linear Currents”. *NDT&E Int* 44, 718–720, (2011).

52) W. Gospel. et al, “Sensors a Compréhensive Survey”. In: Boll, R and K.J. Overshott, eds. *Magnetic sensors*. New York, VCH Publishers Inc. 4(9), (1989).

53) N. N. Zatsepin and V. E. Shcherbinin, "Calculation of the Magnetostatic Field of Surface Defects". Defectoskopiya, vol. 5, 50-65, (1966).

54) C. R. Edwards and S. B. Palmer, "The Magnetic Leakage Field of Surface-breaking Cracks". *Journal of Physics D, Applied Physics,* vol. 19, 657-673, (1986).

55) M. Abe, S. Biwa and E. Matsumoto, "Three Dimensional Evaluation of Parallel-piped Flaw using Amorphous MI Sensor and Neural Network in Biaxial MFLT". *Proceedings of 3rd International Conference on Sensing Technology*, 238-241, (2008).

56) Montgomery, P. Wild and L. Clapham. "Factors Affecting Magnetic Flux Leakage Inspection of Tailor-Welded Blanks". *Research in Non-destructive Evaluation* 17(2), 85-99, (2006).

57) G.S. Park, and S.H. Park. "Analysis of the Velocity-induced Eddy Current in MFL Type NDT". *IEEE Transactions on Magnetics* 40(2), 663-666, (2004).

58) D.L. Atherton, C. Jagadish, P. Laursen, V. Storm, F. Ham, and B. Scharfenberger, "Pipeline Inspection-tool Alters MFL Signals". *Oil and Gas Journal*, **88**:84 (1990).

59) D.L. Atherton and E. Quek, *Canadian Electrical Engineering Journal*, **13**(1):27 (1998).

60) J.B. Nestleroth, and T.A. Bubenik, "Pipeline Integrity". *The Gas Research Institute*, (1999).[Online].Availableat:http://www.battelle.org/pipetechnology/MFL/MFL98Main.html. [Accessed 10 Sept. 2016].

61) W. S. Singh, S. Thirunavukkarasu, S. Mahadevan, B.P.C. Rao, C. K. Mukhopadhyay and T. Jayakumar, "Three-Dimensional Finite Element Modelling of Magnetic Flux Leakage Technique for Detection of Defects in Carbon Steel Plates". *IOP publishing Ltd. Non-Destructive Evaluation Division, Indira Gandhi Centre for Atomic Research*, (2010).

62) J. Fei, X. Zuo, Y. He, G.Y Tian and T. Zhang, "The Extraction of Characteristic Quantity of Shallow Defects in Pulsed Magnetic Flux Leakage Signal". *Proceedings of the 17th International Conference on Automation & Computing*, University of Huddersfield, Huddersfield, UK, September, 225-229, (2011).

63) Singh, W. Sharatchandra et al, "Finite Element Model-based Approach for Magnetic Flux Leakage Testing of Steel Plates Using 2D Tandem GMR Array Sensors". *Insight-Non-Destructive Testing and Condition Monitoring* 56(12), 683-690, July (2014).

64) J. Wu, Y. Sun, Y. Kang and Y. Yang, "Theoretical Analyses of MFL Signal Affected by Discontinuity Orientation and Sensor-Scanning Direction". *IEEE Transactions on Magnetics* 51(1), article no 6200207, (2015).

65) L. Udpa, S. Mandayam, S. Udpa, W. Lord, and Y. Sun, "Magnetic Flux Leakage Inspection of Gas Pipelines". Neural networks for signal characterization, compensation

and identification (Topical Report: GRI-96)," tech. rep., *Gas Research Institute*, Chicago, IL, (1996).

66) S. Mandayam, W. Lord, L. Udpa, and S. Udpa, "Wavelet-based Permeability Compensation Technique for Characterizing Magnetic Flux Leakage Images". *NDT&E International*, 30(5), 297-303, (1997).

67) L. Udpa and VV. Lord, "A Discussion of the Inverse Problem in Electromagnetic NDT". *In Review of Progress in Quantitative Non-destructive Evaluation* (D. O. Thompson and D. E. Chimenti, eds.), vol. 5, 375-382, New York: Plenum Press. (1986).

68) V. F. Shcherhinin et al, "Determination of the Dimensions of Operational Cracks of Gas pipes by Methods of Magnetic Flaw Detection". *Russian Journal of Non-destructive Testing,* vol. 29, 123-130, October (1993).

69) O. A. Bulychev, A. S. Shleenkov, and V. E. Shcherbinin, "Method of Determining the Crack Width in Ferromagnetic Products". *Positive decision of VNIIGPE,* November (1991).

70) P. Hopkins, "The Assessment of Pipeline Defects During Pigging Operations". *In Pipeline Pigging Technology* (J. Tiratsoo, ed.), 303-324, Houston, TX: Gulf Publishing Company, 2 ed., (1992).

71) Darabi, Akbar, and X. Maldague. "Neural Network Based Defect Detection and Depth Estimation in TNDE". *NDT & E International* 35(3), 165-175, (2002).

72) C. Mandache and L. Clapham, "A Model for Magnetic Flux Leakage Signal Predictions". *J. Phys. D: Appl. Phys*, 36(20), 2427- 2431, Oct. (2003).

73) C. Edwards and S. B. Palmer, "The Magnetic Leakage Field of Surface Breaking Cracks". *J. Phys. D: Appl. Phys*, 19(4), 657-673, April (1986).

74) W. Lord, "Applications of Numerical Field Modelling to Electromagnetic Methods of Non-destructive Testing". *IEEE Trans. Mag.* MAG-19, 2437 (1983)

75) F. Forester, "New Findings in the Field of Non-destructive Magnetic Leakage Field Inspection". *NDT Int*, 19, 3–14, (1986).

76) Brudar, B, "Magnetic Leakage Gelds Calculated by the Method of Finite Differences". *NDT International* 18, 353, (1985).

77) D.L. Atherton, "Finite Element Calculation of Magnetic Flux Leakage Detector Signals". M.G. Daly, *NDT Int.* **20**, 235, (1987).

78) [Online]. Available at: http://www.wfndec.org/benchmarkproblems.htm. [Accessed 27 Nov. 2016].

79) Z. Zeng, Y. Tian, S. Upda and L. Upda, "*Rev. Quant. NDE* **23**, 1553, (2004)

80) J. Etcheverry, A. Pignotti, G. Sanchez and P. Stickar, "Defect Signal Enhancement in Inspection Lines by Magnetic Flux Leakage". *Rev. Quant. NDE* **22,** 1824, (2003)

81) M. Ruch, J.P.A. Bastos, “Numerical Simulation of a Magnetic Flux Leakage Benchmark Problem”. *Insight* 46 (12), 736, (2004).

82) V. Lunin and D. Alexeevsky, “Numerical Prediction of Signal for Magnetic Flux Leakage Benchmark Task”. *Rev. Quant. NDE* 22, 1830, (2003).

83) H. Zuoying, Q. Peiwen and C. Liang, “3D FEM Analysis in Magnetic Flux Leakage Method”. *NDT&E Int.* 39, 61-66 (2006).

84) W. Han. et al. “Defect Profile Estimation from Magnetic Flux Leakage Signal via Efficient Managing Particle Swarm Optimization”. *Sensors* 14(6), 10361-10380, (2014).

85) J. Wilson and G. Y. Tian. “Pulsed Electromagnetic Methods for Defect Detection and Characterisation”. *NDT & E International* 40(4) 275-283, (2007).

86) Y. Cheng and K. Rong, “Research on Visual Detection Technology using Eddy Current Magnet Excitation Device”. *Proceedings of IEEE international Conference on Applied Superconductivity and Electromagnetic Devices,* 149-151, (2009).

87) L. Yong, J. Wilson, and G. Y. Tian, “Experiment and Simulation Study of 3D Magnetic Field Sensing for Magnetic Flux Leakage Defect Characterisation”. *NDT & E International* 40(2) 179-184, (2007).

88) M. Ravan, R. K. Amineh, S. Koziel, N. K. Nikolova, and J. P. Reilly, “Estimation of Multiple Surface Cracks Parameters Using MFL Testing”. URSI *International Symposium on Electromagnetic Theory IEEE,* 891-894, (2010).

89) Y. Sun, and Y. Kang, “A New MFL Principle and Method Based On Near-Zero Background Magnetic Field”. *NDT & E International* 43(4), 348-353, (2010).

90) V. Suresh and A. Abudhahir, “An Analytical Model for Prediction of Magnetic Flux Leakage from Surface Defects in Ferromagnetic Tubes”. *Measurement Science Review*, 16(1), 8-13, (2016).

91) Tang, Ying et al, “Experimental and Finite Element Analysis Study of 3D Magnetic Field Sensing for Pulsed Magnetic Flux Leakage Defect Characterisation”. *Insight - Non-Destructive Testing and Condition Monitoring* 53(9), 497-506, (2011).

92) Y. Tang, M. Pan and C. F. Luo, “Feature Extraction Based on the Principal Component Analysis for Pulsed Magnetic Flux Leakage Testing”. *International Conference on Mechatronic Science, Electric Engineering and Computer*, 19-22, August (2011). Jilin, China.

93) V. Yang, G. Zhang, G. Liu and S. Gao, “Effect of Lift-off on Pipeline Magnetic Flux Leakage Inspection”. *17th World Conference on Non-destructive Testing*, 25-28, October (2008), Shanghai, China.

94) Z. Deng et al. “Effects of Surface Roughness on Magnetic Flux Leakage Testing of Micro-Cracks”. *Measurement Science and Technology* 28(4), 045003, (2017).

95) J. Wu, et al. “A Lift-Off-Tolerant Magnetic Flux Leakage Testing Method for Drill Pipes at Wellhead”. *Sensors* 17(1), 201, (2017).

96) J. Feng et al. “A Sensor Lift-off Modification Method of Magnetic Flux Leakage Signal for Defect Profile Estimation”. *IEEE Transactions on Magnetics*, 1-1, (2017).

97) A. Sophian, G.Y. Tian, and S. Zairi, “Pulsed Magnetic Flux Leakage Techniques for Crack Detection and Characterisation”. *Sensors and Actuators A: Physical* 125(2), 186-191, (2006).

98) H. M. Kim et al, “A Study on the Estimation of Defect Depth in MFL type NDT System”. School of Electrical Engineering, Pusan National University, Busan, South Korea, gspark@pusan.ac.kr (2014).

99) H. M. Kim and G. S. Park, “A Study on the Estimation of the Shapes of Axially Oriented Cracks in CMFL Type NDT System”. *IEEE Transactions on Magnetics* 50(2), 109-112, (2014).

100) A. Sophian, G.Y. Tian, D. Taylor and J. Rudlin, “Flaw Detection and Quantification for Ferromagnetic Steels using Pulsed Eddy Current Techniques and Magnetization”. *WIT Transactions on Engineering Sciences,* vol. 44, 1743-3533, (2003).

101) R. Gomez, E. Mcloone, S. Irwin, G.W. “Orthogonal Wavelet Network Construction Using Local Regularization”. *In Proceedings of the First International IEEE Symposium*, Varna, Boulgaria, 271–276, (2002).

102) R. Christen, A. Bergamini, “Automatic Flaw Detection in NDE Signals Using a Panel of Neural Networks”. *NDTE Int*. 39, 547–553, (2006).

103) H. Kyungtae, “3-D Defect Profile Reconstruction from Magnetic Flux Leakage Signatures Using Wavelet Basis Function Neural Network”. *Ph.D. Thesis*, Iowa State University, Ames, IA, USA, (2000).

104) P. Ramuhalli, L. Udpa, S.S. Udpa, “Electromagnetic NDE Signal Inversion by Function-Approximation Neural Networks”. *IEEE Trans. Magn*. 38, 3633–3642, (2002).

105) A. Joshi, L. Udpa, S. Udpa, A. Tamburrino, “Adaptive Wavelets for Characterizing Magnetic Flux Leakage Signals from Pipeline Inspection”. *IEEE Trans. Magn*. 42, 3168–3170, (2006).

106) Q. Jiang, T. Wang, Q. Liu, H. Jiang, “Analysis of the Magnetic Flux Leakage Field of Pipeline Defect Based on Radial Basis Function Neural Network”. *Nondestruct. Test*. 24, 515–518, (2002).

107) T. Wang, X. Liu, X. Qin, T. Shang, “Spectrum Entropy and its Application in Characteristics Abstraction of Magnetic Flux Leakage Signals”. *J. Tianjin Univ.* 37, 216–220, (2004)

108) M. Wei, S. Jin, Y. Li, Q. Cui, “Two Dimensional Profile Reconstruction and Process Technology for Pipeline Defect. *Acta Pet. Sin*. 24, 98–101, (2004).

109) M. Wei, S. Jin, Y. Li, Q. Cui, “Study on Wavelet Compression Technique for Magnetic Flux Leakage Image of Oil and Gas Pipeline Defects”. *OptoElectron. Eng*. 31, 58–60, (2004).

110) L. Yang, X. Chen, J. Wei, “Signal Processing Technology in Oil-Gas Pipeline Magnetic Flux Leakage Inspection”. *J. Shenyang Polytech. Univ.* 21, 516–518, (1999).

111) L. Yang, F. Ma, S. Gao, “Quantitative Recognition of Pipeline Defects Based on Neural Network and Data Fusion. *Nondestruct. Test*. 28, 281–284, (2006).

112) Y. Li and G.Y. Tian, “Numerical Simulations on Electromagnetic NDT at High Speed”. *Insight-Non-Destructive Testing and Conditioning Monitoring*”. 48(2), 103-108, (2006).

Chapter 3: Theoretical Background of MFL Investigation

3.1) Introduction

This chapter explains the theoretical background of MFLNDE. It describes the analytical and numerical modelling techniques for solving MFL problems, as well as the experimental method. The basic Maxwell's equations governing the MFLNDE phenomena are also described, in order to understand the basic theory in which the research methodology used in this project is established. The modelling technique for solving the MFLNDE problems is first utilized prior to the experimental investigation, because of its capability to generate useful predictions of the experimental results. In order to ensure a better description and understanding of the inspection results, graphical visualization of the MFL associated phenomena is presented.

Numerous practical methods are available for solving the problem of crack characterization. However, the numerical approach has proven to be the most practical means of generating the much-desired information about the feasibility of the MFL technique, supported by experimental validation of the predicted results. The MFL numerical modelling is implemented in this work, in order to investigate the MFL testing phenomena, as well as the interaction between the induced magnetic field and crack geometry (forward model). The expected response of the MFL probe being scanned across a hairline crack for a particular experimental condition can be predicted using the simulation technique. The acquired response can then be used to obtain the crack signatures, which is beneficial for an efficient crack quantification.

Also, the inverse model can be developed using the information gathered from the forward model (numerical or analytical model). That is using the results obtained from magnetic field measurements to predict the unspecified specimen properties such as; material thickness, defect geometries, defect position, etc. Table 3.1 shows the two types of modelling process, with their unknown input and predicted output.

Table 3.1 Types of Modelling.

Model Classification	Unspecified Input	Predicted Result
Forward	Specimen Properties	Magnetic Field
Inverse	Magnetic Field measured	Specimen Properties

As regards to specimen properties, the signals predicted with the aid of the theoretical models are compared with the measured signals. The inverse process is iterative and the iteration steps continue until the error between the predicted and measured value is minimal. The theoretical models are very beneficial tools for visualizing the magnetic field distribution pattern around the MFL probe and the test piece. In addition, they are very helpful mechanisms for probe design and experimental setup. They also provide a better understanding of the underlying physics surrounding the MFL problem. Amongst the numerous accessible ways of carrying out the crack characterization task, the numerical technique is the most practical and simple approach in obtaining information regarding the practicality of the proposed MFL methods, supported with experimental validation of the predicted results.

3.2) Equations Governing MFL Phenomena

The laws of electromagnetism govern the MFLNDE, as it utilizes electromagnetic field in its entire application. These laws include; Maxwell-Ampere's Law, Gauss's Law and Faraday's Law. The electromagnetic fields at a classical macroscopic level involves solving Maxwell's equations based on specified boundary conditions. These include a set of equations, specified in differential or integral form, showing the electric field and magnetic field relationship within a system.

3.2.1) Differential Form of Maxwell's Equations

$$\nabla \times \boldsymbol{H} = \boldsymbol{J}_c + \frac{\partial \boldsymbol{D}}{\partial t} \qquad \text{(Ampere's Law)} \qquad (3.1)$$

Ampere's law in its differential form is shown in equation (3.1), where **H** is the magnetic field, $\boldsymbol{J}_c$ is the current density, **D** is the electric flux density and $\frac{\partial D}{\partial t}$ is the rate of change of the electric flux density with time. The equation states that the circulating magnetic field **H** ($\nabla \times \boldsymbol{H}$ is curl of **H**) is determined by the free current density ($\boldsymbol{J}_c$).

$$\nabla \times \boldsymbol{E} = -\frac{\partial \boldsymbol{B}}{\partial t} \qquad \text{(Faraday's Law)} \qquad (3.2)$$

Faraday's Law in its differential form is shown in equation (3.2), where **E** is the electric field strength, **B** is the magnetic flux density and $\frac{\partial B}{\partial t}$ is the rate of change of magnetic flux density with time. The equation states that the circulating electric field intensity **E** ($\nabla \times \boldsymbol{E}$ is curl of **E**) is determined by the changing magnetic flux density (**B**).

$$\nabla . \boldsymbol{B} = 0 \qquad \text{(Gauss's Law)} \qquad (3.3)$$

Gauss's Law for magnetic field in its differential form is shown in equation (3.3), where **B** is the magnetic flux density. The equation states that the magnetic flux density (**B**) has a divergence equal to zero through any closed surface, i.e. a solenoidal vector field.

3.2.2) Integral Form of Maxwell's Equations

$$\oint_c \boldsymbol{H} \cdot dl = \int_s \left(\boldsymbol{J}_c + \frac{\partial \boldsymbol{D}}{\partial t}\right) \cdot ds \qquad \text{(Ampere's Law)} \qquad (3.4)$$

Ampere's Law in its integral form is shown in equation (3.4), it states that a circulating magnetic field (**H**) will be produced around a surface by an electric current flowing through that same surface.

$$\oint_c \boldsymbol{E} \cdot dl = -\frac{\partial}{\partial t}\int_s \boldsymbol{B} \cdot ds \qquad \text{(Faraday's Law)} \qquad (3.5)$$

Faradays Law in its integral form is shown in equation (3.5). This law shows the relationship between electric circuit and magnetic field. It states that when an electrical conductor is brought under the influence of magnetic field and if the flux linked with this conductor due to the magnetic field is changed, an electromotive force (emf) is induced in the conductor which is proportional to the rate of change of the flux linkage. The negative sign means that the induced current generated by the changing flux acts against the change in Magnetic flux (Lenz Law).

$$\oint_c \boldsymbol{B} \cdot ds = 0 \qquad \text{(Gauss's Law)} \qquad (3.6)$$

Gauss's Law integral form is shown in equation (3.6). This law states that the total magnetic flux through a closed surface is zero.

For a static case, that is a dc (direct current) phenomenon, the entire derivatives with respect to time will be zero ($\frac{\partial}{\partial t} = 0$).

$\nabla \cdot \boldsymbol{A} = \left(\frac{\partial A_x}{\partial x} + \frac{\partial A_y}{\partial y} + \frac{\partial A_z}{\partial z}\right)$ Is the divergence in the Cartesian coordinate ($\boldsymbol{A}$ is the magnetic vector potential). $\nabla \cdot \boldsymbol{A}$ is equal to zero, since the number of field lines that enter the surface also exit the surface, thus the field lines begin with a positive charge and end with a negative charge (the net flux is zero). $\nabla \times \boldsymbol{A} = \begin{matrix} \hat{\imath} & \hat{\jmath} & \hat{k} \\ \frac{\partial}{\partial x} & \frac{\partial}{\partial y} & \frac{\partial}{\partial z} \\ A_x & A_y & A_z \end{matrix}$ is the curl operator in the Cartesian coordinate, i.e. a measure of the amount of field circulating around a point.

In a closed system, the electromagnetic phenomena can be described on a microscopic level provided the Maxwell's equations are used in association with the fundamental relationships shown in equation (3.7) and (3.8), describing the properties of linear materials.

$$\boldsymbol{B} = \mu_0\mu_r\boldsymbol{H} = \mu\boldsymbol{H} \qquad (3.7)$$

$$\boldsymbol{J}_c = \sigma\boldsymbol{E} \qquad (3.8)$$

Where μ_0 is the permeability of free space and μ_r is the relative permeability of the material used. Equation (3.9) below can be derived from equation (3.1), (3.7) and (3.8).

$$\nabla \times \boldsymbol{H} = \boldsymbol{J}_c = \sigma \boldsymbol{E} \tag{3.9}$$

The curl of the magnetic vector potential $\nabla \times \boldsymbol{A}$ can be used to calculate the magnetic flux density as shown in equation (3.10).

$$\boldsymbol{B} = \nabla \times \boldsymbol{A} \tag{3.10}$$

The following section provides an overview of the direction taken in this project and the capabilities of the proposed methods in providing an enhanced crack detection and characterization, for MFLNDE.

3.3) Magnetic Flux Leakage Modelling

Modelling is frequently employed to simulate the MFL phenomena. It provides a good relationship between simulation and experimental investigation, hence, giving a better understanding and description of the various physical phenomena emerging from actual experimental investigation. In MFL inspection, the developed models are principally employed for simulating the MFL tests. This yields the desired results for both the forward and inverse problems, by predicting the resultant signals corresponding to various experimental conditions and crack geometries. The outcome of the simulation analysis is beneficial in establishing the relationship between the induced magnetic field in the test sample and the crack under scrutiny, which gives rise to the resultant leakage field signal. It can also be used to formulate the defect algorithms for signal interpretation, probe design and for system optimization.

The MFL modelling technique can be classified based on two techniques; 1) the analytical modelling technique (magnetic dipole modelling) by Zatsepin and Shcherbinin [1] and 2) the Numerical modelling technique (finite element modelling) by Hwang and Lord [2]. The Analytical modelling approach gives a definite closed form solution to the differential equations, which are developed from Maxwell's

equations. Also, the governing equations are solved by separation of variables, and can be utilized for solving both 2D and 3D problems. It is also restricted to solving canonical problems such as; cylindrical, spherical and planar geometries (limited to simple geometries). The numerical modelling approach is also solved using the Maxwell's equations. However, they are based on approximation of the result rather than the precise solution. Unlike analytical modelling, the numerical modelling approach is not limited to simple geometries; hence, it can be used for more complicated geometries (non-uniform surfaces and complex crack geometries).

3.3.1) Analytical Modelling Method for Solving MFLNDE Problems

The Analytical modelling method has the advantage of producing a quick and precise solution to the controlling partial differential equations, which is useful for the inverse problem of MFLNDE. Here, defects are assumed as magnetic dipoles. Zatsepin and Shcherbinin first introduced the magnetic dipole modelling technique for solving MFL problems.

The Magnetic Dipole Modelling (MDM) technique is presented in this section. A simple dipole model is established, representing the 3D MFL of a defect located on the surface of a ferromagnetic pipeline. Here, Z. Huang and P. Que [3], extended the dipole model presented by Zatsepin and Shcherbinin, to develop an analytical expression for the 3D MFL at a point in half-space at the top of a cylindrical defect filled with air in a ferromagnetic medium. The equations used are derived from Maxwell's equations. The cylindrical defect used is presented in Fig. 3.1.

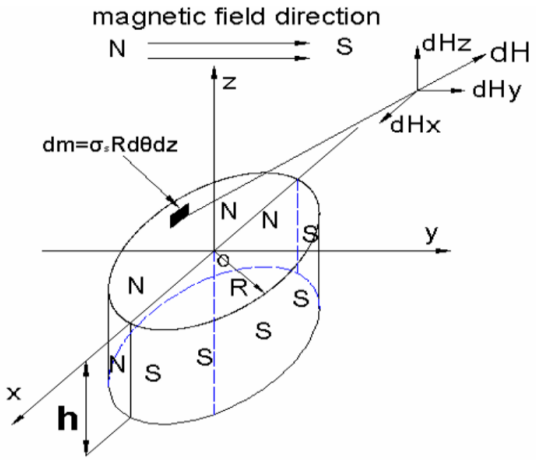

Figure 3.1. A cyclindrical defect representation in dipolar form [3].

The centre of the defect is positioned at the point of origin of x - y plane. Its central axis is along the z axis and the induced magnetic field is along the y-axis. A non-ferromagnetic material with permeability similar to that of air is used to fill the cylindrical defect. The magnetic field diverges in the vicinity of the low permeability defect, resulting to a dipole magnetic charge on the cylindrical walls. An assumption that the charge is uniformly distributed in the cylinder was made. R is the radius of the cylindrical defect, h is the defect depth, while θ is the angle measured from the positive x-axis component to the magnetic charge. The lift-off of the sensor and the magnetic charge of the cylinder are denoted by l and σs respectively. As a result of the different magnetic polarities, half of the cylinder possesses a negative magnetic charge while the remaining half possesses a positive magnetic charge. The differential charge element (dm) is given by equation (3.11);

$$dm = \sigma s R d\theta dz \tag{3.11}$$

A value of 1 is given to the charge density (σs). The magnetic field developed by the differential charge element (dm), at a distance r, is given by equation (3.12);

$$dH = \frac{dm}{4\pi r^3} r \tag{3.12}$$

The leakage field signal in the inspection area, that is; the position parallel to the x-y plane, which has a positive z coordinate value was studied in the work [3]. First, the defect part with a positive polarity is examined. As displayed in Fig. 3.1, the distance

rp from the differential elemental charge (dm) to any inspection point is given by equation (3.13);

$$r_p = [(x - Rcos\theta)^2 + (y + Rsin\theta)^2 + (l - z)^2] \tag{3.13}$$

By merging equation (3.12) and (3.13), the y and z components of the magnetic field at a distance r_p are given by equation (3.14) and (3.15) respectively;

$$dH_z^p = \frac{Rd\theta dz}{4\pi r_p^3}(l - z) \tag{3.14}$$

$$dH_y^p = \frac{Rd\theta dz}{4\pi r_p^3}(y + Rsin\theta) \tag{3.15}$$

The z component of the leakage field on the positively polarized region of the cylinder can be obtained by integrating the region as shown in equation (3.16);

$$H_z^p = \frac{R}{4\pi}\int_0^\pi \int_{-b}^0 \frac{(l-z)}{[(x-Rcos\theta)^2+(y+Rsin\theta)^2+(l-z)^2]^{3/2}} dzd\theta \tag{3.16}$$

The leakage field H_z^p can be expressed as shown in equation (3.17), by integrating the dz element.

$$H_z^p = \int_0^\pi \left(\frac{1}{\sqrt{(x-rcos\theta)^2+(y+Rsin\theta)^2+h^2}} - \left(\frac{1}{\sqrt{(x-rcos\theta)^2+(y+Rsin\theta)^2+(h+b)^2}}\right)d\theta \right. \tag{3.17}$$

A similar approach is used to obtain the z axis component of the leakage field in the negatively polarized region of the cylinder, except that the area integrated is in the opposite direction to the former (counter clockwise direction). Hence, the leakage field in the negatively polarized region is given by equation (3.18);

$$H_z^n = -\frac{R}{4\pi}\int_0^\pi \int_{-b}^0 \frac{(l-z)}{[(x-Rcos\theta)^2+(y+Rsin\theta)^2+(l-z)^2]^{3/2}} dzd\theta \tag{3.18}$$

Similar to the approach used to obtain the z component of the magnetic field on the positively and negatively polarized region of the cylinder, the y component of the magnetic leakage field can be obtained using equation (3.19) and (3.20);

$$H_y^p = \frac{R}{4\pi}\int_0^\pi \int_{-b}^0 \frac{(y+Rsin\theta)}{[(x-Rcos\theta)^2+(y+Rsin\theta)^2+(l-z)^2]^{3/2}} dzd\theta \tag{3.19}$$

$$H_y^n = -\frac{R}{4\pi}\int_0^\pi \int_{-b}^0 \frac{(y-Rsin\theta)}{[(x-Rcos\theta)^2+(y-Rsin\theta)^2+(l-z)^2]^{3/2}} dzd\theta \tag{3.20}$$

The total magnetic flux leakage in the z and y direction are given by equation (3.21) and (3.22) respectively. Fig. 3.2a and Fig. 3.2b shows the leakage field profiles in the z and y directions respectively.

$$H_z = H_z^p + H_z^n \tag{3.21}$$

$$H_y = H_y^p + H_y^n \tag{3.22}$$

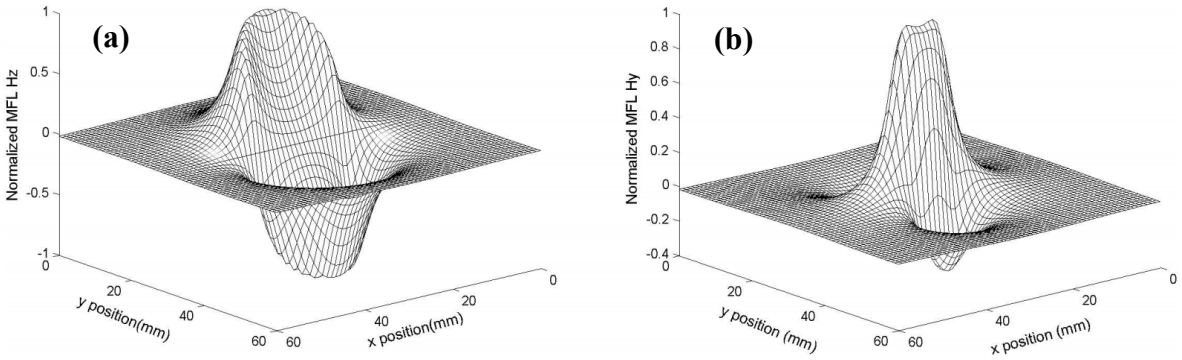

Figure 3.2. An analyticaly predicted magnetic flux leakage from a cylindrical defect with a diameter of 10 mm and depth of 8 mm; a) z compoent and b) y component [3].

3.3.2) Numerical Modelling Method for Solving MFLNDE Problems

The numerical modelling techniques, such as the Finite Element Modelling (FEM) relies on the utilization of iteration methods for solving MFLNDE problems, with the condition that the problems domain being considered is separated into several parts of elements which constitute a mesh [4]. The FEM simulation packages that are commercially available are; MagNet by Infolytica, ANSYS Multiphysics, COMSOL Multiphysics, OPERA, JSOL, etc. The equations determining the MFLNDE phenomena are substituted with interpolation functions developed in the entire elements in concurrence with the shape function of all the elements. The allocated boundary conditions are used to develop the initial values, which are then iterated on each of the elemental node. Also, the iteration process continues until the least acceptable error is achieved.

One of the benefits of FEM numerical modelling is the ability to compute a wide range of physics and geometry. Another benefit over other approximation methods is that the FEM method can significantly improve the accuracy of the approximated solution of a problem, compared to the Finite Difference Method (FDM) [5]. Numerical methods such as the Boundary Element Method (BEM) and FDM are not capable of solving nonlinear problems [5]. Therefore, they are not suitable for MFL simulation. Hence, FEM is preferred for solving the electromagnetic field equations controlling the MFL system. The numerical modelling technique of MFLNDE involving static and time-stepping problem solving, has enormous advantages over the analytical approach, especially when inspecting materials with complex defect shapes, as well as samples with irregular shaped surfaces (non-uniform surfaces) [6]. The numerical modelling method provide an improved explanation of the problem properties and geometries through discretization; hence, they are more furnished to present better fits to the nonlinear MFLNDE problems [5, 6]. The desired accuracy can be obtained while using the numerical method with additional flexibility in modelling complicated cases, which is not attainable with both the analytical and experimental methods [7]. Nevertheless, the numerical method usually depends heavily on the elemental and mesh conditions. Utilizing a denser mesh will yield an improved computational accuracy, while suffering the drawback of longer computational time. Numerous simulations have been performed in this study, involving both static (DC) and time-stepping (pulse) investigations in the 3D setting, to provide comprehensive guidance for the DCMFL and PMFL inspections, implemented in this study.

An introduction to the use of the MagNet Software by Infolytica together with the required information for modelling and solving the DCMFL and PMFL problems are described in section (3.3.3). By utilizing the MagNet simulation software, the DCMFL and PMFL investigation on the influence of surface and far-surface hairline cracks have been performed, by the means of static and time-stepping solving techniques, which uses the static and transient solver respectively. The software package was used to predict the interaction between the induced magnetic field and the various hairline cracks modelled in this work

3.3.3) Solving DCMFL and PMFL Problems via MagNet

The MagNet Software Package by Infolytica was used to perform the numerical modelling, for the work presented in this thesis. The MagNet software is an FEM simulation software, designed for the study of both static and time varying electromagnetic fields [8]. It solves the electromagnetic problems by separating the initial problem domain into an identical system of many smaller subdomains known as finite elements, and by implementing a numerical formulation built on interpolation theory to those elements. The software performs FEM computation for a fast and precise solution to Maxwell's equations. Different modules in MagNet, that is; static, transient or time harmonic solvers, simulate various types of electromagnetic fields used in applications such as; transformers, sensors and machines. To obtain the results for the DCMFL and PMFL investigations, the software was employed in solving the electromagnetic problems through the static and transient solver respectively. The respective model solutions were obtained by calculating the static and time variant field equations, especially for the fields inside the developed models. The models were separated into meshes consisting of tetrahedral-shaped elements, and each of the individual elements is defined by four nodes. The nodes refer to the initial points on the inside and at the edges of the mesh elements. The amount of nodes present indicates the overall amount of solutions for the controlling field equations meeting the boundary conditions in the initial problem domain. A polynomial with unspecified coefficients is used to represent the vector field within the individual element. The solutions to the set of equations for the unspecified coefficients are provided through finite element analysis. The nature of the field and the elemental mesh size determines the accuracy of the result obtained. To obtain a better result with higher accuracy, smaller elements are utilized, especially at the regions with rapidly changing field (crack region). The static results in MagNet are achieved via the static technique, while the transient results are achieved using the time-stepping technique.

The static technique involves magnetizing a part or whole of the test sample, then the resulting flux at the surface region of the sample is recorded to establish its anomalous spatial distribution. Normally, a discretized magnetization close to the

saturation level of the sample is needed. This is because the amplitude of the leakage flux usually corresponds to the level of magnetization. Also, a magnetization level which is too high could cause a decrease in the signal to noise ratio (SNR), because of an offset caused by the background signal component. The magnetization sources that are frequently used for the DCMFL investigation are the electromagnet or permanent magnets. The design and optimization of the DCMFL system requires a thorough understanding of magnetic circuit principles, and the FEM solver happens to be a very powerful and an efficient tool for DCMFL design and analysis. It uses a single nonlinear run for the finite element analysis solution (static analysis of the B-H curve). For this work, a 3D model is used, and the material information is made up of magnetization curves specified up to saturation. The magnetization curve was made smooth to obtain a convergent solution. Also, the transient results start with obtaining a static result for the fields that would occur, provided the conditions at the start time are constant for all the preceding times. Then, the transient result develops from the preceding conditions. For each of the steps used, a fixed interval time steps were employed for the results. The different steps used by MagNet for finite element analysis of DCMFL and PMFL problems are discussed below [9]:

1) **Pre-processing stage**: the pre-processing stage of the finite element problem solving starts with;

i) Formation of the geometrical model components, with the help of the computer aided design drawing tools. Followed by the characterization of the materials physical properties, which includes; its **B**-**H** curve (demonstrating the magnetic properties of the ferromagnetic material used), its electrical conductivity, magnetic conductivity, permeability, permittivity, thermal conductivity, mass density, etc.

ii) Construction of the mesh system with respect to the particular mesh size designated to an individual model component: Here, the solution domain is broken down into a system consisting of smaller elements known as the mesh. The mesh usually comes in various shapes such as; rectangular mesh,

triangular mesh, or other polygonal mesh shapes in the 2D environment and tetrahedral mesh in the 3D environment.

iii) Interpolation function selection: Here, the interpolation functions are specified and are used for interpolating the field variables across the elements. Also, the selected functions are usually polynomials and its degree is built upon the amount of nodes designated to the individual element.

iv) Matrix equation formation: This involves creating the matrix equations for the elements, to associate the coefficients of the matching interpolation function approximation with the values of the node for the initial function. The Galerkin technique of weighted residuals is used to implement the association process.

v) Assembly of the global system equations: The assembly of the global system equations from the matrix equations is performed, for all the mesh elements. The boundary conditions are then introduced into the system equation solution.

2) **Solving stage**: The type of algorithm used here will depend on the type of solver chosen, that is; magnetostatic, time transient or the time harmonic solver. The values of the corresponding fields at all the mesh nodes are provided and the solution of the matrix is established. The solving stage is visible to the user and the overall result of the successive solution processes is shown on the computer screen.

3) **Post-processing stage**: The numerical values of the simulated quantities and fields can be obtained by using either a field line graph or field probe within the designated area of the solution. Also, the results can be easily visualized using shaded, arrow or contour plots, to present information. The MagNet 7.6 software package was chosen for this investigation because of the user-friendliness and its efficiency in using the pre-processors, solvers and post-processors.

3.4) Sample and Yoke Characterization

Prior to the simulation and experimental tests, the typical materials used for the test sample (low carbon steel) and for the magnetization yoke (grain oriented electrical steel) were characterized using a dc hysteresis loop measurement system shown in Fig. 3.3a. The measurement system consisted of an electromagnetic yoke (see Fig. 3.3b) driven by a quasi-dc current supplied by a Kepco amplifier and was used to magnetize the sample. The magnitude of the applied magnetic field (**H**) was measured at the surface of both materials with a Hall probe connected to a gauss meter, which was linked to a personal computer through a GPIB cable. Simultaneously, the magnetic flux density (**B**) values were measured using a GPIB linked flux meter, integrating the voltage from a 20 turn copper coil wound around the centre of both materials, using equation (3.23);

$$B = \frac{1}{NA}\int V(t)dt \tag{3.23}$$

Where, $\boldsymbol{B}$ is the magnetic flux density, N represents the number of copper coils in turns, A represents the cross-sectional area of the sample and yoke materials used. The entire test procedure was controlled with National Instruments LabVIEW code. At the end of the characterization test, the DC hysteresis loop for both materials were shown on the computer screen and the corresponding **B** and **H** data was collected using an external hard drive for further analysis. The acquired **B**-**H** data (initial magnetization curve) was imported into the MagNet 7.6 software and was used in the simulation task to ensure close approximation with the experimental results.

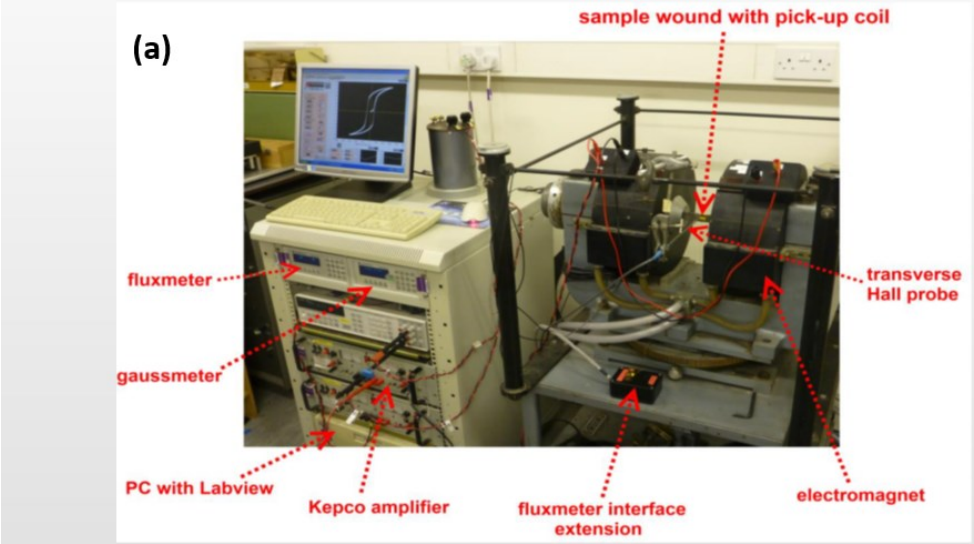

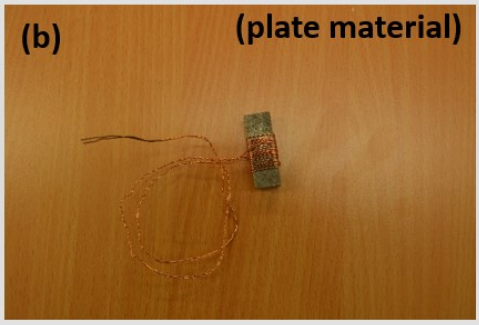

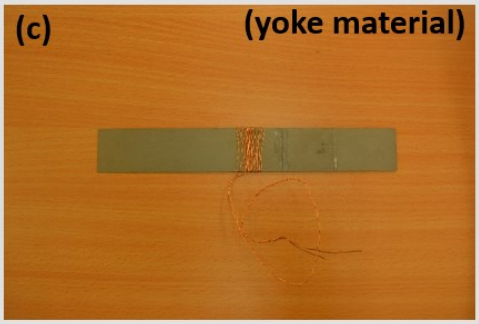

Figure 3.3. Showing a) A picture of the dc hysteresis loop measurement system, b) Low carbon steel cross-section and c) Silicon steel strip (grain oriented electrical steel).

In this work, different samples (low carbon steel, grade: EN3B) with surface hairline cracks of varying depth and width sizes (d/w = 0.2, 0.4, 0.6, 0.8, 1, 2, and 4 mm), and different samples with far-surface hairline cracks of varying depth and width sizes (d/w = 0.2, 0.4, 0.6, 0.8, 1, 2, and 4 mm) were modelled and simulated. All the cracks used in this investigation had a constant length of 10 mm. The depth of the surface cracks refers to the distance from the top surface of the sample to the bottom of the crack, while the depth of the far-surface cracks refers to the distance from the bottom surface of the sample to the top of the crack with an opening at the bottom of the sample. The far-surface cracks are located 9.8, 9.6, 9.4, 9.2, 9, 8 and 6 mm below the top surface of the samples. The dimension of the sample used was 350 mm × 60 mm × 10 mm with a conductivity of 1.17×10^7 S/m. The excitation yoke (silicon iron) used had a leg height of 80 mm, leg length of 30 mm, leg width of 60 mm, leg spacing of 240 mm with a conductivity of 2.17×10^6 S/m. The yoke was wound with 300 turns of copper wire with a diameter and conductivity of 0.5 mm and

1.12×10^7 S/m respectively. This set-up was used to simulate the axial ($\boldsymbol{B_x}$), radial ($\boldsymbol{B_y}$) and tangential ($\boldsymbol{B_z}$), components of the leakage field for both the surface and far-surface hairline cracks via the MagNet 7.6 software.

3.5) Experimental Method for Solving MFLNDE Problems

The experimental system of MFL investigation are also governed by the Maxwell's equations. Hence, the theoretical background also comes into play in the experimental investigation of MFLNDE. The practical study and interpretation of the measured MFL signals can be carried out side by side with the analysis of the electromagnetic phenomena, which are invariable with the theoretical background. The experimental investigation is based on the validation of the numerical simulation results, for the characterization of various hairline cracks. In consideration of the two methods employed in this research, that is; DCMFL and PMFL techniques, two different experimental MFL set-ups were used. The test samples used for the investigation were soft ferromagnetic low carbon steel plates (EN3B grade) with various wall thicknesses. A soft ferromagnetic material (yoke; silicon steel) was used in order to enable an easy magnetization and demagnetization of the sample, as well as to obtain a high magnetic flux density with a moderate field due to its high magnetic permeability. Each of the test samples used has a well-defined hairline crack, which is aligned perpendicular to the scanning axis and field orientation. Also, the hairline cracks are located at various depths within the test sample. The depth of the cracks used ranges from 0.2 mm to 4 mm with a constant width and length of 0.2 mm and 10 mm respectively, representing both mild and severe cases of naturally occurring hairline cracks in pipeline structures. The hairline cracks are used in the study to investigate different positions of small cracks in pipeline structures.

An Indication of any variation in magnetic properties due to the presence of a hairline crack can be obtained by performing a line scan across the sample. However, to achieve spatial information corresponding to the hairline crack, it is vital to gather information over an area of the sample. The experimental set-up used for the MFLNDE investigation consists of an excitation source (a DC power supply,

a magnetization yoke and a magnetization coil for the DCMFL technique as shown in Fig. 3.4 and a signal generator, a power amplifier, a magnetization yoke and a magnetization coil for the PMFL technique as shown in Fig. 3.5).

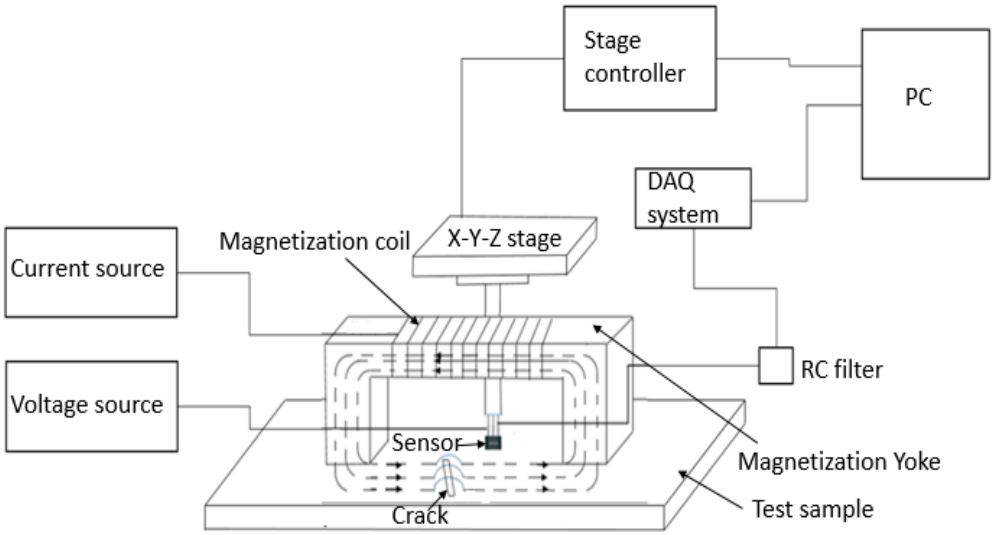

Figure 3.4. The schematic diagram of the DCMFL experimental probe system set-up used in this work.

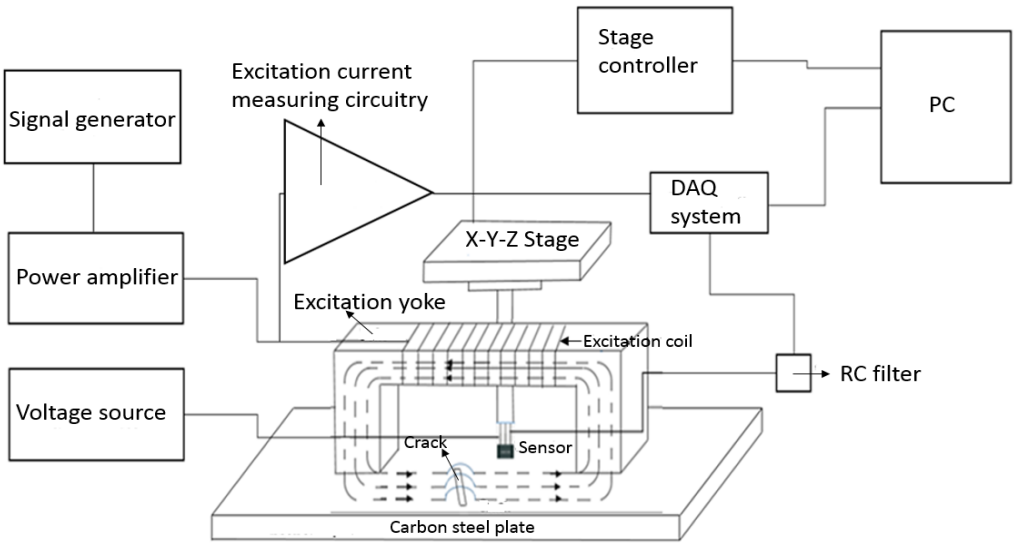

Figure 3.5. The schematic diagram of the PMFL experimental probe system set-up used in this work.

These were used for generating the required magnetic field that is induced into the test sample under scrutiny. Then, a sensing module (Hall Effect Sensor) was used to

measure and evaluate the resultant leakage field generated from the hairline cracks. The sensor was held in place by a 3D printed sensor holder attached to an x-y-z translation stage. The x-y translation stage was used to mechanically move the sensor along the crack region, to measure the magnetic field variation occurring at the vicinity of the crack. The x and y translation stages moves the sensor in the x and y directions respectively, while the z stage was used to adjust the distance between the test sample surface and the lower tip of the sensor (sensor lift-off). Data collected from the sensor was digitized using a digital conversion card and then stored in a computer. A LabVIEW program was developed and used in conjunction with the digital conversion card. The LabVIEW interface was used to visualize data and to communicate with the motors and sensor electronics. The LabVIEW graphical interface (control panel) was employed to initialize the measurement parameters and to collect data. Samples of the resultant signals are collected at 1600 samples per second (1.6 kHz), for each scanning cycle. The objective here was to establish a relationship between the leakage field distribution and the crack parameters, i.e., the crack location, orientation, size and shape. The data obtained is presented in a 3D image form, representing the leakage field distribution pattern in the vicinity of the crack. The 3D image gives a clear and easy interpretation of the existence of a hairline crack on the surface or reverse side of the test sample. It is expected that the 3D image representation of the results obtained (leakage field distribution) can be utilized in monitoring the growth of hairline cracks in pipeline structures over time.

The automated and precise results for the experiment are provided by signal conditioning and processing. A line scan will be performed first, across the engineered hairline cracks (electro discharge machined (EDM) cracks), to measure the leakage field generated. Secondly, an area scan will be performed within the crack vicinity, to achieve a spatial information to the various hairline cracks investigated. A description of the Hall Effect sensor used in this investigation is presented in the subsequent section, describing its mode of operation and applications. The results obtained through modelling, either analytical or numerical significantly depend on experimental confirmation to verify and justify the modelling predictions. The problem of trial and error is significantly decreased through the modelling technique. It also aids in the selection of the right test components as well as providing a reliable alternative to practical experimental

examination, which are more challenging, tedious, hazardous, and expensive to execute.

A significant advancement in the practical experimental approach in solving MFLNDE problems (hairline crack detection and characterization) has been achieved through a solid link between the numerical and experimental methods in MFLNDE. Besides the useful guidelines for system improvement and experimental design, which the numerical modelling technique offers such as: selection of the best excitation frequency, system optimization, selection of sensor type, sensor design and result interpretation. Numerical modelling with its flexibility and efficiency has also helped in providing an alternative means of assessing experimental systems and method. Hence, the use of modelling in conjunction with experiments has provided enormous assistance in tackling the forward and inverse problems of MFLNDE.

3.6) Research Methodology

Numerous investigations were carried out in this research work, employing the use of both FEM numerical modelling and experimental techniques. The investigation was based on the visualization and rapid 3D imaging of the resultant leakage field due to hairline cracks. This was performed through the use of direct current and pulsed current magnetization techniques. This was used to tackle the problem of hairline crack detection, characterization and quantification, for an efficient and complete MFLNDE assessment, as mentioned in Chapter 2. The research centres on the characterization and quantification of the responses of the magnetic field interactions with surface and far-surface hairline cracks existing in ferromagnetic pipeline structures. The analysis of the simulation results obtained via numerical modelling was used for the recognition of the useful magnetic field signatures, corresponding to the hairline crack geometries and profile. Besides the ability to model the various hairline cracks investigated, the simulation performed using the FEM numerical modelling method has proven to yield a satisfactory accuracy in the MFL inspection results.

In order to predict the expected responses from the various hairline cracks inspected, numerical simulations were implemented before practical experiments, employing both DCMFL and PMFL approach. The first stage was to design and optimize the probe for the MFL investigation. The ability to accurately detect, study and interpret the MFL signals in order to quantify cracks is significantly affected by several parameters. Such parameters include; crack orientation, crack geometry (length, width and depth), material permeability, material thickness, magnet system (strength, material, reluctance and lift-off) and sensor system used (type, location and lift-off). The manner in which these parameters affects the acquired signal from hairline cracks was first investigated via the simulation technique and the DCMFL method. This was used for the optimization of the MFL measurement tool used throughout this work.

An examination of the best excitation pulse period for the detection and characterization of both surface and far-surface hairline cracks was first performed using the PMFL technique. Then, the influence of pulse width variation on the magnetic field distribution, which affects the detection capability of various hairline cracks located at different depths in the specimen was explored. To accomplish this task, different excitation periods and pulse widths were investigated and the features contained in the transient signals were analyzed. The detection and characterization of the various hairline cracks investigated using the PMFL approach is achieved via an enhanced visualization and 3D imaging of the leakage field distribution. The transient responses of the various excitation periods and pulse widths investigated are obtained as the probe is scanned in the vicinity of the cracks. These were in the time and frequency domain. It showed the variation of the leakage field amplitude and profile with change in excitation period as well as change in pulse width. Also, different depth information which are related to the skin effect phenomena were established, and interpreted by studying the resultant leakage field distribution for different pulse widths. The examination was useful in determining the best excitation period and pulse width to be used in the detection, characterization and quantification of the hairline cracks investigated.

The forward approach was employed for the hairline crack characterization, based on the visualization of the resultant leakage field, resulting from the interaction between

the induced magnetic field in the specimen and the hairline crack geometries, modelled in the 3D setting in MagNet. The characterization technique was based on how the leakage field distribution varies with the various hairline cracks with different sizes. Information from the leakage field distribution pattern are then extracted and used in characterizing the various hairline cracks investigated. From the simulation results obtained, the feasibility of the experimental method in characterizing hairline cracks using the resultant leakage field distribution was checked.

The FEM simulation conducted in MagNet (DCMFL and PMFL) was able to provide a comprehensive model-prediction of the field pattern in the vicinity of each of the hairline cracks examined, hence, giving a better understanding of the controlling phenomena surrounding the MFL technology, as well as providing an avenue for feature extraction from the responses obtained.

Experimental examinations were implemented in order to confirm the predicted results and to show the practicality of the proposed methods in furnishing the vital information regarding localized hairline cracks. According to Fig. 3.6, the research covers; 1) Analysis of the capabilities and limitations of the DCMFL inspection technique, for detecting and characterizing surface and far-surface hairline cracks, based on visualization and 3D fast imaging of the resultant leakage field distribution. 2) Analysis of the capabilities and potential of the PMFL technique, to eliminate the limitations of the DCMFL technique for hairline crack detection and characterization. 3) Quantitative non-destructive testing of hairline cracks, using the magnetic field signatures obtained from the interactions between the induced magnetic field and the localized hairline cracks in the pipeline structures. 4) An assessment of the practicality of the proposed PMFL method for hairline crack detection, characterization and quantification on ferromagnetic pipeline structures.

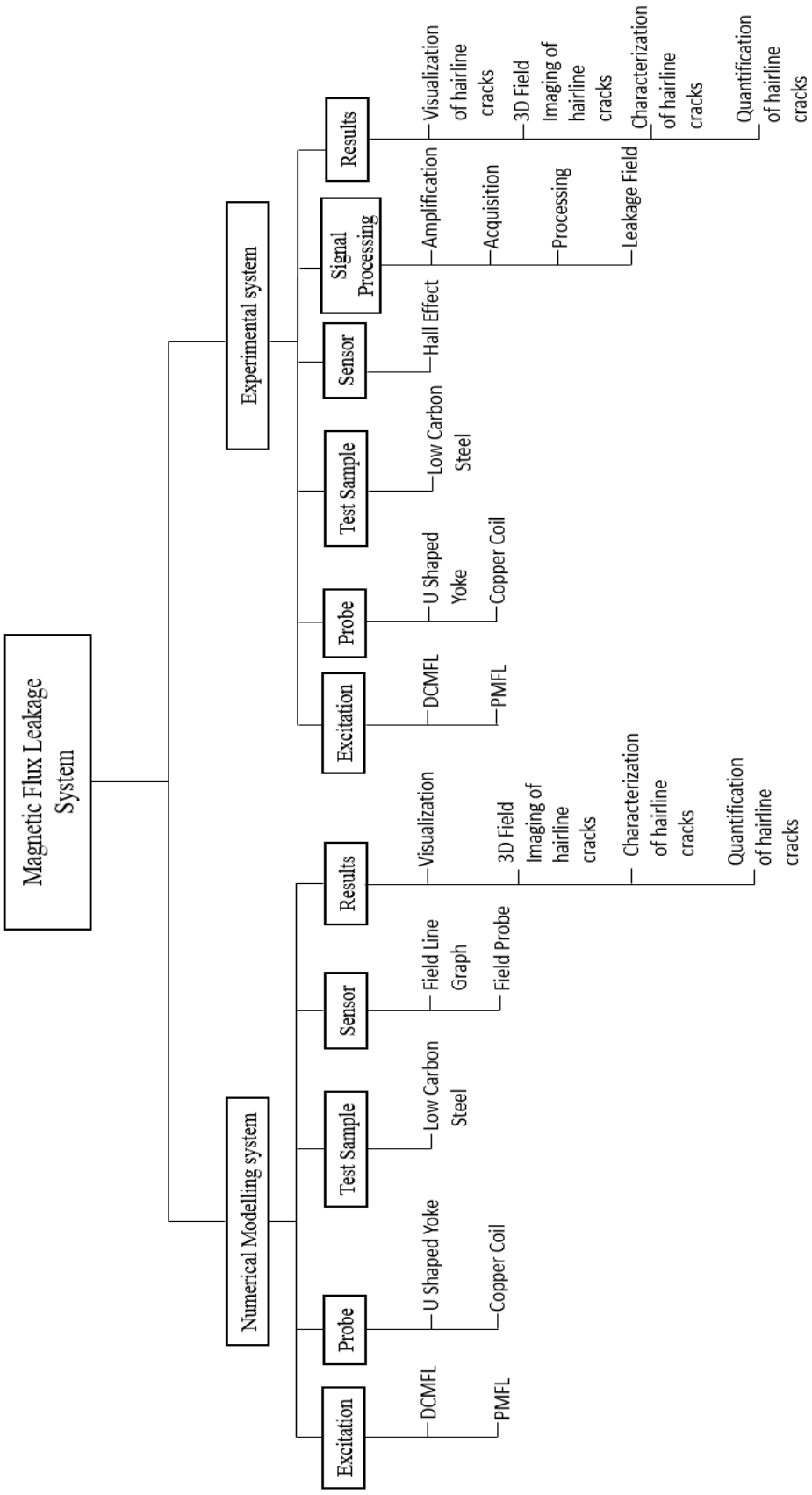

Figure 3.6. The magnetic flux leakage inspection system tree diagram.

3.7) Sensor Selection

Sensors are vital components in the operation of most engineering devices and are generally based on a wide range of underlying physical principles of operation. Considering the vast number of sensor types available in the market, the selection of the most suitable sensor for a new application is the task for the design Engineer. A systematic approach should be adopted in choosing the most appropriate sensor for a particular application. Many of the existing magnetic field sensors are based on the integration of mechanical and electrical characteristics. The selection of the most suitable magnetic field sensor for a particular application is dependent on the matching operating characteristics of the sensor to the specific requirements of the application, i.e. the sensor's sensitivity, accuracy, operating temperature, drift, sensing frequency, resolution, operating environment, reliability and size. Also, the selection of a suitable sensor type will depend on its achievable high stability and gain of the modern day electronics, which includes the sensors ability to convert the power of a stimulus (leakage field) into the power of an electrical signal efficiently. Then the final selection criteria will be based on further analysis and considerations such as sensor size, impedance matching, cost and working space.

Different sensor types such as; Coil sensors (pick-up coils), Giant Magnetoresistive (GMR) sensors, Anisotropic Magnetoresistive (AMR) sensors, Tunnelling Magnetoresistive sensors, or Hall Effect sensors can be potentially used for magnetic field measurements. The coil sensor consists of a multi-turn loop with a core material of high permeability, which increases the efficiency and response of the coil sensor. It has a low power consumption and high frequency range ($10^{-3} - 10^{6}$ Hz). However, the response of the coil sensor is limited by different sources of noise, such as thermal noise and electrical noise. Also, the conventional coil sensor system (pick-up coil) is not very sensitive to low frequency fields, where the electromotive force developed around the loop is equivalent to the rate of change of the field, instead of the field magnitude/amplitude. Hence, the coil performance reduces as frequency decreases (i.e. low sensitivity at low frequency). Hall Effect sensors consist of a thin plate of conducting material with four electrical contacts at its periphery. They present an affordable and productive means of investigating the

presence of defects within pipeline structures, by effectively measuring the field variation in the vicinity of the defect. They also have a higher sensitivity, higher stability and higher operating temperature compared to coil sensors. The magnetoresistive sensors (AMR, GMR and TMR sensor) are manufactured with an advanced thin film element, which provides them with an improved characteristic of higher sensitivity (for low magnetic fields only) higher accuracy, higher output, and higher stability with less temperature drift, compared to coil sensors and Hall Effect sensors. The sensitivity of the magnetoresistive sensors is quantified based on their MR ratio, which is the rate of change of the resistance in the sensing element. Table 3.2 compares the AMR, GMR and TMR sensors based on their MR ratio, output voltage and operating temperature.

Table 3.2. A comparison between the AMR, GMR and TMR sensors

Parameters	**AMR**	**GMR**	**TMR**
MR Ratio (%)	3	12	100
Output Voltage (mV)	150	570	3330
Temperature dependency (25 - 125 °C)	-29	-23	-13

Based on the information presented in Fig. 3.7, which shows the response characteristics of the GMR sensor (see Fig. 3.7a), the TMR sensor (see Fig 3.7b) and the Hall Effect sensor. It can be seen that the linear range for a typical GMR sensor (AA002-02), TMR sensor (TMR2701) and Hall Effect sensor (A1302KUA-T) is 0.3 mT – 1.4 mT, 0.01 mT – 1.5 mT (i.e. 0.1 O_e – 15 O_e) and 0.1 mT – 170 mT respectively. This means that GMR and TMR sensors are best suited in applications where a low magnetic field signal is to be measured, since the linear range for both sensors is very small, especially for the TMR sensor (below 1.5 mT). However, the Hall Effect sensor has a much wider linear range, which makes it a better choice for applications where a larger magnetic field signal is to be measured.

(a)

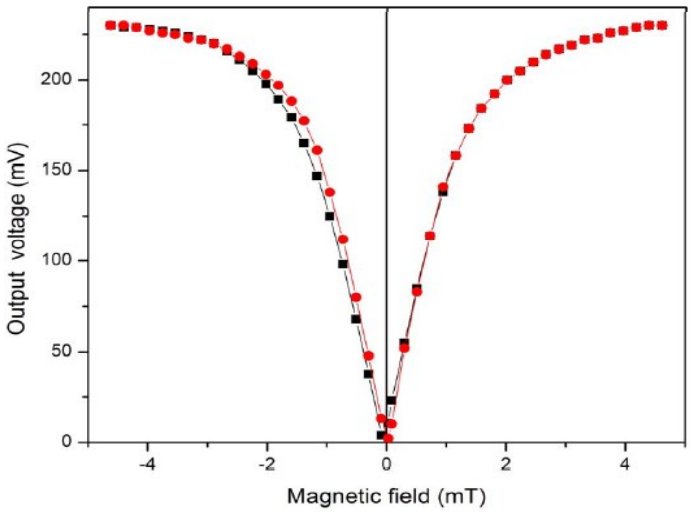

(b)

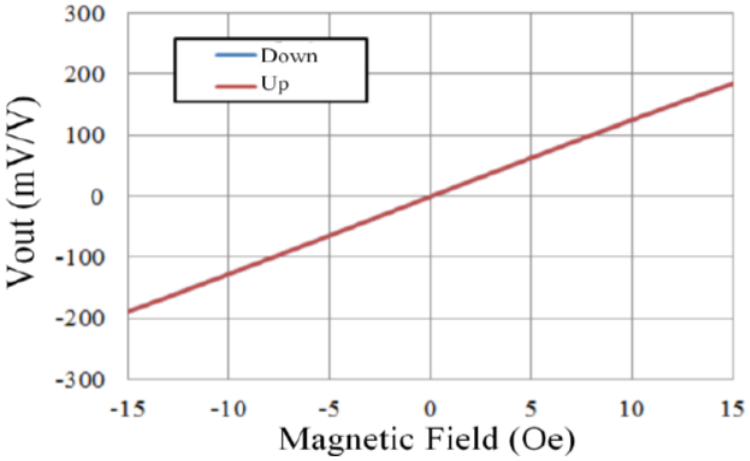

(c)

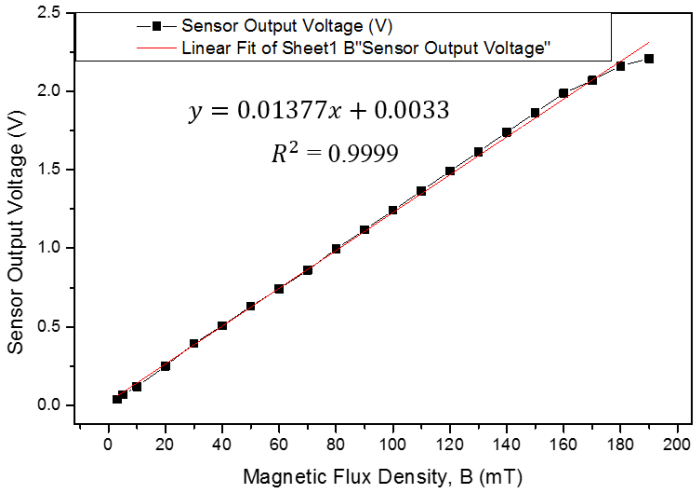

Figure 3.7. Response of the a) GMR sensor [10], b) TMR sensor [11] and c) Hall Effect sensor to an applied magnetic field.

According to the simulation result obtained in this work, which is presented in chapter 4; section 4.3.1, a peak leakage field amplitude ($\boldsymbol{B_x^{peak}}$) of 29.31 mT was generated by a 4 mm deep, 0.2 mm wide and 10 mm long surface hairline crack (hairline crack with the highest leakage field signal). Also, a $\boldsymbol{B_x^{peak}}$ amplitude of 4.28 mT was generated by a 0.2 mm deep, 0.2 mm wide and 10 mm long far-surface hairline (hairline crack with the least leakage field signal). Despite the higher sensitivity of the GMR and TMR sensors compared to other sensor types, they cannot be used to detect the leakage field generated by the hairline cracks investigated in this work. This is because both sensors have a linear range below this field range (below 29.31 mT), and would not be able to output a signal proportional to the strength of the leakage field generated by the hairline cracks. This problem can be solved by using the A1302KUA-T type Hall Effect sensor, which has a much larger linear range with a good sensitivity of 0.0138 V/mT. Therefore, a Hall Effect sensor was chosen for the detection and characterization of the surface and far-surface hairline cracks investigated in this work.

3.8) Hall Effect Sensor Operation

This section will provide a brief discussion on the mode of operation and applications of the magnetic field sensor (Hall Effect Sensor) used in this research. Hall Effect sensors are manufactured in form of a thick semiconductor film and measure the magnitude of the magnetic flux density (**B**). The use of the "Hall Effect" is the most common technique of measuring magnetic fields. Hall Effect sensors are well known and have numerous applications. They are used in vehicles as wheel speed sensors and in crankshafts as position sensors. They are also employed as switches, proximity sensors, MEMS compasses etc. Higher clearances between the inspection head and the magnetic field being detected can be achieved using Hall Effect sensors. Thus, allowing for inspection of non-uniform surfaces, such as; welded, cracked and corroded surfaces on pipelines, storage tanks, rail heads, bridges and other ferromagnetic steel structures.

When a current is induced in a thin conductive sample, the charge carriers will flow through the sample in a straight line, from one side of the sample to the other as shown in Fig. 3.8a. However, when a magnetic field is brought in the vicinity of the sample, the initial flow of the charge carriers will be disturbed, as a result of a force known as the Lorentz force (F_e). This will cause the negative charged particles to divert to one side of the sample and the positive charged particles will move to the opposite side of the conductive sample, as shown in Fig. 3.8b. The force developed due to the magnetic field is given by equation (3.24);

$$F_e = evB_n \tag{3.24}$$

Where F_e is the force acting on the electrons, e is the electron charge ($-1.6 \times 10^{-19}\ C$), v represents the electron velocity through the wire and B_n is the tangential magnetic field component. A measurable voltage will be obtained by putting a meter between the two sides of the sample. The effect of obtaining a measurable voltage is termed the "Hall Effect". This is named after Edwin Hall, who first ascertained this effect in 1879. The basic hall element of the Hall Effect sensors usually supplies very small voltage of a few microvolts per tesla (μV/T), hence, these devices are usually fabricated with built in high gain amplifiers, to provide the required output voltage (measurable voltage). The Hall voltage can be expressed as shown in equation (3.25).

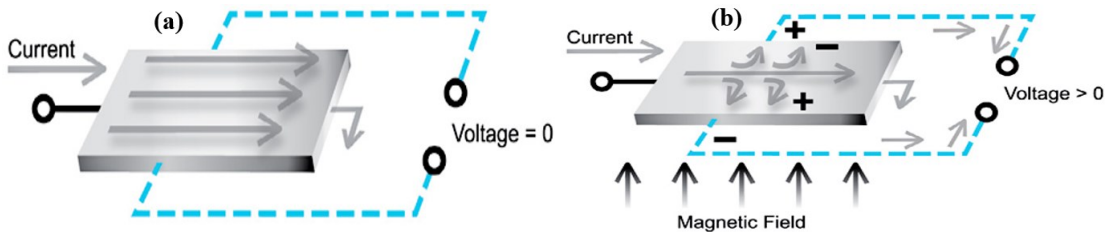

Figure 3.8. The thoery of Hall Effect sensor operation; a) Hall probe with zero magnetic field and b) Hall probe with non-zero magnetic field [12].

$$V_H = R_H I \frac{B}{t} \tag{3.25}$$

Where V_H is the Hall voltage, R_H is the Hall coefficient which is fixed for a given material, I is the induced current in the conductive sample, $\boldsymbol{B}$ is the magnetic flux

density and t is the thickness of the probe. The Hall voltage is proportional to the magnetic flux density (**B**), provided the temperature is constant.

Hall Effect sensors can have analogue and digital output. The analogue output Hall Effect sensor is also known as a linear Hall Effect sensor. It consists of a voltage regulator, a hall element and an amplifier, as shown in the circuit schematic displayed in Fig. 3.9. From the schematic circuit shown, it can be observed that the output of the sensor is analogue, and the output is proportional to the hall element or the magnetic flux density (**B)** being measured. This type of sensor provides a steady output voltage that increases with increasing magnetic field detected. The increase in the output voltage provided by the analogue Hall Effect sensor will continue until it starts to approach saturation. At this point, any further increase in the magnetic field detected will not yield a proportional increase in the output voltage, rather it will further push/force the output voltage into saturation. The analogue sensors are utilized for proximity measurement because of their continuous linear output.

However, the digital output Hall Effect sensors have only two output states, which are the on and off states. The digital sensors have an added element as illustrated in the circuit schematic displayed in Fig. 3.10. The added element is the Schmitt trigger, which provides hysteresis or provide various threshold levels, hence, the output is either high or low. The hysteresis provided by the Schmitt trigger helps to remove any oscillation of the sensor output signal, as the digital output sensor approaches and leaves the magnetic field. An example of the digital output Hall Effect sensor is the Hall Effect switch. The Hall Effect switch is usually utilized as limiting switch in 3D printers and for detection and positioning in industrial automation systems.

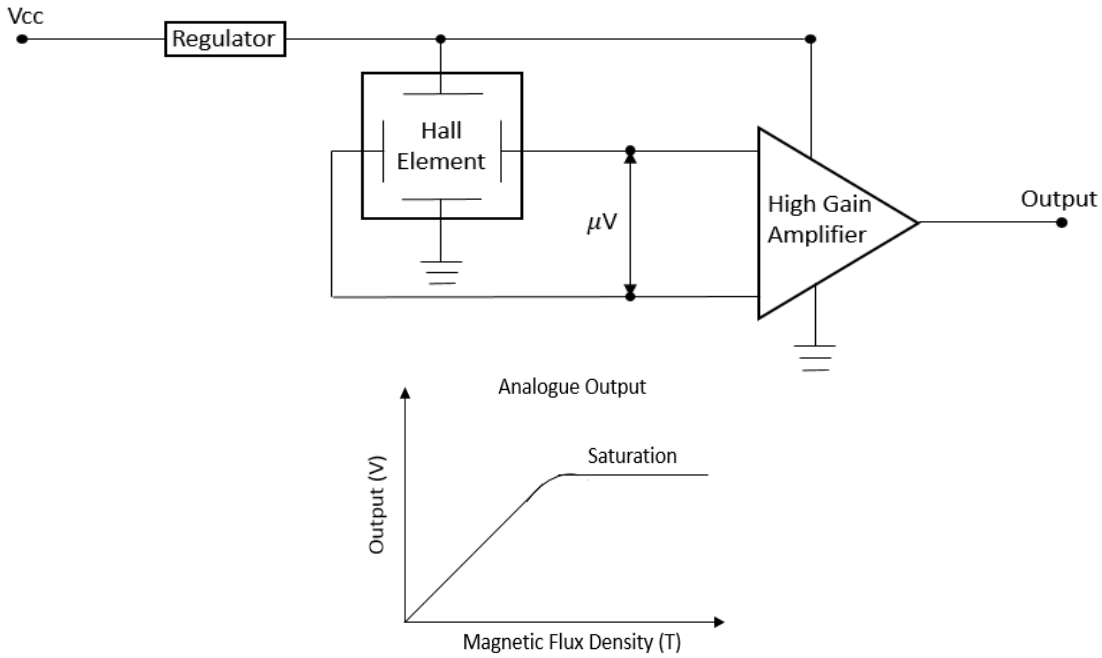

Figure 3.9. A schematic diagram of an anologue output Hall Effect sensor.

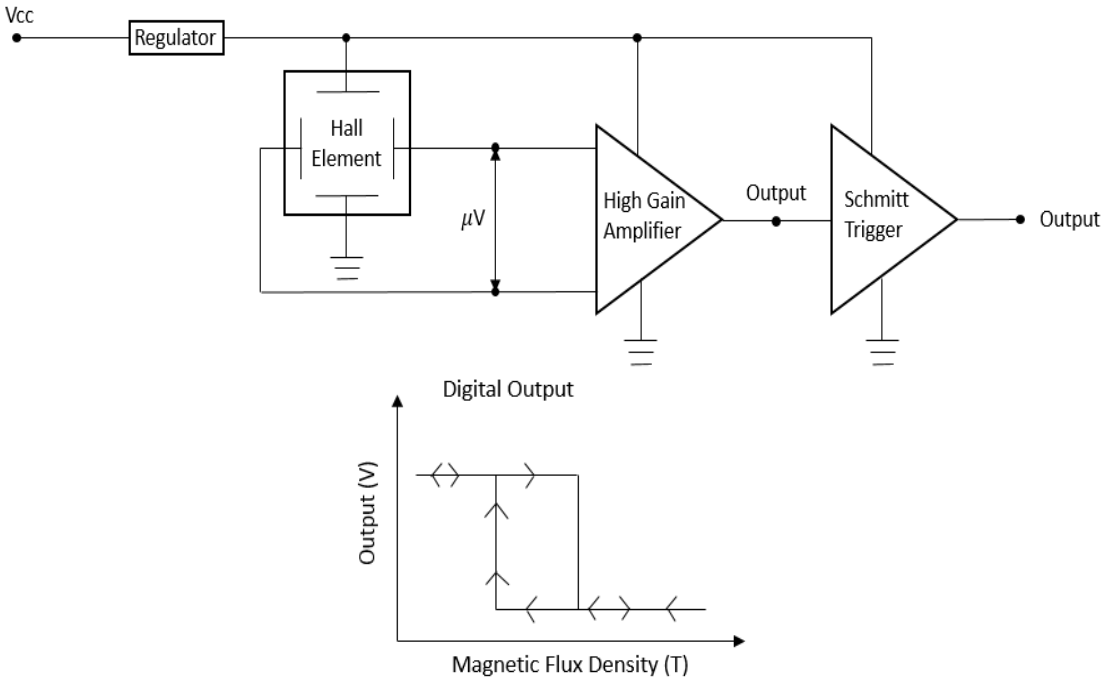

Figure 3.10. A schemtic diagram of a digital output Hall Effect sensor.

The Ratiometric linear Hall Effect sensor is used in this work. This is a type of linear output Hall Effect sensor, hence, it yields a voltage output that is proportional to the stength of the magnetic field being detected. It has a bipolar supply differential

amplifier that outputs a voltage, which is half (50 %) of the supplied voltage when no magnetic field is being detected, and it operates through a wide range of temperature that is; between -40 °C to 150 °C [13]. This unique characteristic of this sensor makes it suitable for a wide range of industrial application where high accuracy is desired. The inbuilt circuitry of the sensor provides temperature compensation, which helps to: minimize the inherent drift in the sensitivity of the Hall element, outputs small and fixed impedance, provides a small signal with high gain amplifier, has a corrective and effective offset cancellation performance [11]. The sensor circuitry also includes an inbuilt chopper, which helps in the stabilization of the small voltage signal produced over the hall element, which usually causes a problem in signal processing. Hence, ensuring a correct and steady output over the detailed operating temperature and voltage limits.

Hall Effect sensors presents an affordable and productive means of investigating the presence of cracks within pipeline structures, by effectively measuring the field variation in the vicinity of the cracks. Furthermore, Hall Effect sensors have a higher sensitivity to low frequencies compared to using impedance measurements (coils; most suitable for high frequency measurement), hence, more effective in detecting deep or far-surface hairline cracks. Also, the Hall Effet sensors are very suitable for detecting high magnetic fields, compared to GMR and TMR sensors whose sensitivity decreases with increasing magnetic field.

3.9) Chapter Summary

An introduction to Maxwell's equations that describe electromagnetism, as well as the equations obtained from them has been described in this Chapter. In addition, the finite element numerical modelling and experimental technique to solving the MFLNDE problems were discussed. The methodology for this work through FEM and experimental examinations; by means of visualization and 3D imaging of the resultant leakage field distribution, using both the DCMFL and PMFL techniques were presented.

Subsequent to the illustration of the implementation of study for this project, the remaining part of this thesis (Chapters 4-6) will report on the findings of the investigation on hairline crack detection and characterization. The investigation is performed using the FEM numerical simulation technique, supported with practical experiments. The hairline crack characterization task is accomplished through an enhanced visualization and 3D imaging of the resultant responses, caused by the interaction between the induced magnetic field and the crack geometries, while employing the DCMFL and PMFL techniques.

3.10) References

1) N. Zatsepin and V. Shcherbinin, “Calculation of the Magnetostatic Field of Surface Defects. I. Field Topography of Defect Models”. Defektoskopiya 5, 50–59, (1966).
2) J. Hwang and W. Lord, “Finite Element Modelling of Magnetic Field/ Defect Interactions”. *ASTM J. Test. Eval*, 3(1), 21–25, (1975).
3) Z. Huang and P. Que, “Three Modelling Methods in MFL Testing”. *17th World Conference on Non-destructive Testing*. 25-28, October (2008).
4) J. Reddy, “An Introduction to the Finite Element Method”. McGraw-Hill Education, (2005).
5) Y. Li, G.Y. Tian and S. Ward, “Numerical Simulation on Magnetic Flux Leakage Evaluation at High Speed”. *NDT E Int* 39(5), 367–373, (2006).
6) F.I. Al-Naemi, J.P. Hall and A.J. Moses, “FEM Modelling Techniques of Magnetic Flux Leakage-type NDT for Ferromagnetic Plate Inspections”. *J. Magn. Magn. Mater* 304(2), 790–793, (2006).
7) Electromagnetic Testing, “Non-destructive Testing Handbook”, 3rd Edition, Vol. 5. ASNT Press, ISBN 1-57117-116-9, (2004).
8) Infolytica Coperation, “2D/3D Electromagnetic Field Simulation Software”. [Online]. Available at: http://www.infolytica.com/en%5Cproducts/magnet/. [Accessed 12 Nov 2017].
9) L. Mierczak, “Evaluation of Structural Integrity of Steel Components by Non-destructive Magnetic Methods”. In Electrical and Electronic Engineering. Volume, *PhD Thesis: Cardiff University,* (2016).
10) J. Aguila-Munoz et al, “Crack Detection in Steel Using a GMR-Based MFL Probe with Radial Magnetization”. CONIELECOMP, 23rd International Conference on Electronics, Communication and Computing, (2013).
11) Multi-Dimension Sensing the Feature, “High Sensitivity and Low Hysteresis TMR Linear Sensor (TMR2701 Datasheet)”. [Online]. Available at: http://www.dowaytech.com/en/1397.html. [Accessed 13/12/2017].
12) Design World, “Hall Effect Sensor Operation”. (2017). [Online]. Available at: http://www.designworldonline.com/choose-your-best-pneumatic-cylinder-sensor-here/. [Accessed 5 August. 17].
13) Gospel, w. et al, “Sensors a Comprehensive Survey”. In: Boll, R and Overshot, K.J. eds. *Magnetic sensors*. New York, VCH Publishers Inc. 4-9. (1989).

Chapter 4: DCMFL Technique for Hairline Crack Detection and Characterization

4.1) Introduction

Pipelines are very useful structures for transportation, in the oil, gas and petrochemical industries. They are usually located in very hazardous environments (e.g. underground), thus, the hydrous medium at the top and bottom surfaces usually attack such pipelines. This can cause tiny cracks to develop, which grows over time. The developed cracks threaten the pipe's integrity. Hence, periodic pipeline inspection to locate the presence of cracks is essential, especially at its early stage, in order to prolong its service lifetime, as well as to prevent unwanted hazards. Numerous NDE techniques exist, which could be potentially applied in order to achieve a quick and complete pipeline inspection. However, in comparison with other NDE techniques, the MFL method offers several advantages such as: easy implementation, efficient inspection, low cost, etc. Moreover, pipelines are manufactured with ferromagnetic materials with high magnetic permeability, thus, making the MFL method very suitable for detecting and evaluating cracks in such pipelines.

DCMFL investigation, based on visualization and rapid 3D imaging of the resultant leakage field distribution caused by hairline cracks is presented in this chapter. The hairline crack detection and characterization task is accomplished via the use of both FEM numerical simulations and practical experimental analysis. The FEM conquers numerous challenges and drawbacks encountered in NDE analysis, hence, it is considered suitable in the area of leakage field calculation. It has also proven to be a better approach for the design and specification of MFL measurement probe systems. Furthermore, by using the FEM simulation approach, detection mechanisms can be studied and understood in detail, thus, providing a sound theoretical guidance for an optimal MFL probe design, as well as ensuring a reliable signal detection analysis.

First, the manner at which the magnetization methodology (magnetization current, yoke shape, yoke dimensions, yoke lift-off and yoke permeability) and the sensing methodology (sensor lift-off and position) influence the detection sensitivity of the acquired MFL signal due to hairline cracks is investigated, via a series of FEM numerical simulations. These signal influencing factors and parameters were used to systematically optimize the MFL measurement tool, in order to increase the detectability of both surface and far-surface hairline cracks. The research subsequently advances to the use of direct current technique (DCMFL) for the detection and characterization of surface and far-surface hairline cracks, with different depth and width sizes. The investigations were performed in the 3D environment, using the MagNet 7.6 software by Infolytica. The accuracy and practicality of the FEM optimized DCMFL measurement tool in detecting hairline cracks is assessed via practical experiments, using a 6 mm and 10 mm thick low carbon steel plates.

4.2) Optimization of the MFL Inspection Tool via FEM Computation

This section focuses on the optimization of the MFL measurement system used for this investigation, by employing the FEM numerical simulation technique, in order to increase the detection sensitivity of the experimental measurement system presented in the subsequent section. FEM simulations are very helpful in improving the detection sensitivity of the feeble leakage field from both surface and far-surface hairline cracks significantly. For instance, crucial leakage field influencing parameters can be optimized. This includes; the magnetization current, the coil structure, the induced magnetic field magnitude and orientation, the yoke clearance from the test sample surface (yoke lift-off), the yoke shape, yoke geometry, yoke permeability, etc. Also, the sensor parameters such as; the sensor size, position, orientation and its clearance from the test sample surface (sensor lift-off) can be optimized. By so doing, the largest possible sensor signal variation in the vicinity of the hairline cracks will be achieved. Adequate magnetization is the key to successful MFL testing. If the wall of the pipeline is not well magnetized, the existing cracks cannot leak sufficient magnetic flux that can be detected, or the feeble leakage flux

produced could be obscured by noise. Therefore, the magnetization power is the crucial factor influencing the MFL inspection system's accuracy. The stronger the magnetic field applied, the greater the magnetic flux leakage that will be developed. So, a high enough magnetic field should be induced in the test sample in order to achieve a strong magnetization, and to ensure that the sample wall attains moderate saturation. Also, a suitable magnetizer wall thickness (yoke thickness) as well as a suitable pole spacing (yoke leg spacing) should be chosen, since this will mean an increased magnetic force between the yoke and test sample. Hence, the driving power between the yoke and sample is increased, enabling the highest leakage signal possible.

The axisymmetric MFL model used for the FEM analysis consists of; a U-shaped silicon steel yoke, an excitation coil with 300-turns of copper wire with a conductivity of 1.12×10^7 S/m, low carbon steel plates with dimensions of 350 mm $\times$ 60 mm $\times$ 10 mm and a field probe. The excitation coil was modelled at the top horizontal section of the yoke and was used to magnetize the yoke in the axial direction (along the sample length). The field probe was used to measure the resultant leakage field signal caused by the crack, at a user specified sensor lift-off. The FEM simulation first tackled the geometrical shapes of the model through a number of different mesh elements with various shapes and sizes, then it substitutes the non-linear magnetic properties of the materials used in the form of parameters into the finite element equation [1].

A summary of the thermal and electrical parameter values for the low carbon steel plate and silicon steel yoke used in the simulation are listed in table 4.1.

Table 4.1 The thermal and electrical parameters for the sample (plate) and yoke used in MagNet.

Parameters	**Sample**	**Yoke**
Thermal heat capacity, C_p [J/kg.C]	475.0	711.8
Thermal conductivity, k [W/(mC)]	44.1	48.3
Thermal diffusivity, $\propto [m^2/s]$	1.72×10^{-5}	1.49×10^{-5}
Mass density, d [kg/m^3]	7801.0	7817.0
Electrical conductivity, δ [S/m]	1.32×10^6	2.17×10^6
Electric permittivity, ε_r [F/m or A]	1.0	1.0
Maximum relative permeability	100.0	4000.0

Prior to the simulation task conducted in MagNet, a dc measurement system (electromagnet driven by a quasi dc current by national instrument) was used to obtain the **B-H** loop of a typical low carbon steel sample (mild steel-EN3B grade) and the **B-H** loop of a typical silicon steel material (yoke) as shown in Fig. 4.1 (these are the exact same materials used in the later experimental investigation). The acquired **B-H** loop data for both materials were utilized in the MagNet software, to ensure close approximation with the experimental system.

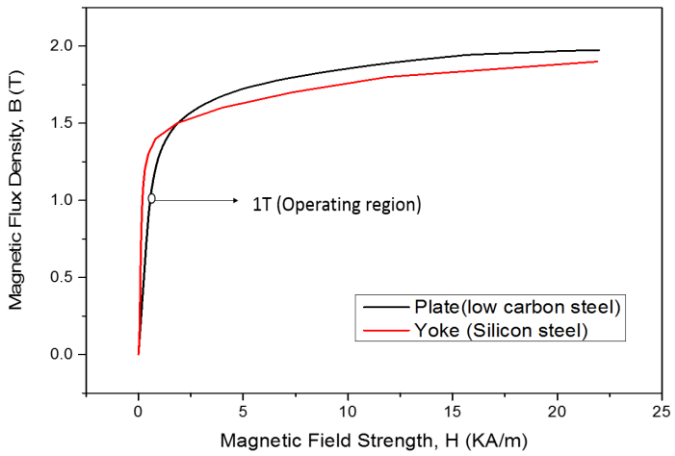

Figure 4.1. The **B-H** curve for the low carbon steel plate and silicon steel yoke obtained using the dc measurement system (electromagnet driven by a quasi dc current by national instrument).

The 3D static solver in MagNet was used to build the simulation model of the probe and sample in order to achieve a better illustration of the problem. Boundary conditions were utilized and set in a region sufficiently larger than the region of interest in order not to affect the result. A smaller mesh size of 0.02 mm is used on the inside and outside region of the cracks, in order to improve the result accuracy. The MFL probe optimization task was implemented with a 0.8 mm deep, 0.2 mm wide and 10 mm long surface and far-surface hairline cracks, while using a 10 mm thick plate. These cracks were modelled at the centre of the test plates (region with most uniform field). The results acquired from the axial field component ($\boldsymbol{B_x}$) and the radial field component ($\boldsymbol{B_y}$) were utilized for the MFL probe optimization.

For an improved representation of the magnetic field in the modelled MFL test system, results were acquired by solving along the x, y and z plane, in order to acquire the **B** field profiles produced when a crack exists and when it does not. The

acquired data is then utilized for calibration, so that the output highlights when the test plate is faulty and when it's not. Fig. 4.2 and Fig. 4.3 presents the solution along a line in the x direction of the plate (axial distance), from -10 mm to 10 mm, showing the leakage field ($\boldsymbol{B_x}$) obtained when no crack exist and when a crack exist respectively. As can be seen in Fig. 4.2, a U shaped profile is obtained when no crack exists and a uniform magnetization is achieved at the centre of the plate. This is because a higher leakage flux is produced at the ends of the line. That is; at the region where the yoke legs meet with the test plate. This means that both the **B** and **H** field measurements will be greater at the yoke leg regions, compared to that at the centre of the plate, where the field is more uniform. Hence, the hairline cracks were positioned at the centre of each plate, in order to obtain a more uniform and accurate result.

When a 0.8 mm deep surface and far-surface hairline cracks were modelled at the centre of the plate, a higher leakage flux was obtained in the vicinity of the cracks, as displayed in Fig. 4.3. The output data for when a crack exist is subtracted from the output data for when a crack does not exist. By subtracting the two outputs from one another, results in **B** measurements that are caused by the crack only and not the leakage field arising from the magnetization yoke and coils (background noise) is acquired.

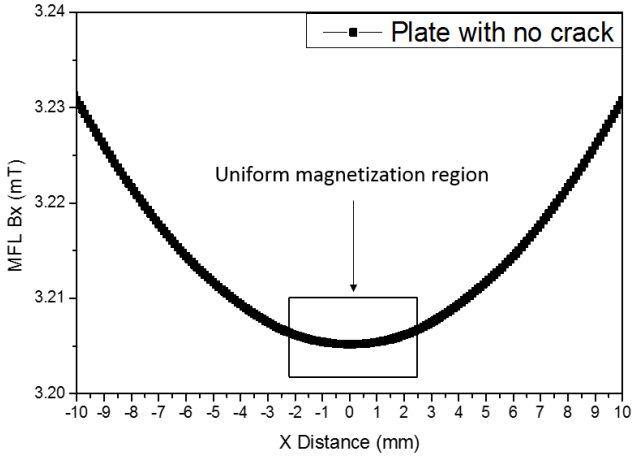

Figure 4.2. The simulated output profile of the MFL signal ($\boldsymbol{B_x}$) when a crack do no exist.

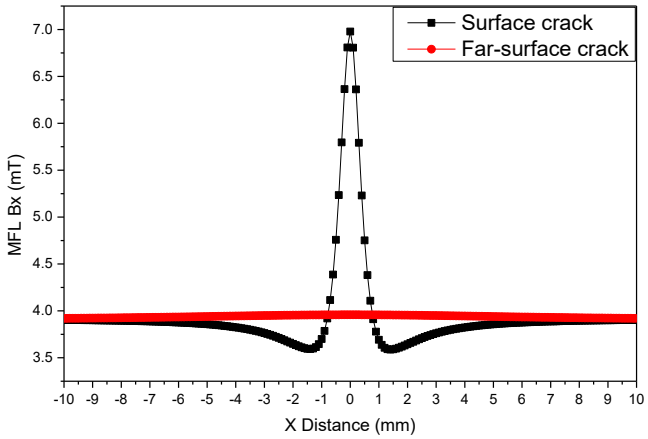

Figure 4.3. The simulated output profile of the MFL signal ($\boldsymbol{B_x}$) due to a 0.8 mm deep, 0.2 mm wide and 10 mm long surface and far-surface hairline cracks (8% wall loss).

4.2.1) Yoke Shape Optimization

The magnetization power of the yoke is a very crucial factor which significantly affects the performance of the modelled MFL measurement system. The yoke has two basic functions; one is to provide the much desired near saturation magnetic field in the test sample, in order to enable a sizable leakage field to occur at the crack site. The other is to provide a suitable axial bias magnetic field in the sample for the MFL testing. Different yoke shapes were modelled in this work to ascertain if the variation in yoke shape would influence the flux induction into the test plate, and to determine if it will increase the leakage field generated due to the presence of both surface and far-surface hairline cracks. An MFL test system that yields a larger output is desired, since it translates to the sensing module detecting larger fluctuations in leakage fields more easily. Also, a test system which is efficient is required, since the leakage flux from an abysmally designed yoke would affect or swamp the feeble magnetic field emanating from the hairline cracks.

Two different yoke shapes were compared, a square yoke and a curved yoke as shown in Fig. 4.4a and Fig 4.4b respectively. Both were modelled in the 3D environment in Magnet. A direct current is passed through the magnetization coil in each case, so as to magnetize the test plate through the yokes. Measurements of the resultant leakage field from the modelled hairline cracks in each case were recorded,

in order to determine the yoke design that would yield the best overall performance in-terms of the leakage field magnitude obtained. Fig. 4.4a shows the **B** field results of the initial model (square yoke) developed in MagNet. As demonstrated, most of the flux generated is restrained within the silicon steel yoke and the low carbon steel plate. However, a small percentage of the total field generated leaks away into the surrounding air. The greater magnetic flux density developed in the yoke and plate when compared to that in the surrounding air is because of their higher magnetic permeability compared to air. The higher magnetic field in the test plate compared to that in air, confirms the fact that the magnetic field flows more freely through it. Hence, less magnetizing force will be required to induce **B** into the plate, than to force flux through the surrounding air. Also, the magnetic flux density is strongest in the test plate, compared to that in the magnetization yoke. This is because magnetic flux always follows the track that offers the lowest resistance when a ferromagnetic material is magnetized and a significant amount of the generated flux will settle at the walls of the material [2]. This means that flux will flow more freely in a material with greater thickness (yoke with 30 mm wall thickness) compared to one with lesser thickness (test plate with 10 mm wall thickness). This is due to an increased area offered by the thicker material, thus reducing the amount of flux lines intersecting each other. This will in-turn result to a lower magnetic flux density in the thicker material (yoke) compared to that in the thinner one (test plate).

A curved yoke was modelled next as shown in Fig. 4.4b, to confirm whether a significant increase in the amount of leakage field will occur at the hairline crack region, thereby yielding a more sensitive system. The variation in flux generated at the yoke edges, comparing the square yoke and the curved yoke can be seen in Fig. 4.4a and Fig. 4.4b respectively. As shown in Fig. 4.4a, the square yoke causes a higher concentration of flux at the yoke edges (flux bunching), resulting in a higher magnetic reluctance for the flux path. However, a curved shape at the yoke edges as shown in Fig. 4.4b creates an easier path than a straight edge design with square edges. This is because magnetic flux trails the path that offers the least resistance (curved yoke), which is usually the shortest inner path of the yoke.

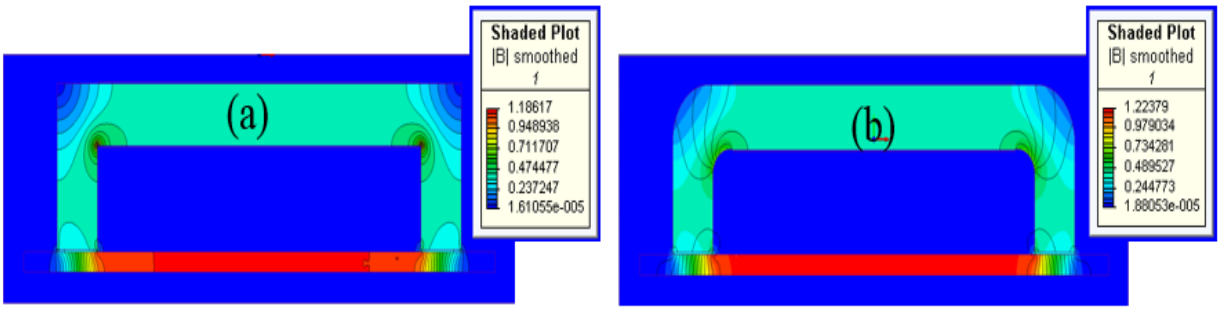

Figure 4.4. The model-predicted field distribution pattern for; a) Square yoke and b) Curved yoke.

The results acquired for a 0.8 mm deep, 0.2 mm wide and 10 mm long surface and far-surface hairline cracks is presented in Fig. 4.5. It shows the leakage fields (Fig. 4.5a ($\boldsymbol{B_x}$)) and (Fig. 4.5b ($\boldsymbol{B_y}$)) obtained for both surface and far-surface hairline cracks, comparing the square yoke and the curved yoke designs. As can be seen, the use of a curved yoke results in greater leakage flux at the crack site and therefore producing a greater output signal. That is, a peak leakage field ($\boldsymbol{B_x^{peak}}$) amplitude of 8.8 mT and 4.5 mT was acquired for the surface and far-surface hairline cracks respectively, while using the curved yoke design. However, a $\boldsymbol{B_x^{peak}}$ amplitude of 7.1 mT and 3.9 mT was acquired for the same surface and far-surface hairline cracks while using the square yoke design. This is because of the difference in geometry, as the flux in the curved yoke follows an easier path and smoothly guided into the test plate. Therefore, a curved yoke design is chosen for this investigation.

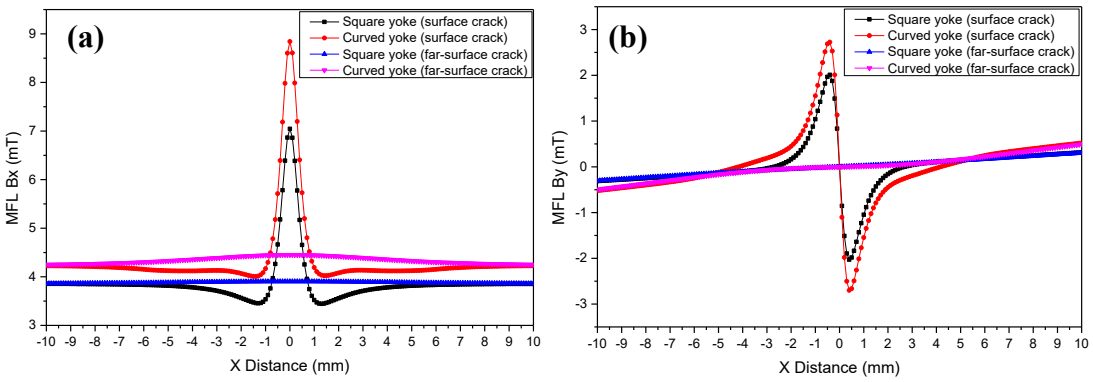

Figure 4.5. The simulated MFL signals due to a 0.8 mm deep, 0.2 mm wide and 10 mm long surface and far-surface hairline cracks, comparing the square and curved yoke designs; a) $\boldsymbol{B_x}$ field component and b) $\boldsymbol{B_y}$ field component.

4.2.2) Yoke Parameter/Geometry Optimization

The magnetic flux leakage generated for both surface and far-surface hairline cracks were simulated, with the sole aim of analyzing the effects of the yoke parameters on the sample magnetization and leakage flux developed. Subsequently, the following yoke parameters; leg height, leg length, leg width and leg spacing, were optimized using the MFL signal ($\boldsymbol{B_x^{peak}}$) amplitude acquired from a 0.8 mm deep, 0.2 mm wide and 10 mm long surface and far-surface hairline cracks.

4.2.2.1) Yoke Leg height

Fig. 4.6a shows a slight decrease in the $\boldsymbol{B_x^{peak}}$ amplitude for both the surface and far-surface hairline cracks as the yoke leg height is varied from 20 mm to 160 mm in steps of 20 mm, when other parameters are held constant. Similar findings have been shown elsewhere [3, 4]. The yoke with a leg height of 20 mm produced the highest signal output. However, using a yoke with a very low height ($<$ 80 mm) will produce more stray fluxes, which do not follow the proposed path of the magnetic circuit, rather they cut through from one end of the circuit to the other (top of yoke to plate). Hence, they do not add up to the flux generated in the test plate. Such stray fluxes are capable of causing inaccurate measurements of the true magnitude of MFL signal, which could lead to cracks being missed or undersized, especially for hairline cracks. Therefore, a yoke leg height of 80 mm was chosen for this investigation.

4.2.2.2) Yoke Leg length

The information displayed in Fig. 4.6b shows that the $\boldsymbol{B_x^{peak}}$ amplitude increases as the leg length of the yoke is varied from 5 mm to 40 mm in steps of 5 mm, when other parameters are fixed. This is because the magnetic flux is increased as the reluctance of the magnetic circuit decreases ($\Phi = \frac{MMF}{S}$), due to an increase in the

cross sectional area of the yoke ($s = \frac{L}{\mu_0 \mu_r A}$). Where Φ, MMF and S, are the magnetic flux, the magnetomotive force and magnetic reluctance respectively, while A and L are the cross sectional area of the yoke and length of yoke respectively. Similar result is shown in [4]. Hence, a yoke leg length of 30 mm was selected.

4.2.2.3) Yoke Leg width

Fig. 4.6c demonstrates an increase in the $\boldsymbol{B_x^{peak}}$ amplitude for both the surface and far-surface hairline cracks as the yoke leg width is varied from 10 mm to 60 mm in steps of 10 mm, when other parameters are kept constant. The increase in the leakage field ($\boldsymbol{B_x^{peak}}$) amplitude recorded is due to an increase in the magnetic flux (Φ) generated as the reluctance (S) of the magnetic circuit is decreased, due to an increase in the cross sectional area (A) of the yoke. Similar finding is reported in [4, 5]. Using a yoke with a leg width of 60 mm resulted to a greater leakage field amplitude at the crack site compared to the 10 mm, 20 mm, 30 mm, 40 mm and 50 mm leg widths. Also, by using a yoke leg width of 60 mm which matches with the width of the test plate, the amount of stray fields developed due to unequal proportion of the yoke leg width compared to the test sample width will be significantly reduced. Therefore, a yoke leg width of 60 mm was chosen. Moreover, the effect of the yoke leg width on the MFL signal was found to be more compared to the yoke leg length and height.

4.2.2.4) Yoke Leg spacing

Fig. 4.6d shows that the $\boldsymbol{B_x^{peak}}$ amplitude decreases for the surface hairline crack as the yoke leg spacing is varied from 50 mm to 350 mm in steps of 50 mm, when other parameters are held constant. This is due to a decrease in the magnetic field strength as the distance between the yoke legs increases. However, the $\boldsymbol{B_x^{peak}}$ amplitude for the far-surface crack is found to increase from 50 mm up to 250 mm, then began to

drop as the distance is increased further. This is suspected to be associated with the lateral spread (broad profile) of the MFL signal at the vicinity of the far-surface crack, when compared to the narrow confinement of the MFL signal at the surface crack region. Therefore, a yoke leg spacing of 240 mm was chosen.

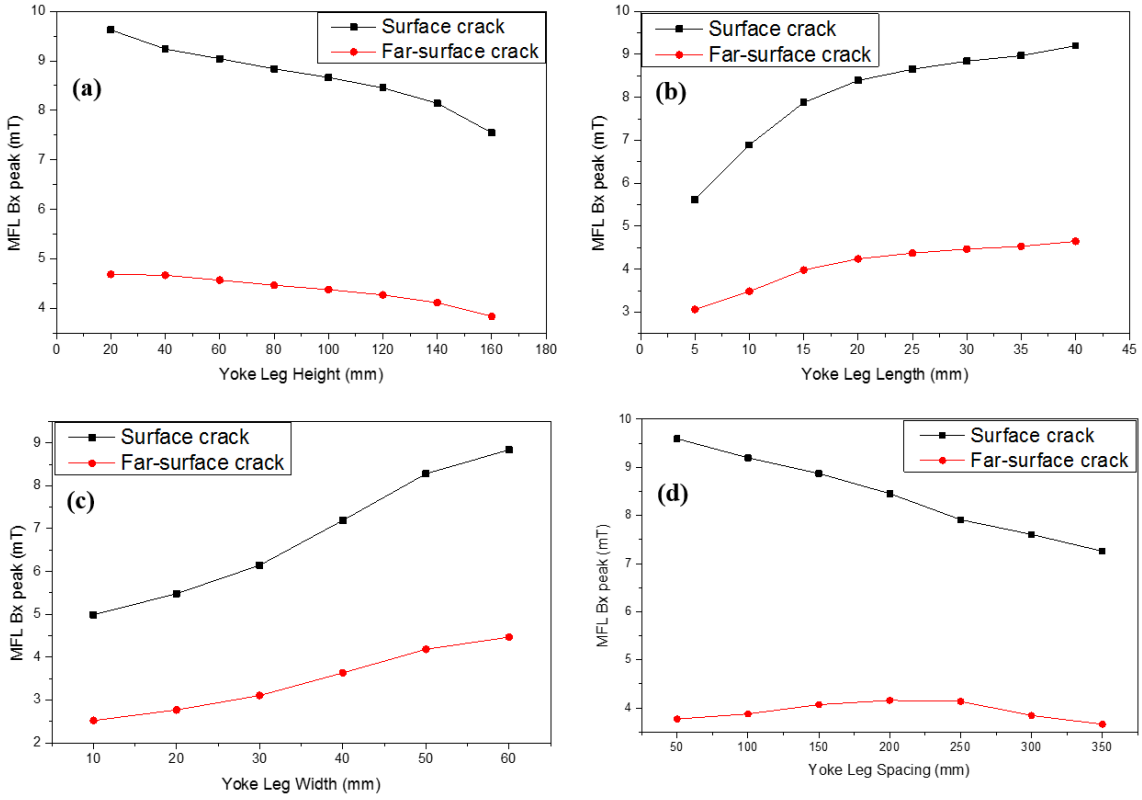

Figure 4.6. The relationship between the simulated MFL signal peak amplitude ($\boldsymbol{B_x^{peak}}$) and the; a) Yoke leg height, b) Yoke leg length, c) Yoke leg width and d) Yoke leg spacing.

4.2.3) Yoke Permeability Optimization

The magnitude of the magnetic flux generated in the test plate significantly depends on the permeability and size of the material used for the yoke as well as the test plate. Low carbon steel materials (e.g. mild steel) are usually used for the manufacture of most pipeline structures and they come with similar permeabilities and thicknesses. Therefore, the yoke permeability, yoke size and the yoke clearance from the plate surface are the main factors determining the amount of flux generated

in the test plate. Therefore, the permeability of the material used for the yoke construction will play an important role in controlling the magnitude of the magnetic flux density (**B**) established within the test plate, which in-turn will determine the amount of flux leakage that will occur at the crack region. The higher the permeability of the material used for the yoke, the greater the flux density generated in the sample, thus, the greater the leakage field that will be measured at the crack region. According to Fig. 4.7, it can be seen that the $\boldsymbol{B_x^{peak}}$ amplitude obtained at the vicinity of a 0.8 mm deep, 0.2 mm wide and 10 mm long surface and far-surface hairline cracks increases rapidly as the maximum relative permeability (μ_{rmax}) of the yoke material is varied from 1 to 10^4. However, above this range (10^4 -10^6), the rate of increase is reduced (almost constant) due to an almost saturation of the test plate. At this point, further increase in the yoke permeability results in a negligible increase in the magnetic flux density developed in the test plate and thus, a negligible change in the leakage field amplitude ($\boldsymbol{B_x^{peak}}$) measured. Hence, a yoke permeability of 4000 was chosen for the FEM and experimental investigation.

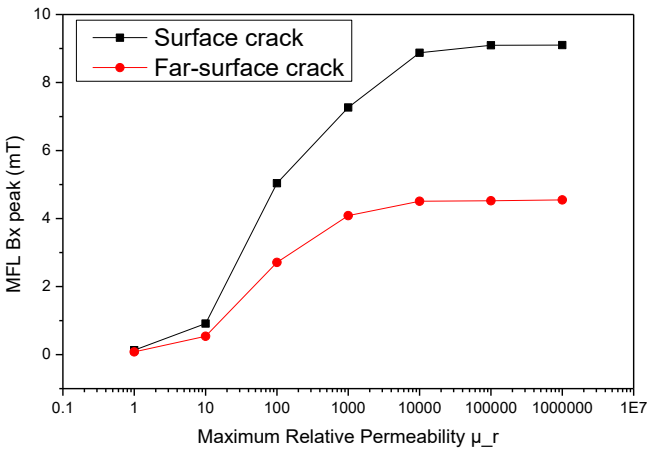

Figure 4.7. The relationship between the MFL signal peak amplitude ($\boldsymbol{B_x^{peak}}$) and the yoke permeability, for a 0.8 mm deep surface and far-surface hairline cracks.

4.2.4) Yoke and Sensor Lift-off Optimization

The MFL technique is a non-contact method of NDE. Hence, the ability to accurately detect a hairline crack using the MFL approach significantly depends on the magnitude of the magnetic flux induced into the test sample through the magnetization yoke (yoke lift-off), as well as the clearance between the magnetic sensor and the test sample surface (sensor lift-off). This section investigates the influence of the magnetizer (yoke) lift-off and sensor lift-off on the amplitude and detectability of the feeble leakage field signal from both surface and far-surface hairline cracks. This is explored using the 3D FEM simulation in MagNet. Fig 4.8a and Fig 4.8b shows the inspection layout used to examine the effect of yoke lift-off and sensor lift-off respectively, on the detectability of both surface and far-surface hairline cracks.

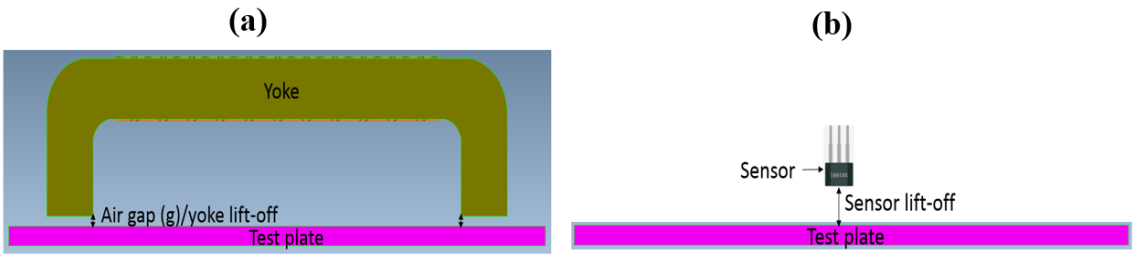

Figure 4.8. The FEM models for investigating the effect of; a) Yoke lift-off and Sensor lift-off on the acquired MFL signal.

First, the yoke lift-off was varied from 0.5 mm to 5 mm with a constant sensor lift-off of 0.5 mm, in order to simulate the different levels of yoke lift-off. The effect on the resultant leakage field signal due to a 0.8 mm deep, 0.2 mm wide and 10 mm long surface and far-surface hairline crack is recorded as shown in Fig. 4.9. As can be observed from the magnetic flux leakage comparison graph shown in Fig. 4.9, an inverse relationship exists between the resultant MFL signal and the yoke lift-off. That is, the $\boldsymbol{B_x}$ (see Fig. 4.9a) and $\boldsymbol{B_y}$ (see Fig. 4.9b) signal amplitudes decreases significantly with increasing yoke lift-off value. This is because of a decrease in the magnetic flux flowing into the test sample from the yoke as the air-gap between the yoke and the test sample is increased, since the air-gap consumes part of the

magnetic flux in the magnetic circuit. As shown in Fig. 4.4, the stray fields/fringing fields, which extends further away from the perimeter of the yoke legs adds to the reluctance of the circuit, therefore, causing a drop in the; magnetic flux (Φ) generated, a drop in the magnetic flux density developed in the test sample and hence, a drop in the leakage field occurring at the crack region. Moreover, a greater percentage change in the reduction of $\boldsymbol{B_x}$ and $\boldsymbol{B_y}$ amplitudes is observed at lower levels of yoke lift-off, when compared to higher levels of yoke lift-off.

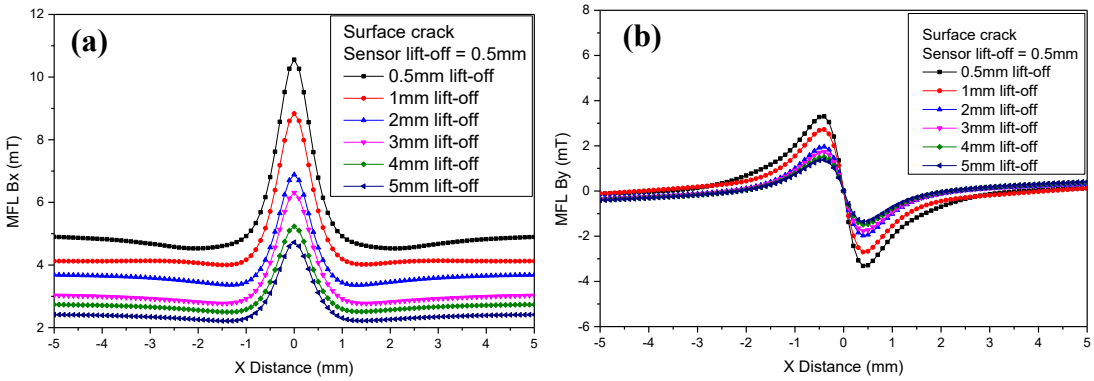

Figure 4.9. The simulated MFL signal amplitudes for a 0.8 mm deep surface hairline crack at different yoke lift-off values, with a constant sensor lift-off of 0.5 mm; a) $\boldsymbol{B_x}$ component and b) $\boldsymbol{B_y}$ component.

The sensor lift-off was varied next, from 0.5 mm to 5 mm with a constant yoke lift-off of 0.5 mm, in order to investigate the different levels of sensor lift-off. The effect on the resultant MFL signal for the same 0.8 mm deep, 0.2 mm wide and 10 mm long surface and far-surface hairline cracks is recorded, as shown in Fig. 4.10. As can be observed, an inverse relationship exists between the resultant MFL signal and the sensor lift-off. That is, the $\boldsymbol{B_x}$ (see Fig. 4.10a) and $\boldsymbol{B_y}$ (see Fig. 4.10b) signal amplitudes decrease significantly with increasing sensor lift-off value. The reduction in the leakage field signal observed as the sensor lift-off is increased is attributed to the attenuation of the leakage field (field spreading) as the gap between the sensor and the crack is increased. Also, a greater percentage change in the reduction of $\boldsymbol{B_x}$ and $\boldsymbol{B_y}$ amplitudes is observed at lower levels of sensor lift-off when compared to higher levels of sensor lift-off.

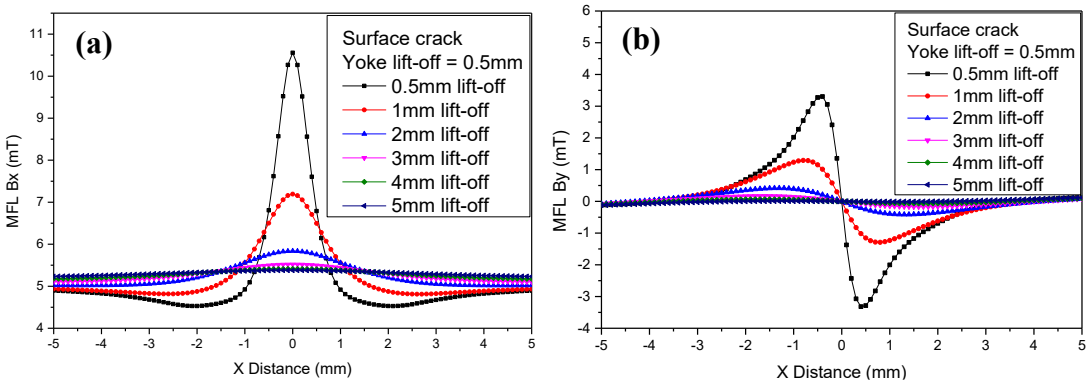

Figure 4.10. The simulated MFL signal amplitudes for a 0.8 mm deep surface hairline crack at different sensor lift-off values, with a constant yoke lift-off of 0.5 mm; a) $\boldsymbol{B_x}$ component and b) $\boldsymbol{B_y}$ component.

Finally, both the yoke and sensor lift-offs are varied simultaneously from 0.5 mm to 5 mm for the same crack size, in order to examine the different levels of probe lift-offs. The influence on the resultant MFL signal is recorded as shown in Fig. 4.11. According to the information presented in Fig 4.11, the $\boldsymbol{B_x}$ (see Fig. 4.11a) and $\boldsymbol{B_y}$ (see Fig. 4.11b) signal amplitudes decreases significantly as the yoke and sensor lift-offs are increased simultaneously. The reduction in the MFL signal is because of the decrease in the magnetic flux flowing through the magnetic circuit as the air-gap (g) between the yoke and the test sample is increased, as well as the attenuation of the leakage field as the gap between the sensor and the crack is increased. A greater percentage change in the reduction of $\boldsymbol{B_x}$ and $\boldsymbol{B_y}$ amplitudes is observed at lower levels of sensor and yoke lift-offs when compared to higher levels of yoke and sensor lift-offs.

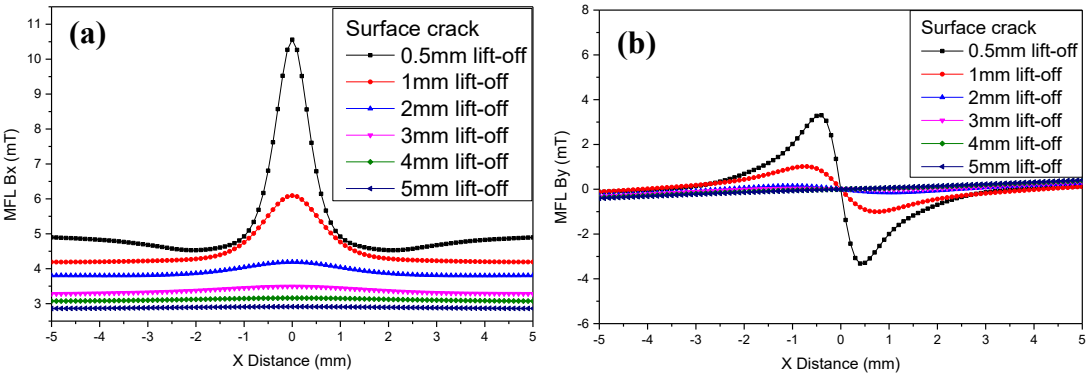

Figure 4.11. The simulated MFL signal amplitudes for a 0.8 mm deep surface hairline crack as the yoke and sensor lift-offs are varied simultaneously; a) $\boldsymbol{B_x}$ component and b) $\boldsymbol{B_y}$ component.

A plot showing the relationship between the magnetic flux leakage peak amplitude and lift-off is shown in Fig. 4.12. It compares the influence of all the three forms of lift-off on the leakage field amplitude, for a surface hairline crack (see Fig 4.12a) and for a far-surface hairline crack (see Fig. 4.12b). As can be seen, all the three lift-off forms have a significant effect on the leakage field amplitude, that is; the leakage field ($\boldsymbol{B_x^{peak}}$) amplitude decreases with increasing magnetizer or sensor lift-off.

For the surface crack plot shown in Fig. 4.12a, the sensor lift-off shows a considerable greater effect (reduction) on the $\boldsymbol{B_x^{peak}}$ amplitude at lower lift-off values (3.5 mm lift-off and below) compared to a yoke lift-off of the same magnitude. At higher lift-off values (about 4 mm lift-off and above) the effect of yoke lift-off dominates. However, the yoke and sensor lift-off simultaneously yields the greatest reduction in the simulated $\boldsymbol{B_x^{peak}}$ amplitude. For the far-surface crack plot shown in Fig. 4.12b, the yoke lift-off produces the greatest reduction in the predicted $\boldsymbol{B_x^{peak}}$ amplitude, while the sensor lift-off produces the least effect. Hence, a yoke lift-off of 0.5 mm and a sensor lift-off of 0.5 mm is chosen for this investigation, except where stated otherwise.

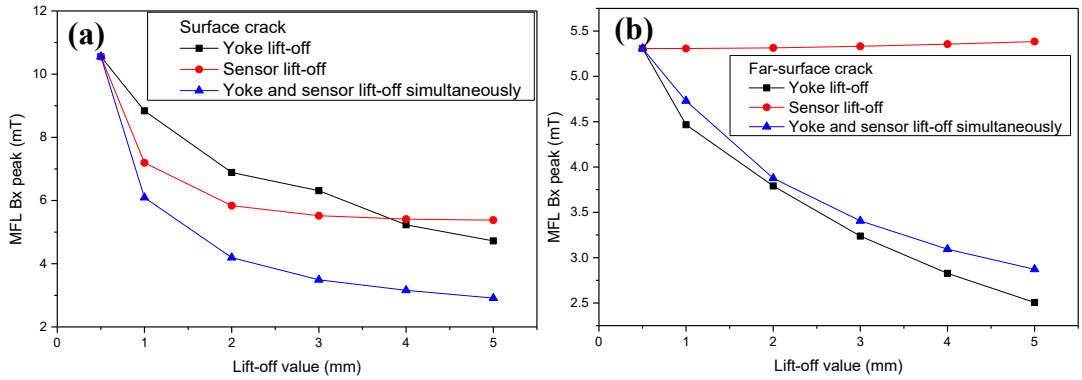

Figure 4.12. A plot showing the relationship between the simulated MFL peak amplitude ($\boldsymbol{B_x^{peak}}$) and lift-off, comparing all the three lift-off forms while using a 0.8 mm deep; a) Surface hairline crack and b) Far-surface hairline crack.

4.2.5) Magnetization Current Optimization

It is necessary to optimize the magnetization current used in order to ensure a measurable leakage field signal from both surface and far-surface hairline cracks. Here, the magnetization current is varied from 1 A to 10 A in steps of 1 A, in order to simulate the leakage field signal obtainable at different current levels.

Firstly, the magnetic flux density (**B**) induced in a crack-free plate at different current levels is obtained, as displayed in Fig. 4.13. As can be seen, the simulated magnetic flux density increases with increase in the magnetization level. The relationship between the magnetization current and the simulated magnetic flux density is fairly linear at low current levels. However, this linearity decreases as the current is further increased. The reduction in linearity at higher current levels is attributed to the non-linearity in the **B-H** curve of the low carbon steel plate used, as shown in Fig. 4.1 of section 4.2.

Secondly, the simulated MFL peak ($\boldsymbol{B_x^{peak}}$) amplitude for a 0.8 mm deep surface and far-surface hairline cracks are acquired at different magnetization currents, as shown in Fig. 4.14. As can be seen, the simulated $\boldsymbol{B_x^{peak}}$ amplitude increases with increase in the magnetization level. Thus, it is necessary to induce a large enough magnetic field into the test sample so as to ensure a significant field variation at the crack region, especially for the feeble signal from far-surface hairline cracks. The closer the induced magnetic field is to the saturation of the test sample, the higher the sensitivity, the repeatability and reliability of the MFL approach. This is because the residual magnetism developed from previous scan will be completely eliminated when operating at a region close to the magnetic saturation of the sample used. Therefore, providing an MFL signal that is constant and repeatable for successive scans while performing the experimental test. Also, to prevent the saturation of the MFL sensor and the need to cool down the magnetization coil for longer inspection periods as a result of a too high and steady current, a magnetization current of 4 A corresponding to a magnetic flux density (**B)** of 1.1 T (see Fig. 4.13) is chosen for DCMFL investigation.

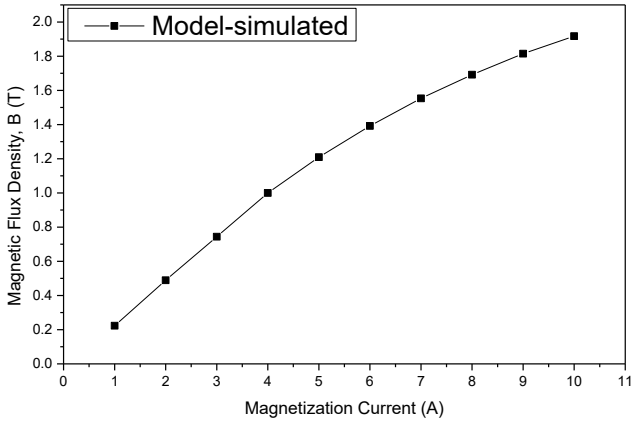

Figure 4.13. The simulated magnetic flux density ($\boldsymbol{B}$) developed in the test plate at different current levels.

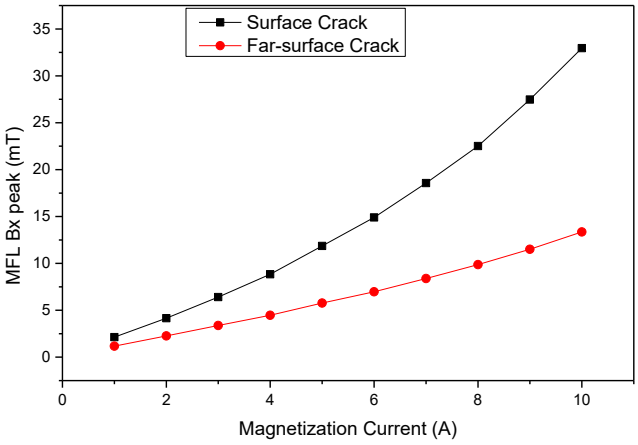

Figure 4.14. The relationship between the simulated MFL peak amplitude ($\boldsymbol{B_x^{peak}}$) and magnetization current, for a 0.8 mm deep, 0.2 mm wide and 10 mm long surface and far-surface hairline cracks.

4.3) FEM Computation Results and Discussions

This section focuses on the detection and characterization of a range of surface and far-surface hairline cracks with different width sizes and depth locations within the test sample, using the FEM numerical simulation technique. Fig. 4.15 shows the optimized MFL probe system used for the simulation. Fig 4.15a shows the probe

model with its optimized dimensions, while Fig. 4.15b and 4.15c illustrates the meshed and solved models respectively.

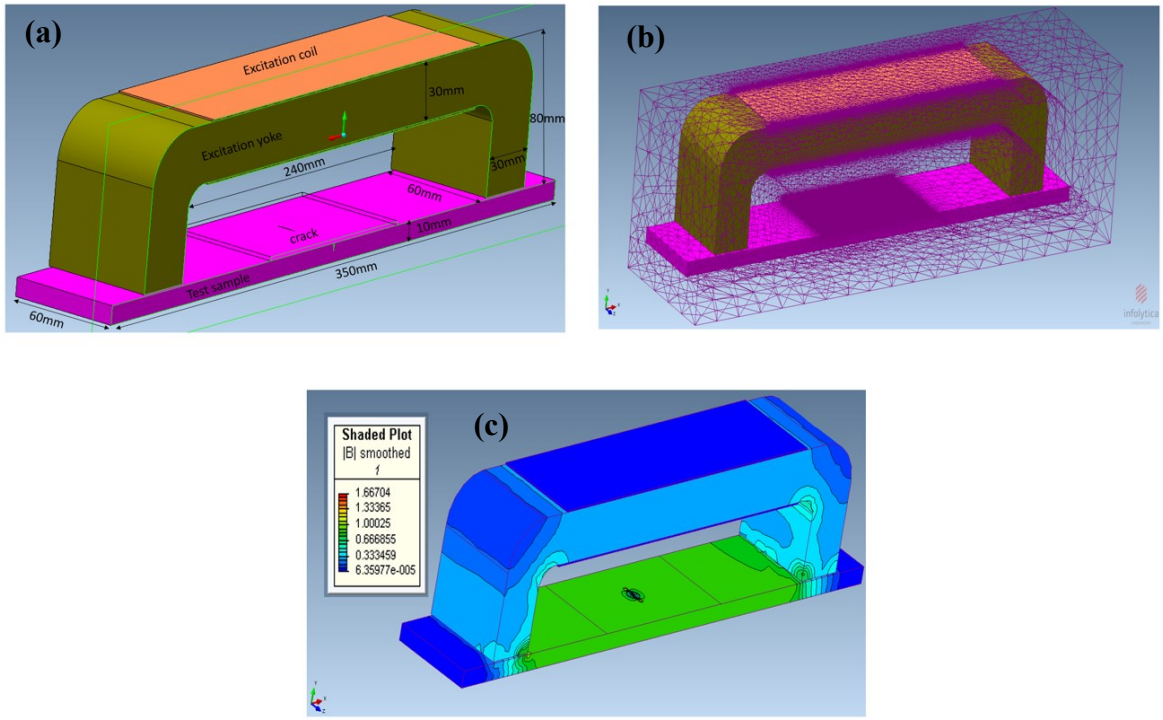

Figure 4.15. The FEM schematic layout of; a) 3D model of the MFL measurement probe used, with optimized dimensions, b) 3D mesh of the MFL simulation model and c) 3D calculated result of the MFL model.

The cracks were modelled at the centre of plate (defined as 0 mm) where the field is most uniform and positioned perpendicular to the applied field orientation, in order to achieve the highest field variation at the crack region. Finer meshes of 0.02 mm was created along the crack region and along the data collection area, in other to improve the result accuracy. The meshes were divided into tetrahedral elements with 1,601,228 degrees of freedom (DOF). The magnetization of the test plate is done through a 300 turn copper coil modelled around the horizontal top section of the yoke, carrying a direct current of 4 A. This generated a magnetic flux density of 1.1 T in the test plate. This set-up was used to predict the axial ($\boldsymbol{B_x}$), radial ($\boldsymbol{B_y}$), and tangential ($\boldsymbol{B_z}$) components of the MFL signal for the surface and far-surface hairline cracks. Both line scan and area scan techniques was used to provide a more refined and enhanced visualization of the crack information and features. The length of all the cracks employed in the simulation is 10 mm. The depth of the surface

cracks refers to the distance from the top surface of the sample to the bottom tip of the crack, while the depth of the far-surface cracks refers to the distance from the bottom surface of the sample to the top tip of the crack with an opening at the bottom of the sample as shown in Fig. 4.16a (surface cracks) and Fig 4.16b (far-surface cracks).

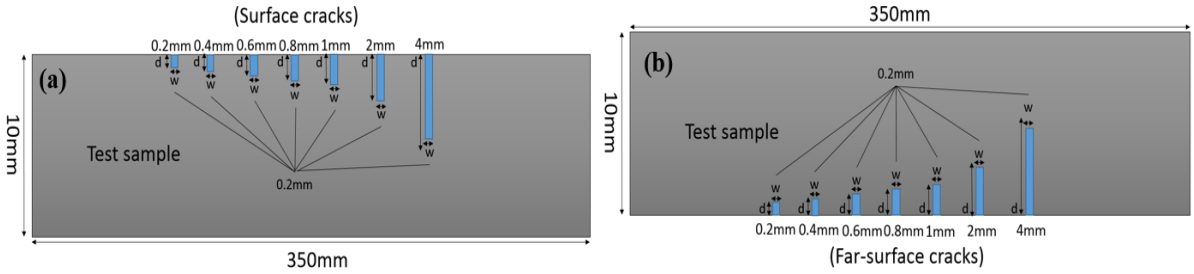

Figure 4.16. A schematic layout of the test sample with; a) surface cracks and (b) far-surface cracks.

One of the main aims of the simulation study is to explore the effect of various crack geometries (sizes) on the leakage field amplitude and distribution pattern. The investigation considers mainly rectangular standalone cracks, with different depth and width sizes. The magnetic field in the sample wall is simulated, and the characterization of the various cracks is performed with respect to the resultant MFL signal obtained. This method can be easily described as a linear model, consisting of an input, an output and a transfer function. The defect profile is the input, the MFL signal is the output and the signal sensing algorithm is taken as the transfer function. This yields two different but related types of problems. The spatial prediction of the leakage field developed by the wall of the sample in the presence of volumetric crack (forward problem) and vice versa (inverse problem). The computational time for each of the simulated models took about 25 minutes in a dual-core 64-bit processor workstation with 24 GB primary memory. Fig. 4.17 shows the visualization of the simulated $\boldsymbol{B_x}$, $\boldsymbol{B_y}$ and $\boldsymbol{B_z}$ components of the leakage field obtained across a 4 mm deep surface hairline crack in a 10 mm thick plate (40 % wall loss), while maintaining a constant magnetizer lift-off of 0.5 mm and a constant sensor lift-off of 0.5 mm. The unit of percent used is expressed as the ratio of crack depth to the sample wall thickness. It can be seen from Fig. 4.17 that the simulated leakage field signal for the 4 mm deep surface hairline crack varies with relative position of the field probe to the crack axis, with the highest signal amplitude recorded at the crack centre.

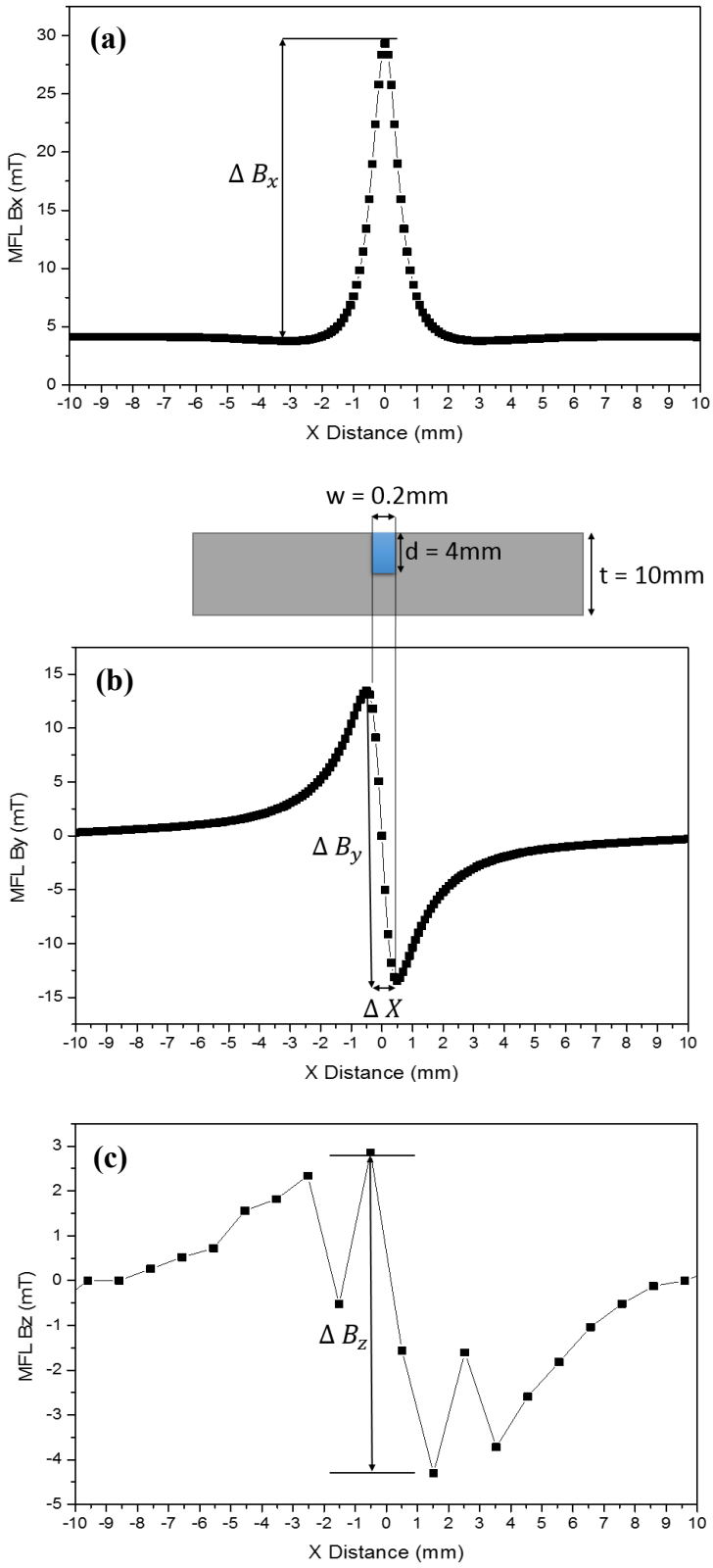

Figure 4.17. The simulated MFL signal for a 4mm deep surface hairline crack; a) $\boldsymbol{B_x}$ field component, b) $\boldsymbol{B_y}$ field component and c) $\boldsymbol{B_z}$ field component.

Fig. 4.18 shows the 3D imaging of the simulated leakage field ($\boldsymbol{B_x}, \boldsymbol{B_y}$ and $\boldsymbol{B_z}$) distribution pattern, obtained in the vicinity of the same 4 mm deep surface hairline crack. The measurement area presented is a surface of 20 mm × 20 mm, with a constant step size of 0.5 mm in the x and y directions. The numbers for the colour scale are all in mT.

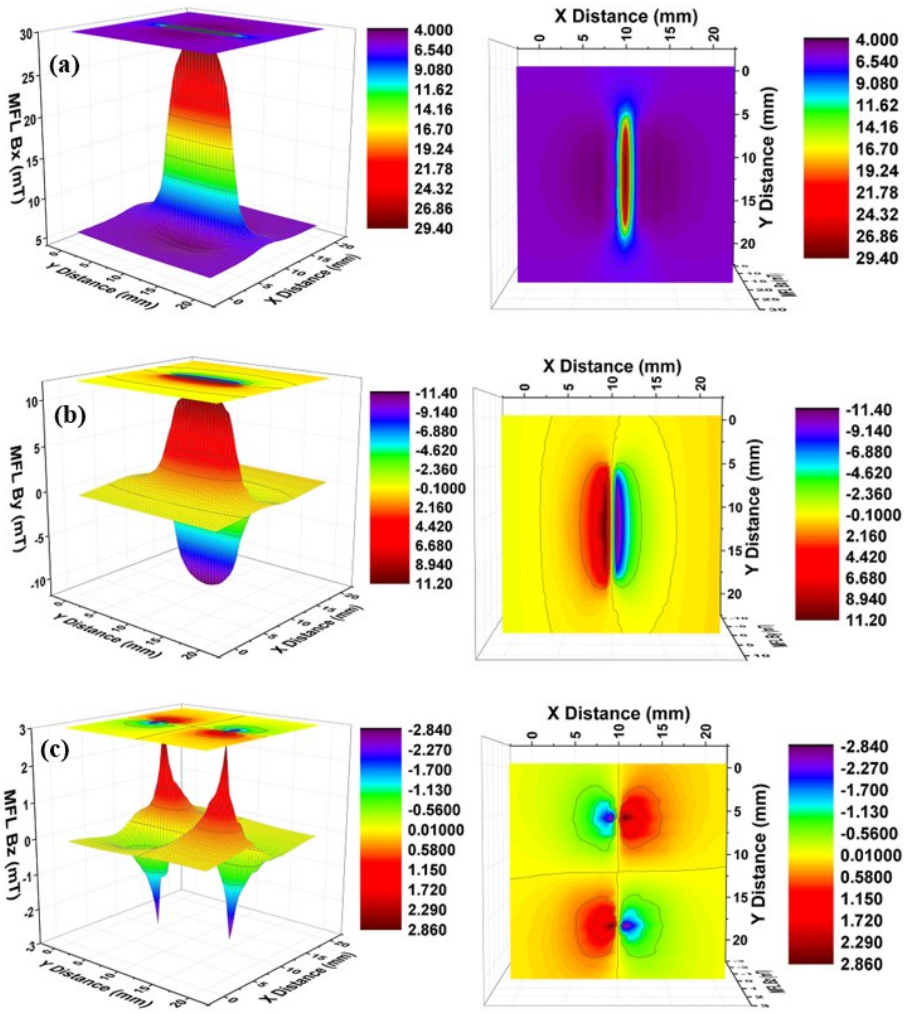

Figure 4.18. A 3D illustration of the simulated MFL signal for a 4mm deep surface hairline crack; a) $\boldsymbol{B_x}$ field component, b) $\boldsymbol{B_y}$ field component and c) $\boldsymbol{B_z}$ field component.

The axial ($\boldsymbol{B_x}$) component of the MFL signal is a unipolar waveform (see Fig. 4.18a) and its profile is significantly dependent on the ratio of the crack depth to the crack width. The radial ($\boldsymbol{B_y}$) component of the MFL signal exhibits a bipolar sine like waveform with equal amplitudes at the peak and trough of the signal (see Fig. 4.18b). The $\boldsymbol{B_y}$ signal profile is symmetrical about the origin (0 mm), which is the

centre of the crack. The peak (maximum amplitude) and trough (minimum amplitude) of the $\boldsymbol{B_y}$ signal represents the crack edges. The signal amplitude denoted by $\Delta\boldsymbol{B_y}$ (see Fig. 4.17c) indicates the signal strength and is significantly determined by the ratio of the crack depth to crack width, when all other signal influencing parameters are kept constant. The distance between the peak and the trough, which is denoted by ΔX reflects the width of the crack and can be quantitatively used to estimate the width size of the crack under scrutiny. The tangential ($\boldsymbol{B_z}$) component of the MFL signal exhibits both positive and negative polarity (see Fig. 4.18c) and it demonstrates both the width and length of the hairline crack under test. Hence, the shape and approximate size (length and width) of hairline cracks could be obtained from the distribution patterns of the $\boldsymbol{B_x}$, $\boldsymbol{B_y}$ and $\boldsymbol{B_z}$ leakage field signals.

4.3.1) Detection and Characterization of Hairline Cracks with Different Depth Sizes

An FEM simulation benchmark was developed for detecting and characterizing hairline cracks with different depth sizes. Here, different hairline cracks with varying depth sizes (w = 0.2 mm and l = 10 mm) were accurately modelled on the surface and far-surface of the test plates and simulated in MagNet. The leakage field generated by each of the crack depths were then acquired and analyzed using the simulated $\boldsymbol{B_x}$ and $\boldsymbol{B_y}$ signal amplitudes. Seven different plates were tested, and the dimensions of the various surface and far-surface hairline cracks inspected are listed in table 4.2. A constant magnetizer lift-off of 0.5 mm and sensing lift-off of 0.5 mm was used.

The relationship between the simulated MFL signal amplitude and the depth of various surface and far-surface hairline cracks are shown in Fig. 4.19 and Fig. 4.20 respectively. x = 0 mm is the central major axis of the crack. As can be seen, a small change in the depth of either a surface or far-surface hairline crack causes a significant change in $\boldsymbol{B_x}$ and $\boldsymbol{B_y}$ signal amplitudes. This shows that the leakage field generated due to the presence of a surface or far-surface hairline crack is strongly dependent on the crack depth. The change in the signal amplitude for the surface and

far-surface crack is similar for the same change in crack depth, except that the overall signal level is lower for the far-surface cracks when compared to a surface crack of the same size. Also, the lateral spread of the leakage field is found to increase with increasing crack location below the sample surface. The broader signal width observed for the far-surface cracks when compared with an equivalent surface crack is attributed to the lateral spread of magnetic field at the vicinity of the far-surface cracks.

Fig 4.21 shows a plot which compares the $\boldsymbol{B_x^{peak}}$ amplitude (see Fig. 4.21a) and the $\boldsymbol{B_y^{peak}}$ amplitude (see Fig. 4.21b), obtained for both surface and far-surface hairline cracks with varying depth sizes as a function of crack depth. It can be seen that the MFL peak amplitude increases as the crack depth is increased, and the relationship between them is linear when other parameters are kept constant. It is evident from both plots that the system can discriminate the various hairline cracks inspected according to their depth sizes, by just using the peak amplitude of the leakage field signal. Also, it can be seen from both plots that the system can discriminate the various hairline cracks inspected according to their various locations within the test sample (i.e. separate surface cracks from far-surface cracks), except for the 4 mm ($\boldsymbol{B_x^{peak}}$ = 6.64 mT) deep far-surface hairline crack, which generated a signal greater than the signals generated by a 0.2 mm ($\boldsymbol{B_x^{peak}}$ = 5.08 mT) and 0.4 mm ($\boldsymbol{B_x^{peak}}$ = 6.33 mT) deep surface hairline cracks. The modelled DCMFL inspection system is able to detect as small as a 0.2 mm deep surface hairline crack and a 0.2 mm deep far-surface hairline crack located 9.8 mm below the plate surface.

Table 4.2. Details of the surface and far-surface hairline cracks with varying depths, modelled in the test plate.

Plate Number	**Crack Type**	**Crack Depth d (mm)**	**Crack Location h (mm)**	**MFL(B_x^{peak}) (mT)**
Plate 1	Surface	0.2	0.0	5.08
	Far-surface	0.2	9.8	4.28
Plate 2	Surface	0.4	0.0	6.33
	Far-surface	0.4	9.6	4.33
Plate 3	Surface	0.6	0.0	7.30
	Far-surface	0.6	9.4	4.38
Plate 4	Surface	0.8	0.0	8.84
	Far-surface	0.8	9.2	4.47
Plate 5	Surface	1.0	0.0	9.74
	Far-surface	1.0	9.0	4.56
Plate 6	Surface	2.0	0.0	16.36
	Far-surface	2.0	8.0	5.16
Plate 7	Surface	4.0	0.0	29.31
	Far-surface	4.0	6.0	6.64

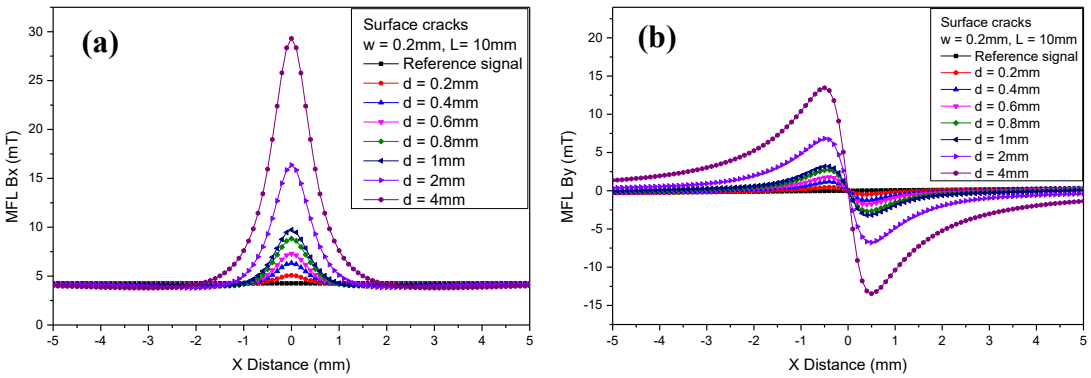

Figure 4.19. The simulated MFL signal amplitudes for different surface hairline cracks with varying depth sizes, as a function of crack position for; a) $\boldsymbol{B_x}$ field component and b) $\boldsymbol{B_y}$ field component.

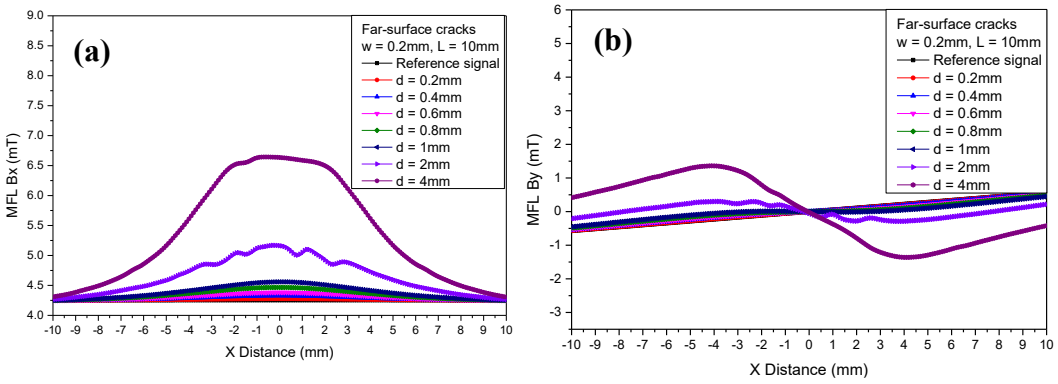

Figure 4.20. The simulated MFL signal amplitudes for different far-surface hairline cracks with varying depth sizes, as a function of crack position for; a) $\boldsymbol{B_x}$ field component and b) $\boldsymbol{B_y}$ field component.

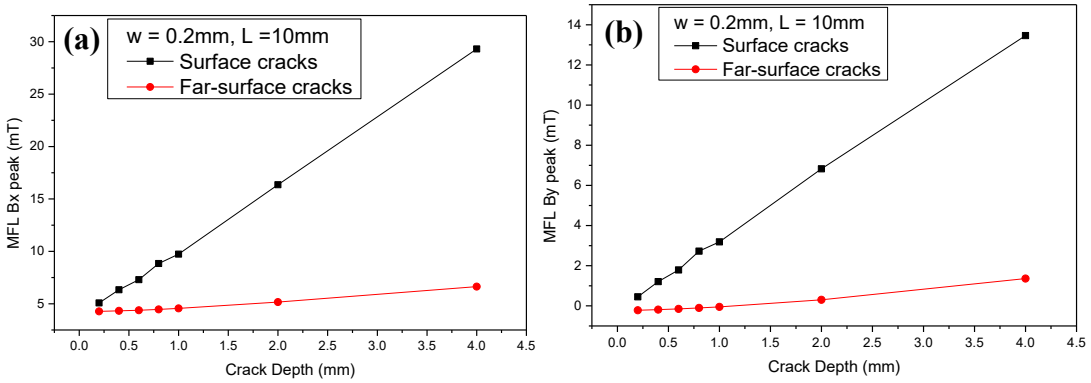

Figure 4.21. A plot comparing the simulated MFL signal peak amplitudes for different crack depths, for both surface and far-surface hairline cracks; a) $\boldsymbol{B_x^{peak}}$ amplitude and b) $\boldsymbol{B_y^{peak}}$ amplitude.

4.3.2) Detection and Characterization of Cracks with Different Width Sizes

This section investigates the capability of the optimized DCMFL inspection system in detecting and characterizing surface and far-surface cracks with varying width sizes (both hairline cracks and larger cracks). Here, different cracks with varying width sizes were carefully modelled on the surface and the reverse side (far-surface) of the test plate. Then the influence of variation in crack width is then investigated using the simulated $\boldsymbol{B_x}$ signal amplitudes for two different crack depths (d = 0.2 mm and d = 4 mm) with a constant crack length of 10 mm. The dimensions of the various surface and far-surface cracks simulated in this section are listed in table 4.3. Fourteen different plates were tested, that is; seven samples with surface cracks of varying width sizes (w = 0.2, 0.4, 0.6, 0.8, 1, 2 and 4 mm, with d = 0.2 mm and 4 mm) and seven samples with far-surface cracks of varying width sizes (w = 0.2, 0.4, 0.6, 0.8, 1, 2 and 4 mm, with d = 0.2 mm and 4 mm). A constant magnetizer lift-off of 0.5 mm and sensing lift-off of 0.5 mm was used.

Fig. 4.22 shows the relationship between the simulated MFL signal ($\boldsymbol{B_x}$) amplitude and the width of various surface (see Fig. 4.22a) and far-surface (see Fig. 4.22b) cracks, with a constant depth and length size of 0.2 mm and 10 mm respectively. Also, Fig. 4.23 shows the relationship between the simulated MFL signal ($\boldsymbol{B_x}$) amplitude and the width of various surface (see Fig. 4.23a) and far-surface (see Fig. 4.23b) cracks, with a constant depth and length size of 4 mm and 10 mm respectively. It can be observed that a small change in crack width causes a significant increase in the $\boldsymbol{B_x}$ signal amplitude for the surface and far-surface cracks. This shows that the resultant leakage field is strongly dependent on the crack width. Also, the variation in the signal amplitude for both types of cracks is similar for the same change in crack width, but the overall signal level is higher for the surface cracks when compared to a far-surface crack of the same size. Also, it can be observed that the leakage field amplitude increases as the width of the surface crack is increased from 0.2 mm to 0.8 mm (see Fig. 4.22a) and from 0.2 mm to 0.6 mm (see Fig. 4.23a). Any further increase in the surface crack width above these points results in a decrease in the leakage field amplitude recorded.

Fig. 4.24 shows a plot, which compares the simulated MFL signal ($\boldsymbol{B_x^{peak}}$) amplitude obtained for both surface and far-surface cracks with varying width sizes, when the crack depth is 0.2 mm (see Fig. 4.24a) and when the crack depth is 4 mm (see Fig. 4.24b). As mentioned earlier, it can be clearly observed that the $\boldsymbol{B_x^{peak}}$ amplitude increases as the surface crack width is increased from 0.2 mm to 0.8 mm (see Fig. 4.24a) and from 0.2 mm to 0.6 mm (see Fig. 4.24b), then it starts to decrease as the crack width is increased further. However, the $\boldsymbol{B_x^{peak}}$ amplitude for the far-surface cracks is found to increase for all the crack widths simulated.

Table 4.3. Details of the surface and far-surface cracks with varying widths, modelled in the test sample.

Plate number	**Crack Type**	**Crack Depth d (mm)**	**Crack Location h (mm)**	**MFL(B_x^{peak}) (mT)**
Plate 1	Surface	0.2 / 4.0	0.0	5.08 / 28.88
	Far-surface	0.2 / 4.0	9.8 / 6.0	4.27 / 6.64
Plate 2	Surface	0.2 / 4.0	0.0	5.35 / 33.20
	Far-surface	0.2 / 4.0	9.8 / 6.0	4.28 / 7.68
Plate 3	Surface	0.2 / 4.0	0.0	5.38 / 34.45
	Far-surface	0.2 / 4.0	9.8 / 6.0	4.29 / 8.05
Plate 4	Surface	0.2 / 4.0	0.0	5.39 / 34.13
	Far-surface	0.2 / 4.0	9.8 / 6.0	4.29 / 8.51
Plate 5	Surface	0.2 / 4.0	0.0	5.36 / 32.75
	Far-surface	0.2 / 4.0	9.8 / 6.0	4.30 / 8.76
Plate 6	Surface	0.2 / 4.0	0.0	4.95 / 26.32
	Far-surface	0.2 / 4.0	9.8 / 6.0	4.32 / 9.20
Plate 7	Surface	0.2 / 4.0	0.0	4.62 / 18.64
	Far-surface	0.2 / 4.0	9.8 / 6.0	4.35 / 9.46

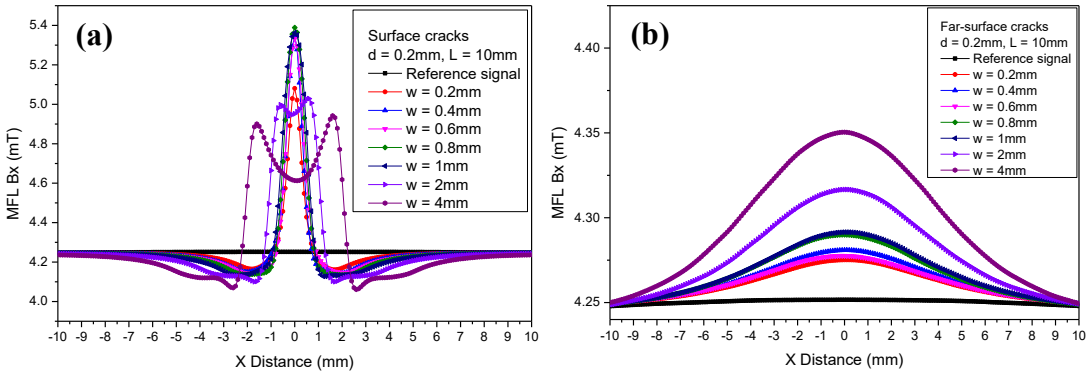

Figure 4.22. The simulated MFL signal ($\boldsymbol{B_x}$) amplitude for different crack widths as a function of crack position for; a) Surface cracks with a constant depth of 0.2 mm and b) Far-surface cracks with constant depth of 0.2 mm.

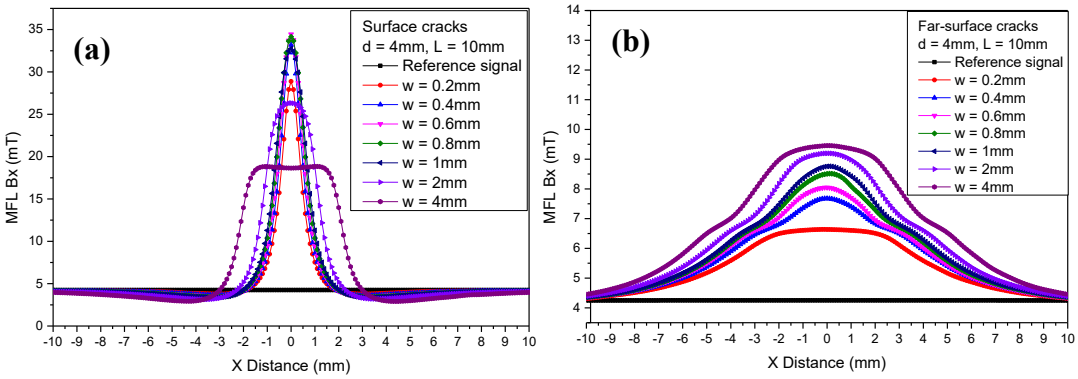

Figure 4.23. The simulated MFL signal ($\boldsymbol{B_x}$) amplitude for different crack widths as a function of crack position for; a) Surface cracks with a constant depth of 4 mm and b) Far-surface cracks with a constant depth of 4 mm.

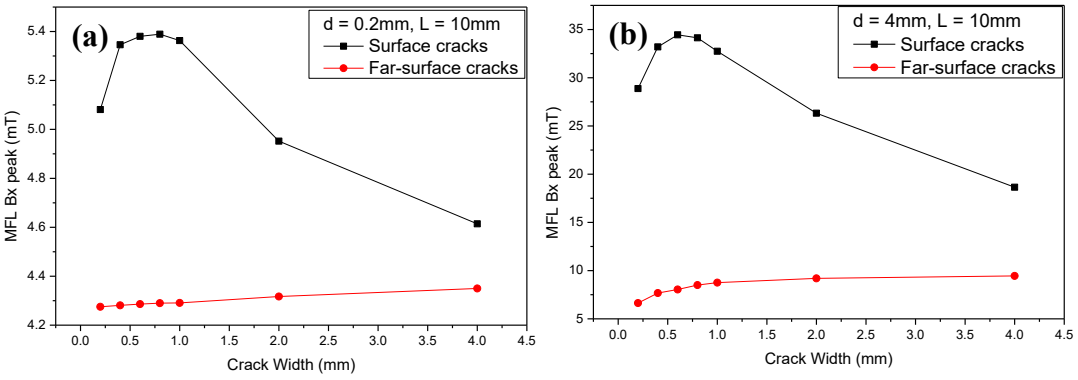

Figure 4.24. A plot comparing the simulated MFL signal amplitude for different crack widths for both surface and far-surface cracks; a) MFL ($\boldsymbol{B_x^{peak}}$) with constant crack depth of 0.2mm and b) MFL ($\boldsymbol{B_x^{peak}}$) with constant crack depth of 4mm.

Contrary to the $\boldsymbol{B_x}$ leakage field signature, the $\boldsymbol{B_y}$ signature is the value of interest, since it provides more information required for crack size (crack width) estimation. Fig. 4.25 shows the $\boldsymbol{B_y}$ leakage field signature obtained for different surface cracks with varying width sizes, with a constant depth and length size. The peak-peak amplitude of the leakage signal (signal strength) is represented by $\Delta \boldsymbol{B_y}$, while ΔX is the distance between the upper and lower peaks of the $\boldsymbol{B_y}$ profile. A plot of ΔX versus the width of the various cracks simulated is shown in Fig. 4.26. The plot shows that the dependency of ΔX on the crack width is linear, for when the crack depth is 0.2 mm (see Fig. 4.25a) and when the crack depth is 4 mm (see Fig. 4.25b). Hence, the width of the various hairline cracks can be estimated using only the ΔX value of the $\boldsymbol{B_y}$ field distribution, for rectangular shaped cracks.

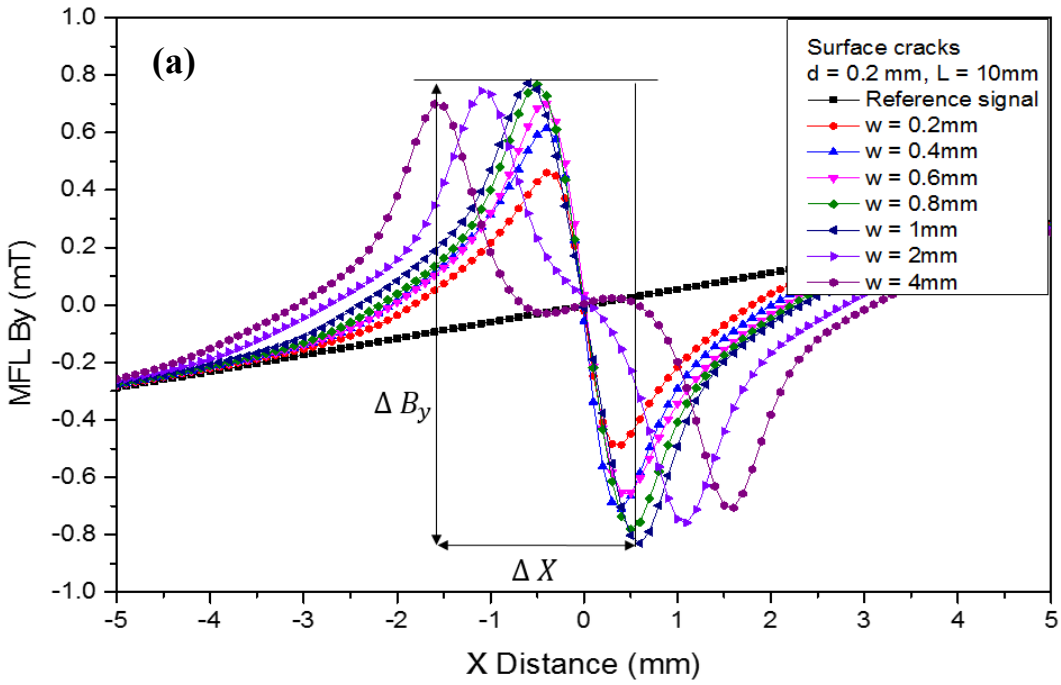

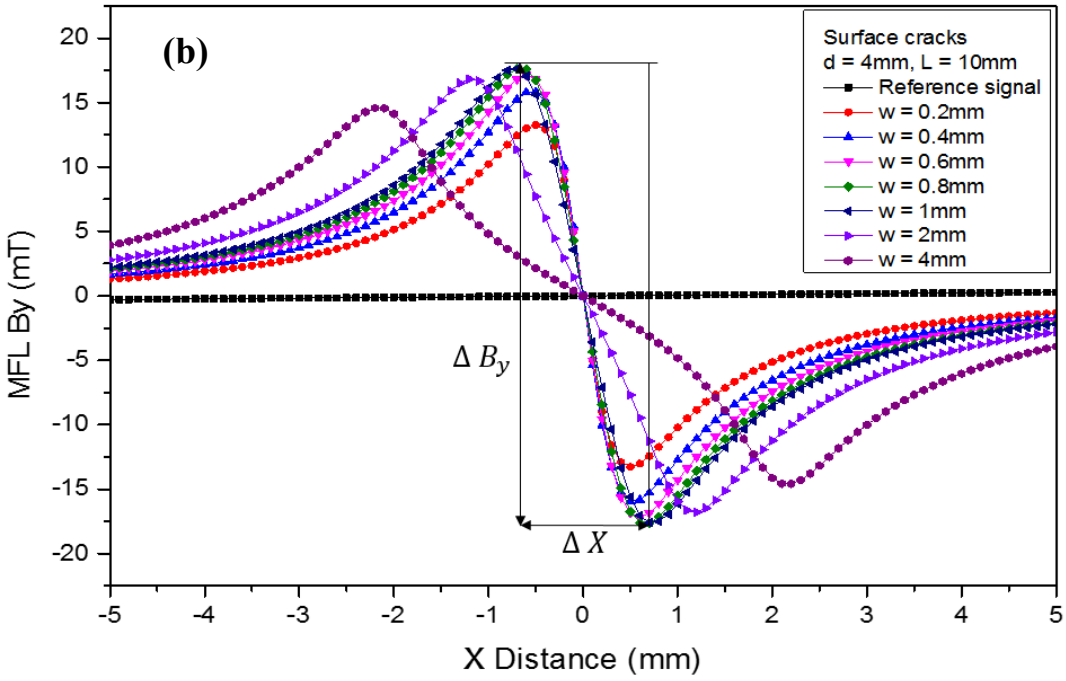

Figure 4.25. The simulated MFL signal ($\boldsymbol{B_y}$) profile for different surface cracks with varying width sizes, as a function of crack position; a) constant crack depth of 0.2 mm and b) constant crack depth of 4 mm.

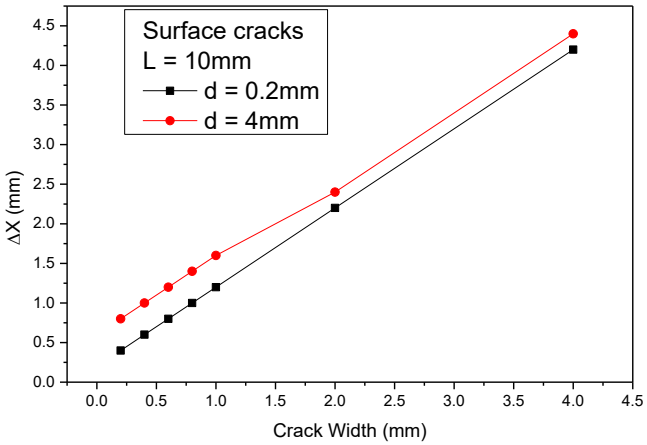

Figure 4.26. A plot showing the realtionship between the crack width and ΔX.

4.3.3) Detection and Characterization of Cracks with Different Depth and Width Sizes

Here, different cracks with varying depth and width sizes, with a constant length size of 10 mm were accurately modelled on the surface and on the far-surface of the test plates (both hairline cracks and larger cracks). The influence of variation in crack depth and width simultaneously is then simulated and analyzed using the axial ($\boldsymbol{B_x}$) leakage field signal. The dimensions of the various surface and far-surface cracks investigated are listed in table 4.4. Fig. 4.27 shows a leakage field ($\boldsymbol{B_x}$) comparison graph obtained while varying the crack depth and width simultaneously from 0.2 mm to 4 mm, for both surface (see Fig. 4.27a) and far-surface (see Fig. 4.27b) cracks. The graphs show a significant increase in the simulated leakage field amplitudes as the crack depth and width are varied simultaneously from 0.2 mm to 4 mm.

Fig. 4.28 shows a plot of the $\boldsymbol{B_x^{peak}}$ amplitude versus crack size in all its forms, for the surface cracks (see Fig. 4.28a) and for the far-surface cracks (see Fig. 4.28b). Fig. 4.28a shows that varying both the surface crack depth and width at the same time, between the 0.2 mm and 1mm range has a slightly greater effect on the $\boldsymbol{B_x^{peak}}$ amplitude compared to varying only the surface crack depth. However, varying only the surface crack depth produces a substantial greater effect above the 1 mm range. Meanwhile, varying only the surface crack width produces the least effect on the simulated $\boldsymbol{B_x^{peak}}$ amplitude. For the far-surface cracks shown in Fig. 4.28b, it can be seen that varying the crack depth and width simultaneously has a greater effect on the simulated leakage field peak amplitude above the 1 mm range, while varying only the crack width produces the least effect on the simulated $\boldsymbol{B_x^{peak}}$ amplitude.

Table 4.4. Details of the surface and far-surface cracks with varying depth and width sizes simultaneously, modelled in the test sample.

Plate Number	**Crack Type**	**Crack Depth & Width d&w (mm)**	**Crack Location h (mm)**	**MFL(B_x^{peak}) (mT)**
Plate 1	Surface	0.2	0.0	5.12
	Far-surface	0.2	9.8	4.28
Plate 2	Surface	0.4	0.0	6.52
	Far-surface	0.4	9.6	4.34
Plate 3	Surface	0.6	0.0	7.90
	Far-surface	0.6	9.4	4.43
Plate 4	Surface	0.8	0.0	8.98
	Far-surface	0.8	9.2	4.54
Plate 5	Surface	1.0	0.0	9.98
	Far-surface	1.0	9.0	4.61
Plate 6	Surface	2.0	0.0	13.66
	Far-surface	2.0	8.0	5.68
Plate 7	Surface	4.0	0.0	18.65
	Far-surface	4.0	6.0	9.45

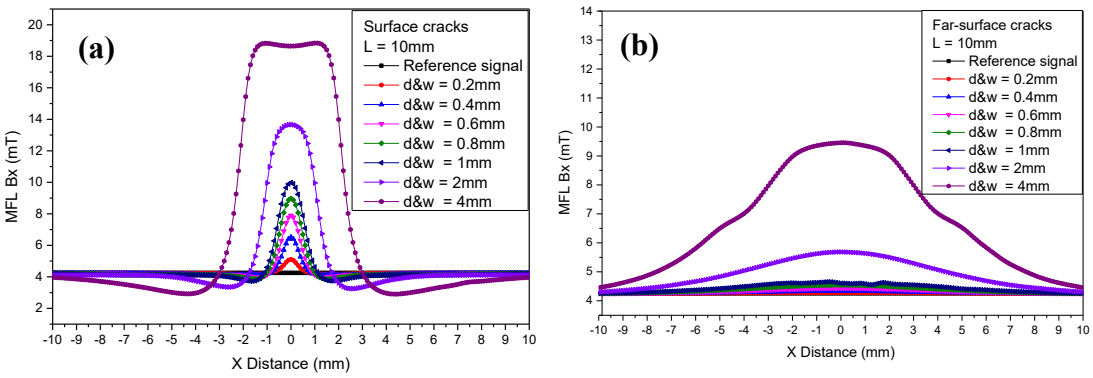

Figure 4.27. The simulated MFL signal ($\boldsymbol{B_x}$) as a function of crack position, obtained when varying the crack depth and width simultaneously; a) Surface cracks and b) Far-surface cracks.

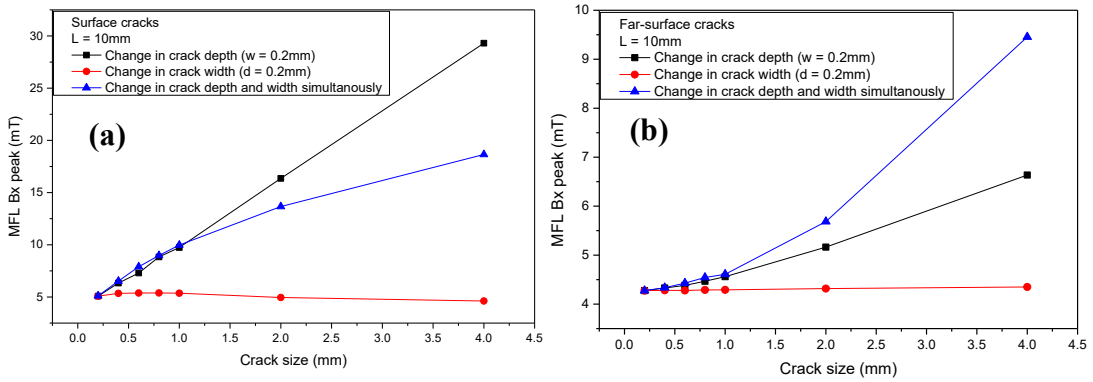

Figure 4.28. A plot comparing the simulated MFL ($\boldsymbol{B_x^{peak}}$) signal amplitude for different crack changing scenarios; a) Surface cracks and b) Far-surface cracks.

4.3.4) The Effect of Plate Thickness on the Detection Sensitivity of Hairline Cracks

This section investigates the influence of the test sample thickness (**t**) on the detectability of various surface and far-surface hairline cracks, using the DCMFL technique. The investigation was carried out using the simulated $\boldsymbol{B_x}$ and $\boldsymbol{B_y}$ leakage field amplitudes, generated due to a 0.8 mm deep, 0.2 mm wide and 10 mm long surface and far-surface hairline cracks. Four different test samples with varying thicknesses, that is; 6 mm, 8 mm, 10 mm and 12 mm where simulated and compared. The yoke was magnetized with a constant current of 4 A, and a total magnetic flux

density ($\boldsymbol{B}$) of 1.32 T, 1.25 T, 1.1 T and 0.88 T was generated in the various plate thicknesses respectively, as shown in table 4.5.

Magnetic flux lines always follow the track that offers the lowest resistance when a ferromagnetic plate is magnetized, and a significant amount of the generated flux will settle at the walls of the plate. This means that if a plate with a thicker wall is used, there will be more magnetic flux flowing freely through the plate due to an increased cross-sectional area. Thus, reducing the amount of flux lines intersecting each other. This will lead to a lower magnetic flux density in the thicker plate. Conversely, if a plate with smaller wall thickness is used, there will be less flux lines flowing freely through the plate due to a reduced area. Thus, increasing the amount of flux lines intersecting each other. This will result to a higher flux density in the thinner plate. This phenomenon is clearly illustrated in table 4.5. The information displayed shows that the 6 mm thick plate (least area) happens to have the highest magnetic flux density ($\boldsymbol{B}$) of 1.32 T, followed by the 8 mm thick plate with a magnetic flux density of 1.25 T, while the 12 mm thick plate (largest area) produced the least magnetic flux density of 0.88 T. This proves that the larger the wall thickness of the pipeline used, the less the magnetic flux density that will be developed and the less the leakage field amplitude that will be measured at the crack site.

The relationship between the simulated MFL signal ($\boldsymbol{B_x}$ and $\boldsymbol{B_y}$) amplitudes and the sample thickness, for both surface and far-surface hairline cracks is shown in Fig. 4.29 and Fig. 4.30 respectively. As can be seen, an increase in plate thickness from 6 mm to 12 mm in steps of 2 mm causes a significant decrease in the simulated $\boldsymbol{B_x}$ and $\boldsymbol{B_y}$ leakage signal amplitudes, for both types of cracks. This shows that the leakage field developed due to the presence of a hairline crack on a pipeline structure would be strongly determined by the pipe wall thickness. This means that given the same size of crack in ferromagnetic pipeline structures with varying wall thicknesses, there will be more flux leakage in the thinner pipe compared to a thicker one due to a higher magnetic flux density developed in the thinner pipe, as a result of a reduced cross-sectional area.

Furthermore, the ability to successfully detect and characterize surface and far-surface hairline cracks in a particular pipe wall using the MFL technique is highly

dependent on the ability of the induced magnetic field to penetrate through the wall of the pipe, as well as the capability of the selected magnetic sensor to detect such cracks at the desired lift-off distance.

Table 4.5. The simulated MFL signal amplitude obtained for different plate thicknesses.

Plate thickness (t) (mm)	**Magnetic flux density B (no crack) (T)**	**MFL B_x^{peak} (mT)**		**MFL $B_x^{peak\ to\ peak}$ (mT)**	
		Surface crack	**Far-surface crack**	**Surface crack**	**Far-surface crack**
6.0	1.32	10.7	5.6	5.78	0.68
8.0	1.25	9.7	5.0	5.16	0.46
10.0	1.1	8.8	4.5	4.65	0.35
12.0	0.88	7.4	4.1	3.32	0.01

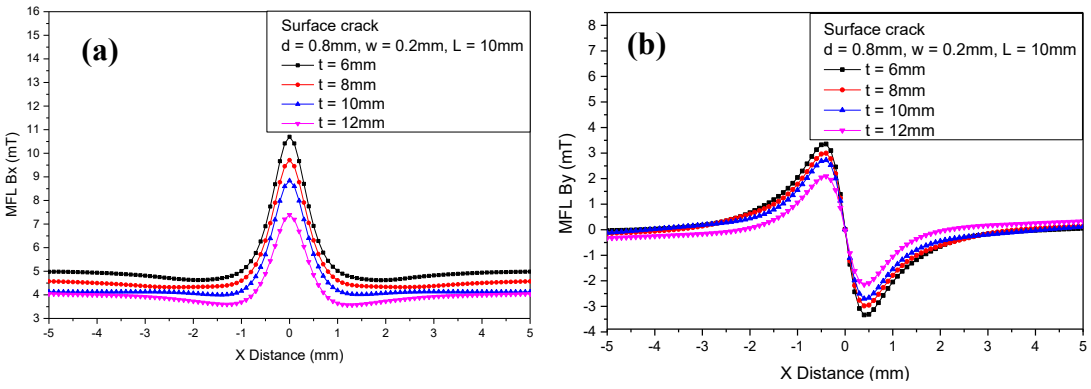

Figure 4.29. The simulated MFL signal amplitude for different surface cracks with varying plate thickness, as a function of crack position for; a) $\boldsymbol{B_x}$ component and b) $\boldsymbol{B_y}$ component.

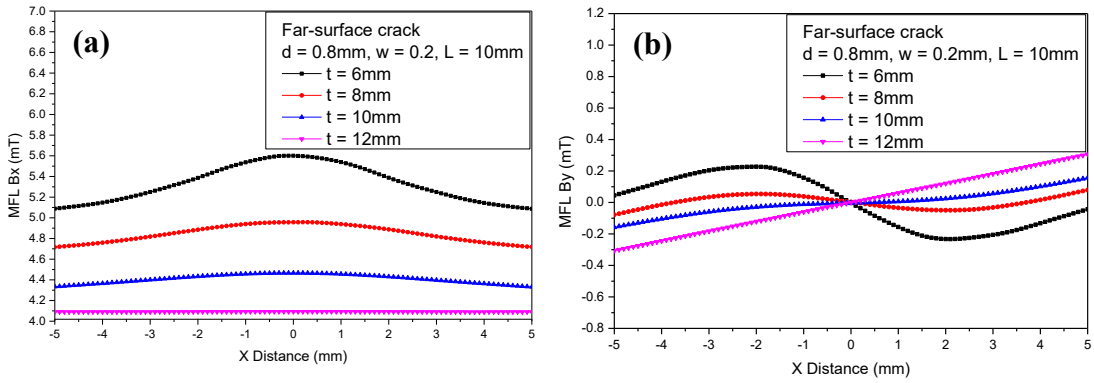

Figure 4.30. The simulated MFL signal amplitude for different far-surface cracks with varying plate thickness, as a function of crack position for; a) $\boldsymbol{B_x}$ component and b) $\boldsymbol{B_y}$ component.

4.3.5) The Effect of Sensor Lift-off on the Detection Sensitivity of Hairline Cracks

This section investigates the capability of the optimized MFL inspection probe system to detect and characterize various surface and far-surface hairline cracks at different sensor lift-offs, using the FEM simulation approach. The clearance between the sensing system and the top surface of the sample is known as the sensor lift-off. This clearance has a crucial influence on the acquired leakage field signal amplitude, and this influence is expected to be at its minimum in order to ensure a high enough signal to noise ratio. The sensor lift-off investigation was carried out using a 10 mm thick plate. The axial ($\boldsymbol{B_x}$) component of the leakage field was simulated for different hairline cracks, at different sensing lift-offs. The leakage field amplitude ($\boldsymbol{B_x}$) acquired for a 4 mm deep surface hairline crack and a 4 mm deep far-surface hairline crack, at different sensing lift-offs is shown in Fig. 4.31a and Fig. 4.31b respectively. As expected, the $\boldsymbol{B_x}$ amplitude decreased as the sensor lift-off value is increased from 0.5 mm to 9 mm. This proves that lift-offs caused by debris, sands, rocks, welds, etc. during pipeline inspection are capable of causing inaccuracy in the measurement of the true magnitude of the MFL signals. Such inaccuracy could lead to cracks being missed or undersized, especially hairline cracks.

Fig. 4.32 shows the variation of the $\boldsymbol{B_x^{peak}}$ leakage field amplitude with crack depth at different sensor lift-offs, for both surface (see Fig. 4.32a) and far-surface (see Fig.

4.32b) hairline cracks. As can be observed, the $\boldsymbol{B_x^{peak}}$ amplitude decreases significantly as the sensing clearance from the test sample surface is increased, for the same crack size. Also, the rate of decrease is observed to be more pronounced for surface cracks when compared to far-surface cracks of the same size. Furthermore, a greater change in the reduction of $\boldsymbol{B_x^{peak}}$ amplitude was recorded at lower levels of sensor lift-off when compared to higher levels of sensor lift-off. The DCMFL sensing probe was able to detect the 4 mm deep surface and 4 mm deep far-surface hairline cracks up to a sensor lift-off distance of 9 mm

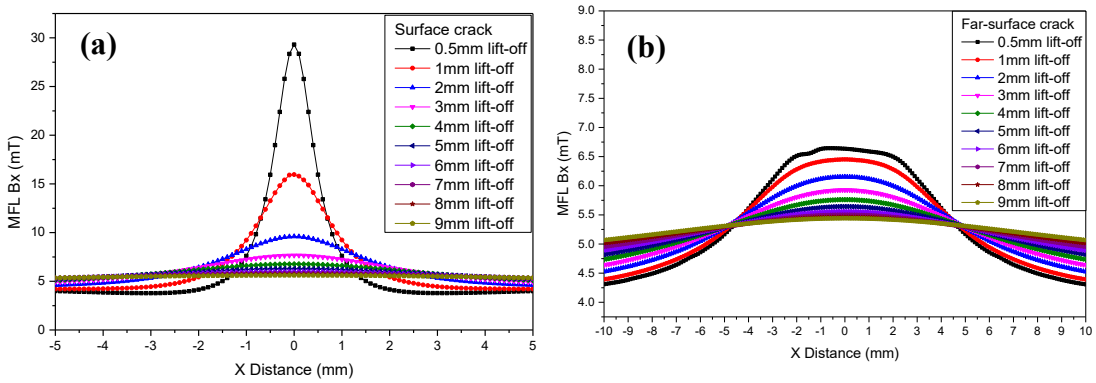

Figure 4.31. The relationship between the simulated MFL signal amplitude ($\boldsymbol{B_x}$) and crack position at different sensor lift-offs, for a) $\boldsymbol{B_x}$ signal amplitudes for a 4 mm deep surface hairline crack and b) $\boldsymbol{B_x}$ signal amplitudes for a 4 mm deep far-surface hairline crack.

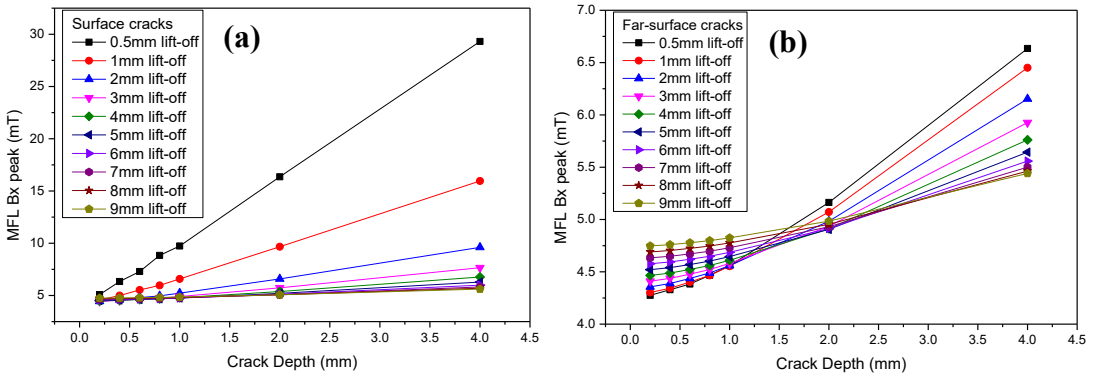

Figure 4.32. A plot showing the simulated MFL signal amplitude ($\boldsymbol{B_x^{peak}}$) as a function of crack depth, at different sensor lift-offs, for; a) Surface hairline cracks and b) Far-surface hairline cracks.

4.4) DCMFL Experimental Investigation

An experimental benchmark was developed and tested in order to confirm the validity of the FEM optimized DCMFL inspection system, as an effective detector of surface and far-surface hairline cracks in pipeline structures. The experimental set-up, procedures and results are presented.

4.4.1) Experimental Set-up for DCMFL Measurements

Based on practical hairline crack detection and characterization requirements, an experimental DCMFL inspection technique was proposed, as illustrated in Fig. 4.33. The measurement set-up used consisted of; an optimized magnetization yoke with a leg height of 80 mm, leg length of 30 mm, leg width of 60 mm, and a leg spacing of 240 mm, a single Hall Effect sensor with dimensions of 4 mm × 3 mm × 0.4 mm (plastic casing), low carbon steel plates (EN3B mild steel) with and without hairline cracks, a DC power supply, an x-y-z translation stage system, a low pass filter, a data acquisition (DAQ) system and a computer. The yoke was wound with 300 turns of firm double-coated and high thermally durable copper wire with a diameter and resistance of 0.5 mm and 1.02 Ω respectively. The magnetization characteristic curves (**B-H** curves) for the silicon steel yoke and the low carbon steel plates used are shown in Fig. 4.1. The measured saturation flux density ($\boldsymbol{B_s}$) for the low carbon steel plates was 1.8 T.

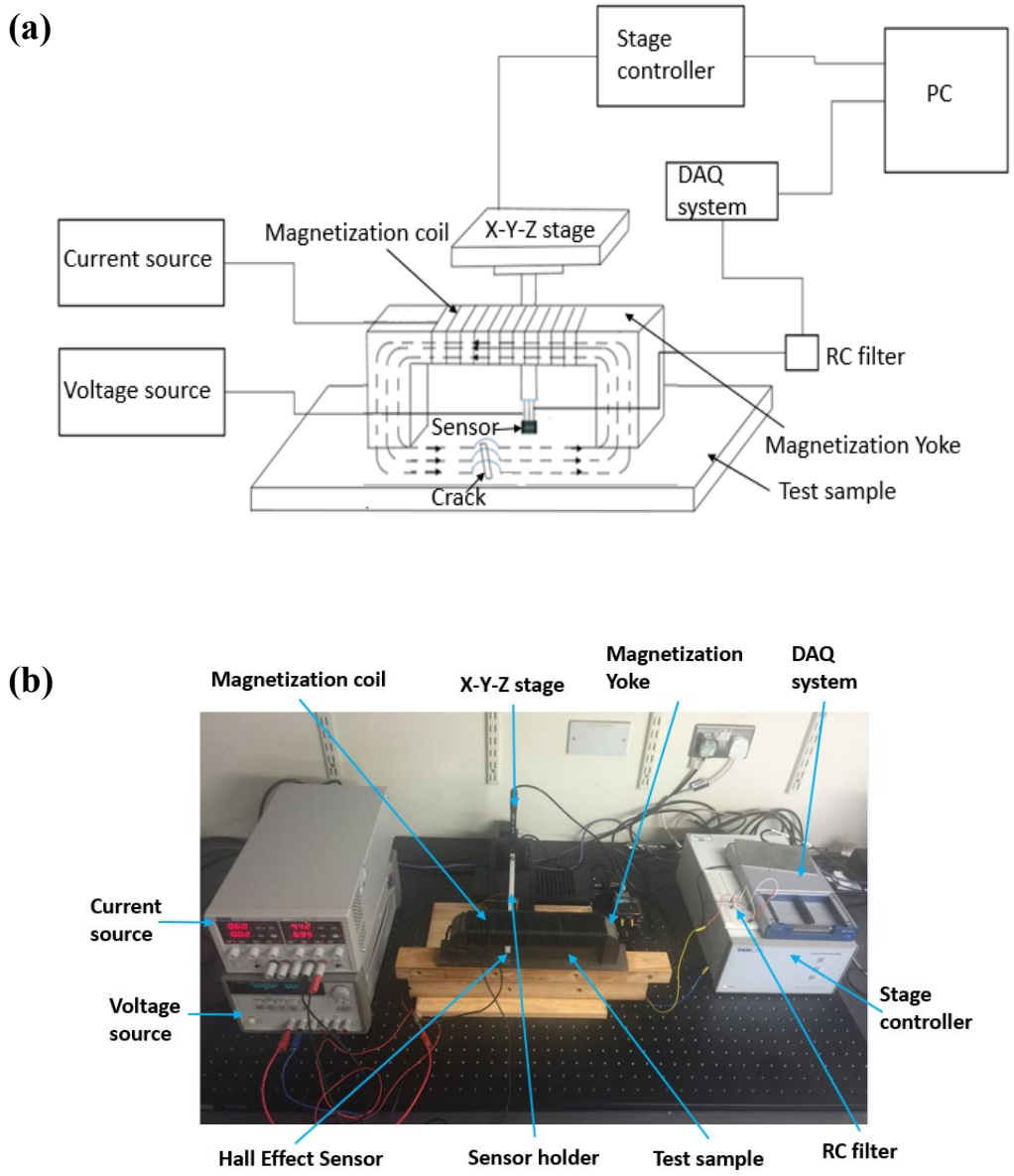

Figure 4.33. The DCMFL experimental probe system set-up used in this work; a) Schematic diagram and b) A photograph.

First, a non-defective plate (plate with no crack) was magnetized with a constant current, from 1 A to 10 A in steps of 1 A. This was done using a DC power supply (E3631A from Keysight) with the sole aim of obtaining the different levels of magnetic flux density developed in the defect free plate, at different current levels. 20 turns of copper wire with a diameter of 0.2 mm was wound around the centre of the defect free plate (region with most uniform field distribution). The outputs (+ve and –ve terminals) of the copper wire was connected to a lakeshore flux meter and the corresponding magnetic flux density induced in the defect free plate at each current level was measured on the flux meter. Fig. 4.34 shows a comparison of the

simulated and measured magnetic flux densities (***B***) developed in the defect free plate, at different magnetization currents. As can be seen, in both cases, the amplitude of ***B*** increases as the magnetization current is increased from 1 A to 10 A, in steps of 1 A. Also, the measured ***B*** amplitude values are within 10 % of the simulated values. The slight variation between the measured and simulated values is because of the stray fields from the yoke legs, which leaks into the surrounding air causing a slight decrease in the measured ***B*** values as compared to the simulated values.

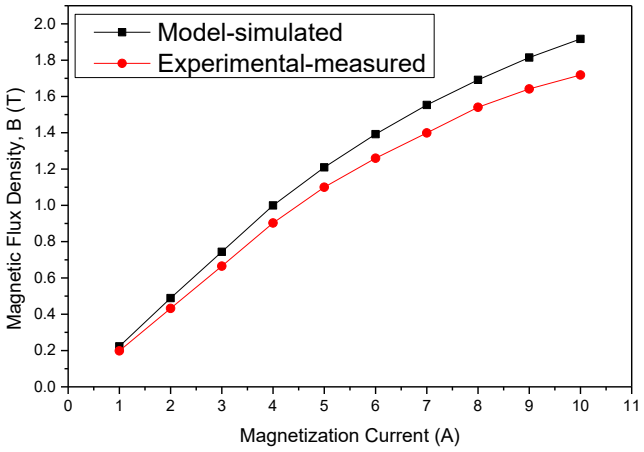

Figure 4.34. A comparison of the simulated and experimental magnetic flux densities (***B***) developed in the defect free plate (10 mm thick) at different current levels.

The preparation of the test samples with well-defined surface and far-surface hairline cracks is a crucial success factor to obtaining accurate test results. Different surface and far-surface hairline cracks with varying depth sizes were artificially fabricated by electro discharge machining (EDM) technique, at Cardiff University. The dimensions of the different hairline cracks fabricated are shown in table 4.2 of section 4.3.1. The depths of the cracks used ranges from 0.2 mm to 4 mm with a constant width and length of 0.2 mm and 10 mm respectively, representing both mild and severe cases of naturally occurring hairline cracks in pipeline structures. Fourteen sets of low carbon steel plates with dimensions of 350 mm × 60 mm × 10 mm and 350 mm × 60 mm × 6 mm (10 mm and 6 mm thick plates) were tested. A precise distance (h) from the plate surface exists for different far-surface cracks as illustrated in table 4.2.

A 100 mm motorized linear translation stage from Thorlabs was used to move the sensor along the sample surface in precise steps. The x-y-z translation stage used has a bidirectional repeatability of 1 µm, a minimum achievable incremental movement of 0.1 µm and a maximum velocity and acceleration of 30 mm/s and 30 mm/s^2 respectively. The central platform of the translation stage is held by 4 recirculating ball carrier bearings, which were mounted to accurately aligned guide rails. A smooth movement is provided by the translation stage through a backlash free precision lead screw, which is instantaneously driven by a hybrid 2-phase stepper motor that can make 409,600 steps per revolution, with a positioning resolution lower than 100 nm. The stepper motors of the translation stage are driven by a BSC202 series benchtop controller. The unit integrates the state-of-the-art digital signal processors with minimal noise analogue electronics and ActiveX® software technology, to enable an easy micro-stepping of all the stage axis. The x-y-z translation stage was connected to the computer through a USB port. In order to drive the translation stage, an instrument control and signal processing toolboxes were installed in LabVIEW. Prior to taking measurements, the communication between the instruments and computer was set-up.

The entire measurement set-up was mounted on a non-magnetic breadboard from Thorlabs. The probe position was maintained for all the measurements taken. x = 0 mm is the central major axis of the crack. Both line scan and area scan techniques were employed to ensure complete visualization of hairline crack features. Measurements were made by scanning a single Hall Effect sensor (A1302KUA-T from Allegro microsystems) across the centre (line scan) or over the area (surface scan) of each hairline crack, with a fixed scan step size and sensor lift-off of 0.5 mm and 0.5 mm respectively. Measurements were repeated 10 times in order to confirm the reproducibility of the results. The Hall Effect sensor was held in place by a 3D printed sensor holder attached to the translation stage and positioned perpendicular to the field orientation, to measure the axial ($\boldsymbol{B_x}$) component (along the scanning direction) of the leakage field signal. The sensor output is filtered by a low-pass filter with a cut-off frequency of 10 Hz, as shown in Fig 4.35. The filtered output is digitized by a high performance data acquisition system (NI-USB-6366 from National Instruments), with 16-bit analogue to digital conversion card with a maximum sampling rate of 2 MS/s/ch. For each scanning cycle, data were collected

at 1600 S/s (1.6 kHz). The digitized data is then stored in a computer for signal processing. Data processing was done within LabVIEW program and using Microsoft's Excel and Origin 9.0 program. The developed LabVIEW program (code) can implement excitation generation, instrumentation controls, probe control, scanning settings, measurement signal acquisition, processing and presentation of inspection results. The LabVIEW program was also used to visualize data and to communicate with the sensor electronics.

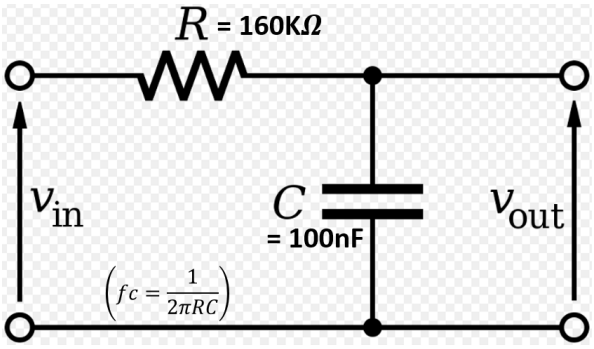

Figure 4.35. Schematic diagram of the RC low pass filter configuration used for the DCMFL Test.

The DCMFL inspection set-up developed allows for real time data of the scan to be viewed and monitored as the inspection advances, via the LabVIEW user interface (front panel), as shown in Fig. 4.36. This is considered a very vital feature as it shows the operator when a crack is detected in a pipeline structure and when a re-scan is needed. At the top of the panel is a column of instructions used to control the x and y translation stage to travel at specified x and y distances along the sample surface, indicating the start (x start and y start) and end (x end and y end) positions as well as the desired scan step size (x delta and y delta). However, the z stage only travels in the z direction (up and down), and is used to adjust the distance between the sensor and the sample surface (sensor lift-off). The wait instruction (x wait and y wait) is used to specify the delay time before the next scan step, in both the x and y directions. The home command is used to instruct either stage to move to the default position, usually the starting position of each axis. The table at the top right corner stores the sensor output values in volts at each scanning step, while the waveform chart at the bottom right corner is used to display the MFL signal pattern (leakage field signature) during the inspection. For easy visualization of the inspection results, a 3D map illustrating the output of the sensor, as a function of x-y displacements are plotted within the LabVIEW panel, as the scan progresses.

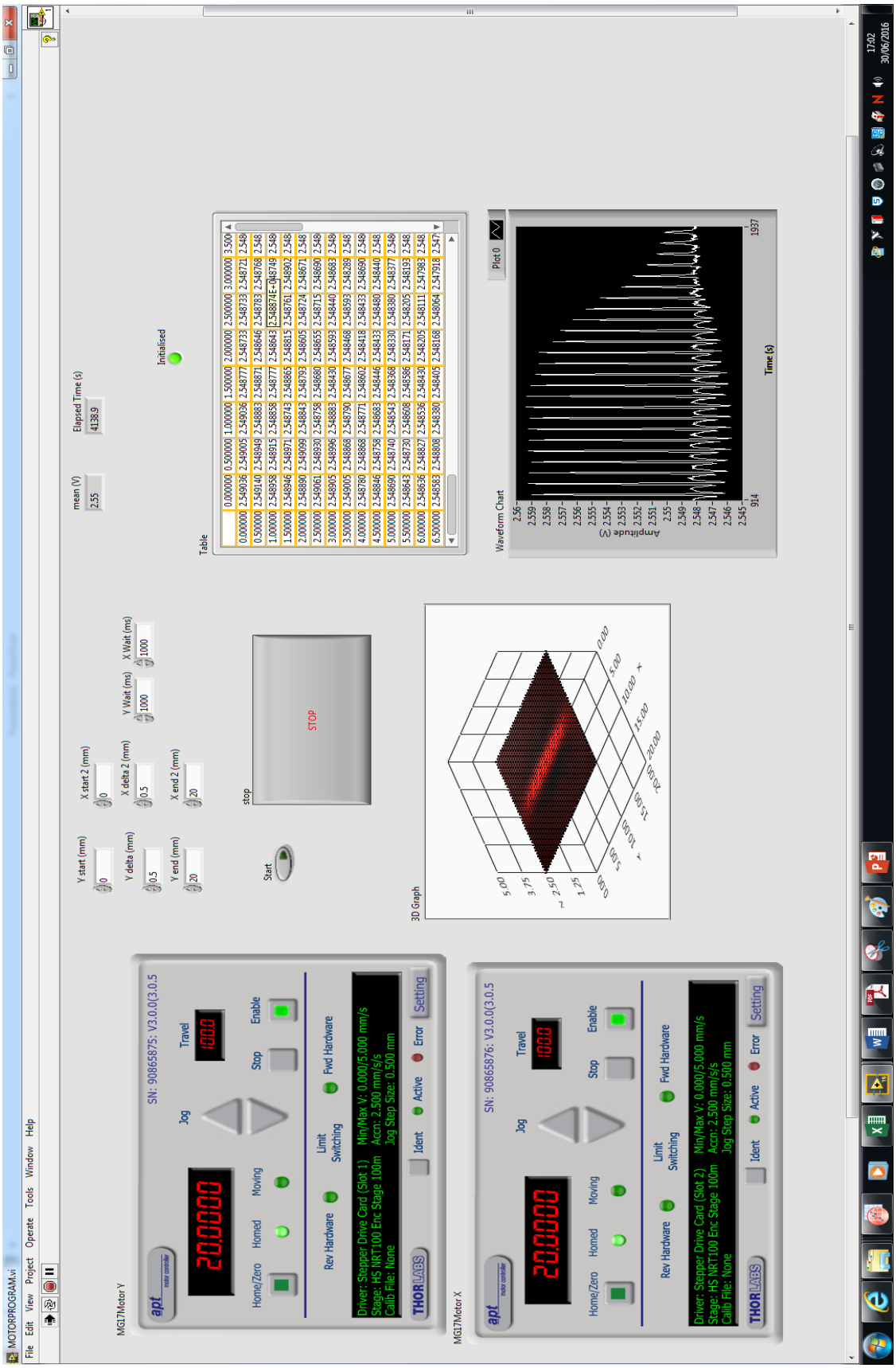

Figure 4.36. The Labview interface for the DCMFL inspection system.

4.4.2) Hall Effect Sensor set-up and Characterization

Hall Effect sensors provide a cheap and effective means of investigating the presence of cracks in ferromagnetic components, by measuring the magnetic field variations caused by such cracks. They are more sensitive to low frequency excitations compared to impedance measurements [6], hence, they are more suited for far-surface hairline crack detection. They are especially suitable for detecting high magnetic fields, compared to GMR and TMR sensors, whose sensitivity decreases with increasing magnetic field. In addition, they have a better temperature characteristic and stability compared to other sensors and measurement components (coils) [7], thus, it is considered a better choice for the measurement of the leakage fields from hairline cracks, in this work. The schematic diagram of the Ratiometric linear Hall Effect sensor used in this work, alongside it dimensions is displayed in Fig. A.1 in appendices A.

Prior to the experimental part of this project, the operation, characteristics and sensitivity of the Ratiometric linear Hall Effect sensor used (A1302KUA-T from Allegro microsystems) was investigated. The investigation was carried out in order to obtain a means of calibrating and converting the leakage signal detected by the sensor in volts to tesla, which will be useful in calibrating the result that will be obtained in subsequent experiments. First, a simple circuit design was constructed for the sensor electronics using a breadboard, as shown in Fig. 4.37. An input voltage of 5 V magnitude was supplied to the sensor using a dc power supply, while the output terminal of the sensor was connected to an oscilloscope to read off the corresponding output voltage. The Ratiometric Hall Effect sensor was seen to output about 2.5 V when no magnetic input was applied, which is half of the supply voltage.

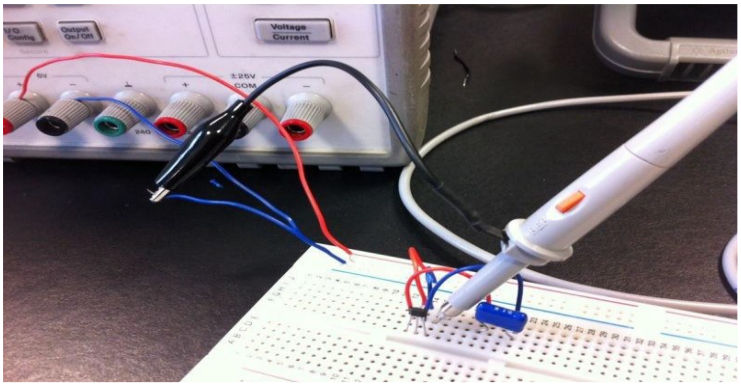

Figure 4.37. The initial sensor circuit construction connected to a DC power supply.

After testing the mode of operation of the Ratiometric Hall Effect sensor, an appropriate circuitry was then designed for the sensor using a printed circuit board (PCB). The schematic diagram of the sensor circuit used is shown in Fig. 4.38. The bypass capacitor shown is used for decoupling, that is; it separates one part of the circuit from the other in other to minimize or possibly cancel out the effect of noise, which might cause a decrease in the sensitivity of the sensor. The bypass capacitor cancels out the effect of noise by increasing the signal to noise ratio of the circuit. The pin 1 of the sensor is the connection to the source voltage (VCC), pin 2 is the connection to the ground (GND) and pin 3 is the output voltage connection (VOUT), this is shown clearly in table 4.6.

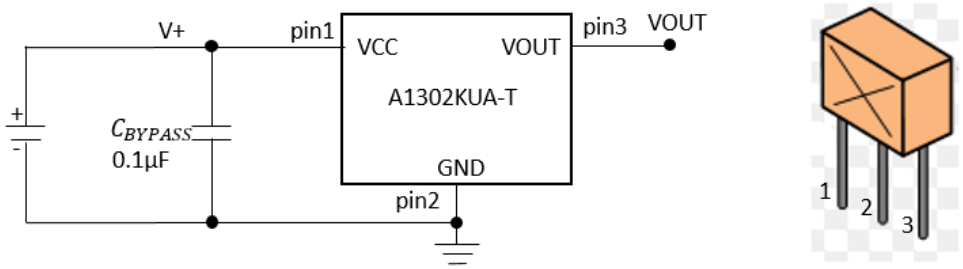

Figure 4.38. The Hall Effect sensor operating circuit design and pin arrangement.

Table 4.6. Showing the sensor pins with their respective connection terminals

Terminal	Pin Connection	Function
VCC	1	Input power supply (source voltage).
VOUT	3	Output signal; also used for programming.
GND	2	Ground.

Moreover, the sensor is expected to go into the slot made on the 3D printed sensor holder attached to the x-y-z translation stage as shown in Fig. 4.39a, to enable an easy movement along the sample surface. Hence, it cannot be directly connected to the circuit shown in Fig. 4.38. Therefore, a suitable circuit (PCB) design was made using the design spark software as shown in Fig. 4.39b. Here, the sensor is linked to the circuit board with wires (wires soldered to the PCB board) to enable an easy insertion of the sensor head into the slot made on the 3D sensor holder, as shown in Fig. 4.39c.

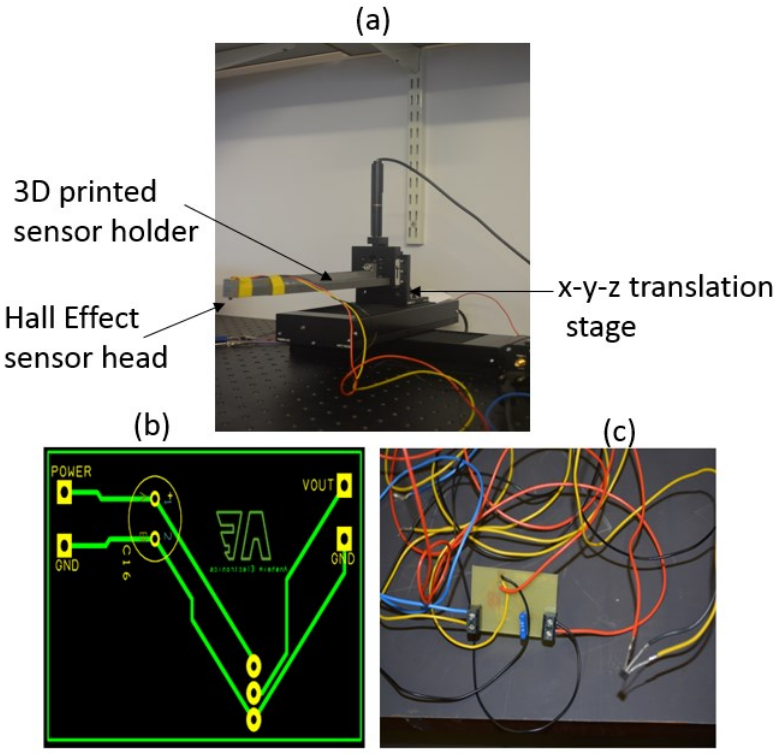

Figure 4.39. Showing; a) Hall Effect sensor fitted into the 3D printed sensor holder slot mounted on the x-y-z translation stage, b) PCB circuit design (using the design spark software) for the sensor connection and c) a picture of the sensor circuitry (sensor electronics) after it was fabricated.

4.4.2.1) Volts to Tesla Calibration

The voltage output from the Ratiometric Hall Effect sensor is proportional to the magnetic field strength being detected and was calibrated in units of V/mT. For this reason, an appropriate set-up was constructed for the Hall Effect sensor calibration, using a solenoid with a total length of 585 mm and diameter of 60 mm as shown in Fig. 4.40. The solenoid was wound with 475 turns of thermally durable copper wire, with a diameter of 2 mm, a resistance of 1 Ω and generated a uniaxial magnetic field (z-axis). Hence, the sensor was positioned at the centre of the solenoid such that it measures the z-field component. The sensor output was connected to an oscilloscope in order to measure the resultant magnetic field generated in the solenoid in volts. Different current levels were applied to the coil and this generated different magnetic field magnitude in the z direction. When the magnetic field in the solenoid changes, the output voltage of the sensor read at the oscilloscope changes. Therefore, the magnetic flux density corresponding to a particular current level can be calculated using the formula that describes the magnetic flux density produced at the centre of the solenoid, which is expressed in equation (4.1) [8, 9];

$$\boldsymbol{B} = \frac{\mu_0 NI}{\sqrt{l^2+4r^2}} \tag{4.1}$$

Where, $\boldsymbol{B}$ is the magnetic flux density generated in the solenoid in tesla, μ_0 is the permeability of free space, N is total number of copper wire wrapped around the solenoid, I is the current applied to the coil, l is the total length of the solenoid and r is the radius of the solenoid. Fig. 4.41 shows the output characteristic of the Ratiometric linear Hall Effect sensor used for the calibration task. The Hall Effect sensor sensitivity was found to be 0.0138 V/mT at 5 V biasing voltage. The sensor's linear response is in the range ±170 mT but saturates when the magnetic flux density exceeds ±170 mT. The measured Hall output voltage linearity has a coefficient of determination (R^2) equal to 0.9999. This means that the Ratiometric Hall Effect sensor possesses the capability to linearly amplify a feeble Hall signal as well as cancel out large offsets. Hence, the Hall Effect sensor is suitable for the detection and characterization of the feeble leakage field signal generated by the surface and far-surface hairline cracks investigated in this work. Also, the capability of the Hall

Effect sensor to cancel out large offsets (i.e. the quasi static output voltage that exists in the absence of a magnetic field) means that it can be utilized where low frequency magnetic field signals have to be detected, which particularly makes it suitable for detecting far-surface hairline cracks in pipeline structures.

The Hall sensor output values obtained in the subsequent experiments were converted to magnetic flux density (mT), using the sensor's sensitivity value. That is; $B(mT) = \frac{Voltage}{0.0138}$ $(using\ 0.0138V/mT)$.

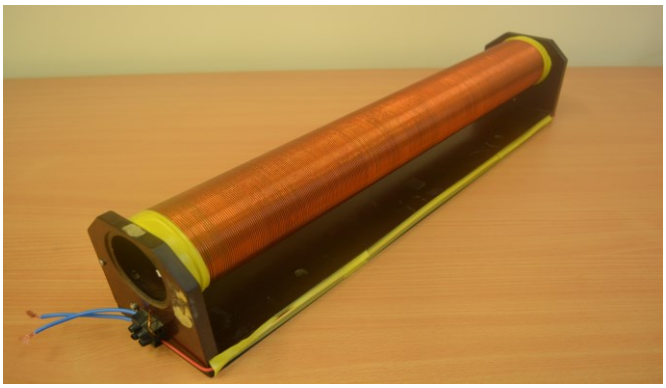

Figure 4.40. The solenoid used for the Ratiometric Hall Effect Sensor calibration.

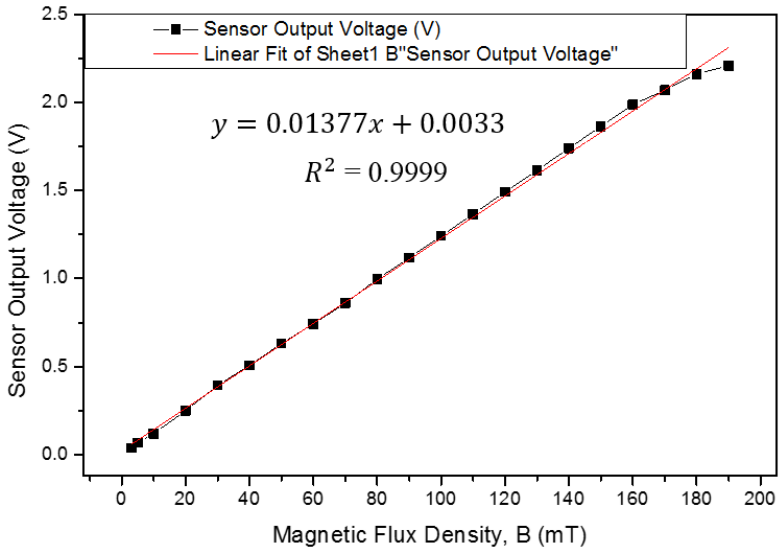

Figure 4.41. The Ratiometric Hall Effect sensor output voltage, as a function of magnetic flux density

4.4.3) Experimental Results and Discussions

In this section, the detection sensitivity of the FEM optimized DCMFL measurement system is assessed experimentally, using a 10 mm thick and a 6 mm thick low carbon steel plates. The test plates were magnetized with a direct current of 4 A. This generated a magnetic flux density (**B**) of 1.0 T and 1.29 T in the 10 mm and 6 mm thick plates respectively.

4.4.3.1) Repeatability Test for DCMFL Measurements

First, the repeatability of the FEM optimized DCMFL measurement system was examined experimentally, by acquiring the leakage field signal ($\boldsymbol{B_x}$) generated by a 4 mm deep surface hairline crack and a 4 mm deep far-surface hairline crack. Measurements were repeated 10 times in order to verify the reproducibility of the measurement results, since the success of the DCMFL investigation is dependent on the satisfactory reproducibility of the results obtained. The measured MFL signal amplitude ($\boldsymbol{B_x}$) as a function of scanning distance, for the 4 mm deep surface hairline crack and the 4 mm deep far-surface hairline crack, showing the standard error information (error bars) is illustrated in Fig. 4.42. It can be seen from Fig. 4.42 that the experimental DCMFL system maintained a good repeatability (minimal error). The maximum standard deviation recorded for the surface and far-surface hairline cracks were 1.74×10^{-4} mT and 9.2×10^{-5} mT respectively. The standard deviation quantifies the amount of variation or dispersion of the data set collected from the sensor, and was found to be low $\left(SD = \sqrt{\frac{\sum(x-\bar{x})^2}{n-1}}\right)$. The low/minimal standard deviation means that the data points tends to be close to the mean of the set, which shows a high repeatability of the data collected over the scanned region as illustrated in Fig. 4.42

The standard error and percentage error were calculated using equations 4.2 and 4.3 respectively. Where SD is the standard deviation, n is the number of measurements, a is the average value of the ten measurements and $SE_{\bar{x}}$ is the standard error (i.e. the

standard deviation of its sampling distribution or an estimate of the standard deviation). The maximum percentage error recorded for the surface and far-surface hairline cracks were 0.9 % and 0.23 % respectively, which shows a high measurement precision of the data collected from the Hall Effect sensor over the entire scanned region.

$$SE_{\bar{x}} = \frac{SD}{\sqrt{n}} \tag{4.2}$$

$$\%\ Error = \frac{SD}{a} \times 100 \tag{4.3}$$

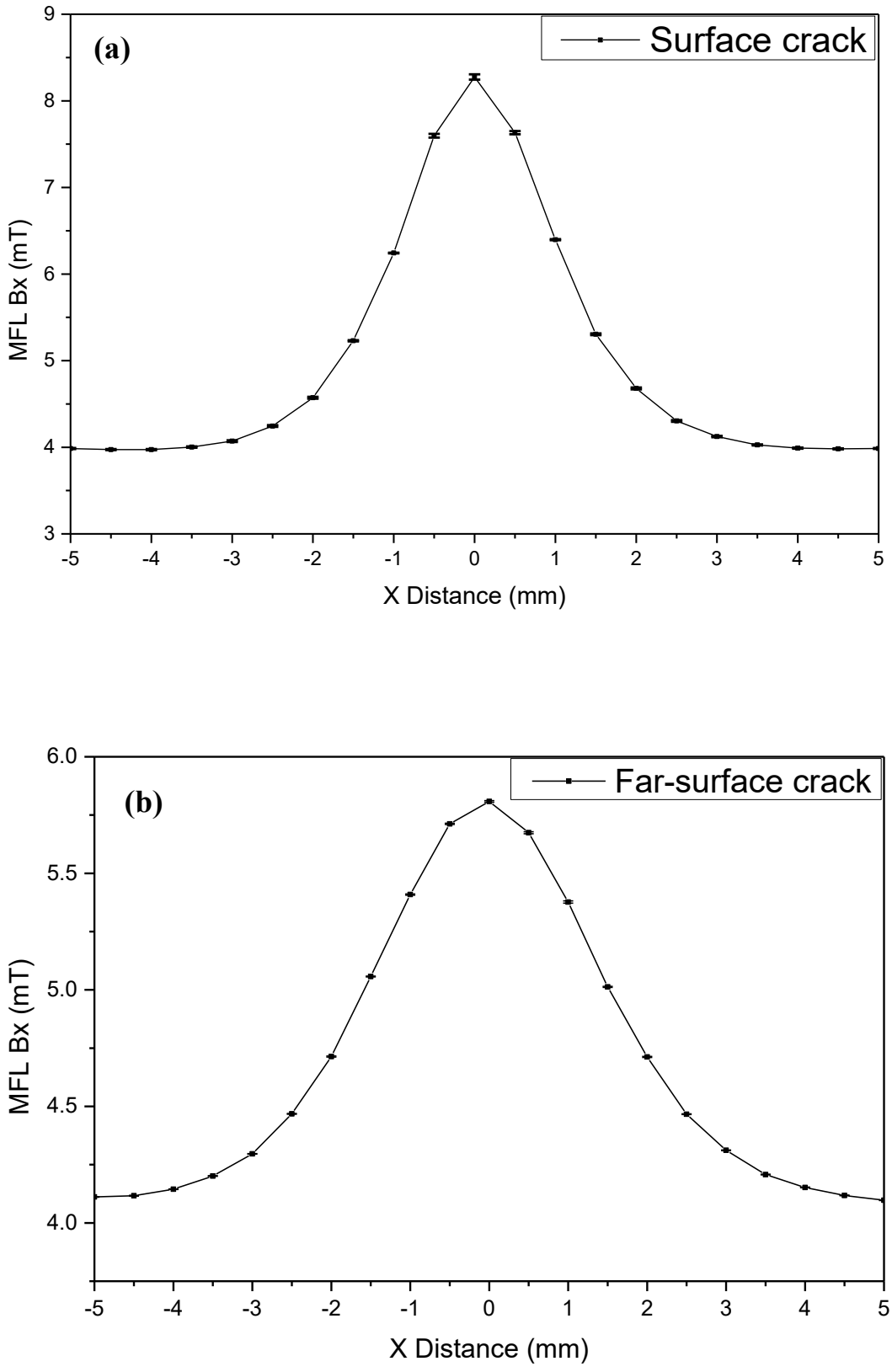

Figure 4.42. The measured MFL signal amplitude ($\boldsymbol{B_x}$) as a function of scanning distance for; a) 4mm deep surface hairline crack (standard error), and d) 4mm deep far-surface hairline crack (standard error).

4.4.3.2) Detection and Characterization of Hairline Cracks with Different Depth Sizes

The characterized Hall Effect sensor was scanned across a range of surface and far-surface hairline cracks and the $\boldsymbol{B_x}$ component of the leakage field was acquired. The depth sizes of the hairline cracks inspected ranges from 0.2 mm to 4 mm, with a constant width and length of 0.2 mm and 10 mm respectively. This was used to analyze the effect of crack depth variation on the resultant leakage field distribution and to ascertain the maximum penetration depth of the induced magnetic field in the test plates. The dimensions of the various surface and far-surface hairline cracks tested are clearly displayed in table 4.7, along with their respective peak leakage field amplitudes ($\boldsymbol{B_x^{peak}}$). Both line scan and area scan techniques were used to provide a more refined and enhanced visualization of the crack information and features. The results obtained from a line scan across various hairline cracks, with different depth sizes are presented in Fig. 4.43. It shows the relationship between the measured $\boldsymbol{B_x}$ leakage field amplitude and the depth of various surface (see Fig. 4.43a) and far-surface (see Fig. 4.43b) hairline cracks, as a function of scanning distance. The MFL signals were extracted 0.5 mm above the sample surface (0.5 mm sensor lift-off). A good correlation was found to exist between the $\boldsymbol{B_x}$ leakage field characteristic (signature) obtained experimentally and that obtained via simulation (see Fig. 4.17a).

Table 4.7. Details of the various surface and far-surface hairline cracks with varying depth sizes, present in a 10 mm thick plate, along with their respective peak MFL signal amplitudes.

Plate number	**Crack Type**	**Crack Depth d (mm)**	**Crack location h (mm)**	**MFL(B_x^{peak}) (mT)**
Plate 1	Surface	0.2	0.0	4.32
	Far-surface	0.2	9.8	4.16
Plate 2	Surface	0.4	0.0	4.46
	Far-surface	0.4	9.6	4.20
Plate 3	Surface	0.6	0.0	4.64
	Far-surface	0.6	9.4	4.25
Plate 4	Surface	0.8	0.0	4.80
	Far-surface	0.8	9.2	4.30
Plate 5	Surface	1.0	0.0	4.96
	Far-surface	1.0	9.0	4.38
Plate 6	Surface	2.0	0.0	5.72
	Far-surface	2.0	8.0	4.90
Plate 7	Surface	4.0	0.0	8.09
	Far-surface	4.0	6.0	5.83

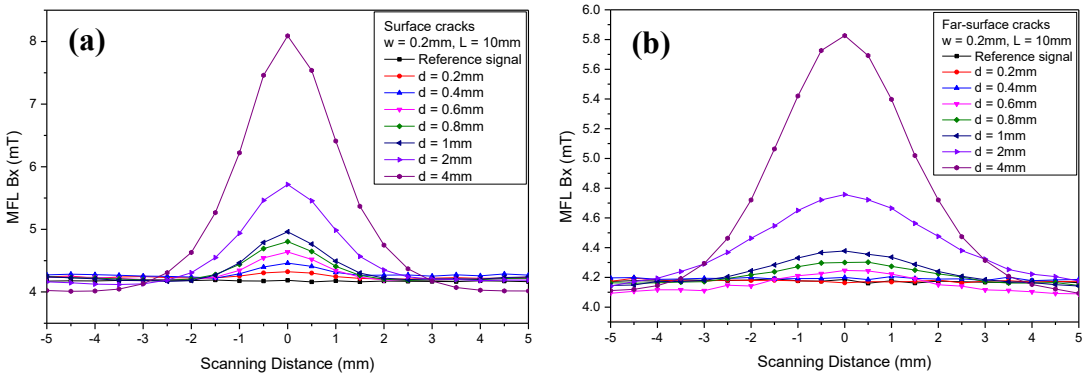

Figure 4.43. A line scan of the measured MFL signal ($\boldsymbol{B_x}$) amplitude for different crack depths, as a function of scanning distance for; a) Surface hairline cracks present in a 10 mm thick plate and b) Far-surface hairline cracks present in a 10 mm thick plate.

A photograph of a typical EDM surface hairline crack, present in a 10 mm thick plate is shown in Fig. 4.44. The crack is rectangular in shape, with a dimension of 10 mm × 0.2 mm × 4 mm (40 % surface wall loss). Fig. 4.45a and Fig. 4.45b shows the 3D imaging of the $\boldsymbol{B_x}$ leakage field distribution, obtained in the vicinity of a 4 mm deep surface hairline crack and a 4 mm deep far-surface hairline crack respectively. The induced magnetic field lies along the axial direction, whereas the cracks are positioned tangentially to the field orientation. A Corresponding axial line scan across the centre of the 4 mm deep surface hairline crack and the 4 mm deep far-surface hairline crack are shown in Fig. 4.43a and Fig. 4.43b respectively. The analysis of the MFL signature from the Hall Effect sensor for both types of crack shows pronounced effect of metal loss on the axial leakage field profile. As the tangentially oriented cracks are detected, the amplitude and distribution patterns of the leakage fields are altered with respect to the crack shape and size (length and width). Also, the measured leakage field signal for both cracks vary with relative position of the sensor to the crack axis, with the peak amplitude recorded at the crack centre. The peak values of the leakage field signal ($\boldsymbol{B_x^{peak}}$) for the 4 mm deep surface and the 4 mm deep far-surface hairline cracks are 8.1 mT and 5.8 mT respectively.

Also, the distinction between a surface and a far-surface crack can be interpreted from the resultant leakage field profile, which shows a significantly lower signal value as well as a broader signal width for the far-surface crack, compared to a higher signal value and narrower signal width observed for the surface crack of

equivalent size. The lower signal level recorded for the far-surface crack is due to a reduced magnetic flux leakage intensity with increasing crack location from the sample surface, while its broader signal width is attributed to the lateral spread of magnetic field (inherent divergent effect) at the vicinity of the far-surface crack. The relationship between the size and shape of both hairline cracks and the leakage field signal can be established from the imaged field distribution, by analyzing the distribution change of the flux in the length and width directions. Moreover, some useful features can be acquired from the mapped out images, such as the; crack type, crack position, crack orientation and dimensional information. However, for non-uniform crack shapes (complex geometry), such mapped out images may not disclose very useful information regarding the geometries of the cracks.

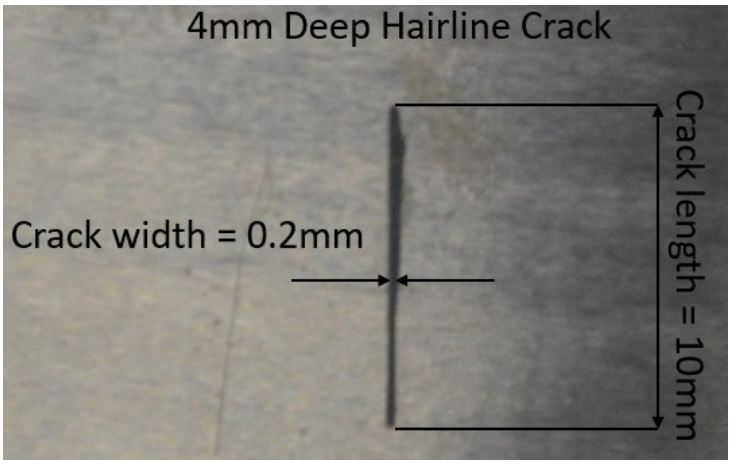

Figure 4.44. A 4 mm deep rectangular shaped hairline crack (40 % wall loss) presenet on a 10 mm thick low carbon steel plate (crack width = 0.2 mm and crack length = 10 mm).

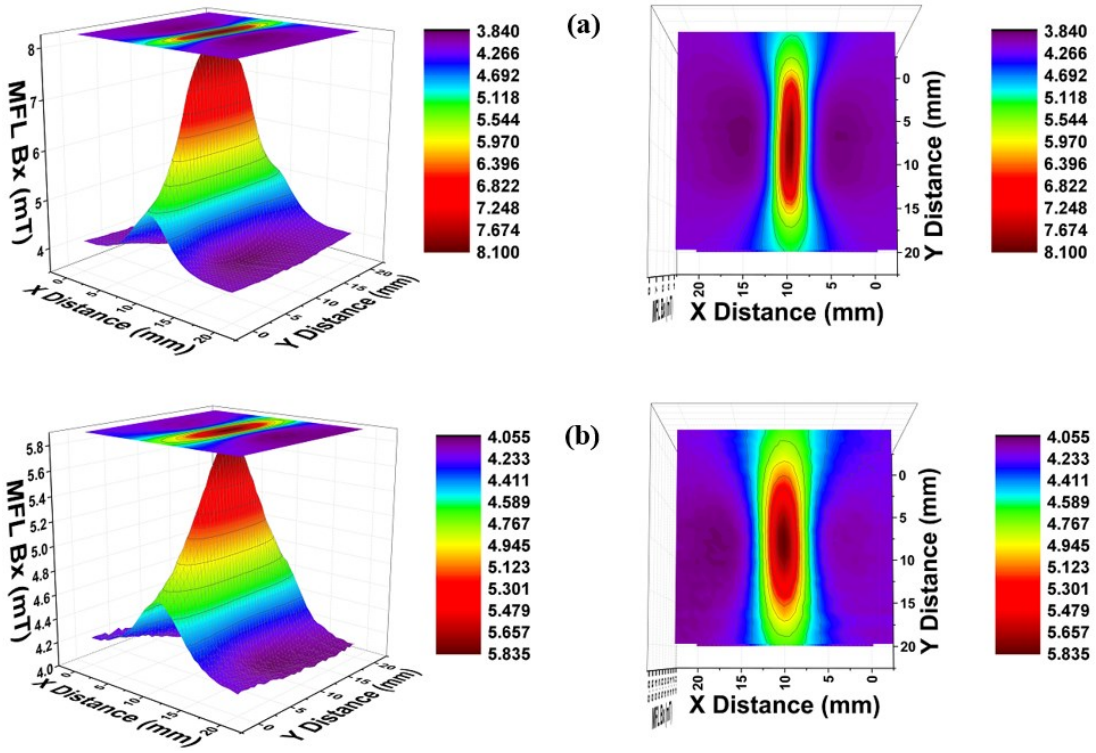

Figure 4.45. A 3D illustration of the measured MFL ($\boldsymbol{B_x}$) signals for a 4 mm deep; a) Surface hairline crack in a 10 mm thick plate and b) Far-surface hairline crack in a 10 mm thick plate.

Fig. 4.46 and Fig. 4.47 show the results obtained from an area scan in the vicinity of all the surface and far-surface hairline cracks respectively, as a function of x and y distances. The scanned area represents a surface of 20 mm × 20 mm, with a constant scan step size of 0.5 mm in the x and y directions. A peak leakage field ($\boldsymbol{B_x^{peak}}$) amplitude of 4.32 mT, 4.46 mT, 4.64 mT, 4.80 mT, 4.96 mT, 5.72 mT and 8.09 mT was recorded for the 0.2 mm, 0.4 mm, 0.6 mm, 0.8 mm, 1 mm, 2 mm and 4 mm deep surface hairline cracks respectively. Likewise, a $\boldsymbol{B_x^{peak}}$ amplitude of 4.16 mT, 4.20 mT, 4.25 mT, 4.30 mT, 4.38 mT, 4.90 mT and 5.83 mT was recorded for the far-surface hairline cracks respectively. The increasing proportion of the signal's amplitude for the surface hairline cracks are; 3.1 %, 3.9 %, 3.3 %, 3.2 %, 13 % and 29 % respectively, while the increasing proportion of the signal's amplitude for the far-surface hairline cracks are; 1.0 %, 1.2 %, 1.2 %, 1.8 %, 11 %, and 16 % respectively.

Also, based on the information displayed in both figures, it can be seen that the Hall Effect sensor is able to detect as small as a 0.2 mm deep surface hairline crack (2% surface wall loss) and a 0.6 mm deep far-surface hairline crack (6% far-surface wall

loss), located 9.4 mm below the surface of a 10 mm thick plate, with a good signal to noise ratio. However, the sensor was not able to detect a 0.2 mm and a 0.4 mm deep far-surface hairline cracks, located 9.8 mm and 9.6 mm below the plate surface respectively. Thus, the maximum penetration depth achieved in the 10 mm thick plate was 9.4 mm. This means that surface hairline cracks with depth size of 0.2 mm and above and far-surface hairline cracks with depth size of 0.6 mm and above, in a 10 mm thick pipeline structure can be effectively detected and evaluated while using the newly developed DCMFL inspection system. Moreover, the leakage field amplitude and distribution pattern for the far-surface hairline cracks were found to be lower and broader respectively, when compared to the leakage field amplitude and distribution pattern for an equivalent surface hairline crack (see Fig 5.46 and Fig. 5.47). This is due to the field dispersion (field spreading) occurring at the far-surface crack vicinity, which increases with increasing crack location from the sample surface. Also, the leakage field dispersion leads to an attenuation of the measured leakage field amplitude.

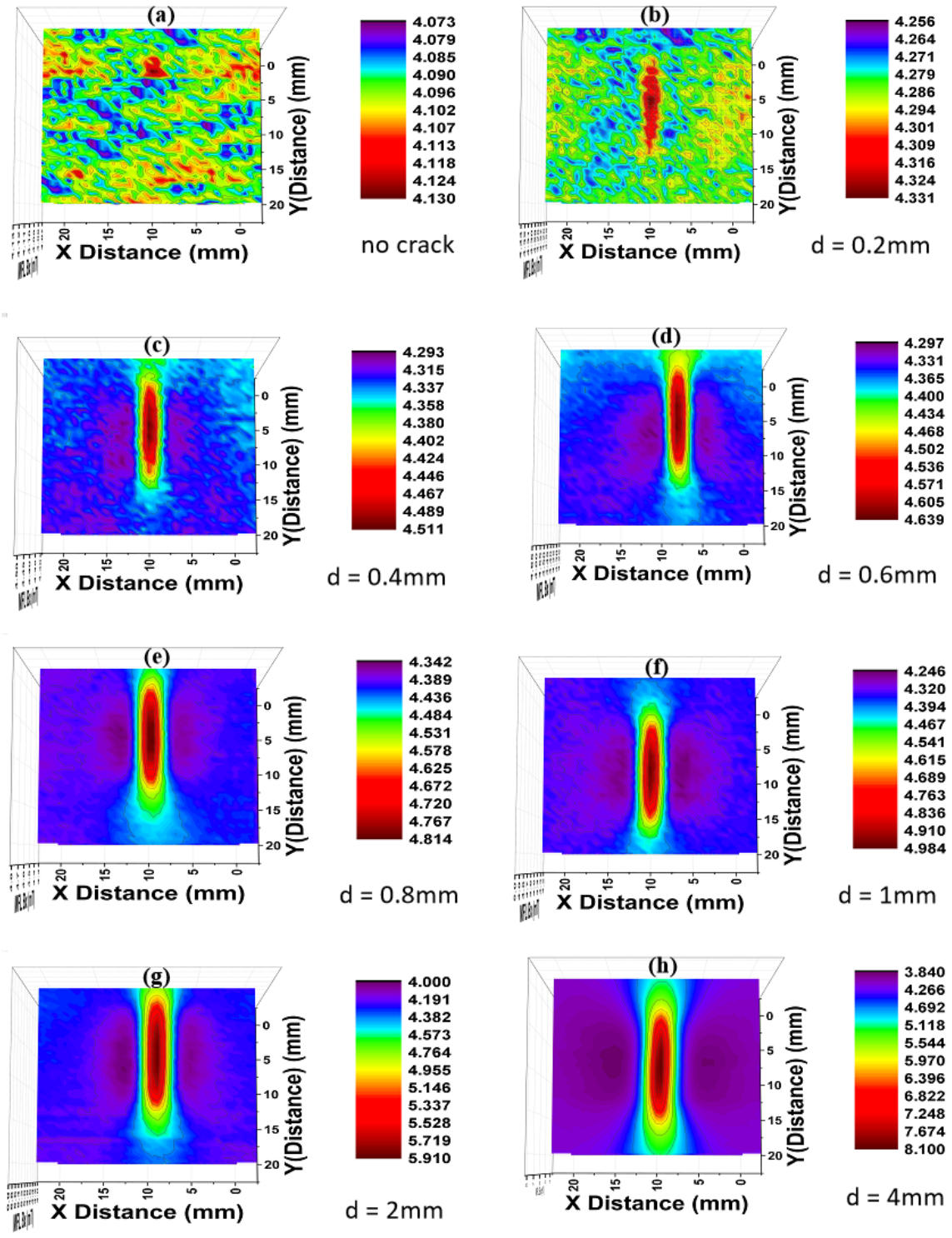

Figure 4.46. An area scan of the measured MFL signal ($\boldsymbol{B_x}$) amplitude for different surface hairline cracks with varying depth sizes, as a function of x and y distances.

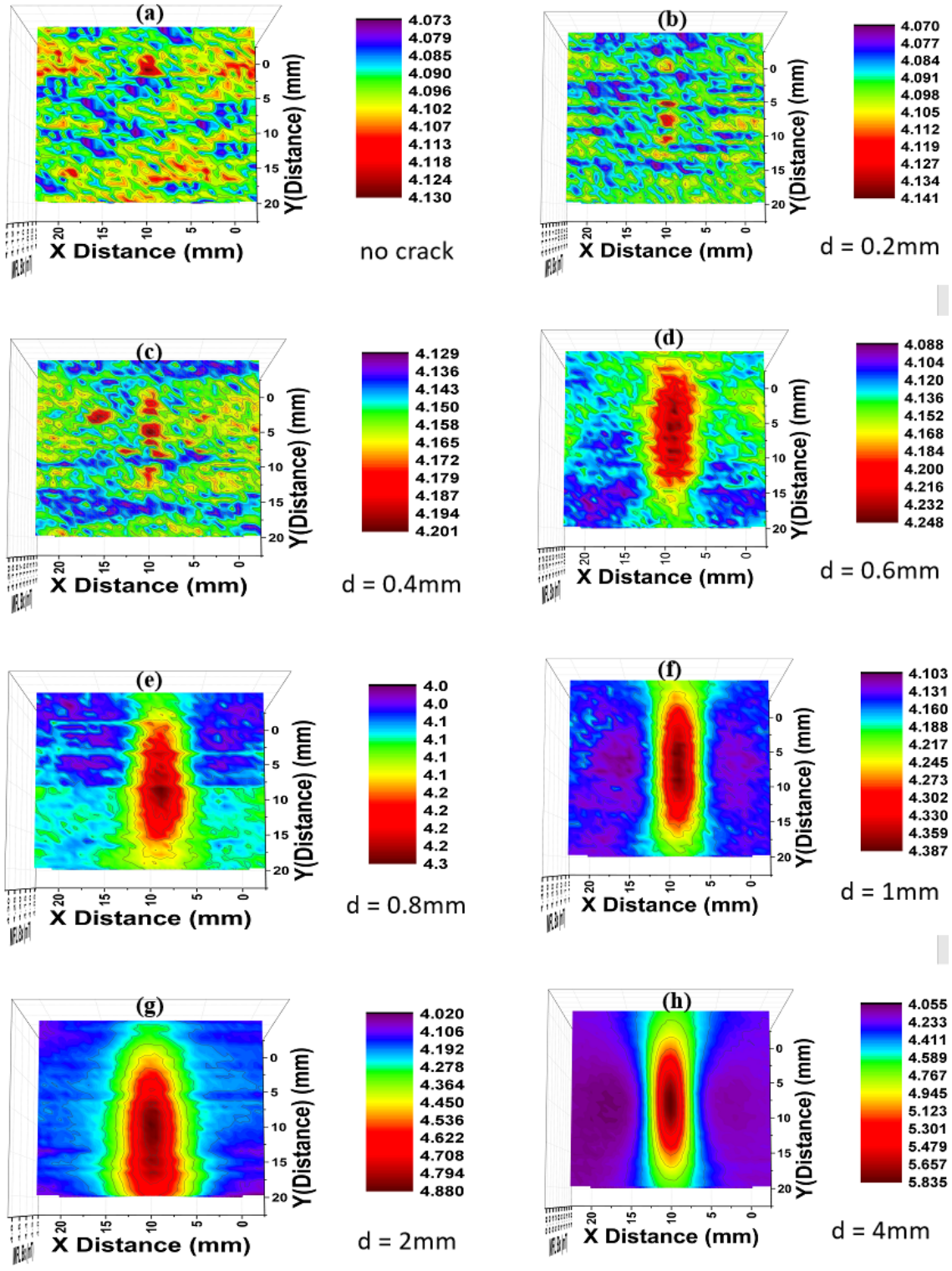

Figure 4.47. An area scan of the measured MFL signal ($\boldsymbol{B_x}$) amplitude for different far-surface hairline cracks with varying depth sizes, as a function of x and y distances.

4.4.3.3) The Effect of Plate Thickness on the Detection Sensitivity of Hairline Cracks

The influence of test sample thickness on the detection sensitivity of surface and far-surface hairline cracks was investigated experimentally, by comparing the measured leakage field signal for 10 mm and 6 mm thick plates. The dimensions of the various surface and far-surface cracks inspected while using a 6 mm thick plate are shown in table 4.8, along with their respective peak leakage field ($\boldsymbol{B_x^{peak}}$) amplitudes.

Table 4.8. Details of the various surface and far-surface hairline cracks with varying depth sizes, present in a 6 mm thick plate, along with their respective peak MFL signal amplitudes.

Plate number	**Crack Type**	**Crack Depth d (mm)**	**Crack Location h (mm)**	**MFL(B_x^{peak}) (mT)**
Plate 1	Surface	0.2	0.0	4.98
	Far-surface	0.2	5.8	4.94
Plate 2	Surface	0.4	0.0	5.2
	Far-surface	0.4	5.6	4.98
Plate 3	Surface	0.6	0.0	5.41
	Far-surface	0.6	5.4	5.08
Plate 4	Surface	0.8	0.0	5.63
	Far-surface	0.8	5.2	5.2
Plate 5	Surface	1.0	0.0	5.84
	Far-surface	1.0	5.0	5.33
Plate 6	Surface	2.0	0.0	6.78
	Far-surface	2.0	4.0	6.09
Plate 7	Surface	4.0	0.0	9.63
	Far-surface	4.0	2.0	7.75

Fig. 4.48 shows the output of the Hall Effect sensor ($\boldsymbol{B_x}$) for both surface (see Fig. 4.48a) and far-surface (see Fig. 4.48b) hairline cracks, as a function of scanning distance, for the 6 mm thick plate. A $\boldsymbol{B_x^{peak}}$ amplitude of 4.98 mT, 5.20 mT, 5.41 mT, 5.63 mT, 5.84 mT, 6.78 mT and 9.63 mT was recorded for the 0.2 mm, 0.4 mm, 0.6 mm, 0.8 mm, 1 mm, 2 mm and 4 mm deep surface hairline cracks respectively as shown in table 4.8. Likewise, a $\boldsymbol{B_x^{peak}}$ amplitude of 4.94 mT, 4.98 mT, 5.08 mT, 5.20 mT, 5.33 mT, 6.09 mT and 7.75 mT was recorded for the far-surface hairline cracks respectively. The increasing proportion of the signal's amplitude for the surface hairline cracks are; 4.2 %, 3.9 %, 3.9 %, 3.6 %, 13 % and 29 % respectively, while the increasing proportion of the signal's amplitude for the far-surface hairline cracks are; 1.0 %, 2.0 %, 2.3 %, 2.4 %, 12.5 %, and 21.4 %.

As can be observed from both plots, the sensor is able to detect a 0.2 mm deep surface hairline crack (3.3 % surface wall loss) and a 0.2 mm deep far-surface hairline crack (3.3 % far-surface wall loss), located 5.8 mm below the plate surface (the sensor detected all the hairline cracks inspected). The sensor's peak signal ($\boldsymbol{B_x^{peak}}$) amplitude as a function of crack depth, for the 10 mm and 6 mm thick plates are compared in Fig. 4.49. As can be seen, the $\boldsymbol{B_x^{peak}}$ amplitude increases with increasing crack depth, for both plate thicknesses. However, the sensor signal amplitude is higher for the 6 mm thick plate when compared to the 10 mm thick plate, for similar crack depths. This is caused by the reduction in magnetic flux intensity ($\boldsymbol{B}$) with increasing plate thickness, hence, resulting to a weaker leakage flux in the 10 mm thick plate compared to the 6 mm thick plate. Also, it can be observed from Fig. 4.49 that there is an overlap in surface and far-surface leakage field values. Therefore, discrimination between the two types of cracks (surface and far-surface hairline cracks) will be difficult while using just the leakage field amplitude, except for surface hairline cracks with depth greater than 2 mm.

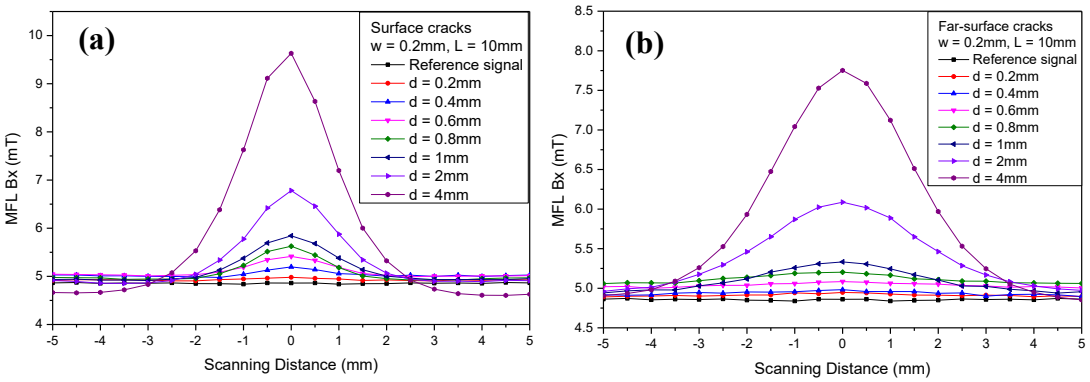

Figure 4.48. The measured MFL signal peak amplitudes ($\boldsymbol{B_x}$) for different crack depths as a function of crack position for; a) Surface hairline cracks in a 6 mm thick plate and b) Far-surface hairline cracks in a 6 mm thick plate.

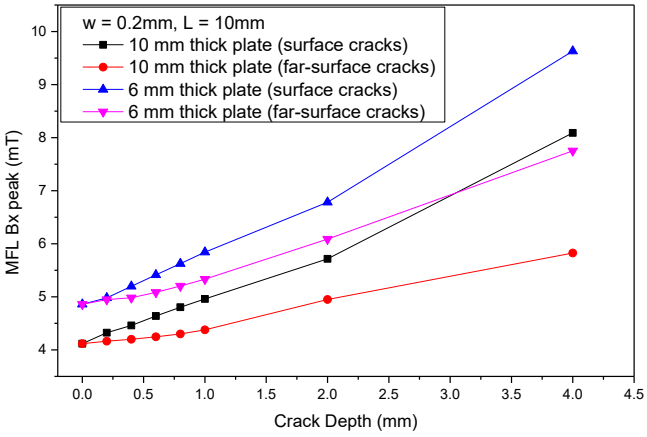

Figure 4.49. A plot comparing the measured MFL ($\boldsymbol{B_x^{peak}}$) signal amplitude produced by both surface and far-surface hairline cracks, for 10 mm and 6 mm thick plates.

4.4.3.4) The Effect of Sensor Lift-off on the Detection Sensitivity of Hairline Cracks

To meet the sensor clearance requirements for MFL testing of pipeline structures, a sensor lift-off tolerant MFL inspection tool is necessary. To ensure an efficient and successful pipeline inspection using the MFL testing technique, one of the major challenges to overcome is how to test unclean pipe surfaces, that is; pipeline surfaces with rock particles, muds, debris, welds, plants, sand, oil stains, etc. For most

conventional MFL inspection techniques, the magnetic sensors are usually positioned very close to the test sample surface in order to maintain a high enough sensitivity to the existing defects. That is; to achieve the highest possible signal variation at the crack vicinity. This usually results in virtually zero clearance between the sensor and the test sample surface. The disadvantage of having the sensor very close to the sample surface is a short life span of the sensing probes, as they may be seriously worn out or damaged during high speed inspection. This might also lead to the problem of recalibration as a result of variations in the sensor clearance from the pipe surface, caused by extreme wear and tear of the sensor. Hence, a high lift-off tolerant MFL inspection system is essential, in order to enable the sensor to be positioned at higher lift-off distances while still maintaining a good inspection sensitivity.

In this work, the sensor clearance from the test sample surface is varied using the z axis translation stage and its influence on the acquired leakage field signal is recorded for different surface and far-surface hairline cracks, while keeping other signal influencing parameters constant. Here, the sensor lift-off was varied from 0.5 mm to 12 mm in order to investigate the different levels of sensor lift-offs possible. Fig 4.50 shows the measured MFL ($\boldsymbol{B_x}$) signal amplitude as a function of scanning distance, for both the 4 mm deep surface hairline crack (see Fig. 4.50a) and the 4 mm deep far-surface hairline crack (see Fig. 4.50b). Like the simulation result, the MFL signal amplitude decreases with increasing sensor lift-off value. Also, the reduction in the $\boldsymbol{B_x}$ signal amplitude as the sensor lift-off is increased was found to be higher for lower levels of sensor lift-off, compared to higher levels of sensor lift-off.

A plot showing the variation of the measured $\boldsymbol{B_x^{peak}}$ amplitude as a function of crack depth, at different sensor lift-offs, for all the surface and far-surface hairline cracks inspected is displayed in Fig. 4.51a and Fig. 4.51b respectively. One can clearly see that the $\boldsymbol{B_x^{peak}}$ amplitude decreases significantly, as the sensor lift-off is increased. Also, it can be seen from the both plots that the rate of decrease in the $\boldsymbol{B_x^{peak}}$ amplitude as the sensor lift-off is increased, is higher for lower levels of sensor lift-off, compared to higher levels (i.e. $\boldsymbol{B_x^{peak}}$ drops off at a decreasing rate with sensor lift-off distance).

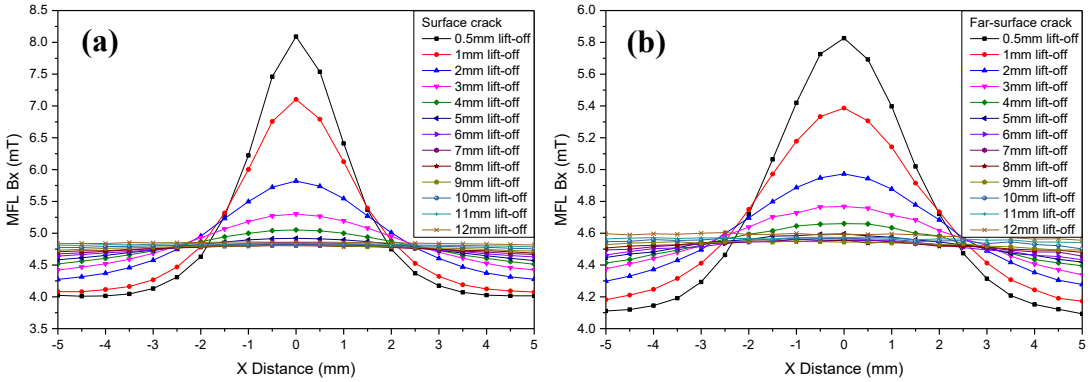

Figure 4.50. The relationship between the measured MFL ($\boldsymbol{B_x}$) signal amplitude and crack position, at different sensor lift-offs, for a) A 4 mm deep surface hairline crack and b) A 4 mm deep far-surface hairline crack.

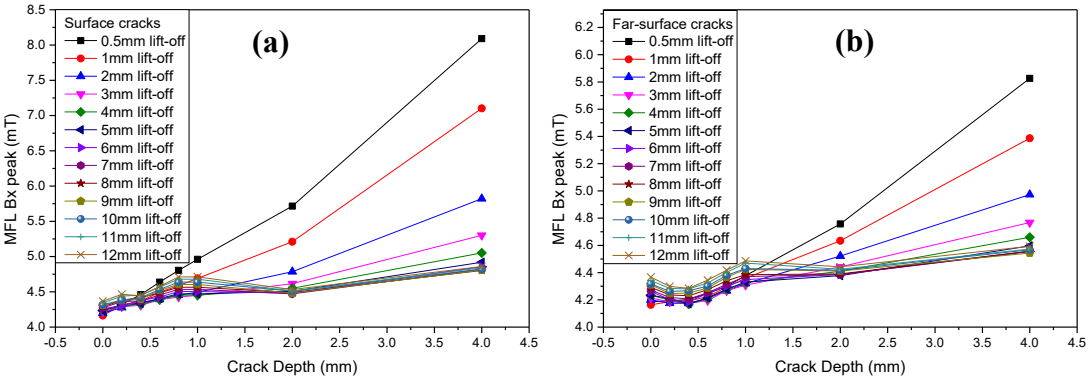

Figure 4.51. A plot showing the measured MFL signal amplitude ($\boldsymbol{B_x^{peak}}$) as a function of crack depth, at different sensor lift-offs, for; a) Surface cracks and b) Far-surface cracks.

The limit of detection for each of the surface and far-surface hairline cracks with different depth sizes are shown in Fig. 4.52. As can be observed, the limit of detection for the surface hairline cracks is significantly higher than that for the far-surface hairline cracks. The lower detection limit recorded for the far-surface hairline cracks as compared to the surface hairline cracks is attributed to field spreading (field dispersion) occurring at the far-surface crack region, which causes an attenuation of the leakage field signal generated by the far-surface hairline cracks. Therefore, the sensor is able to detect the leakage field signal generated by the surface hairline cracks at much higher lift-offs, compared to that generated by a far-surface hairline crack of the same size.

The Hall Effect sensor used was able to detect both the 4 mm deep surface hairline crack and the 4 mm deep far-surface hairline crack at 5 mm lift-off. The detection

limits for each of the surface and far-surface hairline cracks inspected are displayed in table. 4.9.

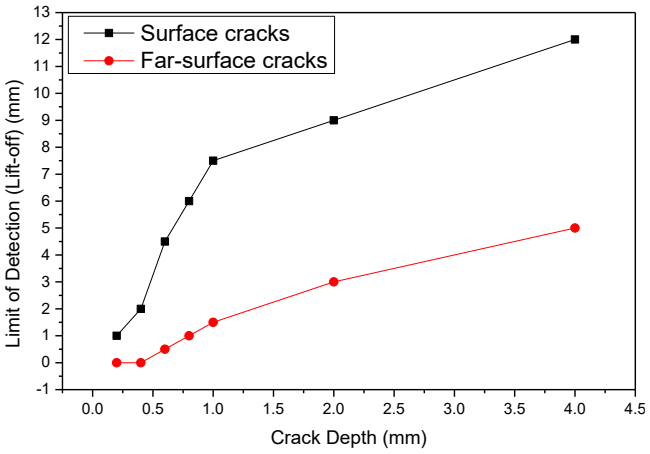

Figure 4.52. A plot showing the detection limit for the various surface and far-surface hairline cracks with different depth sizes.

Table 4.9. The DCMFL sensor detection limit for the various surface and far-surface hairline cracks inspected.

Crack Depth (mm)	**Detection Limit (mm) (Sensor lift-off)**	
	Surface hairline cracks	**Far-surface hairline cracks**
0.2	1.0	0.0
0.4	2.0	0.0
0.6	4.5	0.5
0.8	6.0	1.0
1.0	7.5	1.5
2.0	9.0	3.0
4.0	12.0	5.0

4.4.3.5) Sensitivity Test for Surface and Far-surface Hairline Cracks

The sensitivity of the newly developed DCMFL inspection system to both surface and far-surface hairline cracks is investigated in this section. The sensitivity of the DCMFL system was evaluated by scanning the Hall Effect sensor across various surface and far-surface hairline cracks with varying depth sizes, in a 10 mm thick plate. The inspected hairline cracks were; a 0.2 mm, 0.4 mm, 0.6 mm, 0.8 mm, 1 mm, 2 mm and 4 mm deep surface and far-surface hairline cracks, with a constant width and length of 0.2 mm and 10 mm respectively. The sensitivity of the MFL system to the various hairline cracks was calculated using equation (4.4);

$$SNR = 20log\left(\frac{S}{N}\right) \tag{4.4}$$

Where, SNR is the signal to noise ratio, S is the leakage field peak ($\boldsymbol{B_x^{peak}}$) amplitude generated by a hairline crack and N is the leakage field peak amplitude collected from a crack free region (N = 4.22 mT). A signal to noise ratio of 0.20 dB, 0.48 dB, 0.82 dB, 1.12 dB, 1.40 dB, 2.64 dB and 5.65 dB was calculated for the surface hairline cracks in sequence, while a signal to noise ratio of 0 dB, 0 dB, 0.06 dB, 0.16 dB, 0.32 dB, 1.30 dB and 2.81 dB was calculated for the far-surface hairline cracks in sequence. Fig. 4.53 shows a graph of sensitivity (SNR) versus crack depth. It compares the sensitivity of the newly developed DCMFL inspection system for both surface and far-surface hairline cracks, with varying depth sizes. As can be seen, the sensitivity of the system increases with increasing crack depth for both surface and far-surface hairline cracks, with a lower sensitivity level for the far-surface hairline cracks when compared to a surface hairline crack of the same size. Also, it can be seen that the relationship between the sensitivity of the inspection system and crack depth is linear.

The increasing proportion of the system's sensitivity for the surface hairline cracks (from d = 0.2 mm to 4 mm) was calculated to be 58 %, 41 %, 28 %, 20 %, 47 % and 53 % respectively. Likewise, the increasing proportion of the signal's sensitivity for the far-surface hairline cracks (from d = 0.2 mm to 4 mm) was found to be 0 %, 100 %, 62 %, 50 %, 75 % and 53 % respectively. Table 5.5 shows the sensitivity values for the newly developed DCMFL inspection system to various surface and far-

surface hairline cracks with different depth sizes, as well as the leakage field peak (B_x^{peak}) amplitude measured for each of the hairline cracks inspected.

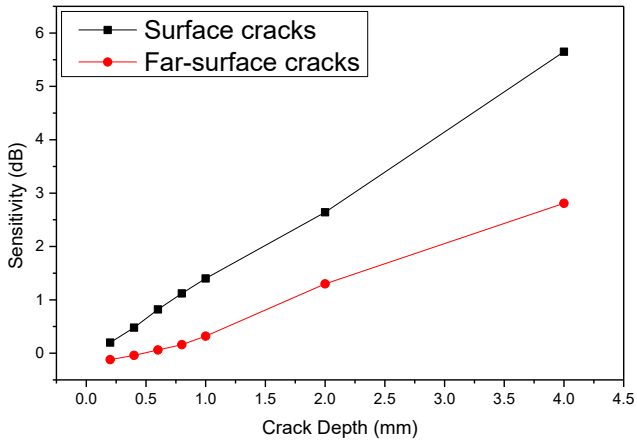

Figure 4.53. A plot comparing the sensitivity of the newly developed DCMFL inspection system for different surface and far-surface hairline cracks with different depth sizes.

Table 4.10. The sensitivity of the DCMFL inspection system to different surface and far-surface hairline cracks with varying depth sizes.

Crack Depth (mm)	**MFL(B_x^{peak}) (mT) Crack signal**		**Detection Sensitivity (dB)**	
	Surface hairline cracks	**Far-surface hairline cracks**	**Surface hairline cracks**	**Far-surface hairline cracks**
0.2	4.32	4.16	0.20	0.0
0.4	4.46	4.20	0.48	0.0
0.6	4.64	4.25	0.82	0.06
0.8	4.80	4.30	1.12	0.16
1.0	4.96	4.38	1.40	0.32
2.0	5.72	4.90	2.64	1.30
4.0	8.09	5.83	5.65	2.81

4.5) Estimation of the Shape and Size of Hairline Cracks using the DCMFL Inspection Technique

The problem of crack shape and size evaluation using the simulated or measured leakage field distribution pattern is termed the inverse problem (crack reconstruction). By studying the leakage field distribution pattern obtained while scanning the sensor in the crack vicinity, practically, it is possible to estimate the approximate shape and dimension of an unknown crack, by solving the inverse problem. To investigate the possibility of achieving such goal, both surface and far-surface hairline cracks were tested using the FEM and experimental approach. Effects were observed using a surface plot of the leakage field distribution pattern acquired (3D imaging of the resultant leakage field distribution). In order ensure that the crack shape/size and the surface plot of the leakage field distribution occupy similar pixel area, an image processing toolbox in Origin Lab software was used for the image analysis.

Thus, a method based on enhanced visualization and 3D imaging of the resultant leakage field distribution is proposed in this section, in order to obtain the approximate shape and size (width and length) of different surface and far-surface hairline cracks, present in ferromagnetic pipeline structures. A range of surface and far-surface hairline cracks with different depth and width sizes were tested, using a 10 mm thick plate. Whenever a tangential hairline crack is detected in the test plate, the amplitude and distribution pattern of the leakage field were changed, based on the shape and size of the crack. The relationship between the leakage field and the hairline crack profile was established, by critically analyzing the interdependency between the two variables. It is important to note that when a crack exist on the magnetized sample, the resultant magnetic field, which leaks into the surrounding air is made up of two contributions. One is the base value as a result of the background field, i.e. signal with no crack present (reference signal). The other is the disturbance field caused by the crack. In order to accurately extract the hairline crack features from the leakage field signal, the method of first differential approach is adopted, so as to separate the crack signal from the reference signal.

If b and b_0 are two different plates with the same magnetic properties and physical size, except that plate b has a crack while plate b_0 does not. The differential crack signal in the axial, radial and tangential directions are acquired using equation (4.5), (4.6) and (4.7) respectively.

$$\Delta \boldsymbol{B}_{xb} = \boldsymbol{B}_{xb} - \boldsymbol{B}_{xb_0} \tag{4.5}$$

$$\Delta \boldsymbol{B}_{yb} = \boldsymbol{B}_{yb} - \boldsymbol{B}_{yb_0} \tag{4.6}$$

$$\Delta \boldsymbol{B}_{zb} = \boldsymbol{B}_{zb} - \boldsymbol{B}_{zb_0} \tag{4.7}$$

Here, the leakage field signal with no crack is subtracted from the leakage signal with a crack to obtain the three components of the leakage signal, that is; $\Delta \boldsymbol{B}_{xb}$, $\Delta \boldsymbol{B}_{yb}$ and $\Delta \boldsymbol{B}_{zb}$. $\boldsymbol{B}_{xb}$, $\boldsymbol{B}_{yb}$, $\boldsymbol{B}_{zb}$ are the disturbance fields generated by a crack (crack signals), $\boldsymbol{B}_{xb_0}$, $\boldsymbol{B}_{yb_0}$, $\boldsymbol{B}_{zb_0}$ are the base values from a crack free region (reference signals) and b represents the various cracks with different depth sizes.

4.5.1) Estimation of the Shape and Size of Hairline Cracks via Simulation

Fig 4.54 and Fig 4.55 shows a surface plot of the simulated crack signals ($\boldsymbol{B}_{xb}$, $\boldsymbol{B}_{yb}$ and $\boldsymbol{B}_{zb}$) and the simulated differential crack signals ($\Delta \boldsymbol{B}_{xb}$, $\Delta \boldsymbol{B}_{yb}$ and $\Delta \boldsymbol{B}_{zb}$) respectively, for a 4 mm deep surface hairline crack and for a 4 mm deep far-surface hairline crack. The measurement area represented is a surface of 20 mm × 20 mm, with a constant step size of 0.1 mm in the x and y directions. It can be seen that the approximate width and length of both hairline cracks can be extracted from the leakage signal widths, in the width and length directions respectively. However, it is challenging to determine the actual depth of the cracks by using the signal width only. This is because the signal width is hardly changed by variation in crack depth, as shown in Fig. 4.43 and Fig. 4.48 of section 4.4.3.2 and section 4.4.3.3 respectively.

The 3D plots of the leakage field signal displayed in this section reveals that the highest signal amplitude occur at the central major axis of the cracks. If the crack is positioned at the reverse side of the plate, the resultant leakage field is more spread

out compared to a surface crack, as a result of lateral field dispersion occurring at the far-surface crack region. Hence, the estimated crack width for the far-surface crack is far larger than the actual crack width (i.e. >> 0.2 mm). This is evident in the simulation results displayed in Figs 4.54d, 4.54e, 4.54f, 4.55d, 4.55e and 4.55f.

As shown in Figs. 4.54b, 4.54e, 4.55b and 4.55e, the width of the surface and far-surface hairline cracks can be measured directly, using the location of the signal peaks in the $\boldsymbol{B}_y$ signal profile of the sensor moving across the crack centre. However, the measurement of the crack depth and length using the $\boldsymbol{B}_y$ signal profile is complicated, and no precise correlation can be utilized (i.e. the $\boldsymbol{B}_y$ spread is unaffected by changes in crack depth and length). Precise measurement of the crack width is mandatory, regardless of the fact that the crack width does not pose a serious danger to the pipeline integrity or service lift-time as compared to the crack depth. However, misinterpretations or errors in the width measurement can result in an error in the depth measurement, which can adversely threaten the pipelines integrity. Notwithstanding, the limit of tolerance for width measurement according to the international standards is as high as ±7.5 mm [10]. Both the width and length of the surface and far-surface hairline cracks can be estimated using the $\boldsymbol{B}_x$ signal profile in the width and length directions respectively. Likewise, the width and length of the surface and far-surface hairline cracks can be obtained using the signal peaks of the $\boldsymbol{B}_z$ spread in the width and length directions respectively as shown in Figs. 4.54c, 4.54f, 4.55c and 4.55f. Comparing the $\boldsymbol{B}_x$ leakage field distribution pattern with that of $\boldsymbol{B}_y$ and $\boldsymbol{B}_z$, it can be seen that the $\boldsymbol{B}_x$ profile provides a clearer idea of the crack shape being investigated. Moreover, it is less tasking to get an idea of the approximate width and length of the hairline cracks from the $\boldsymbol{B}_x$ leakage field distribution pattern, in the x and y directions respectively (see Figs. 4.54a, 4.54d, 4.55a and 4.55d), as compared to using the $\boldsymbol{B}_y$ and $\boldsymbol{B}_z$ leakage field distribution patterns.

The estimated width and length for the 4 mm deep surface hairline crack is approximately 0.8 mm and 12 mm respectively while using the simulated crack signals ($\boldsymbol{B}_{xb}$, $\boldsymbol{B}_{yb}$ and $\boldsymbol{B}_{zb}$), as shown in Figs 4.54a, 4.54b and Fig. 4.54c. However, for the differential crack signals ($\Delta\boldsymbol{B}_{xb}$, $\Delta\boldsymbol{B}_{yb}$ and $\Delta\boldsymbol{B}_{zb}$) the estimated width and length for the same 4 mm deep surface hairline crack is 0.2 mm and 10 mm

respectively, as shown in Figs. 4.55a, 4.55b and Fig. 4.55c. Likewise, an approximate width and length of 4 mm and 15 mm respectively, was estimated for the 4 mm deep far-surface hairline crack while using the simulated crack signals, as shown in Figs. 4.54d, 4.54e and 4.54f. However, for the differential crack signals, the estimated width and length for the same 4 mm deep far-surface hairline crack is 3 mm and 11 mm respectively, as shown in Figs. 4.55d, 4.55e and Fig. 4.55f.

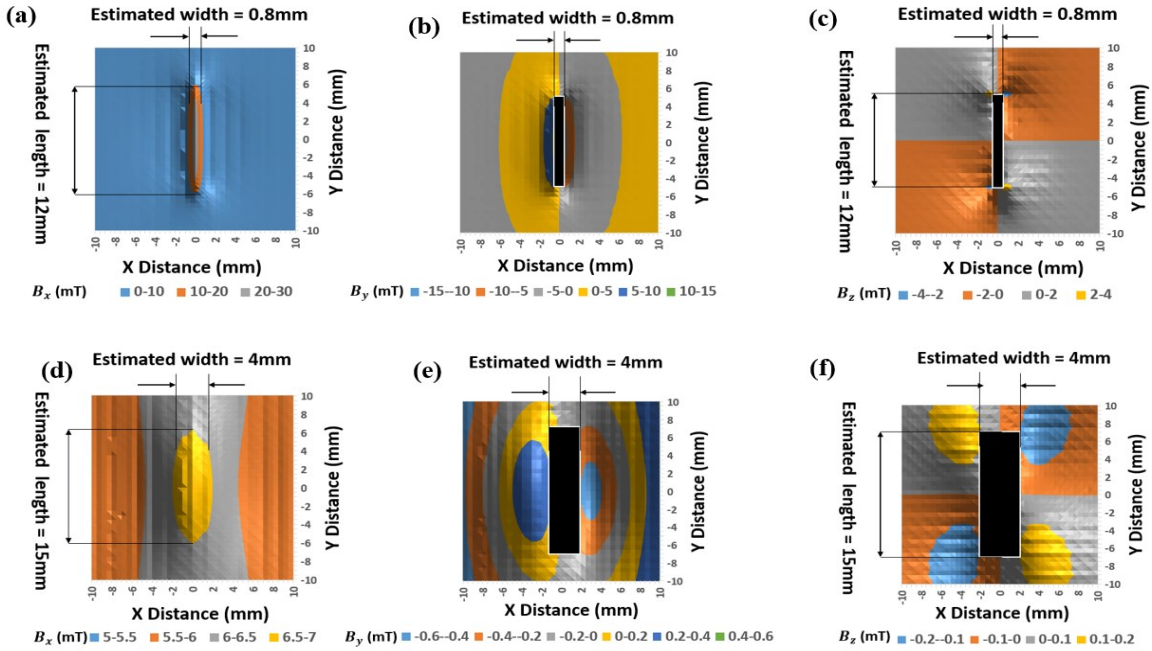

Figure 4.54. The simulated DCMFL crack signals; a) $\boldsymbol{B}_{xb}$ signal for a 4 mm deep surface hairline crack, b) $\boldsymbol{B}_{yb}$ signal for a 4 mm deep surface hairline crack c) $\boldsymbol{B}_{zb}$ signal for a 4 mm deep surface hairline crack, d) $\boldsymbol{B}_{xb}$ signal for a 4 mm deep far-surface hairline crack, e) $\boldsymbol{B}_{yb}$ signal for a 4 mm deep far-surface hairline crack and f) $\boldsymbol{B}_{zb}$ signal for a 4 mm deep far-surface hairline crack.

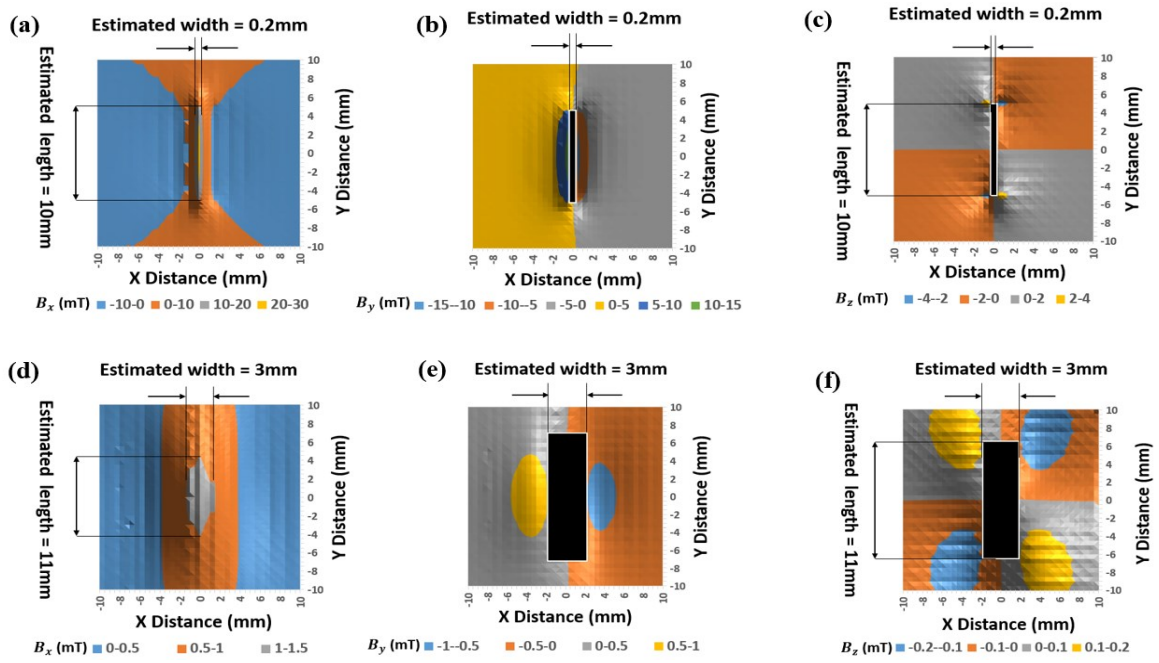

Figure 4.55. The simulated DCMFL differential crack signals; a) $\Delta \boldsymbol{B}_{xb}$ signal for a 4 mm deep surface hairline crack, b) $\Delta \boldsymbol{B}_{yb}$ signal for a 4 mm deep surface hairline crack c) $\Delta \boldsymbol{B}_{zb}$ signal for a 4 mm deep surface hairline crack and d) $\Delta \boldsymbol{B}_{xb}$ signal for a 4 mm deep far-surface hairline crack, e) $\Delta \boldsymbol{B}_{yb}$ signal for a 4 mm deep far-surface hairline crack and f) $\Delta \boldsymbol{B}_{zb}$ signal for a 4 mm deep far-surface hairline crack.

4.5.2) Estimation of the Shape and Size of Hairline Cracks via Experiment

A typical response of the Hall Effect sensor in the axial ($\boldsymbol{B}_x$) direction due to a 4 mm deep surface hairline crack and a 4 mm deep far-surface hairline crack is shown in Fig. 4.56 and Fig. 4.57. Fig. 4.56 is a plot of the measured crack signals ($\boldsymbol{B}_{xb}$) with respect to the sensing path distances, while Fig. 4.57 is a plot of the differential crack signals ($\Delta \boldsymbol{B}_{xb}$). The scanned area represented is a surface of 20 mm × 20 mm, with a constant scan step size of 0.5 mm in the x and y directions. As the rectangular hairline cracks are detected experimentally, the amplitude and distribution pattern of the leakage fields are altered with respect to the shape and size of the cracks. Also, the relationship between the shape/size of the cracks and the resultant leakage signal can be established by analyzing the distribution change of the flux.

Like the simulation results, the broader signal profile observed for the far-surface cracks when compared to a surface crack of the same size, is attributed to the lateral spread of magnetic field at the far-surface crack region. An approximate width and length of 0.8 mm and 12 mm respectively, was estimated for the 4 mm deep surface hairline crack while using the measured crack signal ($\boldsymbol{B}_{xb}$), as shown in Fig. 4.56a. However, for the differential crack signal ($\Delta\boldsymbol{B}_{xb}$), the estimated width and length for the same 4mm deep surface hairline crack is 0.5 mm and 9.75 mm respectively, as shown in Fig. 4.57a. Also, an approximate width and length of 4 mm and 15.5 mm respectively, was estimated for the 4 mm deep far-surface hairline crack while using the measured crack signal, as shown in Fig. 4.56b. However, for the differential crack signal the estimated width and length for the same 4 mm deep far-surface hairline crack is 2.5 mm and 10.75 mm respectively, as shown in Fig. 4.57b. The experimental findings show that the estimation of the size and shape of hairline cracks present on the surface and reverse side of ferromagnetic pipeline structures can be established, using the newly developed DCMFL inspection system.

A comparison of the actual hairline crack dimension (width and length) with that estimated using FEM simulation and practical experiments is displayed in table 4.11. As can be seen, the estimated length and width for the surface and far-surface hairline cracks obtained via simulation is closer to the actual length and width of the inspected hairline cracks when compared to that obtained using practical experiments. This is suspected to be as a result of the 0.1 mm step size used in the simulation compared to the 0.5 mm scan step size used in the experiment, thereby ensuring a better measurement precision (spatial resolution) and accuracy of the data collected from the field probe over the entire simulated area.

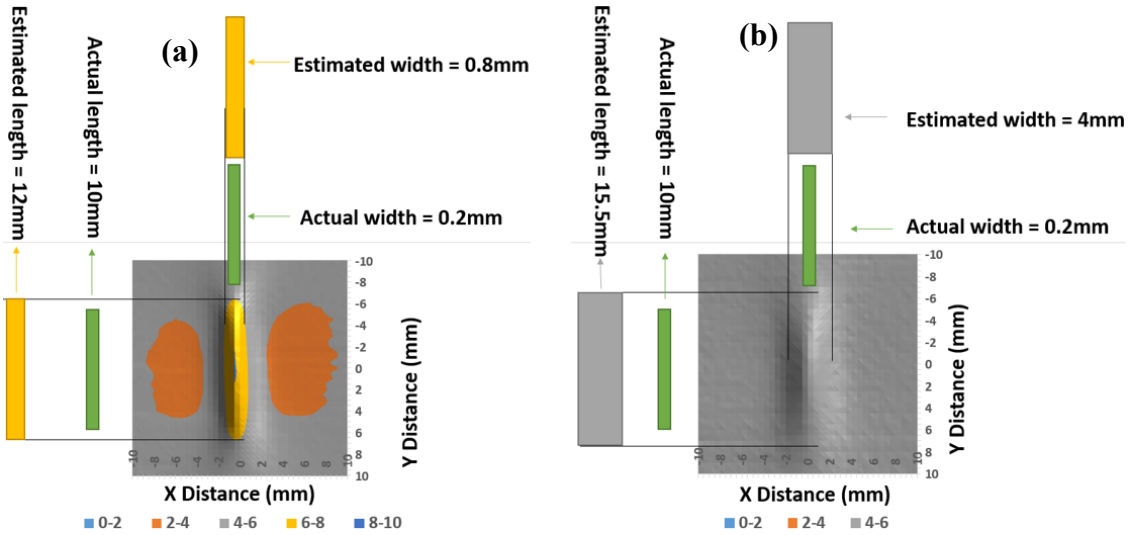

Figure 4.56. The measured DCMFL crack signal ($\boldsymbol{B_{xb}}$) for; a) a 4 mm deep surface hairline crack and b) a 4 mm deep far-surface hairline crack.

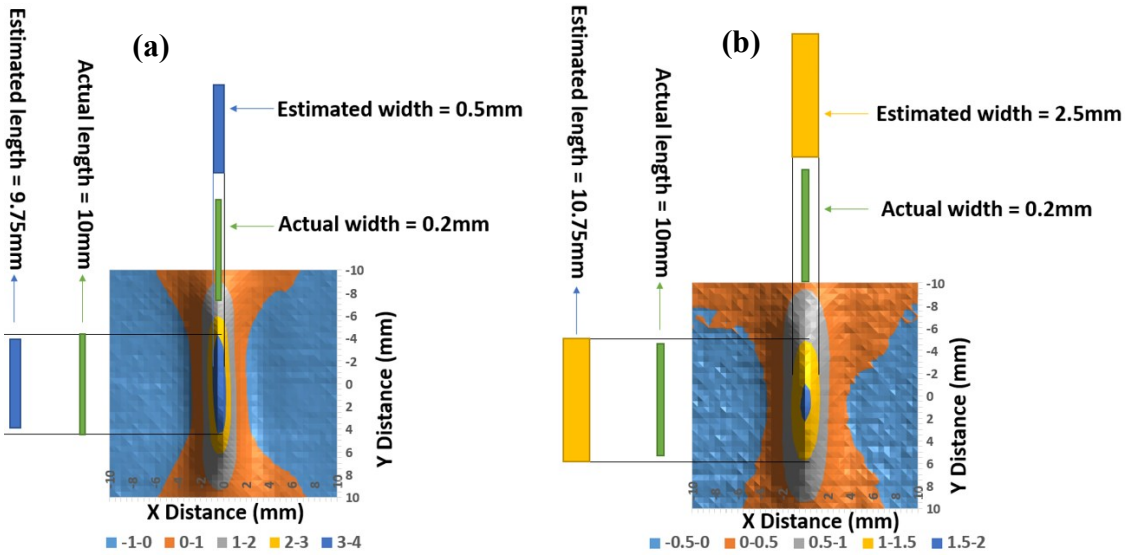

Figure 4.57. The measured DCMFL differential crack signal ($\boldsymbol{\Delta B_{xb}}$) for; a) a 4 mm deep surface hairline crack and b) a 4 mm deep far-surface hairline crack.

Table 4.11. A comparison of the estimated hairline crack dimensions obtained via simulation and practical experiments.

MFL (ΔB_{xb})	**Crack Type**	**Crack Length l (mm)**	**Crack Width w (mm)**	**Crack Depth d (mm)**	**Crack Location h (mm)**
Actual	Surface	10.0	0.2	4.0	0.0
	Far-surface	10.0	0.2	4.0	6.0
Simulated	Surface	10.0	0.2	-	0.0
	Far-surface	11.0	3.0	-	6.0
Measured	Surface	9.75	0.5	-	0.0
	Far-surface	10.75	2.5	-	6.0

4.6) Major Issues of the DCMFL Investigation

According to the simulation results presented in Fig. 4.21a and Fig. 4.21b of section 4.31, the newly developed DCMFL inspection system was not able to separate a 4 mm deep far-surface hairline crack from a 0.2 mm and 0.4 mm deep surface hairline cracks (i.e. unable to discriminate between a shallow surface hairline crack and a deep far-surface hairline crack). Also, the system was not able to detect a 0.2 mm deep (Signal to Noise Ratio (SNR) = 0 dB (sensitivity)) and 0.4 mm deep (SNR = 0 dB (sensitivity)) far-surface hairline cracks, located 9.8 mm and 9.6 mm respectively below the surface of a 10 mm thick plate. Furthermore, based on the experimental result presented in Fig. 4.49 of section 4.4.3.3, there was an overlap in surface and far-surface MFL values, which means that the newly developed DCMFL inspection system is unable to separate surface hairline cracks from far-surface hairline cracks accurately. Moreover, based on the feature extraction investigation for crack shape and size evaluation presented in section 4.5, the simulation and experimental results show that the DCMFL inspection system cannot obtain the approximate depth size

of the inspected surface and far-surface hairline cracks, while using the $\boldsymbol{B_x}$, $\boldsymbol{B_y}$ and $\boldsymbol{B_z}$ leakage field distribution (field profile). This is because the $\boldsymbol{B_x}$, $\boldsymbol{B_y}$ and $\boldsymbol{B_z}$ spread was unaffected by changes in crack depth. Another serious limitation of the proposed DCMFL inspection system is the continuous powering of the excitation coil and yoke (rapid heating), which created the need to cool down the inspection system, especially for longer inspection periods. Hence, the system might not be suitable for inspecting long pipeline structures.

4.7) Chapter Summary

In this chapter, a well-optimized and efficient DCMFL inspection system for industrial steel pipeline inspection based on axial magnetization method has been developed, for detecting and characterizing hairline cracks that are too difficult to be detected using the existing MFL techniques. The magnitude of the leakage field required to accurately detect and characterize both surface and far-surface hairline cracks has been identified, while using the FEM numerical modelling technique. First, the 3D FEM model was used to optimize the magnetization and sensing methodologies, in order to improve the detection sensitivity and testing accuracy of the MFL technique. The simulated results show that the test sample is adequately magnetized when a direct excitation current of 4 A is used. Also, the simulated results show that the investigated surface and far-surface hairline cracks can generate sufficient leakage field to be detected when the excitation yoke is about 80 mm high, 30 mm long, 60 mm wide, and with a leg spacing of 240 mm. The modelled DCMFL system was able to discriminate the various hairline cracks inspected according to their depth sizes, by just using the peak amplitude of the leakage field signal. Also, the system was able to discriminate the various hairline cracks according to their various locations within the test sample (i.e. separate surface cracks from far-surface cracks), except for the 4 mm deep far-surface hairline crack, which provides a signal greater than the 0.2 mm and 0.4 mm deep surface hairline cracks.

The satisfactory performance of the FEM optimized DCMFL measurement tool in detecting hairline cracks, both on the surface and reverse side of the test sample has

been verified via practical experiments. This was done using a 10 mm and 6 mm thick low carbon steel plates, with well-defined EDM hairline slots on the surface and on the reverse side of the test plates. The experimental results showed good agreement with the simulated ones (i.e. measured results are within 10 % of the simulated result). Also, the experimental findings showed that the leakage field signal generated by the 0.2 mm deep, 0.2 mm wide and 10 mm long surface hairline crack (SNR = 0.20 dB (sensitivity)) is detectable, while using a 10 mm thick plate. However, the newly developed experimental DCMFL inspection system struggled in detecting the MFL signal caused by a 0.2 mm deep (SNR = 0 dB (sensitivity)) and 0.4 mm deep (SNR = 0 dB (sensitivity)) far-surface hairline cracks, located 9.8 mm and 9.6 mm respectively below the surface of the same 10 mm thick plate. The farthest far-surface hairline crack that could be detected was a 0.6 mm deep hairline crack, located 9.4 mm below the surface of a 10 mm thick plate. Nevertheless, the system was able to detect and characterize all the surface and far-surface hairline cracks investigated based on their depth sizes, while using a 6 mm thick plate. Moreover, there was an overlap in surface and far-surface values. Therefore, discrimination between the surface and far-surface cracks will be difficult while using just the leakage field amplitude, except for surface hairline cracks with depth greater than 2 mm.

The leakage field signal was strongly determined by the crack depth, a slight variation in the depth size of the hairline crack causes a significant variation in both the simulated and measured MFL values. The MFL sensor used was able to detect both the 4 mm deep surface hairline crack and the 4 mm deep far-surface hairline crack at 5 mm lift-off. This shows that the newly developed system would be very effective and beneficial in applications where large lift-off distances are required. Furthermore, the information acquired from the simulation and experimental investigations shows that; with proper analysis of the imaged leakage field distribution in the $\boldsymbol{B_x}$, $\boldsymbol{B_y}$ and $\boldsymbol{B_z}$ directions, additional useful information that can be used to obtain the shape and approximate size (width and length) of the various hairline cracks present in steel pipelines can be established. However, it was not possible to obtain the approximate depth of the inspected hairline cracks, by just using the information contained in the imaged leakage field distribution (i.e. using the $\boldsymbol{B_x}$, $\boldsymbol{B_y}$ and $\boldsymbol{B_z}$ spread). As reported in section 4.4.3.1, the maximum percentage

error (repeatability) recorded for the surface and far-surface measurements while using the newly developed DCMFL inspection system were 0.9 % and 0.23 % (repeatability) respectively.

A major disadvantage of the newly developed DCMLF measurement system is the continuous powering of the excitation yoke and the excitation coil (overheating), thereby, creating the need to cool down the excitation coil, especially for longer inspection periods (not suitable for inspecting long pipelines). The selected technique to solve the problem of continuous powering and overheating of the excitation coil will be introduced in the next chapter.

4.8) References

1) M. Yilai, R. He, and J. Chen, "A Method for Improving SNR of Drill Pipe Leakage Flux Testing Signals by Means of Magnetic Concentrating Effect". *IEEE Transactions on Magnetics,* 51(9), 1-7, (2015).
2) W. Walters and D. Steely, "Using Magnetic Flux Density to Identify Anomalies in Pipe Wall Thickness". (2010). [Online]. Available at: http://www.pipeinspectionequipment.com. [Accessed 21 Aug. 2017].
3) S. Xiao-Chun, H. Song-ling and Z. Wei, "Optimisation of the Magnetic Circuit in the MFL Inspection System for Storage Tank Floors". *Russian Journal of Non-destructive Testing*, 43 (5), 326-331, (2007).
4) W. S. Singh et al, "Finite element Model-Based Approach for Magnetic Flux Leakage Testing of Steel Plates using 2D Tandem GMR Array Sensors". *Insight-Non-Destructive Testing and Condition Monitoring,* 56, 683-690, (2014).
5) E. Norouzi and H. Ravanbod, "Optimisation of the Flux Distribution in Magnetic Flux Leakage Testing". *Insight*, 51 (10), 563-567, (2009).
6) A. Simm, "Quantitative Interpretation of Magnetic Field Measurements in Eddy Current Defect Detection". In *Electrical, Electronic and Computer Engineering*. Volume, *PhD Newcastle upon Tyne: Newcastle University*, (2012).
7) W. Gospel et al, "Sensors a Compréhensive Survey". *In: Boll, R and Overshot, K.J. eds*. *Magnetic sensors*. New York, VCH Publishers Inc. 4-9, (1989).
8) Felix Kress University of St Andrews, "Using the Sentron Angle Sensor, Linear 2-Axis Hall IC, 2SA-10G probe to check the alignment of a magnetic field". [Online]. Available at:https://eddata.fnal.gov/lasso/summerstudents/papers/2013/Felix-Kress2.pdf. [Accessed 20 Aug. 2016].
9) E. Dennison, "On-Axis Field of a Finite, Straight, Thin Solenoid". [Online]. Available at:http://nbviewer.jupyter.org/github/tiggerntatie/emagnet-py/blob/master/solenoids/thin_solenoid.ipynb. [Accessed 20 Aug. 2016].
10) R. T. Keshwani, "Analysis of Magnetic Flux Leakage Signals of Instrumented Pipeline Inspection Gauge Using Finite Element Method". *IETE Journal of Research,* 55(2), 73-82, (2009).

Chapter 5: PMFL Technique for Hairline Crack Detection and Characterization

5.1) Introduction

This chapter explores the use of PMFL inspection technique for enhanced visualization and 3D imaging of the resultant leakage field distribution due to hairline cracks. The research started by investigating the influence of excitation period variation on the detection sensitivity and characterization of various surface and far-surface hairline cracks, located at various depths in a low carbon steel plate. First, FEM numerical simulation with different excitation pulse periods of constant duty cycle was implemented, in order to visualize the influence of excitation period variation on the time and frequency dependent amplitude in the spectrum analysis, followed by an experimental validation of the FEM results. By analyzing the results obtained, a satisfactory excitation pulse period was identified.

Also, the influence of pulse width variation on the detection sensitivity and characterization of surface and far-surface hairline cracks is explored. The investigation was first carried out using the FEM simulation approach, supported with practical experiments. The information acquired was used to establish a suitable pulse width for an enhanced hairline crack detection, at various depth locations in the test plate.

Subsequently, the investigation advances to the use of the PMFL inspection technique employing the best excitation period and pulse width for detecting and characterizing both surface and far-surface hairline cracks. The PMFL inspection technique provides an alternative and better approach for the detection and characterization of hairline cracks, compared to the DCMFL technique. This is because; the pulsed method used in this case means a significant reduction in the power consumption and thermal effects, compared with the constant powering of the excitation yoke and coil (DCMFL). Hence, eliminating the need to cool the inspection system for longer inspection periods. Moreover, by using the PMFL approach, more information needed for crack characterization can be obtained, that

is; using the features embedded in the time and frequency domain spectrum, which is not available with the DCMFL approach.

5.2) PMFL Crack Detection at Different Depth Locations

When estimating the service life span of ferromagnetic steel structures, precise damage tolerance calculations should be performed with respect to the size and position of discontinuities, especially how they grow over time. This is most applicable in pipelines that are usually manufactured with low carbon steel materials of variable thicknesses. For instance, in the illustration of cracks that exist far below the pipe surface, the penetration depth of the induced magnetic field should be large enough to provide a comprehensive crack detection and characterization. The excitation frequency ($\frac{1}{T}$) required to penetrate the pipeline material can be determined using the skin depth (δ_o) formula as expressed in equation (5.1), that is; the depth below the surface of a conductive sample at which the current density (**J**) has reduced to 1/e, which is about 37% of the current density at the surface ($\boldsymbol{J_s}$).

$$\delta_o = \sqrt{\frac{2}{w\mu\sigma}} \tag{5.1}$$

Here, σ is the electrical conductivity (S/m) of the material used, $\omega = 2\pi f$ is the angular frequency and f is the operating frequency

The PMFL method can provide more information needed for defect depth characterization through time and frequency domain analysis of the leakage field signal, and can be used to determine the size, shape and location of both surface and far-surface defects using the amplitude and distribution pattern of the resultant leakage field. Hence, it provides an added advantage over the traditional MFL methods. Also, with a good signal processing technique and data analysis, further information such as the defect profile can be ascertained. The PMFL probe is operated using pulsed current or voltage as the excitation signal, while the rich frequency components generates information from various depths due to skin effect.

The PMFL inspection technique also possesses a satisfactory penetration depth. Thus, useful information regarding any existing crack in a pipeline structure can be retrieved, because of the low frequency component present in the pulse spectrum. The time and frequency spectrum present in the PMFL signal is dependent on the excitation period and pulse width of the waveform. A typical PMFL excitation pulse waveform is illustrated in Fig. 5.1. The induced magnetic field in the test sample is directly proportional to the applied current, for a current driven excitation system. The PMFL excitation signal contains a range of frequency components that deliver the deeper penetration depth of low frequency excitation and the sensitivity to surface measurements of high-frequency excitation [1]. This makes the PMFL method more flexibility for hairline crack detection and characterization. This research aims at using these rich frequency components to separate hairline cracks located at the sample surface from those located far below the surface. The excitation pulse period and pulse width variation methodology employed in this work extends the earlier research performed using the PMFL method, by identifying and using the best excitation period and pulse width. Thus, providing a suitable magnetic field penetration, for an improved detection and characterization of the surface and far-surface hairline cracks.

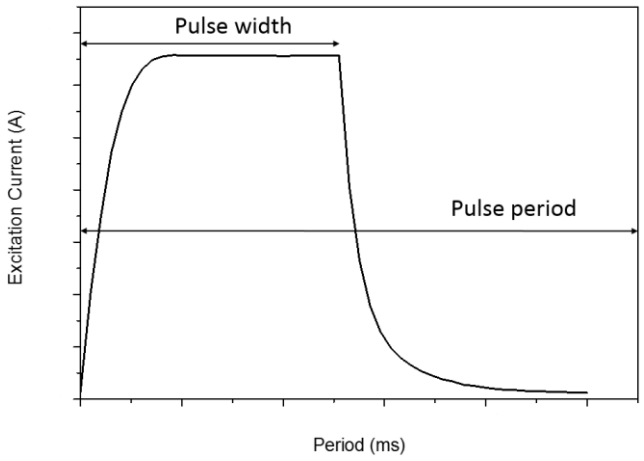

Figure 5.1. A typical PMFL excitation pulse waveform.

5.3) PMFL Investigation via FEM Numerical Computation

PMFL numerical simulations with variable excitation period of constant duty cycle and variable pulse width of constant excitation period are implemented, in order to determine the effect of excitation period and pulse width variations on the magnetic field distribution, which affects the detection sensitivity to surface and far-surface hairline cracks. The excitation period and pulse width variation causes a difference in the frequency spectra, giving more comprehensive information from the frequency broadband harmonics, compared to the information obtainable from a single excitation process (DCMFL).

Fig. 5.2 shows the PMFL inspection probe system used for the FEM investigation. The probe system was modelled as a full model and solved as a 3D transient problem in the MagNet 7.6 software by Infolytica, in order to obtain a better description of the problem. The capability of the modelled PMFL probe system in detecting and characterizing both surface and far-surface hairline cracks, with different depth sizes in a 10 mm thick plate has been assessed. Seven samples with surface hairline cracks of varying depth sizes (d = 0.2, 0.4, 0.6, 0.8, 1, 2, and 4 mm), and seven samples with far-surface hairline cracks of varying depth sizes (d = 0.2, 0.4, 0.6, 0.8, 1, 2, and 4 mm) were simulated. Moreover, these hairline cracks were used to simulate different locations of cracks inside the test plate for different depths of penetration provided by various excitation periods and pulse widths. Boundary conditions are utilized and set in a region larger than the region of interest in order not to affect the result. The model was divided into a mesh of tetrahedral shaped elements. Like the DCMFL simulation model, a smaller mesh size of 0.02 mm is used at the region of interest (crack region) in order to achieve more accurate results, since the quality of the mesh is improved in the region with rapidly changing magnetic field. The cracks were positioned at the 0 mm mark (centre of plate) and were perpendicular to the applied magnetic field orientation. All the cracks investigated had a constant width and length of 0.2 mm and 10 mm respectively. The dimensions of the test plates used is 350 mm × 60 mm × 10 mm with a conductivity of 1.32×10^6 S/m. A silicon steel material is used for the excitation yoke with a leg height of 80 mm, leg length of 30 mm, leg width of 60 mm, leg spacing of 240 mm and a conductivity of 2.17×10^6

S/m. The yoke was modelled with 300 turns of copper coils with a diameter of 0.5 mm and conductivity of 1.12×10^7 S/m. This set-up was used to predict the axial ($\boldsymbol{B_x}$) components of the leakage field, for both surface and far-surface hairline cracks. The computational time for each of the simulated models took about 25 minutes in a dual-core 64-bit processor workstation with 24 GB primary memory.

This current research utilizes the benefits offered by the PMFL technique to characterize hairline cracks based on their depth sizes and location within the test sample, with a direct application to pipelines used in the oil, gas and petrochemical industries.

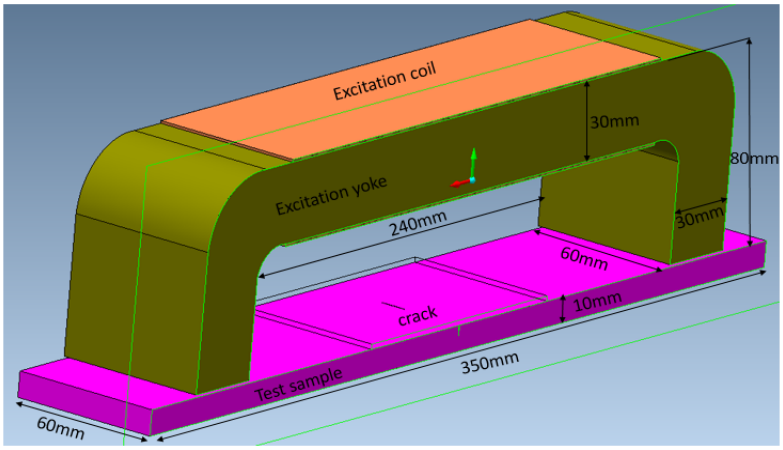

Figure 5.2. The 3D FEM schematic layout of the PMFL inspection probe set-up with dimensions, alongside a defective test plate.

The FEM investigation was performed prior to the experimental investigation, so as to obtain the responses of the PMFL inspection probe in the time and frequency domain. Analyzing the resultant responses will enable a suitable excitation pulse period and pulse width to be identified, based on the required penetration depth to ensure an effective detection and characterization of both surface and far-surface hairline cracks.

5.3.1) Spectrum Analysis and Modelling Results

The schematic layout of the excitation coil, excitation yoke and a non-defective plate, modelled as a full model and solved as a 3D transient problem is shown in Fig. 5.3. To ensure that the simulated responses are not affected by the presence of a crack, the transient response when the field probe is situated directly above a non-defective plate, with a lift-off of 0.5 mm is acquired as shown in Fig. 5.3. This will also act as a reference response in subsequent investigations.

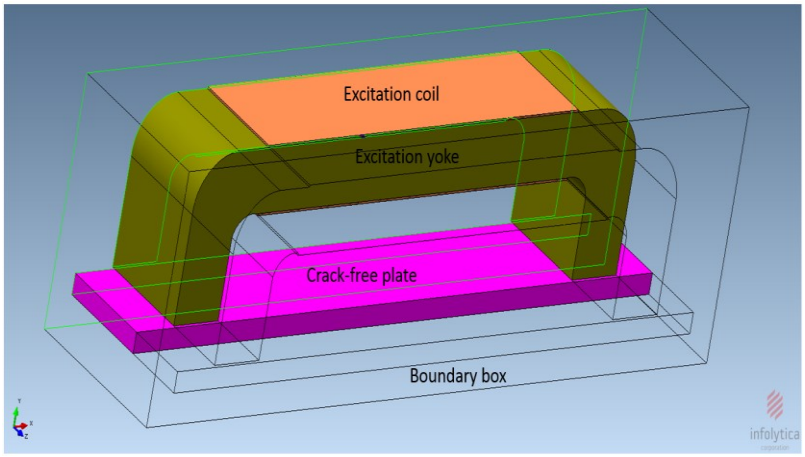

Figure 5.3. The 3D FEM schematic layout of the PMFL measurement probe system above a non-defective test plate.

5.3.1.1) Effect of Excitation Period Variation on Hairline Crack Detection

The influence of excitation pulse period variation on the detectability and characterization of both surface and far-surface hairline cracks is investigated in this section. Here, the excitation coil is driven with a square waveform with; 4 V amplitude voltage, 50 % duty cycle, 10 ns rise time and 10 ns fall time. Six different excitation periods were investigated; 1 ms, 5 ms, 10 ms, 20 ms 100 ms and 500 ms excitation periods. The transient responses were obtained when the field probe is directly above a hairline crack, with a lift-off of 0.5 mm. Multiple load steps were used in the 3D transient solver to ensure accurate simulated results.

The simulated transient responses (time domain representation) from a non-defective plate (reference signals), for; 1 ms, 5 ms, 10 ms, 20 ms, 100 ms and 500 ms excitation periods of constant duty cycle (50 %) are shown in Fig. 5.4. These responses are as a result of the interaction between the induced magnetic field and the secondary magnetic field from the induced eddy current in the conductive sample.

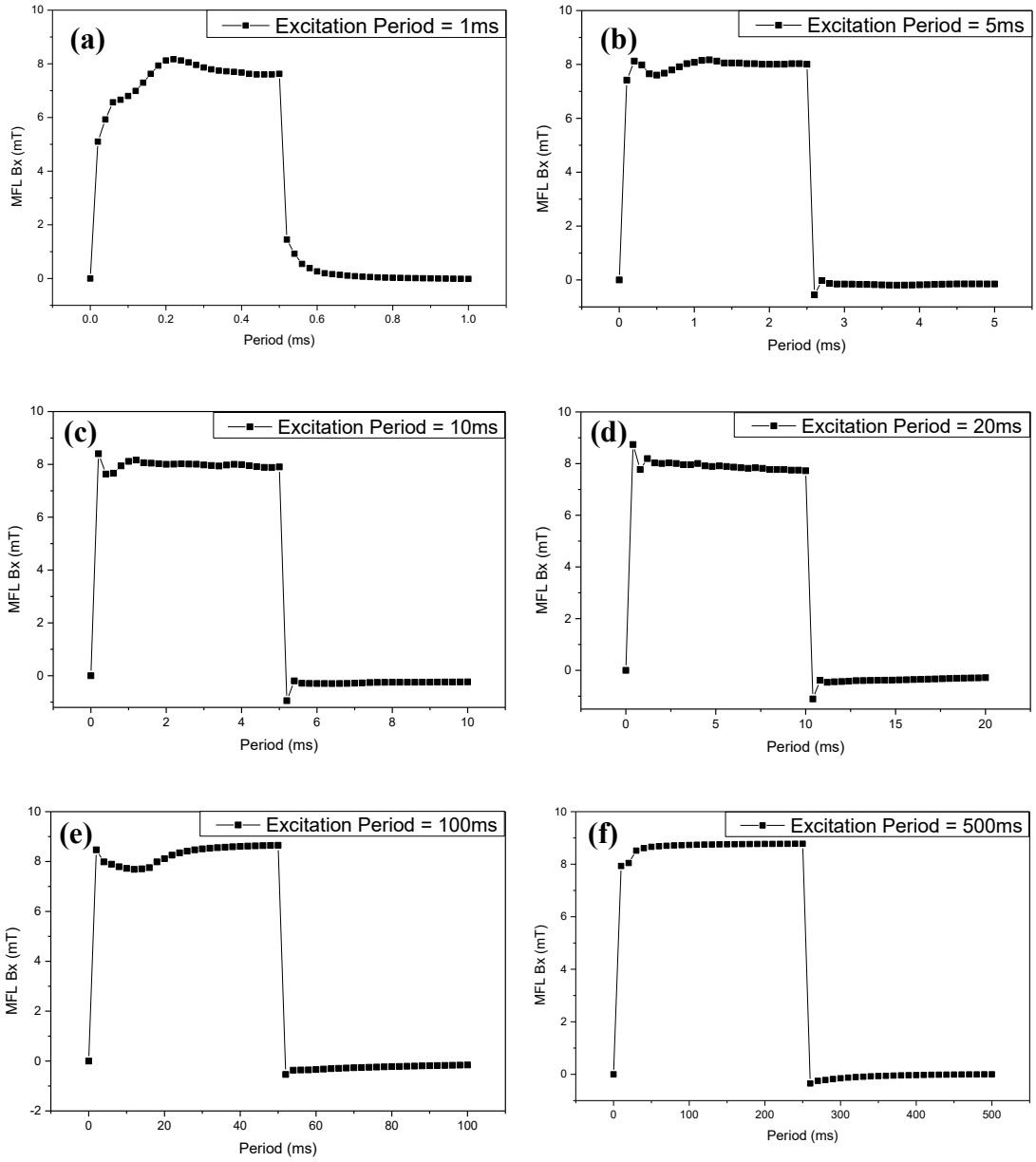

Figure 5.4. Time domain representation – The simulated leakage field ($\boldsymbol{B_{xb_0}}$) signal from a non-defective plate, at different excitation periods of constant 50 % duty cycle; a) 1 ms excitation period, b) 5 ms excitation period, c) 10 ms excitation period, d) 20 ms excitation period, e) 100 ms excitation period and f) 500 ms excitation period.

The difference in the leakage field magnitude generated when there is no crack in the test sample (b_0) is relatively small compared to when there is a crack (b), especially for cracks with very small depth and width sizes (i.e. d = 0.2 mm, and w = 0.2 mm). Therefore, to visualize the slight change in the leakage field magnitude due to the presence of a hairline crack, the leakage field signal with no crack ($\boldsymbol{B}_{b_0}$) is subtracted from that with a crack ($\boldsymbol{B}_b$) to obtain the differential leakage field signal ($\Delta\boldsymbol{B}_b$).

The effect of excitation period variation on the detectability and characterization of the simulated hairline cracks is clearly illustrated in Fig. 5.5. It compares the differential leakage field amplitude ($\Delta\boldsymbol{B}_{xb}$) obtained for both surface (see Fig. 5.5a) and far-surface (see Fig. 5.5b) hairline cracks as a function of crack depth, for different excitation periods of constant duty cycle (50 %). As can be seen from Fig. 5.5a, the modelled PMFL inspection system was able to detect and separate all the surface hairline cracks simulated based on their respective depth sizes using the $\Delta\boldsymbol{B}_{xb}$ amplitude, for all the six excitation periods investigated. The information displayed in Fig. 5.5b show that the 1 ms, 5 ms, 10 ms and 20 ms excitation periods were not able to separate all the far-surface hairline cracks simulated with respect to their depth sizes, although the 20 ms excitation period was able to detect and distinguish between just the 2 mm and 4 mm deep far-surface hairline cracks. However, increasing the excitation pulse period to 100 ms and 500 ms provides a better detection and characterization of all the various far-surface hairline cracks simulated. The differential leakage field amplitudes ($\Delta\boldsymbol{B}_{xb}$) represented in Fig. 5.5a and Fig. 5.5b were collected at $t = 0.5$ ms, 2.5 ms, 5 ms, 10 ms, 20 ms and 20 ms (before steady state) for the 1 ms, 5 ms, 10 ms, 20 ms, 100 ms and 500 ms excitation periods respectively as shown in Fig. A.2 and Fig. A.3 in appendices A.

The use of high excitation frequencies, which corresponds to shorter excitation periods: 1 ms, 5 ms, 10 ms and 20 ms means more magnetic field concentration at the surface layer of the test plate, while the use of low excitation frequencies, which corresponds to longer excitation periods: 100 ms and 500 ms provides higher penetration depth of the induced magnetic field, while still maintaining a good sensitivity to surface measurements. This explains why the 100 ms and 500 ms excitation periods were able to detect and distinguish between both the surface and

far-surface hairlines cracks simulated, while the 1 ms, 5 ms 10 ms and 20 ms excitation periods were only suitable for detecting and characterizing the surface hairline cracks.

In order to reduce the power consumption level as well as to prevent the excitation coils from getting overheated for longer inspection periods (e.g. inspecting long pipelines), an excitation period of 500 ms was preferred over much longer excitation periods.

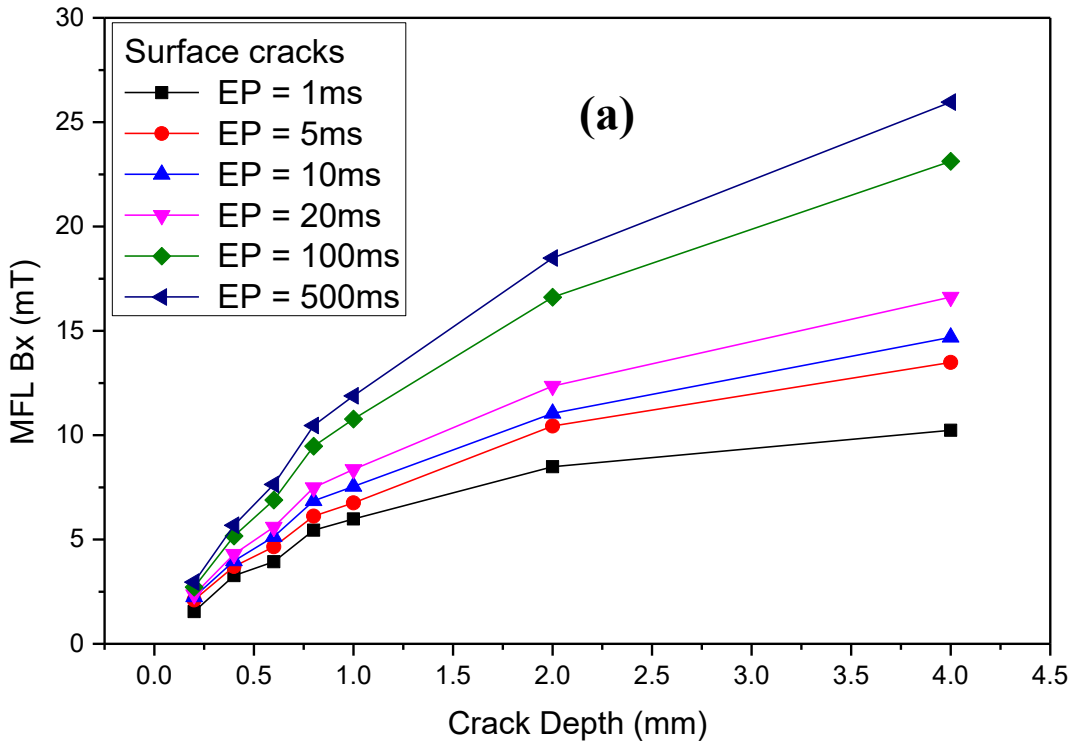

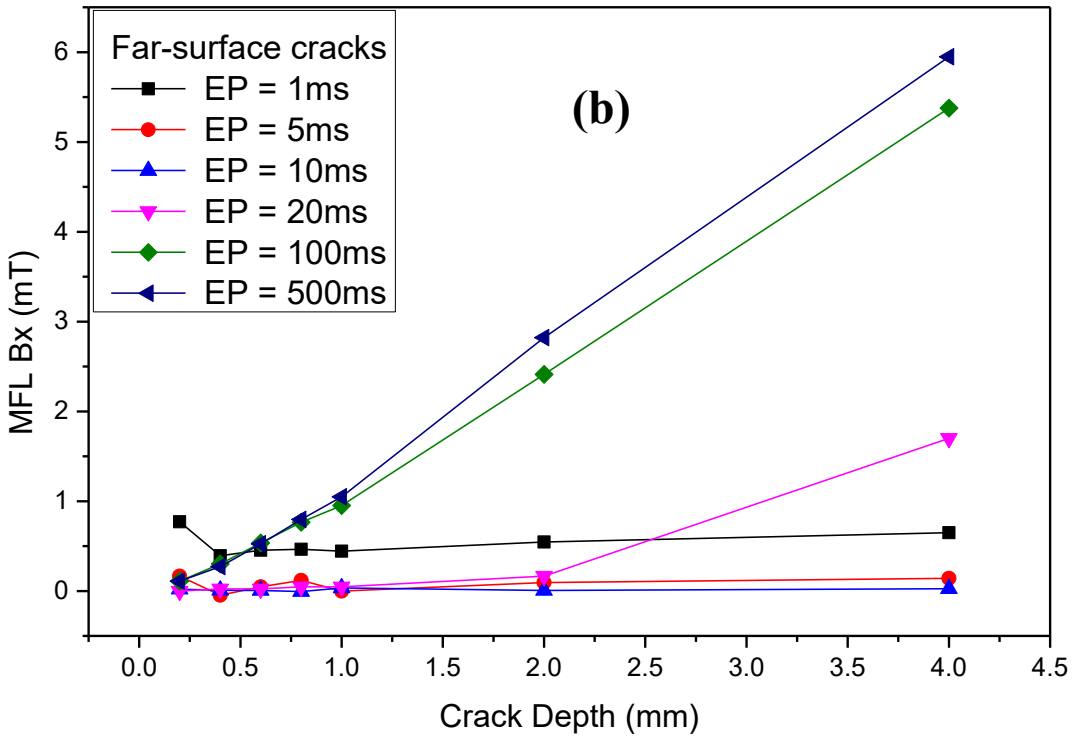

Figure 5.5. A plot of the simulated differential leakage field amplitude ($\Delta \boldsymbol{B}_{xb}$) as a function of crack depth, comparing the effect of different excitation periods on the detectability and characterization of; a) Surface hairline cracks and b) Far-surface hairline cracks.

5.3.1.2) Effect of Pulse Width Variation on Hairline Crack Detection

In this section, the influence of pulse width variation on the magnetic field distribution, which affects the detection sensitivity of the PMFL sensor to various surface and far-surface hairline cracks is explored. Here, the excitation coil is driven with a square waveform with; 4 V amplitude voltage, 500 ms pulse period, 10 ns rise and 10 ns fall time. Six different pulse widths were investigated; 5 ms, 10 ms, 25 ms, 50 ms, 100 ms and 250 ms pulse widths corresponding to; 1 %, 2 %, 5 %, 10 %, 20 %, and 50 % duty cycles.

The simulated transient responses (time domain representation) from a non-defective plate (reference signals), for; 5 ms, 10 ms, 25 ms, 50 ms, 100 ms and 250 ms pulse widths of constant excitation period (500 ms) are displayed in Fig. 5.6. It shows the simulated magnetic flux leakage in the non-defective plate, illustrating the variation

in signal profile as the pulse width is varied between 1 ms and 250 ms. These responses are caused by the interaction between the induced magnetic field and the secondary magnetic field from the induced eddy current in the test plate. The plot also show that the leakage field ($\boldsymbol{B_{xb_0}}$) reaches its peak amplitude (steady state) at 50 ms, corresponding to 10 % duty cycle.

The pulsed signal used in PMFL inspection varies with time, with higher frequency components at the beginning of the pulse waveform, which decreases as time progresses. The PMFL signal induced towards the end of the excitation pulse are more sensitive to cracks located further below the sample surface (far-surface crack), while those at the start of the excitation pulse will be more sensitive to surface cracks. Moreover, the sensitivity of the PMFL inspection probe is highly dependent on the penetration depth of the opposing eddy currents induced by the changing magnetic field, which is inversely proportional to the square root of the frequency. Also, the penetration depth of the induced magnetic field increases with decreasing frequency, decreasing magnetic permeability and decreasing electrical conductivity. The standard depth of penetration (δ_{ec}) refers to the depth at which the eddy current density has decreased to 1/e, which is about 37 % of the surface density. The term 'standard' refers to the plane wave electromagnetic field excitation inside the test sample. Despite the fact that eddy currents penetrate deeper than one standard depth of penetration, it decreases rapidly with increasing depth within a sample. A lot of relevance is attached to the crack depth relationship with skin depth (δ). However, since the formula for skin depth (see equation (5.1) only applies to a completely flat and non-defective sample, thus, this relationship can only give a rough estimate when considering defective samples.

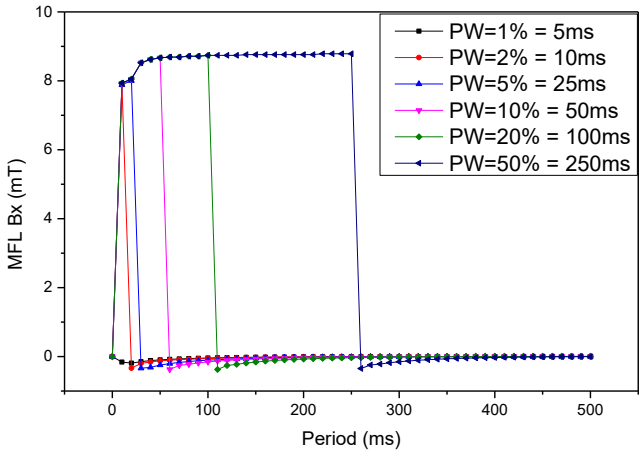

Figure 5.6. Time domain representation - The simulated leakage field ($\boldsymbol{B_{xb_0}}$) signal for a non-defective test plate at different pulse widths of constant excitation period of 500 ms.

By implementing a Fourier transformation, the pulse signal obtained in time domain (see Fig. 5.6) can be represented in the frequency spectrum distribution form, which displays the amplitude (magnitude) variation with frequency as presented in Fig. 5.7. By critically analyzing the simulated frequency spectrum distribution under various pulse widths, the various depth responses that are associated with the eddy current skin effect phenomenon can be acquired.

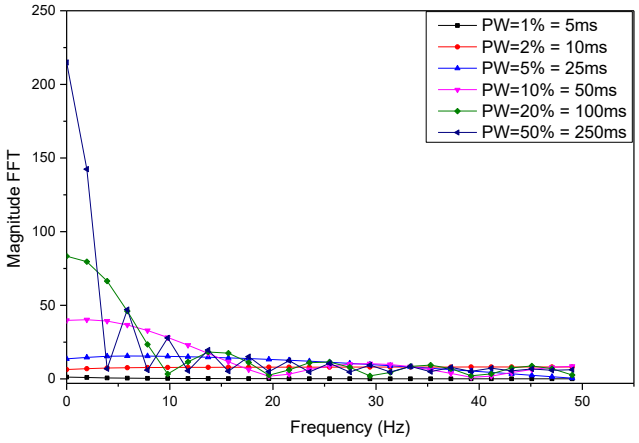

Figure 5.7. Frequency-domain representation - The simulated spectrum distribution of the PMFL signal for a non-defective sample under different pulse widths, demonstrating the change in signal amplitude.

According to the simulated frequency spectrum distribution plot displayed in Fig. 5.7, it can be seen that wider pulse widths: 100 ms and 250 ms are richer than the

narrower pulse widths: 5 ms, 10 ms, 25 ms and 50 ms in the low frequency region, hence, providing a deeper magnetic field penetration, which is suitable for both surface and far-surface hairline crack detection and characterization. However, as the pulse width shortens, the high frequency component dominates, thus, the induced magnetic field in the test plate becomes more concentrated at the surface layer. Since, the excitation frequency used determines the depth of penetration of the induced magnetic field in the test plate, the resultant responses are expected to point out the magnetic field interactions with cracks located at various depths in the test plate. In addition, this will indicate the maximum depth covered by the frequency spectrum for a particular pulse width excitation. The output can be employed in practical application for crack depth characterization and quantification.

The effect of pulse width variation on the detectability and characterization of the simulated hairline cracks is clearly illustrated in Fig. 5.8. It shows a plot which compares the $\Delta \boldsymbol{B}_{xb}$ amplitude obtained for both surface (see Fig. 5.8a) and far-surface (see Fig. 5.8b) hairline cracks as a function of crack depth, for different pulse widths of constant excitation period (500 ms). As can be observed from Fig. 5.8a, the modelled PMFL inspection system was able to detect and separate all the surface hairline cracks simulated based on their respective depth sizes, for all the pulse widths investigated. The information displayed in Fig. 5.8b show that the 5 ms and 10 ms pulse widths were not able to separate all the far-surface hairline cracks according to their depth sizes, although the 10 ms pulse width was able to detect and distinguish between just the 2 mm and 4 mm deep far-surface hairline cracks. However, increasing the pulse width to 25 ms, 50 ms, 100ms and 250 ms provides a better detection and characterization of all the various far-surface hairline cracks simulated. This proves that the induced magnetic fields at the start of the pulse waveform are predominantly composed of high frequency components which corresponds to surface features, while those towards the end of the excitation pulse are mostly made up of low frequency components which corresponds to both surface and far-surface features, for a given ferromagnetic steel pipeline. The differential leakage field amplitudes ($\Delta \boldsymbol{B}_{xb}$) represented in Fig. 5.8a and Fig. 5.8b were collected at $t =$ 5 ms, 10 ms, 25 ms, 20 ms, 20 ms and 20 ms (before steady state) for the 5 ms, 10 ms, 25 ms, 50 ms, 100 ms and 250 ms pulse widths respectively as shown in Fig. A.4 and Fig. A.5 in appendices A.

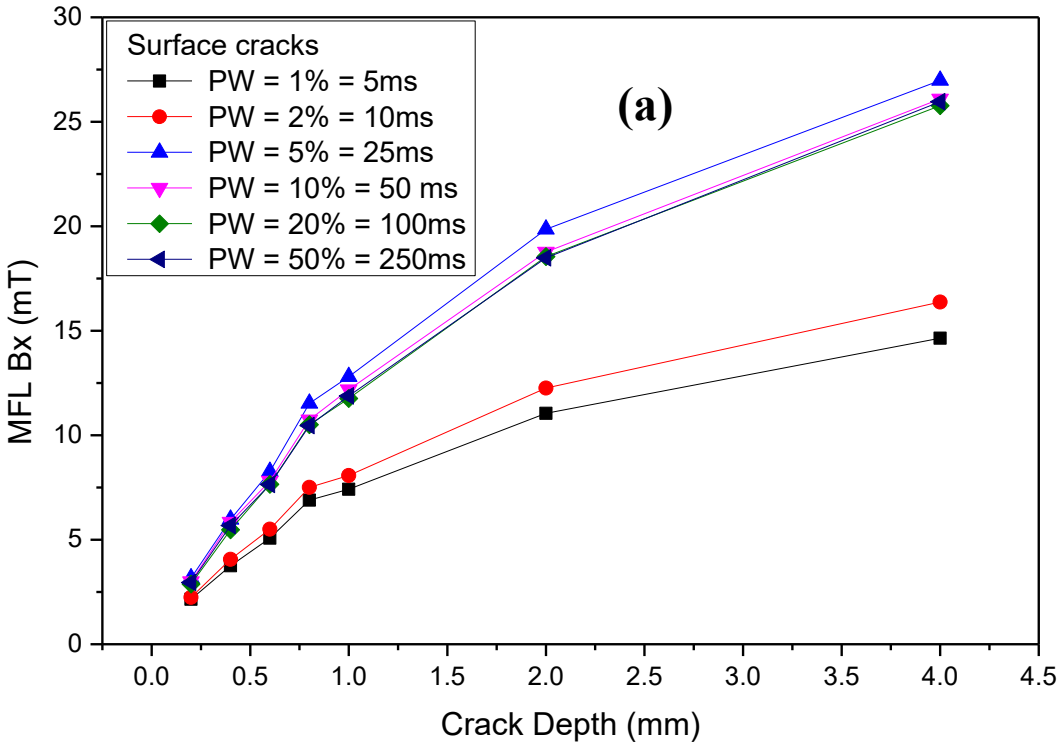

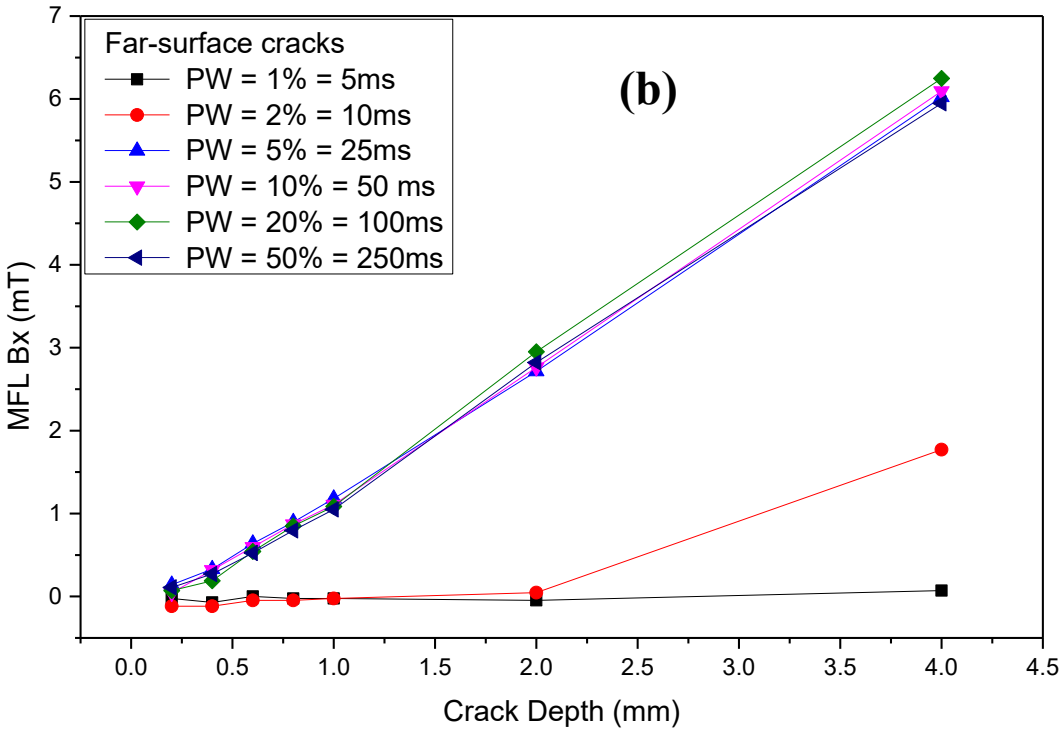

Figure 5.8. A plot of the simulated differential leakage field amplitude ($\Delta \boldsymbol{B}_{xb}$) as a function of crack depth, comparing the effect of different pulse widths on the detectability and characterization of; a) Surface hairline cracks and b) Far-surface hairline cracks.

5.3.1.3) Feature Extraction in Time Domain

At different times in the PMFL excitation cycle, the induced magnetic field possesses different frequency components, which corresponds to different depths of penetration of the induced field at various points in the cycle. This relationship will be employed in this section, in order to separate various hairline cracks located at different depths in the test plate.

The analysis of the data obtained using the PMFL method of NDE is usually implemented using the time domain representation. Here, the PMFL system response obtained from a non-defective plate is taken as the reference signal. There are three different types of typical PMFL response signals, these are; the reference signal, surface crack signal and the far-surface crack signal. With respect to the principle of PMFL testing as well as the crack response signals containing different crack information, various crack features embedded in the time domain spectrum are extracted as follows:

a) ***Amplitude Analysis of the Simulated PMFL Signal***

The peak amplitude of the differential PMFL signal ($\Delta \boldsymbol{B}_{\boldsymbol{xb}}^{\boldsymbol{Peak}}$) comparing both surface and far-surface hairline cracks, as a function of crack depth is shown in Fig 5.9a (25 ms pulse width) and Fig. 5.9b (250 ms pulse width). It can be seen from both plots that the presence of either a surface or far-surface hairline crack causes a significant variation in the $\Delta \boldsymbol{B}_{\boldsymbol{xb}}^{\boldsymbol{Peak}}$ amplitude. The $\Delta \boldsymbol{B}_{\boldsymbol{xb}}^{\boldsymbol{Peak}}$ amplitude increases with increasing surface and far-surface crack depth. Moreover, the overall signal level for the far-surface cracks is far lower when compared to an equivalent surface crack. This is due to an increased distance between the sensing probe and the crack location, thus, resulting in the attenuation of the leakage field signal acquired from the far-surface cracks. It is observable from both plots that the PMFL system can discriminate the various hairline cracks inspected according to their depth sizes, by just using the peak amplitude of the differential leakage field signal. Also, it can be seen from the plots that the system can separate the various hairline cracks according to their various locations within the test sample (i.e. separate surface cracks from far-

surface cracks), except for the 4 mm ($\Delta \boldsymbol{B}_{\boldsymbol{xb}}^{\boldsymbol{Peak}} = 6.31$ mT) deep far-surface hairline crack which provides a signal greater than the 0.2 mm ($\Delta \boldsymbol{B}_{\boldsymbol{xb}}^{\boldsymbol{Peak}} = 3.16$ mT) and 0.4 mm ($\Delta \boldsymbol{B}_{\boldsymbol{xb}}^{\boldsymbol{Peak}} = 6.0$ mT) deep surface hairline cracks. The optimized PMFL inspection system modelled in MagNet was able to detect as small as a 0.2 mm deep surface hairline crack and a 0.2 mm deep far-surface hairline crack, located 9.8 mm below the plate surface. The $\Delta \boldsymbol{B}_{\boldsymbol{xb}}^{\boldsymbol{Peak}}$ values for all the surface and far-surface hairline cracks simulated are presented in table 5.1.

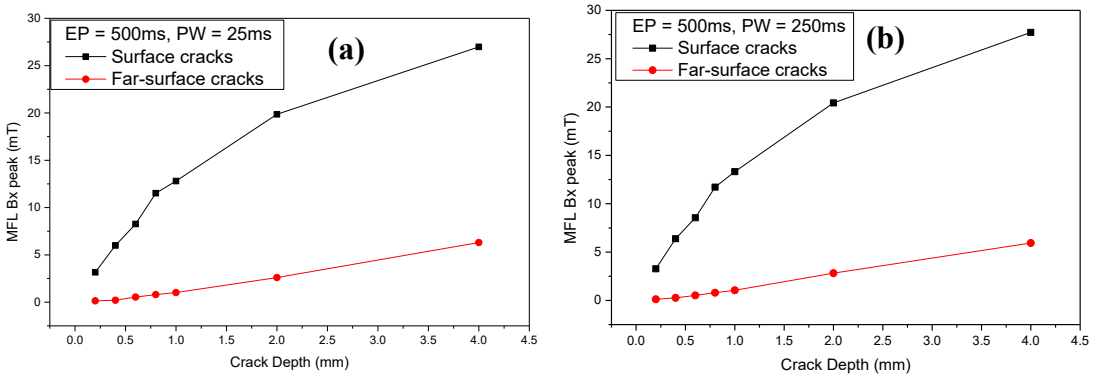

Figure 5.9. Time domain representation – A plot showing the simulated differential leakage field signal peak amplitude ($\Delta \boldsymbol{B}_{\boldsymbol{xb}}^{\boldsymbol{Peak}}$) as a function of crack depth, for both surface and far-surface hairline cracks; a) 25 ms (5%) pulse width and b) 250 ms (50 %) pulse width.

b) *Time to Peak Analysis of the Simulated PMFL Signal*

The time to peak in the PMFL inspection technique indicates the time it takes the leakage field signal to reach its peak amplitude, corresponding to a particular crack information. A comparison between the response signals obtained from; a non-defective plate, a 4 mm deep surface hairline crack and a 4 mm deep far-surface hairline crack is presented in Fig. 5.10a and Fig. 5.10b, showing the simulated crack signals ($\boldsymbol{B}_{\boldsymbol{xb}}$) and the differential crack signals ($\Delta \boldsymbol{B}_{\boldsymbol{xb}}$) respectively (displays only the first 110 ms). As can be seen in both plots, the rising edge of the pulse is distorted as the hairline cracks are detected. Also, the plots show a change in pulse shape as the cracks are detected. The highest rate of change of the pulse signal happens in the initial 25 ms for the 4 mm deep surface hairline crack and in the

initial 16.875 ms for the 4 mm deep far-surface hairline crack. These initial regions of the pulse signal are predominantly composed of high frequency components. Since, higher frequency components correspond to surface features due to the low penetration depth of the induced magnetic field (shallow skin depth) occurring in the test sample at such regions, therefore, shallow surface hairline cracks can be more easily distinguished in this initial stage of the pulse signal (1 ms - 25 ms). This would be very beneficial for identifying the initial stages of surface cracking in the oil and gas pipelines (industrial application).

According to the information displayed in Fig. 5.10, it can be seen that the reference signal, the surface crack signal and the far-surface crack signal possesses different characteristics, in terms of their peak arrival times. The time to peak for the 4 mm deep surface hairline crack happens at a later time of 25 ms, compared to a shorter time to peak of 16.875 ms exhibited by the 4 mm deep far-surface hairline crack, as shown in Fig. 5.10b. This means that; the signal from a surface crack will exhibit a longer time to peak, compared to the signal from a far-surface crack of the same size (i.e. distinction between a surface and a far-surface crack). Fig. 5.11 show a plot of time versus crack depth, demonstrating the variation in the peak arrival time for all the surface and far-surface hairline cracks simulated, using the differential leakage field signal ($\Delta \boldsymbol{B_{xb}}$). As can be seen, the 0.2 mm deep surface hairline crack exhibited the shortest time to peak of 15.625 ms, while the 0.2 mm, 0.4 mm and 0.6 mm deep far-surface hairline cracks exhibited the shortest time to peak of 11.875 ms. However, the 4 mm deep surface hairline crack and the 4 mm deep far-surface hairline crack exhibited the longest time to peak of 25 ms and 16.875 ms respectively. This means that the signal from the shallowest crack will exhibit the shortest time to peak, while the signal from the deepest crack will exhibit the longest time to peak (i.e. distinction between cracks with different depth sizes). Moreover, the difference between a surface crack and a far-surface crack can be easily interpreted from the information displayed in Fig. 5.11, which shows a significantly longer time to peak for the simulated surface cracks, compared to a shorter time to peak exhibited by the far-surface cracks of the same size. Except for the 4 mm deep far-surface hairline crack, which provides a signal with a time to peak equal to the 0.6 mm deep surface hairline crack and greater than the 0.2 mm and 0.4 mm deep surface hairline cracks.

Furthermore, the time to peak variation of the simulated hairline cracks is very small and would be difficult to identify and distinguish for shallow cracks, especially for the 0.2 mm, 0.4 mm, 0.6 mm, 0.8 mm and 1 mm deep surface and far-surface hairline cracks. The results are presented in table 5.1, which show the time to peak variations for all the surface and far-surface hairline cracks simulated in MagNet while using an excitation period of 500 ms and a pulse width of 25 ms.

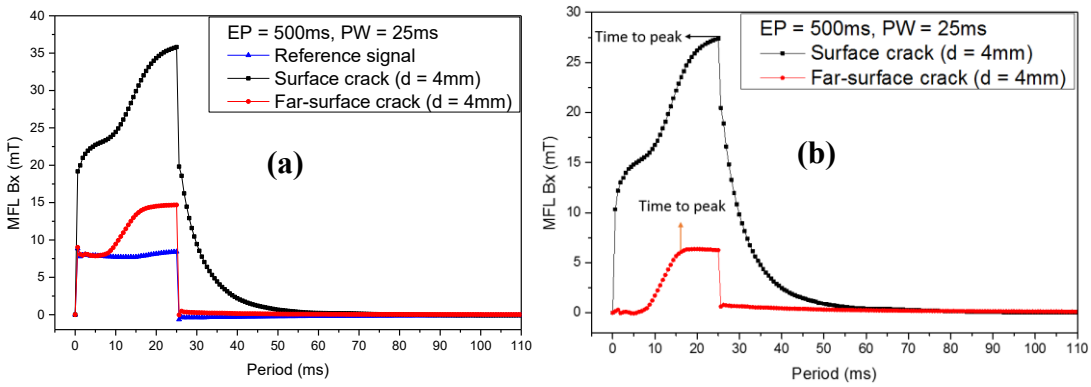

Figure 5.10. Time domain representation - The simulated responses for a reference signal, a 4mm deep surface hairline crack and a 4mm deep far-surface hairline crack; a) Crack signals ($\boldsymbol{B_{xb}}$) and b) Differential crack signals ($\Delta\boldsymbol{B_{xb}}$).

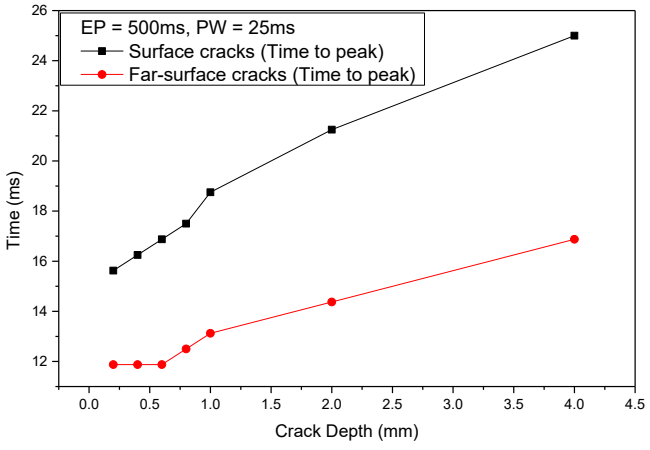

Figure 5.11. Time domain representation - A plot showing the simulated PMFL response signals for both surface and far-surface hairline cracks with varying depth sizes, demonstrating the variation in the signal time to peak.

In addition, the point of intersection of the surface and far-surface crack signals with the reference signal can be used to characterize the various hairline cracks in-terms of their respective locations within the test sample (i.e. distinguish a surface crack from a far-surface crack). As can be seen in Fig. 5.10a, the point of intersection of the surface crack signal and the far-surface crack signal with the reference signal is different. That is; the 4 mm deep far-surface crack signal first descends from its peak level and intersects with the reference signal at 26.25 ms. However, the 4 mm deep surface crack signal descends more gently from its peak level and intersects with the reference signal at 60 ms. In other to obtain an accurate time to peak variation between the respective hairline cracks investigated, 800 load steps (multiple load steps) were used in the transient solver. The time step for the acquired pulse waveform here is 0.625 ms with 500 ms excitation period.

Table 5.1. The simulated PMFL transient responses for both surface and far-surface hairline cracks with varying depth sizes, demonstrating the variation in the MFL signal amplitude and time to peak, using an excitation period and pulse width of 500 ms and 25 ms respectively.

Crack Depth (mm)	**MFL (ΔB_{xb}^{Peak}) (mT)**		**Time to Peak (ms)**	
	Surface cracks	**Far-surface cracks**	**Surface cracks**	**Far-surface cracks**
0.2	3.16	0.14	15.625	11.875
0.4	6.0	0.21	16.25	11.875
0.6	8.27	0.54	16.875	11.875
0.8	11.52	0.80	17.5	12.5
1.0	12.8	1.02	18.75	13.125
2.0	19.86	2.6	21.25	14.375
4.0	26.98	6.31	25.0	16.875

5.3.1.4) Feature Extraction in Frequency Domain

The analysis of the frequency spectrum distribution for the simulated PMFL signals obtained from various surface and far-surface hairline cracks with different depth sizes is presented in Figs 5.12, 5.13 and 5.14. These signals were obtained by subtracting a reference signal amplitude spectrum from the crack signal amplitude spectrum, in order to show any large variations between the non-defective and defective signal amplitude spectrums.

a) Amplitude Spectrum Analysis of the Simulated PMFL Signal

Fig 5.12a and Fig 5.12b shows the frequency domain representation of different response signals corresponding to various surface and far-surface hairline cracks respectively, with different depth sizes. These response signals were obtained while using an excitation pulse period of 500 ms with a pulse width of 25 ms. As can be seen from both plots, the presence of either a surface or far-surface hairline crack causes a notable increase in the acquired signal amplitude (magnitude FFT). This is more clearly portrayed in Fig. 5.13, which compares the differential signal amplitude (magnitude at f = 5 Hz) for both the surface and far-surface hairline cracks, as a function of crack depth. It can be seen that the magnitude of the leakage signal increases with increasing crack depth from left to right, with a significantly lower signal amplitude recorded for the far-surface cracks, compared to the surface cracks of the same size. The information displayed in Fig. 5.13 shows that surface cracks can be easily separated from far-surface cracks, except for the 4 mm deep far-surface hairline crack that provides a signal greater than the 0.2 mm and 0.4 mm surface hairline cracks.

In addition, the characteristic of the response signals in the low frequency region is different for the surface cracks (see Fig 5.12a) when compared to the far-surface cracks (see Fig. 5.12b). That is; the surface crack signals descend more quickly (before 50Hz) compared to the far-surface cracks, which takes longer to get to the 0 mT point (beyond 50Hz).

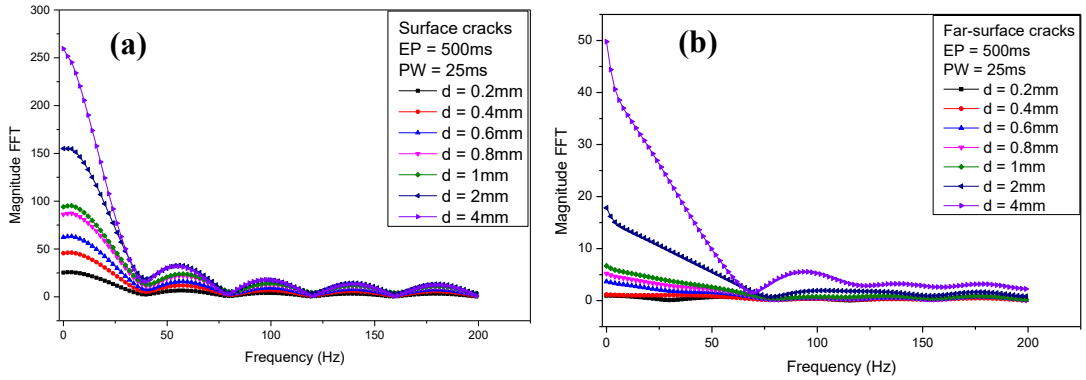

Figure 5.12. Frequency domain representation - The simulated envelope curve of the amplitude spectrum for different crack depths, using an excitation period of 500 ms and pulse width of 25 ms; a) Surface hairline cracks and b) Far-surface hairline cracks.

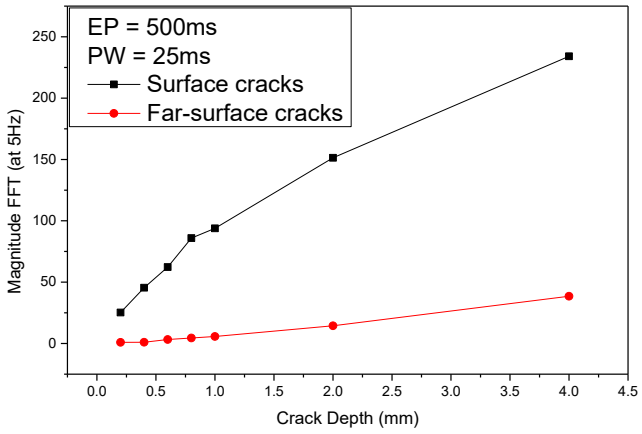

Figure 5.13. Frequency domain representation - A plot showing the simulated differential PMFL signal amplitude (magnitude at f = 5 Hz) as a function of crack depth, for both surface and far-surface hairline cracks.

Fig. 5.14 shows a frequency domain representation of the simulated PMFL signals, comparing the frequency spectrum distribution for a selected surface and far-surface hairline cracks on the same graph. As can be seen, the low frequency components (below 50Hz) has proved to be very effective in distinguishing not just the surface hairline cracks from the far-surface hairline cracks but also discriminating the various hairline cracks according to their depth sizes. This is due to a high penetration depth of the magnetic field (skin effect) occurring in the test sample at this region (below 50 Hz), thus, enabling better detection and characterization of the inspected surface and far-surface hairline cracks. Moreover, discrimination between

surface and far-surface cracks seems possible between 50 Hz and 200 Hz frequency range.

It is therefore certain that the establishment of hairline crack position from the pipeline surface and the distinction between hairline cracks with different depth sizes could be extracted using the proposed PMFL system, for a satisfactory and complete QNDE.

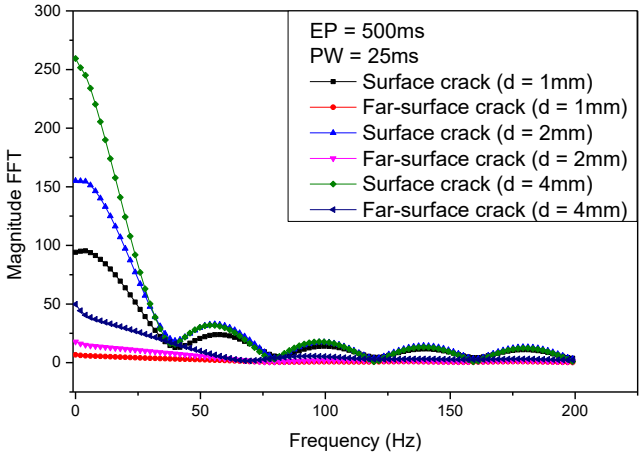

Figure 5.14. Frequency domain representation - A comparison of the simulated frequency spectrum distribution for different surface and far-surface hairline cracks, with varying depth sizes.

5.4) PMFL Experimental Investigation

An experimental benchmark was developed and performed in order to confirm the feasibility of the optimized PMFL inspection system modelled using the FEM software, as an effective detector of surface and far-surface hairline cracks. The experimental procedure and the results obtained are described below.

5.4.1) Experimental Set-up for PMFL Measurements

The developed PMFL experimental measurement system set-up used consisted of; an optimized U-shaped magnetization yoke with leg height, leg length, leg width and leg spacing of 80 mm, 30 mm, 60 mm and 240 mm respectively, defective and non-defective low carbon steel plates (EN3B grade) with dimensions of 350 mm × 60 mm × 10 mm, a 0.5 mm thick excitation copper wire with a resistance of 1.02 Ω, a single Ratiometric Hall Effect sensor (A1302KUA-T from Allegro microsystems) with dimensions of 4 mm × 3 mm × 0.4 mm (plastic casing), an automatic controlled x-y-z translation stage system (Thorlabs), a signal generator (Agilent 33600A series), an amplifier (Kepco), a high performance 16 bit analogue to digital conversion card (DAQ), a current measuring circuitry (ACS712ELC-30A), a low pass filter and a personal computer. The schematic diagram and a photograph of the PMFL experimental set-up used are illustrated in Fig. 5.15a and Fig. 5.15b respectively.

(a)

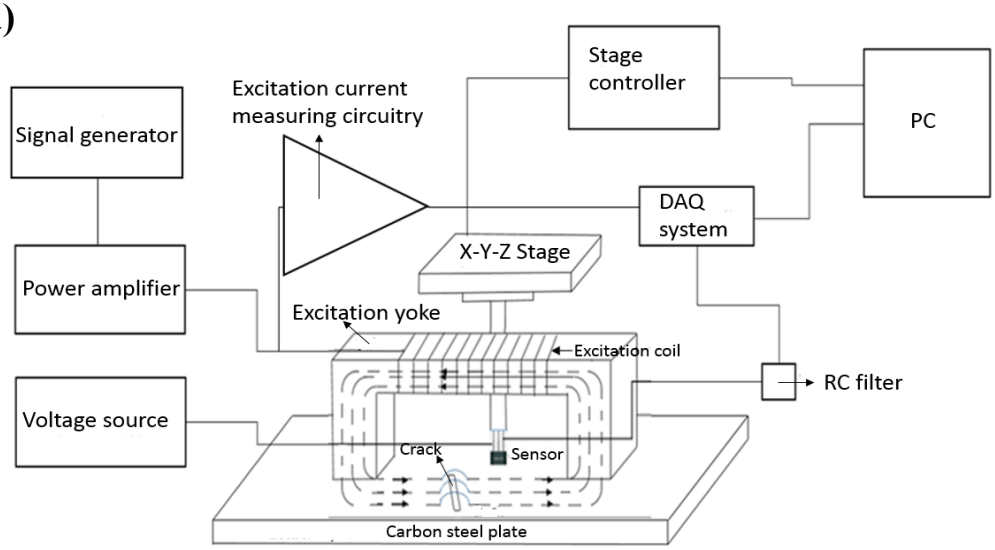

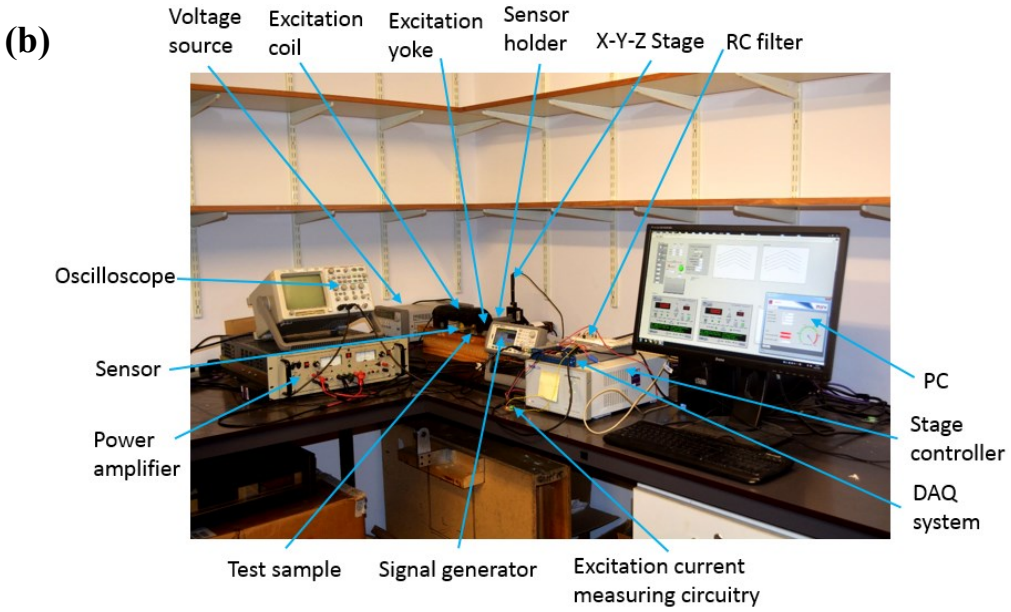

Figure 5.15. The PMFL experimental probe system set-up used in this work; a) Schematic diagram and b) A photograph.

The signal generator was used to provide a square waveform of 1 V amplitude, with a rise and fall time of 10 ns for 500 ms. The square wave is amplified ($\times$ 4) and fed to a 300 turn firm double-coated and high thermally durable copper wire wound around the horizontal top section of a U-shaped silicon-steel yoke. The current measuring circuitry was used to measure the excitation current passing through the copper wire. A 3D printed sensor holder attached to the x-y-z translation stage held the Hall Effect sensor in place. The sensor was positioned perpendicular to the crack orientation such that it measures the axial ($\boldsymbol{B_x}$) component of the leakage field. Measurements were made by scanning the Hall Effect sensor with a sensitivity of 0.0138 V/mT across the various surface and far-surface hairline cracks in steps of 0.5 mm, with a constant sensor lift-off of 0.5 mm. x = 0 mm is the central major axis of the cracks. The positive full cycle of the PMFL inspection system was analyzed and the distribution pattern of the axial ($\boldsymbol{B_x}$) component of the MFL signal was acquired for different hairline cracks.

The position of the inspection probe is unchanged for all measurements. In order to ensure an improved visualization of the hairline crack features, both single and area scan techniques are implemented. To verify the PMFL inspection reproducibility, all measurements were repeated 10 times while keeping the magnetization direction constant, since the PMFL inspection accuracy is dependent on satisfactory

reproducibility of the measurement results. The sensor output is filtered by a low-pass filter with a cut-off frequency of 1.59 kHz, as shown in Fig 5.16. The DAQ system (NI-USB-6366 from National Instruments) was used to digitize the filtered output from the sensor. Data were collected at 1600 S/s (1.6 kHz) for each scanning cycle. The digitized data is stored in a computer for signal processing. The communication with the signal generator, x-y-z translation stage, sensor electronics and visualization of data was done in LabVIEW, while data processing was done within LabVIEW program and using Microsoft's Excel and Origin 9.0 Program.

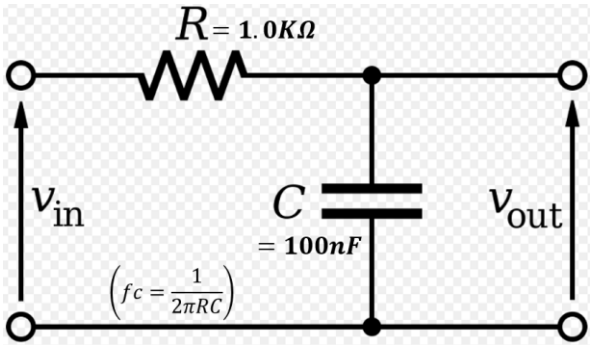

Figure 5.16. Schematic diagram of the RC low pass filter configuration used for the PMFL Test.

Fig. 5.17 shows the LabVIEW user interface used for the PMFL inspection. The developed set-up allows for real time data of the scan to be viewed and monitored by the user as the inspection progresses. The developed PMFL LabVIEW program allows the user to effortlessly set the relevant parameters such as the pulse period, pulse width, pulse amplitude, number of samples, number of pulses, etc. The user can also set the instructions required to control the x and y translation stages to travel at specified x and y distances along the sample surface, as well as the delay time before the next scan step in both the x and y directions. The user can also specify which output voltage to be displayed (i.e. V_{avg}, V_{pp}, V_{max}, V_{min} or V_{std}). For easy visualization of the inspection output, two different 3D maps were used as shown in Fig. 5.17. One of the maps displays the pulse shape as a function of time (3D pulse data) as the scan progresses, while the other shows the operator/user the sensor output as a function of x-y displacements (surface plot), clearly demonstrating the leakage field region (crack position) and distribution pattern.

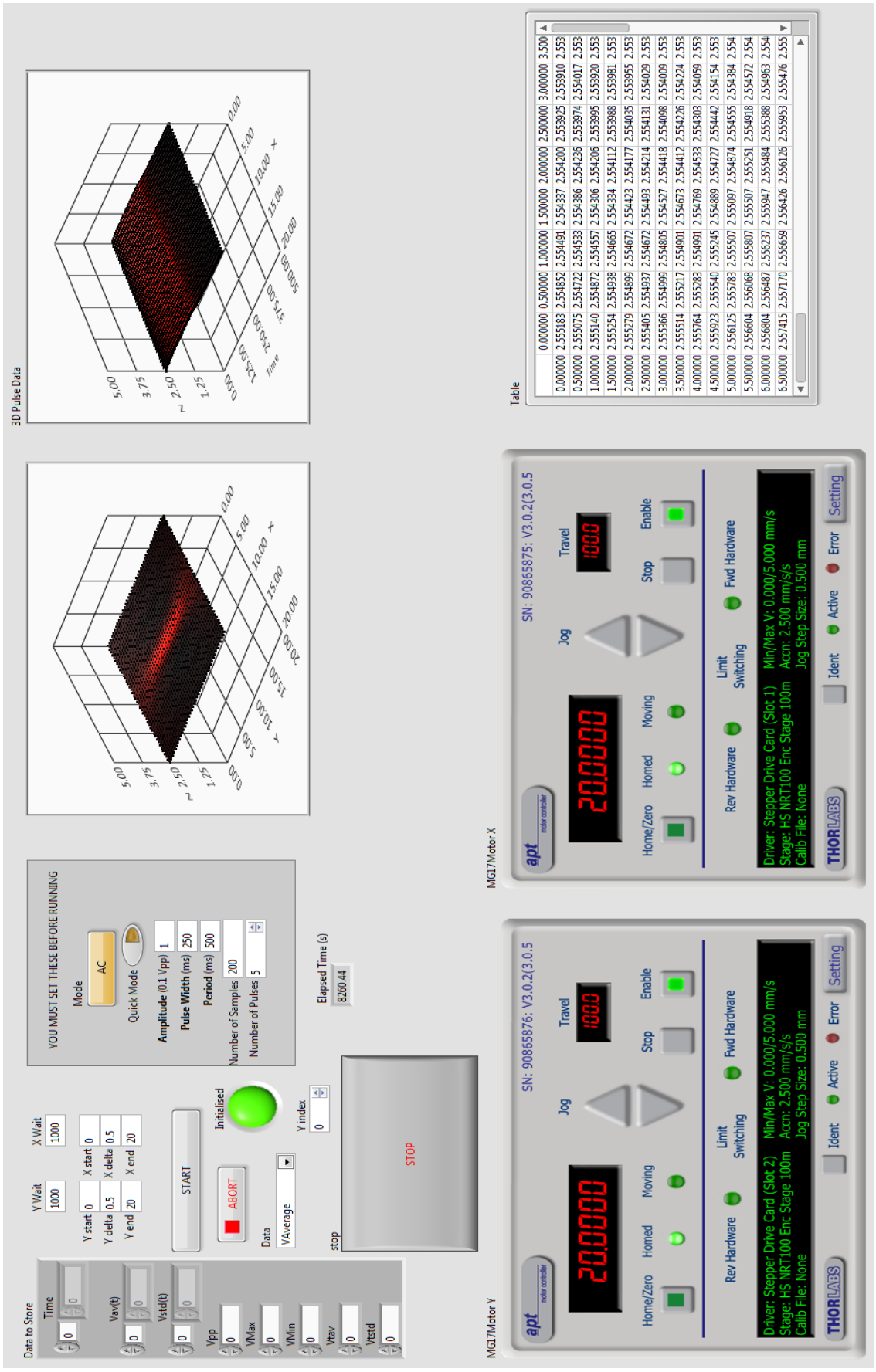

Figure 5.17. The Labview interface for the PMFL inspection system.

5.4.2) Experimental Results and Discussions

In this section, the sensitivity and capability of the developed PMFL inspection system in detecting and characterizing surface and far-surface hairline cracks with different depth sizes is investigated using practical experiments, in order to verify the results obtained via the series of FEM numerical simulations conducted in MagNet.

5.4.2.1) Repeatability Test for PMFL Measurements

First, the repeatability of the optimized PMFL measurement probe system was examined by acquiring the leakage field signal ($\boldsymbol{B_x}$) due to a 4 mm deep surface hairline crack and a 4 mm deep far-surface hairline crack. Each of the measurements was repeated 10 times in order to confirm the repeatability of the measurement results obtained, since the success of the PMFL inspection is dependent on the satisfactory reproducibility of the acquired results. The measured MFL signal amplitude ($\Delta\boldsymbol{B_{xb}}$) as a function of time, for the 4 mm deep surface and the 4 mm deep far-surface hairline cracks, showing the standard error information (error bars) is illustrated in Fig. 5.18. As can be observed, the optimized PMFL system showed a good repeatability (minimal error). The maximum standard deviation recorded for the surface and far-surface hairline cracks were 1.57×10^{-3} mT and 2.1×10^{-3} mT respectively. The standard error and percentages error were calculated using equation (4.2) and (4.3) in section 4.4.3.1. The maximum percentage error recorded for the surface and far-surface hairline cracks were 2.4 % and 1.7 % respectively, which shows a high measurement precision of the data collected from the Hall Effect sensor over the entire scanned region.

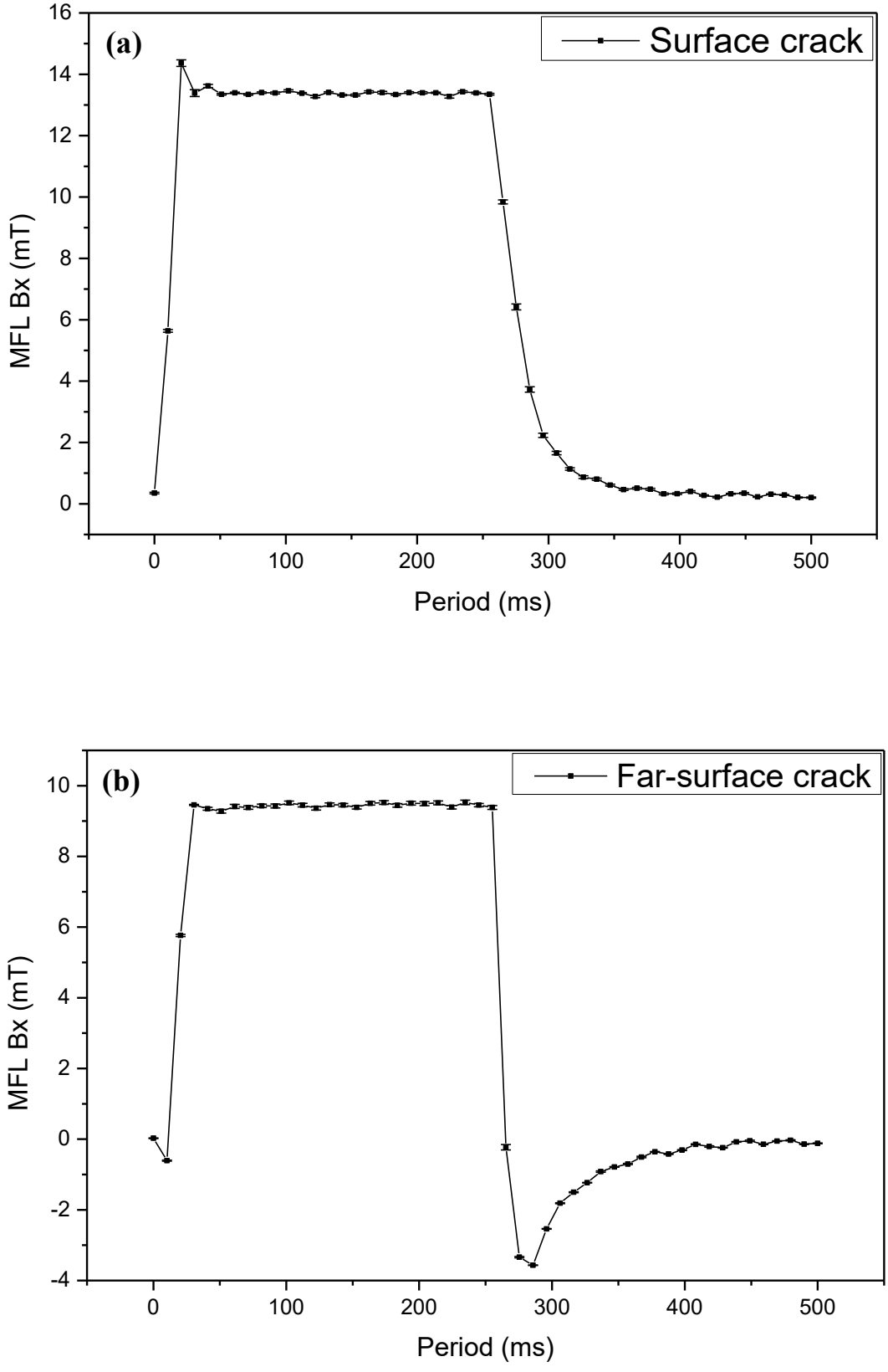

Figure 5.18. Time domain representation - The measured differential MFL signal amplitude ($\Delta \boldsymbol{B_{xb}}$) for; a) 4mm deep surface hairline crack (standard error), and b) 4mm deep far-surface hairline crack (standard error).

5.4.2.2) Effect of Excitation Period Variation on Hairline Crack Detection

An experimental investigation was performed in order to ascertain the influence of excitation pulse period variation on the detectability and characterization of both surface and far-surface hairline cracks, using the experimental procedure described in section 5.4.1. The transient responses were first obtained with a non-defective plate for; 1 ms, 5 ms, 10 ms, 20 ms, 100 ms and 500 ms excitation periods of constant duty cycle (50 %), with a constant sensor lift-off of 0.5 mm. This was used as a reference signal for the subsequent measurements. Multiple load steps were used to ensure accurate results.

Fig. 5.19 show a plot of differential leakage field ($\Delta \boldsymbol{B}_{\boldsymbol{xb}}$) versus crack depth. It compares the differential leakage field ($\Delta \boldsymbol{B}_{xb}$) amplitude obtained for both surface (see Fig. 5.19a) and far-surface (see Fig. 5.19b) hairline cracks, for different excitation periods; 1 ms, 5 ms, 10 ms, 20 ms, 100 ms and 500 ms of constant duty cycle (50 %). The transient responses were obtained when the sensor is directly above a hairline crack, with a lift-off of 0.5 mm. According to the information displayed in Fig. 5.19a, it is evident that all the six excitation periods investigated were able to detect and characterize the various surface hairline cracks inspected with respect to their depth sizes, using the measured $\Delta \boldsymbol{B}_{xb}$ amplitude. According to the information displayed in Fig. 5.19b, it can be observed that the 1 ms, 5 ms, 10 ms and 20 ms excitation periods were not able to detect and distinguish between all the far-surface hairline cracks inspected with respect to their depth sizes, although the 20 ms excitation period was able to detect and distinguish between just the 2 mm and 4 mm deep far-surface hairline cracks. However, increasing the excitation period to 100 ms and 500 ms provides a better detection and characterization of all the six far-surface hairline cracks inspected. Similar to the simulated results presented in Fig 5.5, the differential leakage field amplitudes ($\Delta \boldsymbol{B}_{xb}$) represented in Fig. 5.19a and Fig. 5.19b were collected at $t = 0.5$ ms, 2.5 ms, 5 ms, 10 ms, 20 ms and 20 ms for the 1 ms, 5 ms, 10 ms, 20 ms, 100 ms and 500 ms excitation pulse periods respectively.

Comparing the experimental results presented in Fig. 5.19 with the simulation results displayed in Fig. 5.5, confirms the fact that there is a good agreement between the two, in terms of their abilities and limitations in detecting and characterizing the various surface and far-surface hairline cracks using different excitation pulse periods. The experimental findings support the statement that the use of higher excitation frequencies (shorter excitation periods; 1 ms 5 ms, 10 ms, and 20 ms) causes a field concentration at the surface layer of the test sample, hence, more suitable for surface hairline crack detection and characterization. However, reducing the excitation frequency (longer excitation periods; 100 ms and 500 ms) results in higher magnetic field penetration deep into the test sample, which is suitable for the detection and characterization of both surface and far-surface hairline cracks. This also confirms the fact that the spectrum distribution present in different excitation periods provides diverse depth profiles for the same experimental procedure.

The results presented are the average values of the data acquired by the Hall Effect sensor ($V_{average}$) in order to maintain good measurement precision and to ensure accuracy of the data collected from the sensor over the scanned region. From the PMFL simulation and experimental results obtained, a suitable excitation period of 500 ms (longer excitation period) is preferred for the detection and characterization of surface and far-surface hairline cracks in ferromagnetic pipeline structures. This will ensure sufficient magnetic field penetration deep inside the pipeline material, thereby, allowing for an effective detection and characterization of hairline cracks, especially those that extend deep below the pipe surface.

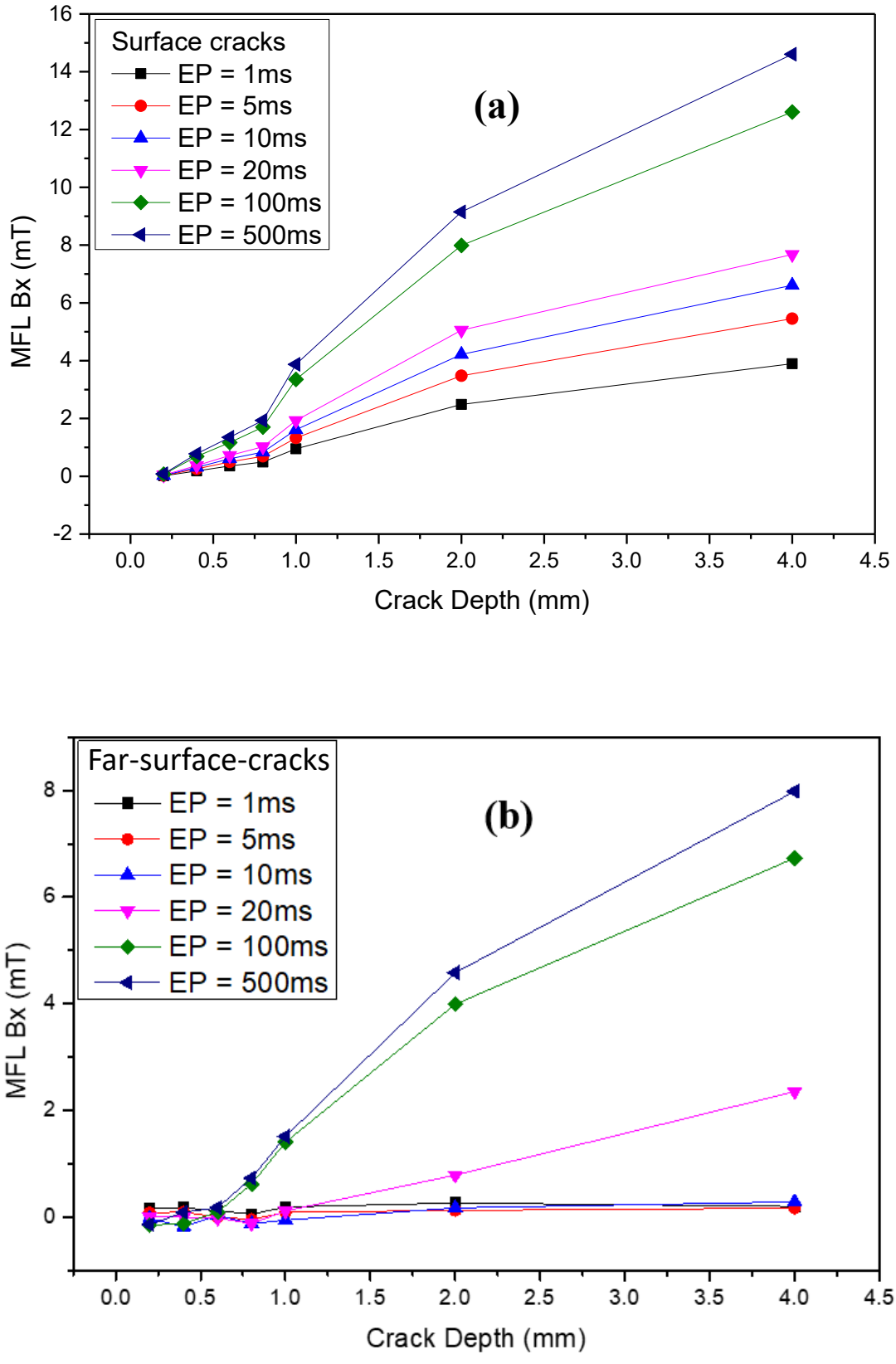

Figure 5.19. A plot of the measured differential leakage field amplitude ($\Delta \boldsymbol{B}_{xb}$) as a function of crack depth, comparing the effect of different excitation periods on the detectability and characterization of; a) Surface hairline cracks and b) Far-surface hairline cracks.

5.4.2.3) Effect of Pulse Width Variation on Hairline Crack Detection

In order to determine the influence of pulse width variation on the detectability and characterization of various surface and far-surface hairline cracks, an experimental investigation was first carried out with different pulse widths of constant excitation period, using a 10 mm thick non-defective plate. This will serve as a reference signal for the subsequent measurements. The excitation current input fed into the excitation coil at different pulse widths, while using the non-defective plate is shown in Fig. 5.20. The result shows that the current amplitude reaches its peak at the 100 ms pulse width, corresponding to 20 % duty cycle.

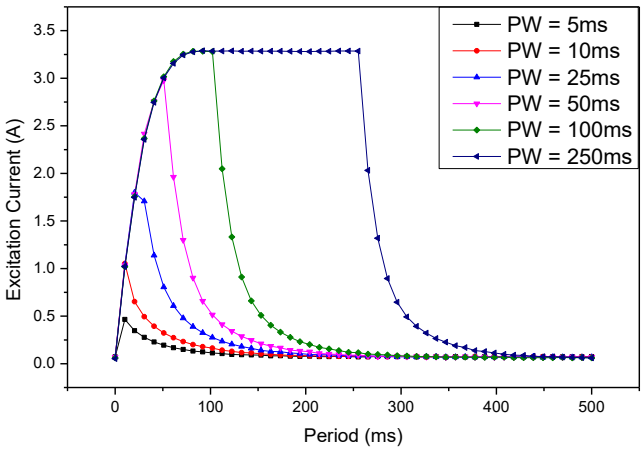

Figure 5.20. Time domain representation - The excitation current input flowing inside the excitation coil at different pulse widths.

Fig. 5.21 shows the measured transient responses ($\boldsymbol{B_{xb_0}}$) obtained with respect to time, while using the non-defective plate. The transient responses were obtained for; 5 ms, 10 ms, 25 ms, 50 ms, 100 ms and 250 ms pulse widths of constant excitation period (500 ms). It shows the different levels of leakage field signal detected by the Hall Effect sensor, demonstrating the signal profile variation as the pulse width is varied from 5 ms to 250 ms. Similar to the simulated result displayed in Fig. 5.6, the measured leakage field ($\boldsymbol{B_{xb_0}}$) reaches its peak amplitude (steady state) at 50 ms corresponding to 10 % duty cycle as shown in Fig. 5.21.

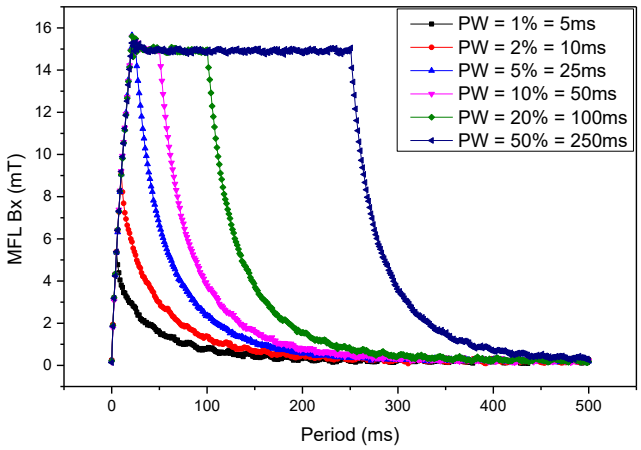

Figure 5.21. Time domain representation - The measured leakage field ($\boldsymbol{B_{xb_0}}$) signal for a non-defective test plate, at different pulse widths of constant excitation period of 500 ms.

Fig. 5.22 shows the frequency spectrum distribution of the leakage field signals obtained by the Hall Effect sensor, for different pulse widths. As can be seen, it illustrates the amplitude variation of the acquired leakage field signals at different frequencies. The various depth responses corresponding with the eddy current skin effect phenomenon, which significantly affects the magnetic field penetration into the test sample can be acquired, by analyzing the frequency spectrum distribution under different pulse widths. As shown in Fig. 5.22, wider pulse widths are richer than the narrower ones in the low frequency region. Hence, the use of wider pulse widths will enable adequate magnetic field penetration into the test sample, which is suitable for the detection and characterization of hairline cracks located at the pipe surface as well as those located further away from the pipe surface.

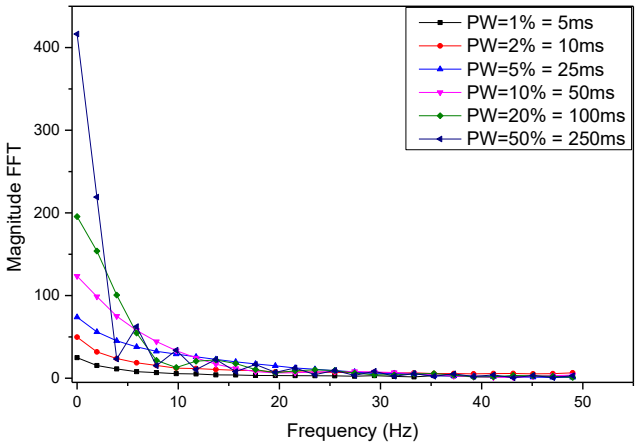

Figure 5.22. Frequency-domain representation - The measured spectrum distribution for a non-defective signal under different pulse widths, demonstrating the change in signal amplitude.

Fig. 5.23 shows a plot of differential leakage field ($\Delta \boldsymbol{B}_{\boldsymbol{xb}}$) versus crack depth. It compares the differential leakage field ($\Delta \boldsymbol{B}_{xb}$) amplitude obtained for both surface (see Fig. 5.23a) and far-surface (see Fig. 5.23b) hairline cracks, for different pulse widths; 5 ms, 10 ms, 25 ms, 50 ms, 100 ms and 250 ms of constant excitation period (500 ms). The transient responses were obtained when the sensor is directly above a hairline crack, with a lift-off of 0.5 mm. According to the information displayed in Fig. 5.23a, it can be observed that all the six pulse widths investigated were able to detect and distinguish between the various surface hairline cracks inspected with respect to their depth sizes, using the measured $\Delta \boldsymbol{B}_{xb}$ amplitude. The information displayed in Fig. 5.23b show that the 5 ms and 10 ms pulse widths were not able to detect and separate all the far-surface hairline cracks according to their depth sizes, although the 10 ms pulse width was able to detect and distinguish between just the 1 mm, 2 mm and 4 mm deep far-surface hairline cracks. However, increasing the pulse width to 25 ms, 50 ms, 100ms and 250 ms provides a better detection and characterization of all the six far-surface hairline cracks inspected. Similar to the simulated results presented in Fig 5.8, the differential leakage field amplitudes ($\Delta \boldsymbol{B}_{xb}$) represented in Fig. 5.23a and Fig. 5.23b were collected at $t = 5$ ms, 10 ms, 25 ms, 20 ms, 20 ms and 20 ms (before steady state) for the 5 ms, 10 ms, 25 ms, 50 ms, 100 ms and 250 ms pulse widths respectively.

Comparing the experimental results presented in Fig. 5.23 with the simulation results displayed in Fig. 5.8, confirms the fact that there is a good agreement between the two, in terms of their abilities and limitations in detecting and characterizing the various surface and far-surface hairline cracks using different pulse widths. The experimental findings support the statement that wider pulse widths; 25 ms, 50 ms, 100 ms and 250 ms are richer in low frequency components and are suitable for the detection and characterization of both surface and far-surface hairline cracks, due to the deeper magnetic field penetration into the sample. However, narrower pulse widths; 5 ms and 10 ms are predominantly composed of high frequency components, which are best suited for the detection and characterization of surface hairline cracks. This also confirms the fact that the induced magnetic field in the excitation cycle possess a variation of frequency components at various time intervals, which corresponds to different depths of penetration at different points in the cycle.

The ultimate decision for a suitable pulse width selection would depend on the required magnetic field penetration for a particular crack depth inspection. In other words, for this current investigation that requires the detection of hairline cracks located deep below the surface of a 10 mm thick plate, a longer pulse width is more suitable to ensure an effective detection and characterization. Hence, a 250 ms pulse width corresponding to 50 % duty cycle was chosen.

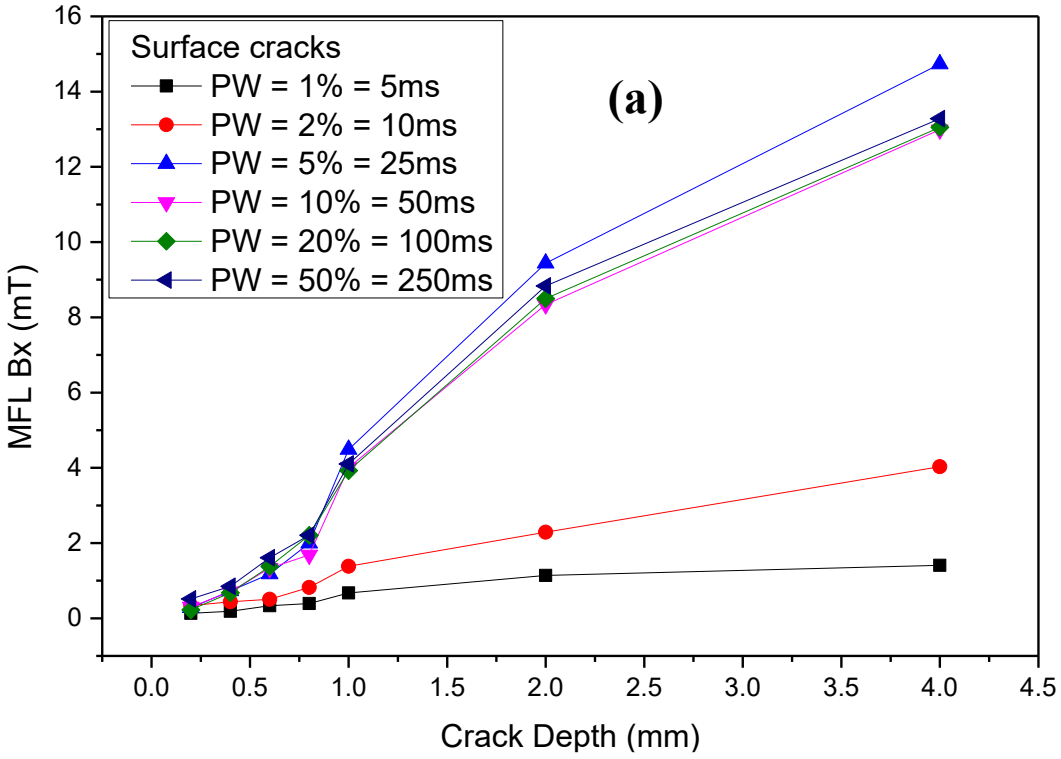

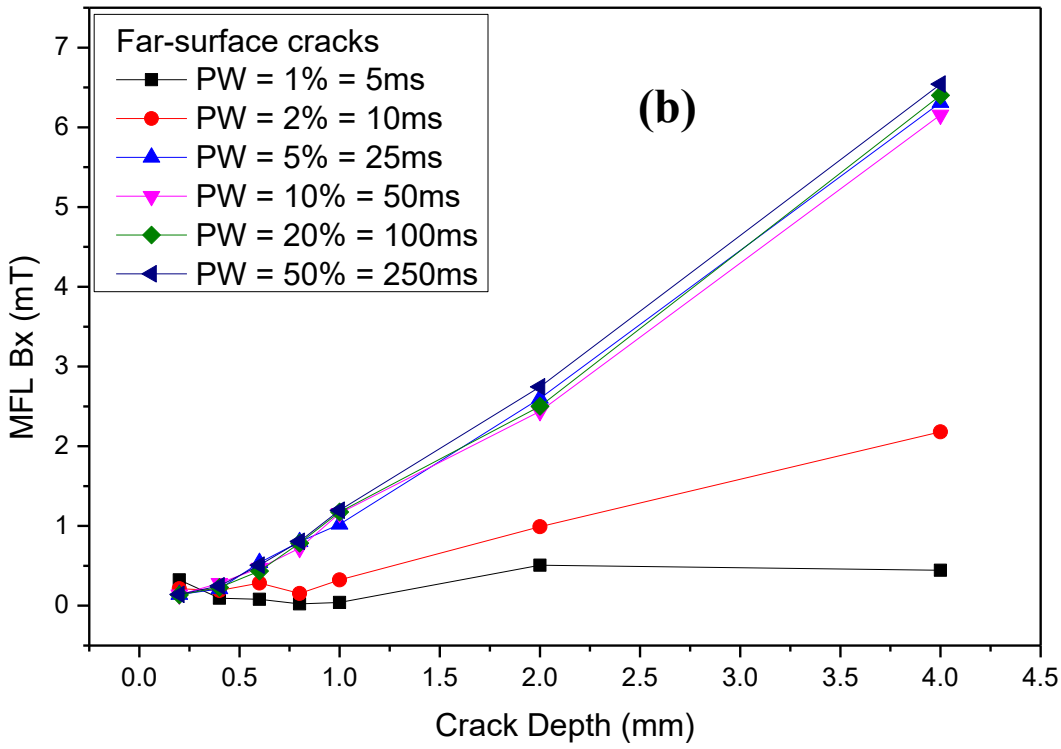

Figure 5.23. A plot of the measured differential leakage field amplitude ($\Delta \boldsymbol{B}_{xb}$) as a function of crack depth, comparing the effect of different pulse widths on the detectability and characterization of; a) Surface hairline cracks and b) Far-surface hairline cracks.

5.4.2.4) Feature Extraction in Time Domain

In this section, the measured leakage field signals will be used to characterize the various hairline cracks located at different depths within the test sample, using their individual transient responses in the time domain. Here, the signal obtained from a non-defective plate is taken as the reference signal. This ensures that the measured responses are not affected by the existence of a crack and would act as a base response in subsequent analysis. According to the principle of PMFL testing and the characteristics of the crack response signals embedded in the various crack information, the different crack features present in the time domain spectrum are extracted as follows.

a) Amplitude Analysis of the Measured PMFL Signal

The measured differential PMFL signal peak amplitude ($\Delta \boldsymbol{B}_{\boldsymbol{xb}}^{\boldsymbol{Peak}}$) obtained for various surface and far-surface hairline cracks with different depth sizes, using a pulse width of 25 ms and 250 ms are shown in Fig. 5.24a and Fig. 5.24b respectively. According to both plots, the presence of either a surface or a far-surface hairline crack causes a notable variation in the measured $\Delta \boldsymbol{B}_{\boldsymbol{xb}}^{\boldsymbol{Peak}}$ signal amplitude. Also, similar to the simulated results presented in Fig. 5.9 of section 5.3.1.3, the $\Delta \boldsymbol{B}_{\boldsymbol{xb}}^{\boldsymbol{Peak}}$ amplitude increases with increasing surface and far-surface crack depth and the overall signal level is lower for the far-surface hairline cracks when compared to a surface crack of the same size. In addition, it can be observed from both plots that there is an overlap in surface and far-surface values. Therefore, discrimination between the surface and far-surface hairline cracks will be difficult, except for surface hairline cracks with depth greater than 2 mm. The $\Delta \boldsymbol{B}_{\boldsymbol{xb}}^{\boldsymbol{Peak}}$ amplitude for all the surface and far-surface hairline cracks inspected are displayed in table 5.2.

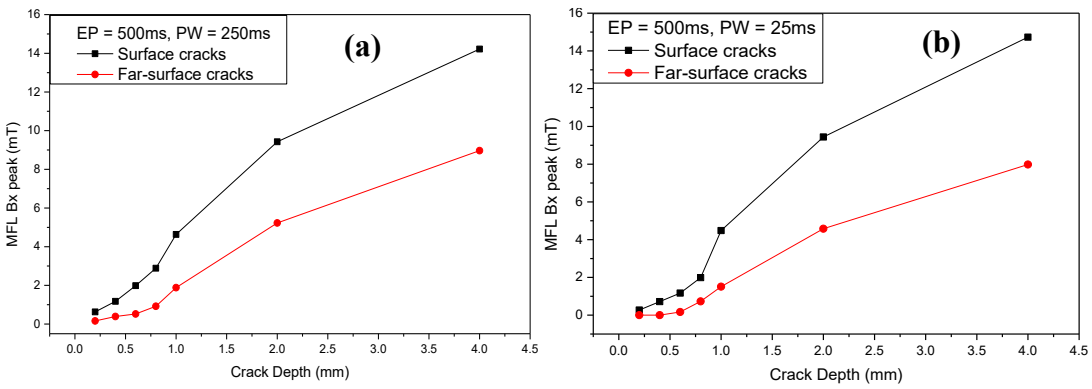

Figure 5.24. Time domain representation - A plot showing the measured differential PMFL signal peak amplitudes ($\Delta \boldsymbol{B}_{\boldsymbol{xb}}^{\boldsymbol{Peak}}$) as a function of crack depth, comparing both surface and far-surface hairline cracks; a) 25 ms (5%) pulse width Surface cracks and b) 250 ms (50 %) pulse width.

b) Time to Peak Analysis of the Measured PMFL Signal

A comparison between the measured response signals obtained from a non-defective plate, a 4 mm deep surface hairline crack and a 4 mm deep far-surface hairline crack, using the crack signal ($\boldsymbol{B}_{\boldsymbol{xb}}$) and the differential crack signal ($\Delta \boldsymbol{B}_{\boldsymbol{xb}}$) is shown in Fig.

5.25a and Fig. 5.25b respectively. Both plots illustrate the variation in the signal shape as the Hall Effect sensor approaches the cracks. As the hairline cracks are detected, the rising edge of the pulse is distorted, with a significant variation in the signal shape between 1 ms and 25.625 ms for the 4 mm deep surface hairline crack and between 1 ms and 18.75 ms for the 4 mm deep far-surface hairline crack. It can be seen from Fig. 5.25 (showing only the first 110 ms) that the reference signal, surface crack signal and far-surface crack signal have different signal characteristics in terms of their peak arrival times. The highest rate of change of the signals happens in the first 25.625 ms, which corresponds to the highest frequency component of the excitation pulse. Hence, this particular region will be more suited for surface crack detection and characterization, due to the high concentration of magnetic field occurring at the surface layer of the test sample (low penetration depth).

The time to peak for the 4 mm deep surface hairline crack occurs at later time of 25.625 ms compared to a shorter time to peak of 18.75 ms recorded for the 4 mm deep far-surface hairline crack as displayed in Fig. 5.25b. Fig 5.26 shows a plot that compares the measured PMFL response signals obtained for both the surface and far-surface hairline cracks with different depth sizes. It illustrates the variation in the peak arrival time for each of the hairline cracks inspected, while using the differential crack signal ($\Delta \boldsymbol{B_{xb}}$). As shown, the 0.2 mm and 0.4 mm deep surface hairline cracks displayed the shortest time to peak of 18.125 ms compared to a longer time to peak of 25.625 ms displayed by the 4 mm deep surface hairline crack. Moreover, it was not possible to detect the 0.2 mm deep far-surface hairline crack while using an excitation pulse period of 500 ms and a pulse width of 25 ms. However, a peak arrival time of 14.375 ms, 14.375 ms, 15 ms, 15.625 ms, 16.875 ms and 18.75 was recorded for the 0.4 mm, 0.6 mm, 0.8 mm, 1 mm, 2 mm and 4 mm deep far-surface hairline cracks respectively. This confirms the simulation result, which shows that the signal from the shallowest crack will exhibit the shortest time to peak, while the signal from the deepest crack will exhibit the longest time to peak.

According to Fig 5.26, the distinction between the surface and far-surface hairline cracks can be seen, which shows a significantly shorter time to peak for the far-surface hairline cracks, compared to the surface hairline cracks of equivalent size. Also, it can be observed from Fig 5.26 that there is an overlap in surface and far-

surface values. Therefore, separation of all the surface cracks from the far-surface cracks will be difficult, except for surface hairline cracks with depth greater than or equal to 0.8 mm. Furthermore, the time to peak variation of the signals is very small, hence, it will be challenging to identify and separate for shallow cracks, most especially for the 0.2 mm, 0.4 mm, 0.6 mm, 0.8 mm and 1 mm deep surface and far-surface hairline cracks. The measured time to peak for all the surface and far-surface hairline cracks inspected experimentally are presented in table 5.2.

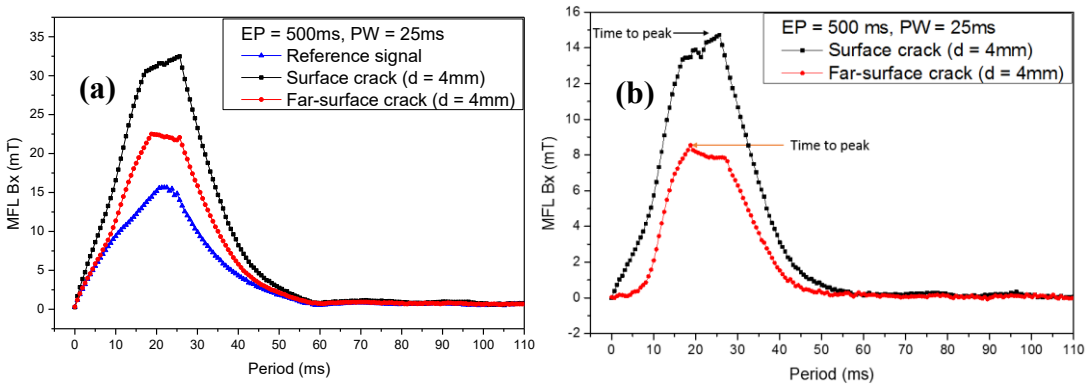

Figure 5.25. Time domain representation - The measured responses for a reference signal, a 4mm deep surface hairline crack and a 4mm deep far-surface hairline crack; a) Crack signals ($\boldsymbol{B_{xb}}$) and b) Differential crack signals ($\Delta\boldsymbol{B_{xb}}$).

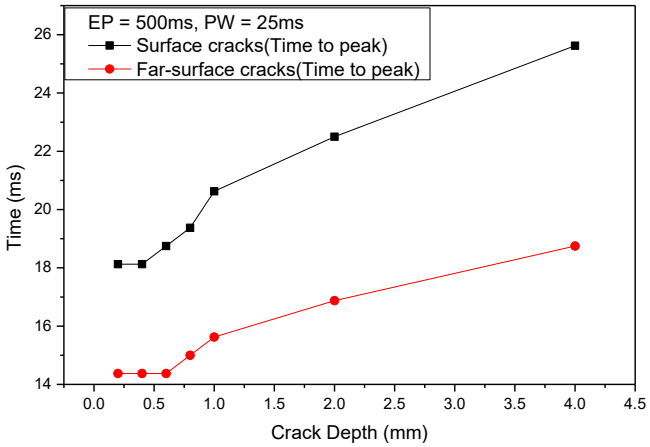

Figure 5.26. Time domain representation - A plot showing the measured PMFL response signals for both surface and far-surface hairline cracks with varying depth sizes, demonstrating the variation in the signal time to peak.

Similar to the simulation result presented Fig. 5.10a, the point at which the surface and far-surface crack signals intersect with the reference signal can be used to characterize the various hairline cracks in-terms of their respective locations within the test sample. As can be seen in Fig. 5.25a, the point at which the surface crack signal and the far-surface crack signal intersect with the reference signal is different. That is; the signal from the 4 mm deep far-surface hairline crack first descends from its peak level and intersects with the reference signal at 47.5 ms. However, the signal from the 4 mm deep surface hairline crack descends more gently from its peak level and intersects with the reference signal at 57.5 ms. In other to obtain an accurate time to peak variation between the respective hairline cracks investigated, 800 load steps (multiple load steps) were used and the time step for the acquired pulse waveform here is 0.625 ms with 500 ms excitation period.

Table 5.2. The measured PMFL response signals for both surface and far-surface hairline cracks with varying depth sizes, demonstrating the variation in the MFL signal amplitude and time to peak, using an excitation pulse period and pulse width of 500 ms and 25 ms respectively.

Crack Depth (mm)	**MFL (ΔB_{xb}^{Peak}) (mT)**		**Time to Peak (ms)**	
	Surface cracks	**Far-surface cracks**	**Surface cracks**	**Far-surface cracks**
0.2	0.27	0.0	18.125	-
0.4	0.72	0.0	18.125	14.375
0.6	1.17	0.17	18.75	14.375
0.8	1.99	0.73	19.375	15.0
1.0	4.48	1.51	20.625	15.625
2.0	9.44	4.58	22.5	16.875
4.0	14.73	7.98	25.625	18.75

5.4.2.5) Feature Extraction in Frequency Domain

The analysis of the frequency spectrum distribution of the PMFL signals obtained experimentally for various surface and far-surface hairline crack with different depth sizes is presented in this section. The signal analyzed is the differential crack signal acquired by subtracting a reference signal from the crack signals in order to show any large difference between the defective and non-defective amplitude spectrum.

a) Amplitude Spectrum Analysis of the Measured PMFL Signal

The frequency domain representation of the measured response signals corresponding to different surface and far-surface hairline cracks with varying depth sizes are shown in Fig. 5.27a and Fig 5.27b respectively. It can be seen from both plots that the presence of either a surface or a far-surface hairline crack causes a significant increase in the measured signal amplitude (magnitude FFT). This effect is clearly illustrated in Fig. 5.28. It compares the amplitude of the measured leakage signal (magnitude at f = 5 Hz) for both surface and far-surface hairline cracks, as a function of crack depth. As can be seen, the magnitude of the leakage signal increases with increasing crack depth, with a significantly lower signal level recorded for the far-surface cracks when compared to the surface cracks of the same size. Also, according to the information presented in Fig. 5.28, discrimination between surface and far-surface cracks is possible, especially for surface hairline cracks with depth greater than 0.8 mm.

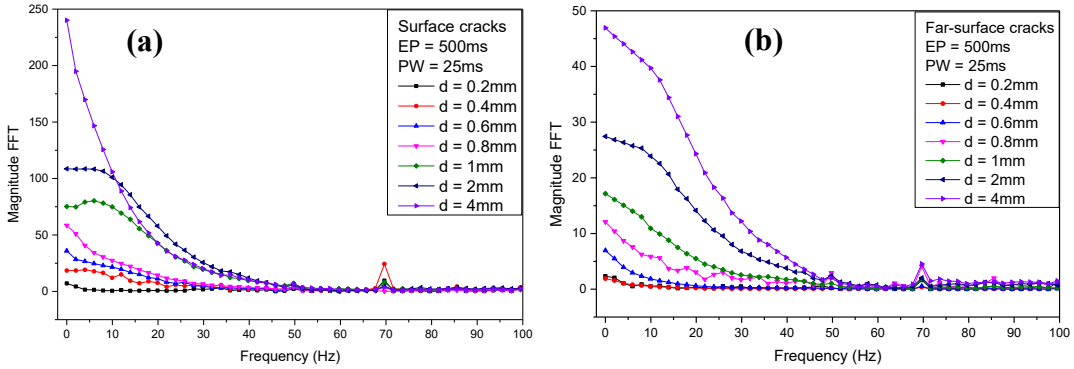

Figure 5.27. Frequency domain representation - The measured envelope curve of the amplitude spectrum for different crack depths, using an excitation period of 500 ms and pulse width of 25 ms; a) Surface cracks and b) Far-surface cracks

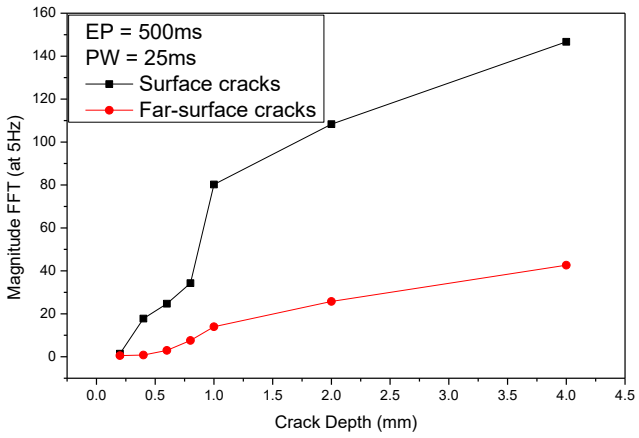

Figure 5.28. Frequency domain representation - A plot showing the measured differential PMFL signal amplitude (magnitude at $f = 5$ Hz) as a function of crack depth, for both surface and far-surface hairline cracks

Fig. 5.29 compares the frequency spectrum distribution for a selected surface and far-surface hairline cracks with different depth sizes on the same graph. It can be seen from the plot that the newly developed PMFL measurement tool can distinguish the various hairline cracks according to their depth sizes and location, using the signal amplitude at the low frequency region. Similar to the simulation result, the PMFL signal characteristic in the low frequency region is different for the surface cracks compared to the far-surface cracks, that is; the surface crack signals descend more quickly from its peak height compared to the signal from the far-surface cracks.

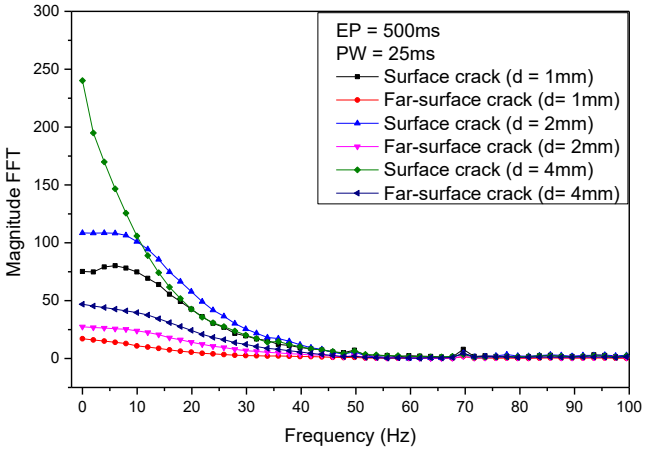

Figure 5.29. Frequency domain representation - A comparison of the measured frequency spectrum distribution for different surface and far-surface hairline cracks with varying depth sizes.

5.4.3) Leakage Field Imaging for Hairline Crack Detection and Characterization

In order to study and analyze the PMFL inspection technique for hairline crack detection and characterization, both line scan and area scan techniques are implemented using practical experiments, to provide enhanced detection and visualization of the crack information and features as illustrated in Fig. 5.30a and Fig. 5.30b respectively. Also, a forward approach for characterizing the various hairline cracks has been adopted, with respect to the information acquired from the imaging of the resultant leakage field distribution caused by the interaction between the induced magnetic field and the hairline crack geometries.

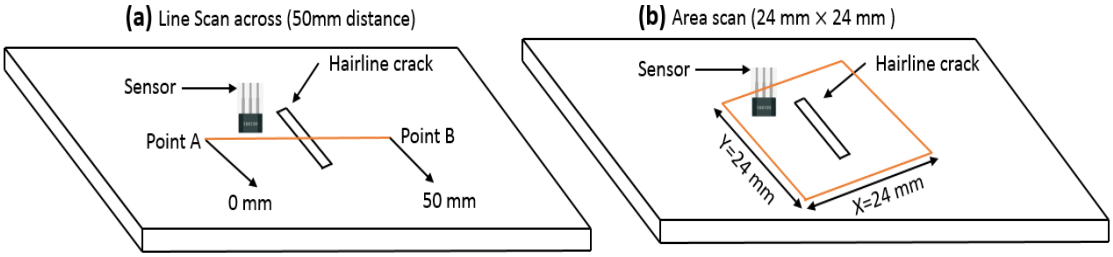

Figure 5.30. An experimental illustration of; a) A line scan across a hairline crack and b) An area scan in the vicinity of a hairline crack.

In the experimental investigation, different low carbon steel plates were used (grade: EN3B), each with a well-defined EDM hairline crack with a different depth information (i.e. d = 0.2 mm, 0.4 mm, 0.6 mm, 0.8 mm, 1 mm, 2 mm and 4 mm). A 10 mm thick non-defective plate and seven 10 mm thick defective plates were tested. All the hairline cracks investigated had a constant width and length of 0.2 mm and 10 mm respectively. A constant lift-off of 0.5 mm was maintained between the Hall Effect sensor and the surface of the test plates, except where mentioned otherwise. The plates were magnetized using a 300 turn excitation coil made from copper wire with a diameter of 0.5 mm, wound around an optimized U-shaped silicon steel yoke. A square waveform of 4 V amplitude with a rise and fall time of 10 ns was fed into the excitation coil in order to magnetize the test plates.

As analyzed in the excitation pulse period and pulse width variation tests, a longer excitation period of 500 ms and wider pulse width of 250 ms (50 % duty cycle) was used in order to ensure adequate magnetic field penetration into the test plates, especially for the plates with far-surface hairline cracks. The distribution pattern of the leakage field ($\boldsymbol{B_x}$) is acquired for the non-defective plate as well as for the plates with various hairline cracks, using the Hall Effect sensor. The differential leakage field signal ($\Delta \boldsymbol{B_{xb}}$) for each of the hairline cracks is then obtained by subtracting the leakage field signal acquired from a non-defective plate from that acquired from the defective plates. The current measuring circuitry (ACS712ELC-30A) was used to obtain the magnitude of the excitation current, passing through the excitation coil at various times in the excitation cycle as shown in Fig. 5.31.

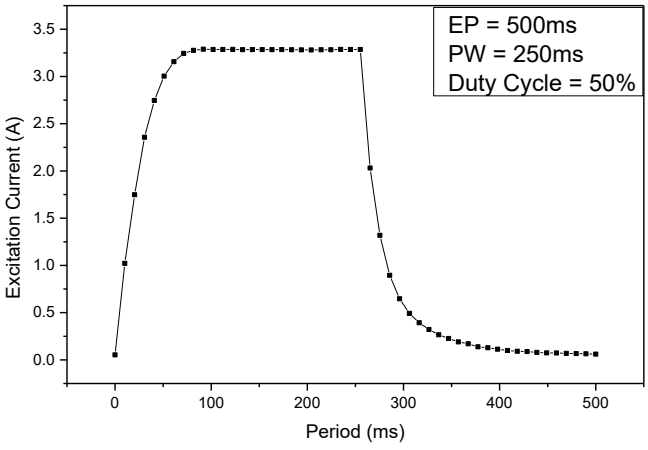

Figure 5.31. Time domain representation - The measured excitation current input flowing inside the excitation coil.

The typical response of the newly developed PMFL inspection system to a 4 mm deep surface and 4 mm deep far-surface hairline cracks (40 % wall loss) is displayed in Fig. 5.32 (line scan) and Fig. 5.33 (area scan). The unit of percent used represents the ratio of the crack depth to sample wall thickness. Fig 5.32 shows a time domain representation of the measured differential crack signal ($\Delta \boldsymbol{B_{xb}}$) obtained from a 50 mm line scan, across both cracks while using a constant scan step size and sensor lift-off of 0.5 mm and 0.5 mm respectively. The plots clearly point out the distinctive change in the pulse shape as the sensor approaches and leaves the hairline cracks, (i.e. an increase and a decrease in the leakage field amplitude as the sensor approaches and leaves the crack site respectively). The measured leakage field signal for both cracks varies with relative position of the sensor to the crack axis, with the highest signal amplitudes recorded at the crack centre (i.e. x = 0 mm).

Fig. 5.33 shows the differential crack signals ($\Delta \boldsymbol{B_{xb}}$) obtained from an area scan in the vicinity of the same 4 mm deep surface and 4 mm deep far-surface hairline cracks. The scanned area represented is a surface of 24 mm × 24 mm in the x and y directions, with a constant scan step size and sensor lift-off of 0.5 mm and 0.5 mm respectively. As can be seen in Fig 5.33, the amplitude and distribution pattern of the leakage fields are altered with respect to the crack shape. Also, the leakage signal measured for both cracks varies with relative position of the sensor to the crack axis, with the peak amplitude recorded at the crack centre (i.e. x = 0 mm and y = 0 mm). The peak amplitude $\Delta \boldsymbol{B_{xb}^{Peak}}$ for the 4 mm deep surface and 4 mm deep far-surface hairline cracks are 14.2 mT and 8.97 mT respectively.

The distinction between a surface and a far-surface hairline crack can be interpreted from the resultant leakage field profile that shows a significantly lower signal value as well as a broader signal width for the far-surface crack, compared to a higher signal value and narrower signal width for the surface crack. The relationship between the size and shape of the cracks and the leakage field signal can be established from the mapped out images (see Fig. 5.33b and Fig. 5.33d), by analyzing the distribution change of the flux. Also, some useful features can be acquired from the imaged field distribution, such as the type, position, orientation and dimensional information of the various hairline cracks. Both the line scan and area scan techniques used were able to show a good indication of the 4 mm deep

surface and the 4 mm deep far-surface hairline cracks inspected, as well as their location and orientation, using the differential crack signal ($\Delta \boldsymbol{B_{xb}}$).

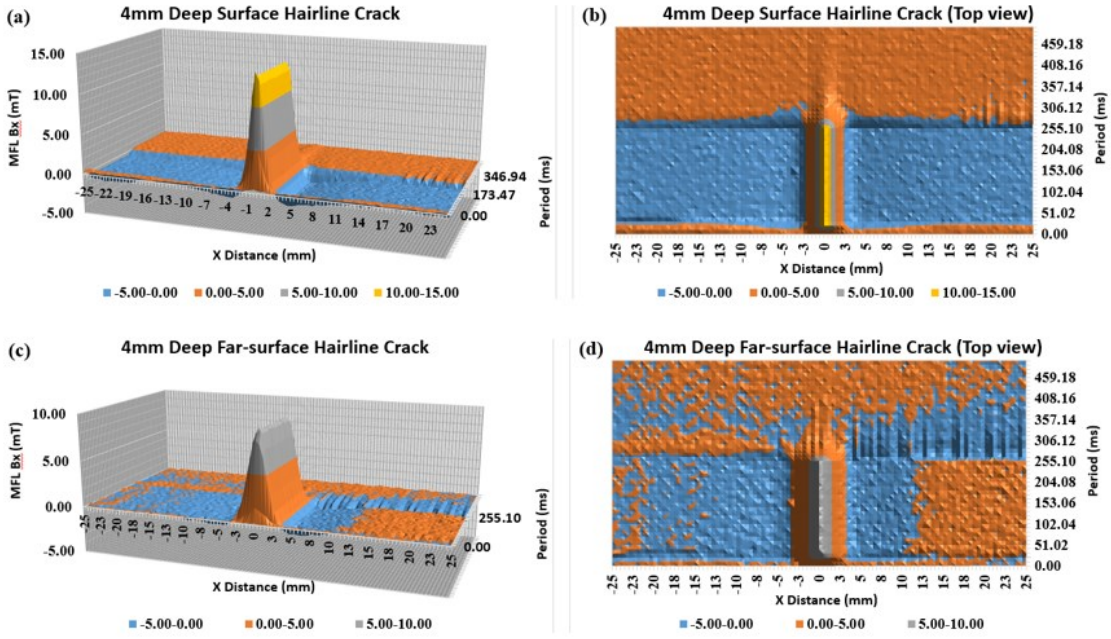

Figure 5.32. Time domain representation - A line scan of the measured differential leakage field signal ($\Delta \boldsymbol{B_{xb}}$) for; a) 4mm deep surface hairline crack, b) Top view of a 4mm deep surface hairline crack, c) 4mm deep far-surface hairline crack and d) Top view of a 4mm deep far-surface hairline crack.

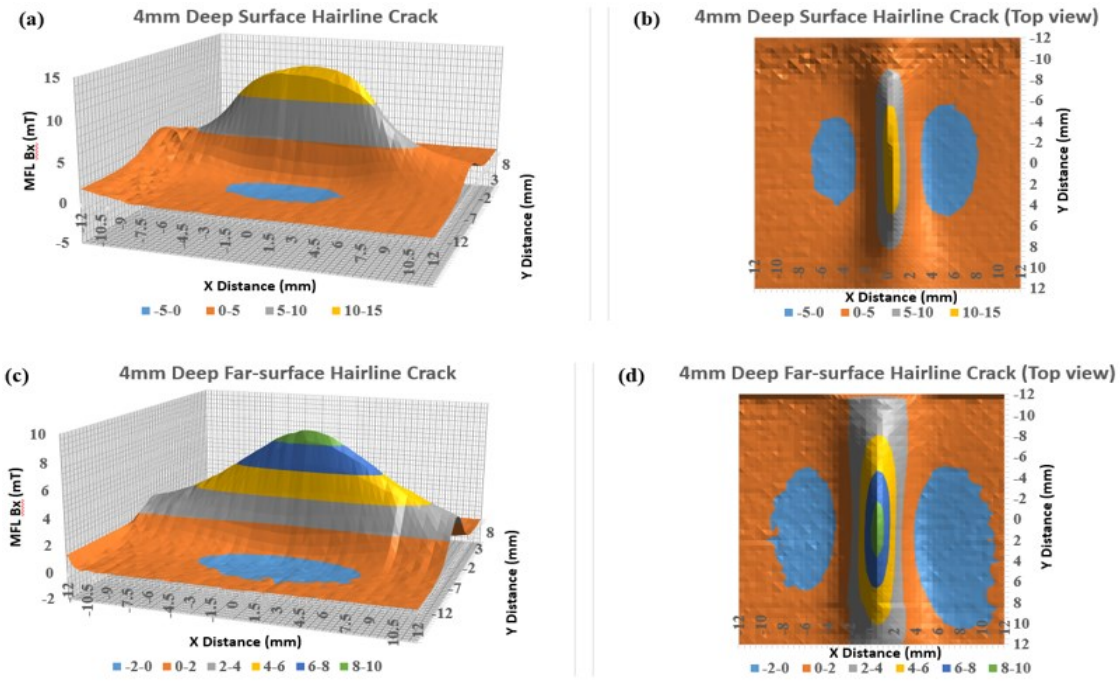

Figure 5.33. An area scan of the measured differential leakage field signal ($\Delta \boldsymbol{B_{xb}}$) for; a) 4mm deep surface hairline crack, b) Top view of a 4mm deep surface hairline crack, c) 4mm deep far-surface hairline crack and d) Top view of a 4mm deep far-surface hairline crack.

An area scan in the vicinity of all the surface and far-surface hairline cracks, with different depth sizes are shown in Fig. 5.34 and Fig. 5.35 respectively. It can be seen that the newly developed PMFL inspection tool is able to detect all the surface hairline cracks investigated as well as a 0.4 mm deep far-surface hairline crack located 9.6 mm below the sample surface. However, the system struggled at detecting the 0.2 mm deep far-surface hairline crack, located 9.8 mm below the sample surface. Hence, the maximum penetration depth that could be achieved with the developed PMFL inspection system is 9.6 mm. This means that hairline cracks located on the reverse side of a 10 mm thick ferromagnetic pipeline structure, with depth size of 0.4 mm and above would be effectively detected and evaluated, using the newly developed and optimized PMFL inspection tool.

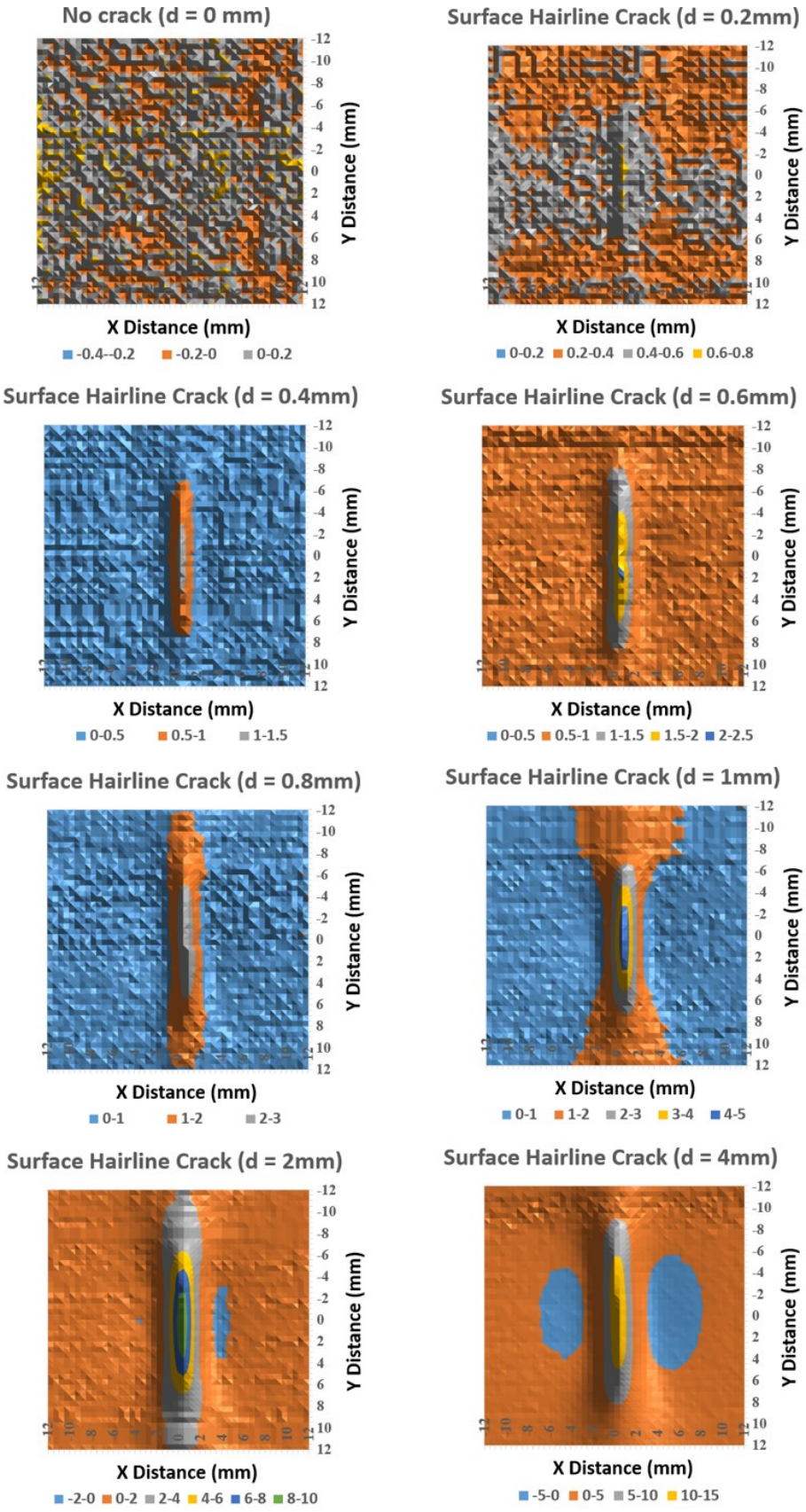

Figure 5.34. An area scan of the measured differential leakage field signal ($\Delta \boldsymbol{B_{xb}}$) for various surface hairline cracks with varying depth sizes, as a function of x and y distances.

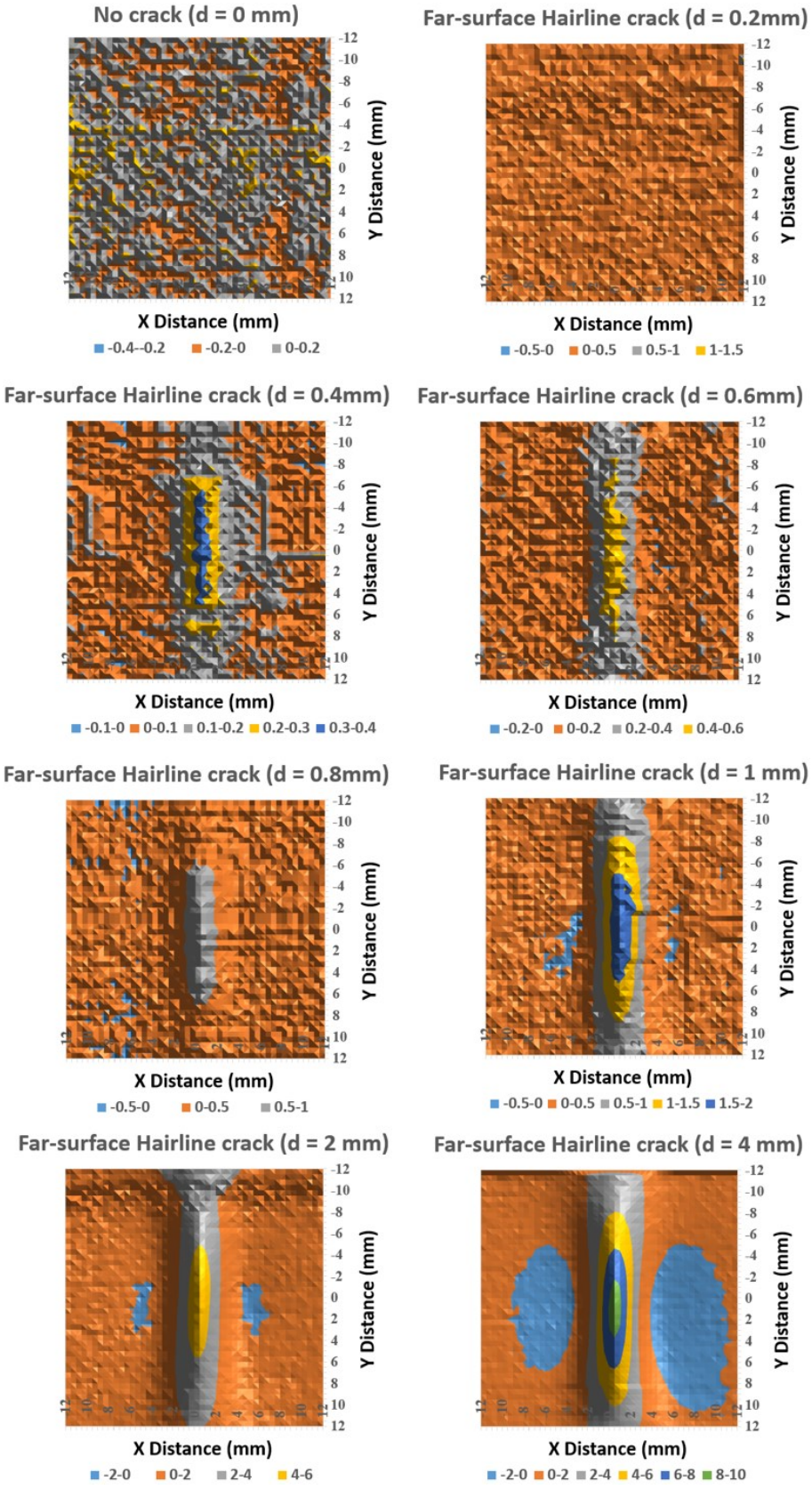

Figure 5.35. An area scan of the measured differential leakage field signal ($\Delta \boldsymbol{B}_{xb}$) for various far-surface hairline cracks with varying depth sizes, as a function of x and y distances.

The corresponding axial line scan across the centre of the various surface and far-surface hairline cracks, with varying depth sizes is shown in Fig. 5.36. The plots show the measured differential leakage field signal ($\Delta \boldsymbol{B_{xb}}$) acquired at the centre of the surface (Fig. 5.36a) and the far-surface (Fig. 5.36b) hairline cracks, as a function of scanning distance. It can be seen that both the surface and far-surface hairline cracks causes a significant increase in the measured leakage field amplitude. Also, the plots clearly show that as the metal loss (crack depth) increases, the amplitude of the axial leakage flux increases for cracks of identical width and length. This shows that the leakage flux in the axial direction is strongly dependent on changes in crack depth.

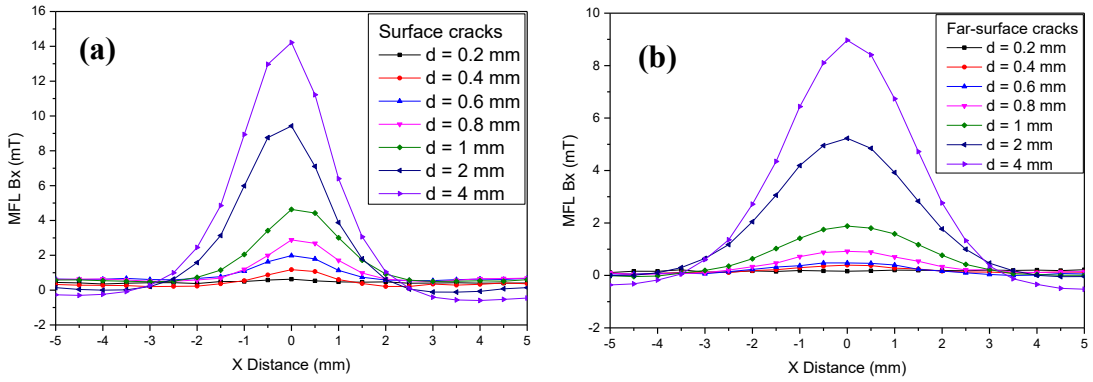

Figure 5.36. The measured differential leakage field signal ($\Delta \boldsymbol{B_{xb}}$) obtained at the centre of each hairline crack, as a function of scanning distance for; a) Surface cracks and b) Far-surface cracks.

Fig. 5.37 shows a comparison of the peak amplitude of the crack signal ($\boldsymbol{B_{xb}^{Peak}}$) and the differential crack signal ($\Delta \boldsymbol{B_{xb}^{Peak}}$) obtained at the centre of the surface and far-surface hairline cracks (2%, 4%, 6%, 8%, 10%, 20% and 40% crack depth to sample wall thickness). The behaviour of the leakage flux for both signals is similar. However, the leakage field amplitude for the crack signals ($\boldsymbol{B_{xb}^{Peak}}$) is higher compared to that of the differential crack signals ($\Delta \boldsymbol{B_{xb}^{Peak}}$). Moreover, the leakage field amplitude increases with increasing crack depth from left to right, and the relationship between the leakage field intensity and the crack depth is fairly linear. The result shows that the axial ($\boldsymbol{B_x}$) component of the leakage field provides good information regarding the crack location, by analyzing the peak points as the sensor scans across the cracks. The result also shows that the leakage signal measured by

the sensor is proportional to the crack depth when other signal influencing parameters (e.g. crack length, crack width, sensor lift-off, etc.) are unchanged.

It can be seen from Fig. 5.37 that the PMFL system can discriminate the various hairline cracks inspected according to their depth sizes, using both the crack signal and differential crack signal. Also, due to the overlap in surface and far-surface values, discrimination of all the surface hairline cracks from the far-surface hairline cracks will be difficult, except for surface cracks with depth greater than 2 mm.

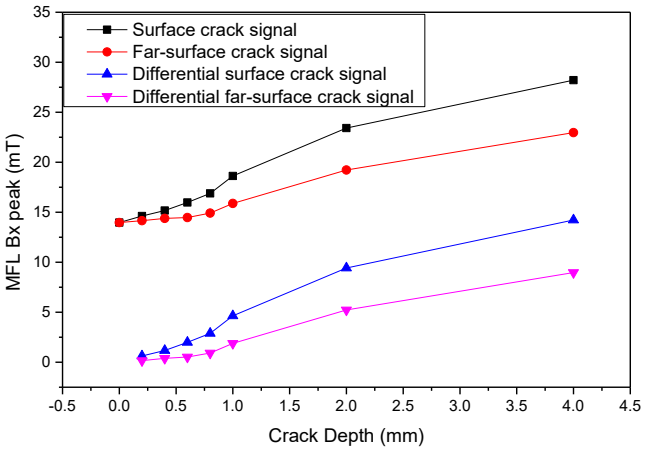

Figure 5.37. The peak amplitude of the measured crack signals ($\boldsymbol{B_{xb}^{peak}}$) and differential crack signals ($\Delta\boldsymbol{B_{xb}^{peak}}$) as a function of crack depth, obtained at the centre of various surface and far-surface hairline cracks.

The dimensions of the various surface and far-surface hairline cracks inspected while using the 10 mm thick low carbon steel plates are clearly presented in table 5.3, along with their respective peak differential leakage field amplitudes ($\Delta\boldsymbol{B_{xb}^{Peak}}$).

Table 5.3. Details of the inspected surface and far-surface hairline cracks with varying depth sizes, present in the 10 mm thick plate, along with their respective peak differential MFL signal amplitudes.

Plate number	**Crack Type**	**Crack Depth d (mm)**	**Crack Location h (mm)**	**MFL(ΔB_{xb}^{Peak}) (mT)**
Plate 1	Surface	0.2	0.0	0.63
	Far-surface	0.2	9.8	0.16
Plate 2	Surface	0.4	0.0	1.17
	Far-surface	0.4	9.6	0.39
Plate 3	Surface	0.6	0.0	1.98
	Far-surface	0.6	9.4	0.52
Plate 4	Surface	0.8	0.0	2.89
	Far-surface	0.8	9.2	0.92
Plate 5	Surface	1.0	0.0	4.64
	Far-surface	1.0	9.0	1.88
Plate 6	Surface	2.0	0.0	9.43
	Far-surface	2.0	8.0	5.23
Plate 7	Surface	4.0	0.0	14.22
	Far-surface	4.0	6.0	8.97

5.4.4) The Effect of Sensor lift-off on the Detection Sensitivity of Hairline Cracks

In order to investigate the lift-off effects and limitations of the newly developed PMFL measurement probe system, the sensor clearance from the sample surface was varied from 0.5 mm to 10 mm. This was used to investigate the influence of sensor

lift-off on the detectability of surface and far-surface hairline cracks, in ferromagnetic steel pipelines. Fig. 5.38 shows the measured differential leakage field amplitude ($\Delta \boldsymbol{B_{xb}}$) as a function of scanning distance, for a 4 mm deep surface hairline crack (see Fig. 5.38a) and for a 4 mm deep far-surface hairline crack (see Fig. 5.38b), at different sensor lift-off. Similar to the DCMFL results, the measured MFL signal amplitude decreases as the sensor clearance from the sample surface is increased. The reduction in the signal amplitude is due to the leakage field attenuation (spreading) as the distance between the plate surface and the sensor increases. Moreover, the reduction in the $\Delta \boldsymbol{B_{xb}}$ amplitude was observed to be higher for lower levels of sensor lift-off when compared to higher levels of sensor lift-offs. Fig. 5.39 shows a plot illustrating the variation of the measured $\Delta \boldsymbol{B_{xb}^{Peak}}$ amplitude with crack depth, at different sensor lift-offs, for both surface (see Fig. 5.39a) and far-surface hairline cracks (see Fig. 5.39b). It can be seen from both plots that the ($\Delta \boldsymbol{B_{xb}^{Peak}}$) amplitude decreases significantly with increasing sensor lift-off value. Also, the rate of decrease of the $\Delta \boldsymbol{B_{xb}^{Peak}}$ amplitude is much higher for lower levels of sensor lift-off, when compared to higher levels of sensor lift-offs.

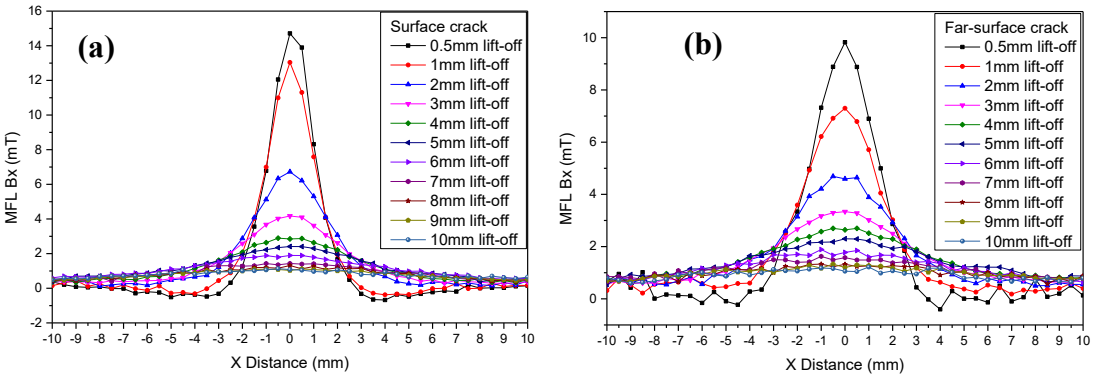

Figure 5.38. The measured differential leakage field signal ($\Delta \boldsymbol{B_{xb}}$) amplitude as a function of scanning distance, at different sensor lift-offs, for a) A 4 mm deep surface hairline crack and b) A 4 mm deep far-surface hairline crack.

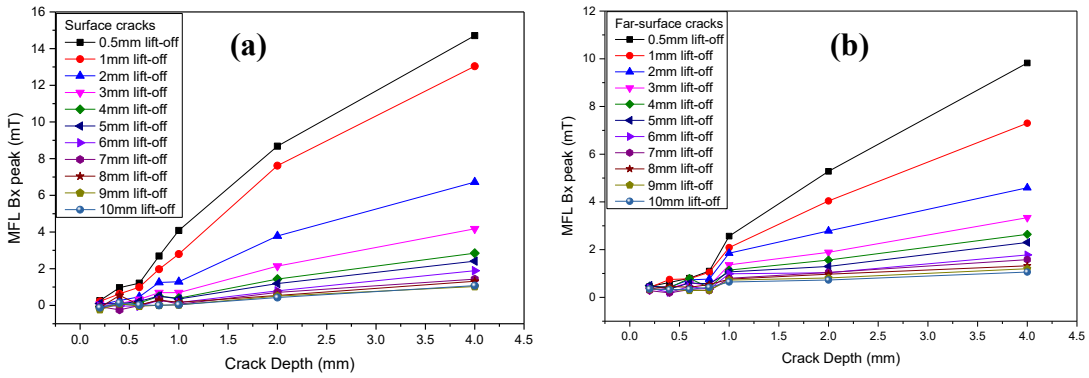

Figure 5.39. A plot showing the measured differential leakage field signal peak ($\Delta \boldsymbol{B}_{\boldsymbol{xb}}^{\boldsymbol{Peak}}$) amplitude as a function of crack depth, at different sensor lift-offs, for; a) Surface cracks and b) Far-surface cracks.

The detection limit for the various surface and far-surface hairline cracks inspected is displayed in Fig. 5.40. The PMFL sensor was able to detect a 4 mm deep surface hairline crack and a 4 mm deep far-surface hairline crack up to a lift-off of 9 mm. The detection limits for all the surface and far-surface hairline cracks investigated is presented in table 5.4.

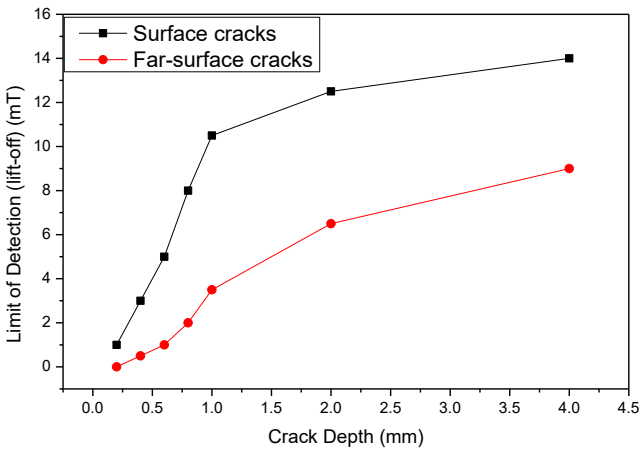

Figure 5.40. A plot showing the detection limits for the various surface and far-surface hairline cracks with varying depth sizes.

Table 5.4. The PMFL sensor detection limit for the various surface and far-surface hairline cracks inspected.

Crack Depth (mm)	Detection Limit (mm) (Sensor lift-off)	
	Surface hairline cracks	Far-surface hairline cracks
0.2	1.0	0.0
0.4	3.0	0.5
0.6	5.0	1.0
0.8	8.0	2.0
1.0	10.5	3.5
2.0	12.5	6.5
4.0	14.0	9.0

5.4.5) Sensitivity Test for Surface and Far-surface Hairline Cracks

The sensitivity of the newly developed PMFL inspection system to both surface and far-surface hairline cracks is investigated in this section. The sensitivity of the PMFL system was evaluated by scanning the Hall Effect sensor across various surface and far-surface hairline cracks with varying depth sizes, in a 10 mm thick plate. The inspected hairline cracks were; a 0.2 mm, 0.4 mm, 0.6 mm, 0.8 mm, 1 mm, 2 mm and 4 mm deep surface and far-surface hairline cracks, with a constant width and length of 0.2 mm and 10 mm respectively. A signal to noise ratio of 0.44 dB, 0.76 dB, 1.2 dB, 1.69 dB, 2.54 dB, 4.53 dB and 6.15 dB was calculated for the surface hairline cracks in sequence, while a signal to noise ratio of 0.15 dB, 0.30 dB, 0.35 dB, 0.61 dB, 1.15 dB, 2.81 dB and 4.36 dB was calculated for the far-surface hairline cracks in sequence. Fig. 5.41 shows a graph of sensitivity (SNR) versus crack depth. It compares the sensitivity of the newly developed PMFL inspection system for both surface and far-surface hairline cracks, with varying depth sizes. As can be seen, the sensitivity of the system increases with increasing crack depth for both surface and

far-surface hairline cracks, with a lower sensitivity level for the far-surface hairline cracks when compared to a surface hairline crack of the same size. Also, it can be seen that the relationship between the sensitivity of the inspection system and crack depth is linear.

The increasing proportion of the system's sensitivity for the surface hairline cracks (from d = 0.2 mm to 4 mm) was calculated to be 42 %, 36 %, 29 %, 33 %, 43 % and 26 % respectively. Likewise, the increasing proportion of the signal's sensitivity for the far-surface hairline cracks (from d = 0.2 mm to 4 mm) was found to be 50 %, 14 %, 42 %, 47 %, 59 % and 34 % respectively. Table 5.5 shows the sensitivity values for the newly developed PMFL inspection system to various surface and far-surface hairline cracks with different depth sizes, as well as the leakage field peak ($\boldsymbol{B_x^{peak}}$) amplitude measured for each of the hairline cracks inspected.

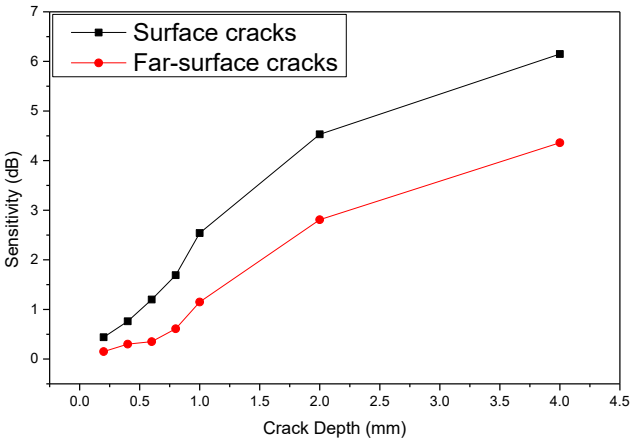

Figure 5.41. A plot comparing the sensitivity of the newly developed PMFL inspection system for different surface and far-surface hairline cracks with different depth sizes.

Table 5.5. The sensitivity of the PMFL inspection system to different surface and far-surface hairline cracks with varying depth sizes.

Crack Depth (mm)	MFL(B_x^{peak}) (mT) Crack signal		Detection Sensitivity (dB)	
	Surface hairline cracks	Far-surface hairline cracks	Surface hairline cracks	Far-surface hairline cracks
0.2	14.62	14.15	0.44	0.15
0.4	15.17	14.39	0.76	0.30
0.6	15.97	14.47	1.20	0.35
0.8	16.88	14.91	1.69	0.61
1.0	18.63	15.87	2.54	1.15
2.0	23.42	19.22	4.53	2.81
4.0	28.21	22.96	6.15	4.36

5.5) Estimation of the Shape and Size of Hairline Cracks using the PMFL Inspection Technique

In this section, an inverse technique is used to reconstruct the various surface and far-surface crack profiles, based on the experimental measurements obtained. Here the resultant leakage field signals acquired from the PMFL sensor are imaged, and the imaged features of the PMFL response are used to estimate the surface and far-surface crack profiles (shape, approximate width and length sizes).

A range of surface and far-surface hairline cracks were inspected using the PMFL experimental approach. A typical response of the PMFL sensor in the vicinity of a 4 mm deep surface hairline crack and a 4 mm deep far-surface hairline crack is displayed in Fig. 5.42 and Fig. 5.43, showing the crack signals ($\boldsymbol{B_{xb}}$) and the differential crack signals ($\Delta\boldsymbol{B_{xb}}$) respectively. As the hairline cracks are detected by

the sensor, the leakage field amplitude and distribution pattern is distorted with respect to the crack orientation, shape and size. Hence, a relationship between the leakage field distribution and the corresponding crack profile can be established by carefully visualizing and studying the correlations between the two variables.

The scanned area presented in Fig 5.42 and Fig. 5.43 is a surface of 24 mm × 24 mm in the x and y directions, with a constant sensor lift-off and scan step size of 0.5 mm and 0.5 mm respectively. A square wave of 4 V, an excitation period of 500 ms and a pulse width of 250 ms corresponding to 50 % duty cycle was used for the driver coil excitation. An approach based on visualization and 3D imaging of the acquired leakage field signal is used to estimate the approximate width and length sizes of the various hairline cracks inspected.

As shown in Fig. 5.42 and Fig. 5.43, the imaged leakage field distribution (both $\boldsymbol{B_{xb}}$ and $\Delta\boldsymbol{B_{xb}}$) demonstrates that the highest signal amplitude occurs at the central major axis of the surface and far-surface hairline cracks. For a far-surface hairline crack, the resultant leakage field signal is more spread out due to the lateral field dispersion occurring at the vicinity of the far-surface crack. Therefore, the estimated width for a far-surface crack will be far larger than the actual crack width (i.e. >> 0.2 mm), when compared to the estimated width for a surface crack of the same size. As can be seen in Fig. 6.42a, an approximate width and length of 2.5 mm and 14.25 mm respectively was estimated for the 4 mm deep surface hairline crack, while using the measured crack signal ($\boldsymbol{B_{xb}}$). However, for the measured differential crack signal ($\Delta\boldsymbol{B_{xb}}$), an approximate width and length of 0.5 mm and 10.6 mm respectively was estimated for the same 4 mm deep surface hairline crack as shown in Fig. 5.43a. Moreover, for the 4 mm deep far-surface hairline crack, an approximate width and length of 3 mm and 11.5 mm respectively was estimated, while using the measured crack signal ($\boldsymbol{B_{xb}}$) as displayed in Fig. 5.42b. However, for the measured differential crack signal ($\Delta\boldsymbol{B_{xb}}$), an approximate width and length of 2 mm and 11 mm respectively was estimated for the same 4 mm deep far-surface hairline crack as shown in Fig. 6.43b.

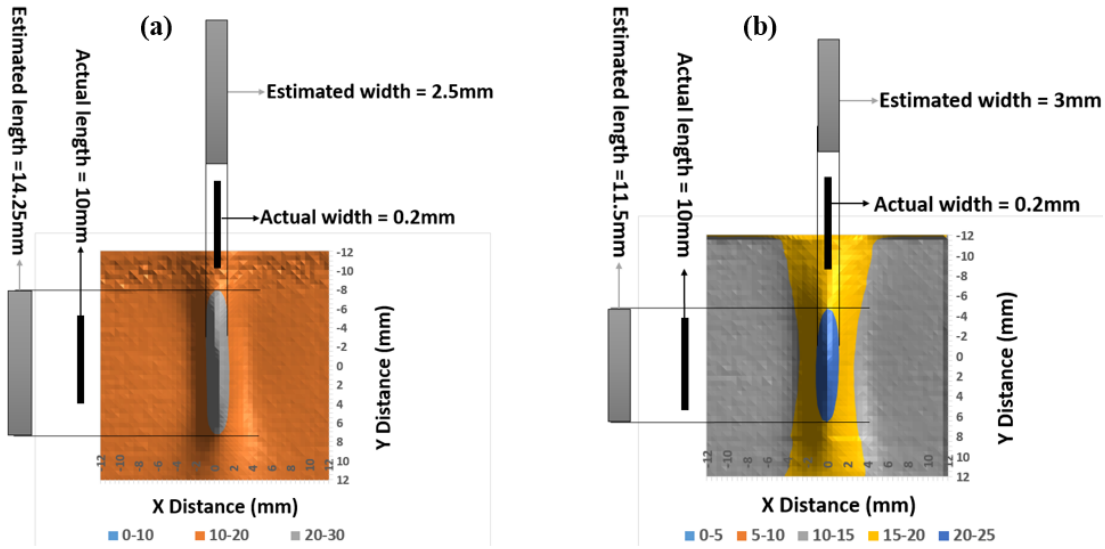

Figure 5.42. The measured PMFL crack signal ($\boldsymbol{B_{xb}}$) for; a) a 4mm deep surface hairline crack and b) a 4mm deep far-surface hairline crack.

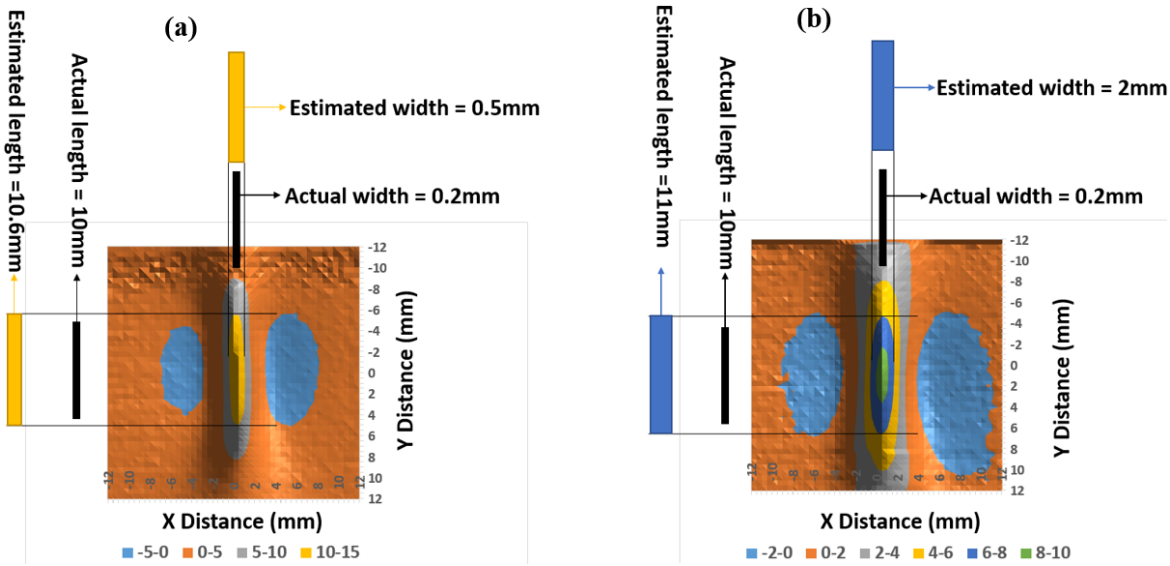

Figure 5.43. The measured PMFL differential crack signal ($\Delta\boldsymbol{B_{xb}}$) for; a) a 4mm deep surface hairline crack and b) a 4mm deep far-surface hairline crack.

The experimental results displayed in this section show that the approximate length and width of both surface and far-surface hairline cracks could be obtained from the width of the differential leakage field signal along the width and length directions respectively. Also, the estimated width for the far-surface hairline crack was found to

be far larger than the actual crack width, when compared to the estimated width for a surface hairline crack of the same size. This is attributed to the lateral spread of leakage field at the far-surface crack region. Moreover, it was not possible to obtain the depth size of the hairline cracks by just using the signal width in the length and width directions, since the signal width in the length and width directions barely changed with crack depth.

A typical response of the PMFL sensor in the axial ($\boldsymbol{B_x}$) direction due to a 4 mm deep surface hairline crack and a 4 mm deep far-surface hairline crack is displayed in Fig. A.6 and Fig. A.7 in appendices A, showing the crack signals ($\boldsymbol{B_{xb}}$) and the differential crack signals ($\Delta\boldsymbol{B_{xb}}$) respectively. Here a scan step size of 0.1 mm is used instead of the initial 0.5 mm scan step size, thereby, ensuring a better measurement precision (spatial resolution) and accuracy of the data collected from the Hall Effect sensor over the entire scanned area.

5.6) Main Issues of the PMFL Investigation

According to the simulation results presented in Fig. 5.9a and Fig. 5.9b of section 5.3.1.3, the newly developed PMFL inspection system was not able to separate a 4 mm deep far-surface hairline crack from 0.2 mm and 0.4 mm deep surface hairline cracks (i.e. unable to discriminate between a shallow surface hairline crack and a deep far-surface hairline crack). Also, the system struggled at detecting 0.2 mm deep (SNR = 0.15 dB (sensitivity)) and 0.4 mm deep (SNR = 0.30 dB (sensitivity)) far-surface hairline cracks, located 9.8 mm and 9.6 mm respectively below the surface of a 10 mm thick plate. Based on the experimental results presented in Fig. 5.37 of section 5.4.3, there was an overlap in surface and far-surface MFL values, which means that the newly developed PMFL inspection system is unable to separate surface hairline cracks from far-surface hairline cracks accurately. Moreover, based on the feature extraction investigation for crack shape and size evaluation presented in section 5.5, the simulation and experimental results show that the PMFL inspection system cannot obtain the approximate depth size of the inspected surface and far-surface hairline cracks, while using the $\boldsymbol{B_x}$, $\boldsymbol{B_y}$ and $\boldsymbol{B_z}$ leakage field

distribution (field profile). This is because the $\boldsymbol{B_x}$, $\boldsymbol{B_y}$ and $\boldsymbol{B_z}$ spread was unaffected by changes in crack depth.

5.7) Thermal Effects Induced via DCMFL and PMFL Methods

Adequate magnetization is key to a successful MFL inspection. The existing hairline cracks will not leak enough magnetic flux to be detected when the pipe wall is poorly magnetized. Hence, the magnetization power of the MFL system is a crucial factor influencing the MFL system's accuracy and reliability. Nevertheless, practical problems such as overheating of the excitation coil, excitation yoke and test sample (pipe) could arise while using a strong magnetization, especially in areas with high resistance and regions with small cross-sectional area. Therefore, special considerations should be taken in selecting the best magnetization level and technique in order to reduce or completely eliminate the problem of overheating.

This section compares the thermal effect caused by the DCMFL and PMFL inspection techniques. It provides a step towards quantifying the heating effect produced by the newly developed DCMFL and PMFL inspection systems, through the analysis of the temperature change at different time intervals. The inspection and analysis was carried out with the aid of a FLIR C2 compact thermal imaging camera as shown in Fig. 5.44. The camera was used to capture the thermal images of the inspection system as well as the test sample during the inspection process. The camera has dimensions of 125 mm × 80 mm × 24 mm with a display resolution of 320 × 240 pixels. It also has an IR camera 80 mm × 60 mm sensor, which can capture thermal measurements in the range of -10 °C to 150 °C, with a sensitivity less than 0.1 °C.

Figure 5.44. A picture of the FLIR C2 compact thermal imaging camera used for the thermal investigation.

In order to analyze the heating effect of the proposed systems, an area scan in the vicinity of a 4 mm deep surface hairline crack was performed, using the DCMFL and PMFL inspection systems. The scan area used was a surface of 20 mm × 20 mm, with a constant scan step size of 0.5 mm in the x and y directions, as shown in Fig. 4.46h. It took about 69 mins to scan the entire area while using both the DCMFL and PMFL inspection systems. The temperature level and distribution pattern around the inspection system as well as in the test sample were captured at time intervals; t = 5 min, 10 mins, 20 mins, 30 mins, 40 mins, 50 mins and 60 mins, using the FLIR C2 camera. Fig. 5.45 shows the thermal images of the heating effect produced while using a direct excitation current of 4 A (see Fig. 5.45a), a pulsed current with a pulse period of 500 ms and pulse width of 250 ms (see Fig. 5.45b) and a pulsed current with a pulse period of 500 ms and pulse width of 25 ms (see Fig. 5.45c). As expected, most of the heat was produced around the excitation coil compared to other areas of the measurement system and sample. Fig. 5.46 shows a plot that compares the heating effect produced by the DCMFL and PMFL inspection systems with respect to time. It can be observed that the temperature increases with scan time, with greater heating rate occurring during the initial part of the scan. A maximum temperature of 56.8 °C, 40.9 °C and 30.7 °C was recorded at t = 60 mins while using the DCMFL inspection system, the PMFL inspection system with a pulse width of 250 ms and the PMFL inspection system with a pulse width of 25 ms respectively. This shows that the heating effect is significantly reduced in the PMFL system. Reductions of 28 % and 50 % in the finial temperature were observed for pulse widths of 250 ms and 25 ms respectively.

(a)

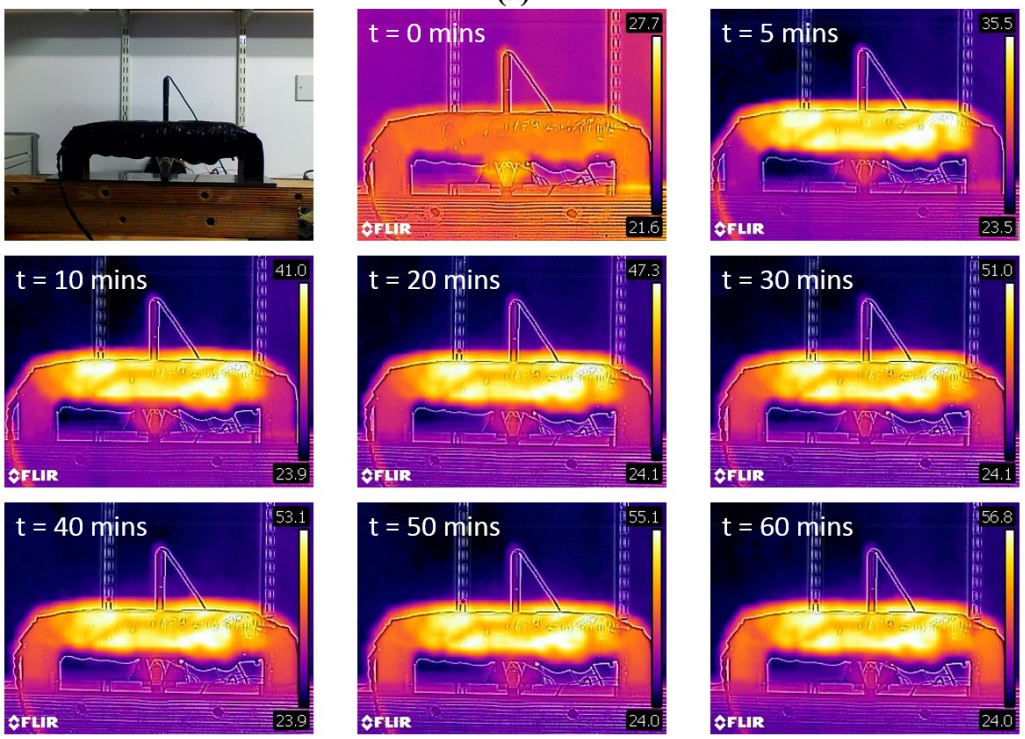
t = 0 mins
27.7
21.6
t = 5 mins
35.5
23.5
t = 10 mins
41.0
23.9
t = 20 mins
47.3
24.1
t = 30 mins
51.0
24.1
t = 40 mins
53.1
23.9
t = 50 mins
55.1
24.0
t = 60 mins
56.8
24.0
FLIR

(b)

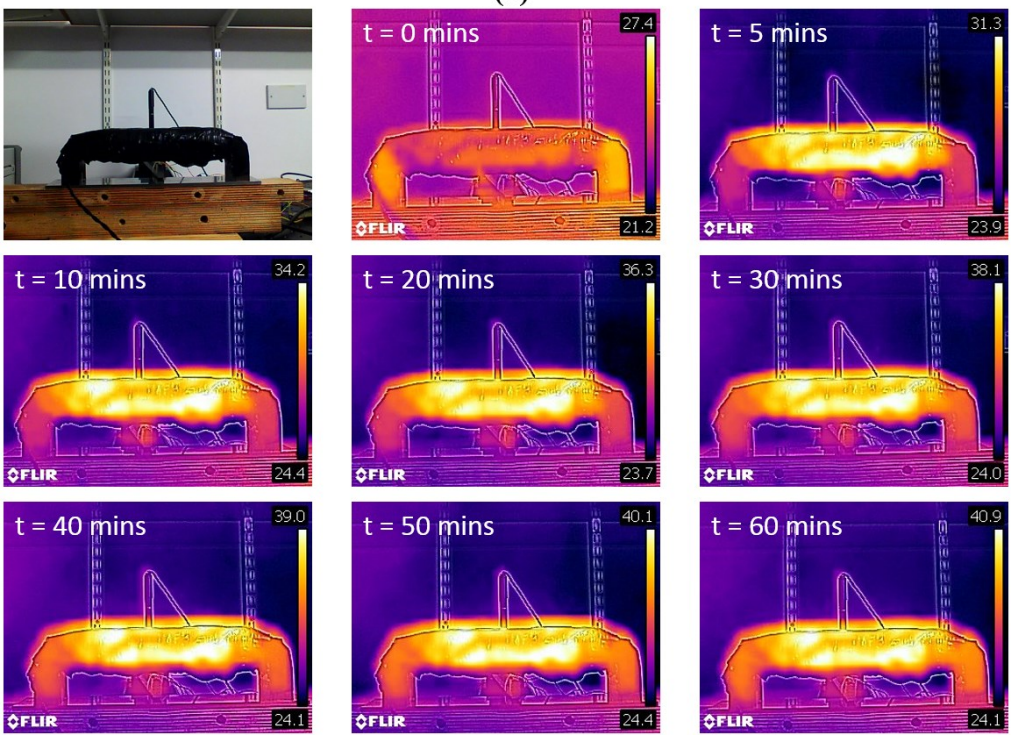
t = 0 mins
27.4
21.2
t = 5 mins
31.3
23.9
t = 10 mins
34.2
24.4
t = 20 mins
36.3
23.7
t = 30 mins
38.1
24.0
t = 40 mins
39.0
24.1
t = 50 mins
40.1
24.4
t = 60 mins
40.9
24.1
FLIR

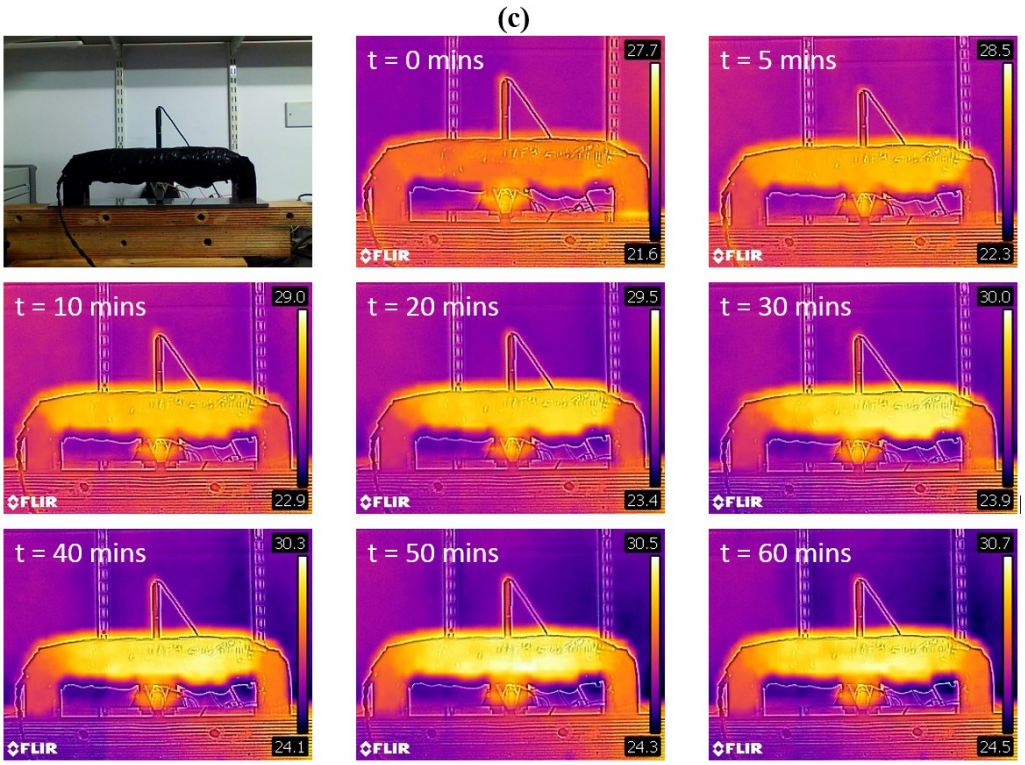

Figure 5.45. A photograph showing the temperature (°C) at different time intervals induced via a) DCMFL inspection at 4A, b) PMFL inspection with 500 ms excitation pulse period and 250 ms pulse width and c) PMFL inspection with 500 ms excitation pulse period and 25 ms pulse width.

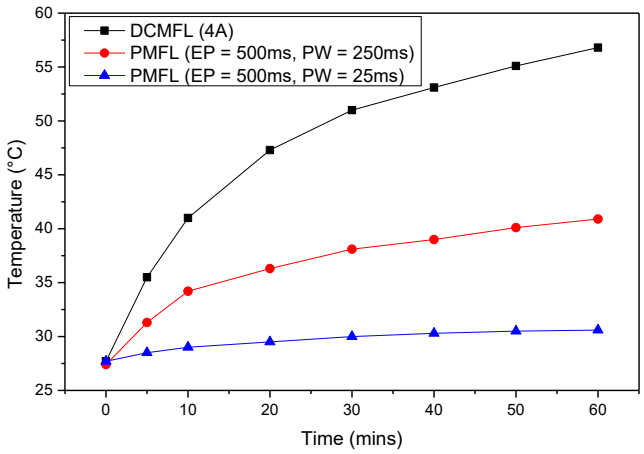

Figure 5.46. A plot showing the measured system temperature (°C) as a function of time for; a) DCMFL inspection at 4A, b) PMFL inspection with 500 ms excitation pulse period and 250 ms pulse width and c) PMFL inspection with 500 ms excitation pulse period and 25 ms pulse width.

Therefore, the newly developed PMFL inspection system has an advantage of a reduced power consumption and thermal effects for hairline crack detection and

characterization, compared with the constant powering of the excitation yoke and coil (DCMFL). Hence, there will be no need to cool down the inspection system for longer inspecting periods while using the newly developed PMFL inspection system (suitable for inspecting long pipelines).

5.8) Effect of Neighbouring Cracks on the Detection Sensitivity of Hairline Cracks

The leakage field signal measured from cracks that are close to one another could misguide to the assumption that a cluster of cracks is a single standalone crack. Therefore, for a particular hairline crack, the presence of multiple nearby cracks in either direction could lead to a misinterpretation of the acquired leakage field amplitude. This could make the characterization and sizing of both surface and far-surface hairline cracks difficult. Hence, such clusters of cracks should be evaluated as special cases while performing the characterization and quantification task.

This section investigates the influence of neighbouring cracks (nearby cracks) on the detection sensitivity to surface and far-surface hairline cracks, using the PMFL experimental technique. The inspection and analysis is carried out using the $\boldsymbol{B_x}$ leakage field component. The rectangular hairline cracks inspected consists of five identical EDM slots made on the surface and on the reverse side of a 10 mm thick plate. The hairline cracks are perfectly aligned with each other and positioned perpendicular to the field orientation. The centre separation between the five artificially fabricated hairline cracks are; d_1 = 1 mm, d_2 = 2 mm, d_3 = 5 mm, d_4 = 10 mm and d_5 = 20 mm. All the hairline cracks inspected has a depth of 4 mm, width of 0.2 mm and length of 10 mm. Fig. 5.47a shows a schematic diagram clearly illustrating the test plate used, alongside the five neighbouring hairline cracks with their respective centre spacing. A photograph of the test plate with hairline cracks after fabrication is displayed in Fig. 5.47b.

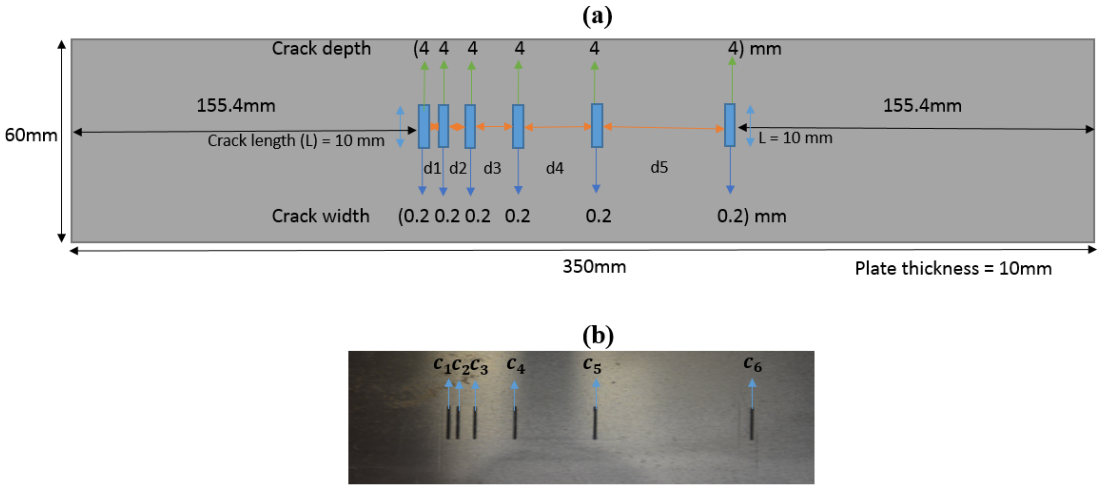

Figure 5.47. Showing a) a schematic layout of the test plate used, alongside the five different neighbouring hairline cracks inspected (d = 4 mm, w = 0.2 mm and l = 10 mm) and b) a photograph of the test plate with the existing hairline cracks after fabrication.

The Hall Effect sensor was scanned across the hairline cracks, with a constant scan step size of 0.5 mm and a constant sensor lift-off of 0.5 mm. The differential leakage field signal was acquired across the scanned region, using an excitation pulse period of 500 ms and pulse width of 250 ms. Fig. 5.48 and Fig. 5.49 shows a time domain representation of the measured differential leakage field amplitude ($\Delta \boldsymbol{B_{xb}}$) across the surface and far-surface hairline cracks respectively. As can be observed, both plots show the distinctive change in the pulse shape as the sensor moves over the hairline cracks. The results displayed for the surface and far-surface hairline cracks are similar, except that the leakage signal amplitude measured for the surface cracks is higher and narrower than that of the far-surface cracks. The acquired leakage field signal varies with relative position of the sensor to the crack axis. The highest signal amplitude is measured at the centre of each hairline crack, while the lowest signal amplitude is measured at the edges between the cracks, as the sensor approaches and leaves the cracks (i.e. a dip at both ends of each hairline crack).

Most importantly, the acquired leakage field ($\Delta \boldsymbol{B_{xb}}$) amplitude is found to increase as the distance of separation (crack spacing (d_n)) between the surface and far-surface hairline cracks increases. Moreover, the leakage field amplitude produced by the first three hairline cracks (i.e. c_1, c_2 and c_3) separated by d_1 = 1 mm and d_2 = 2 mm merges together. The merging of the leakage fields produced by the three identical hairline cracks as portrayed in Fig. 5.48 and Fig. 5.49 could be

misinterpreted to be a leakage field emerging from a single standalone crack (i.e. a single-wide crack). This could result in serious errors in the sizing (geometrical calculation) of such hairline cracks. The leakage field merging phenomena can be seen clearly in Fig. 5.50, which shows the measured $\Delta \boldsymbol{B_{xb}}$ amplitude obtained at t =153.75 ms as a function of scanning distance, for both the surface (see Fig. 5.50a) and far-surface (see Fig. 5.50b) hairline cracks. As can be seen, the leakage field signal produced by the first three hairline cracks merges and appears as though it was caused by a single standalone wide crack.

In addition, both plots (Fig. 5.50a and Fig. 5.50b) show that the detected leakage field ($\Delta \boldsymbol{B_{xb}}$) amplitude increases with increasing crack spacing (d_n), for cracks of identical size, shape and orientation. For the surface hairline cracks, a peak amplitude ($\Delta \boldsymbol{B_{xb}^{Peak}}$) of 8.5 mT, 11.2 mT and 13.2 mT was recorded for C_4, C_5 and C_6 respectively. This shows that a 10 mm increase in the surface crack spacing causes a 24 % increase in the measured leakage field amplitude, while a 20 mm increase in the surface crack spacing causes a 15 % increase in the measured leakage field amplitude. Also, for the far-surface hairline cracks, a peak amplitude ($\Delta \boldsymbol{B_{xb}^{Peak}}$) of 6.6 mT, 8.8 mT and 10.8 mT was recorded for C_4, C_5 and C_6 respectively. This shows that a 10 mm increase in the far-surface crack spacing causes a 25 % increase in the measured leakage field amplitude, while a 20 mm increase in the far-surface crack spacing causes an 18 % increase in the measured leakage field amplitude. Moreover, a greater percentage increase in the measured leakage field peak amplitude ($\Delta \boldsymbol{B_{xb}^{Peak}}$) occurs for shorter crack spacing (d_4 = 10 mm) compared to longer crack spacing (d_4 = 20 mm).

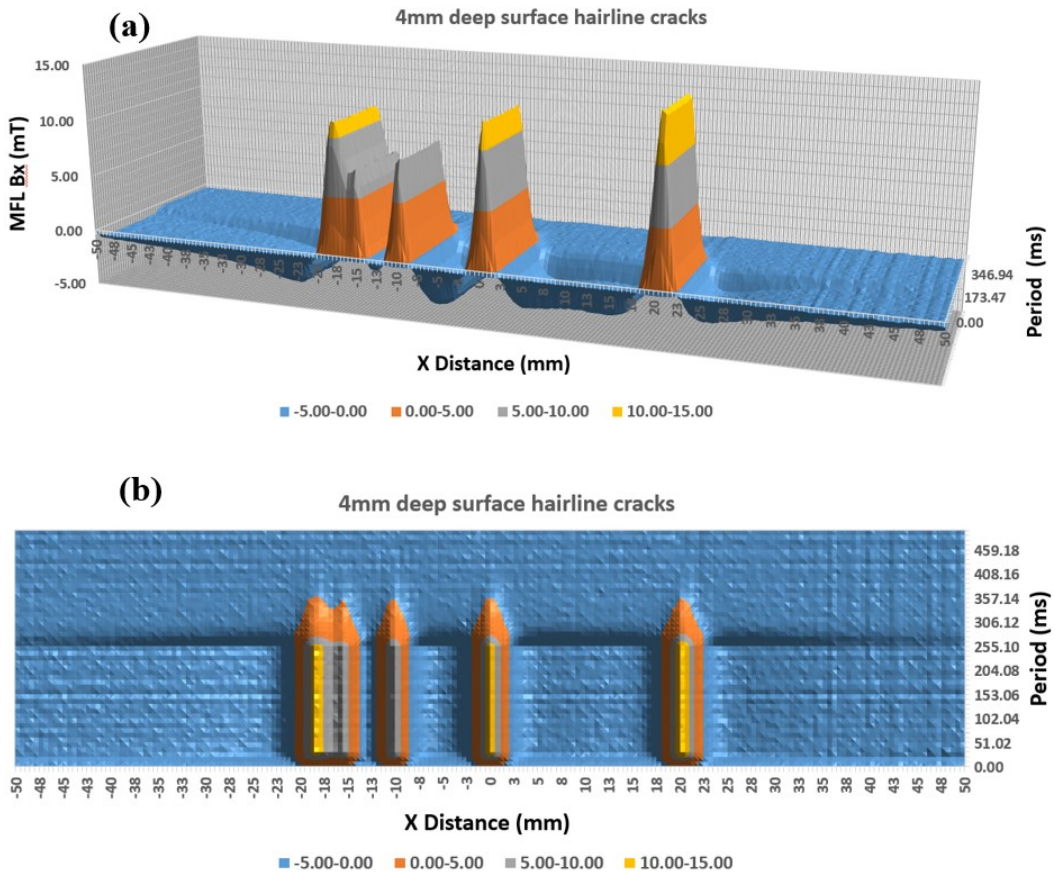

Figure 5.48. Time domain representation - A line scan of the measured differential leakage field distribution ($\Delta \boldsymbol{B}_{xb}$), illustrating the effect of neighbouring hairline cracks on the acquired leakage field amplitude; a) 4mm deep surface hairline cracks, b) Top view of the 4mm deep surface hairline cracks.

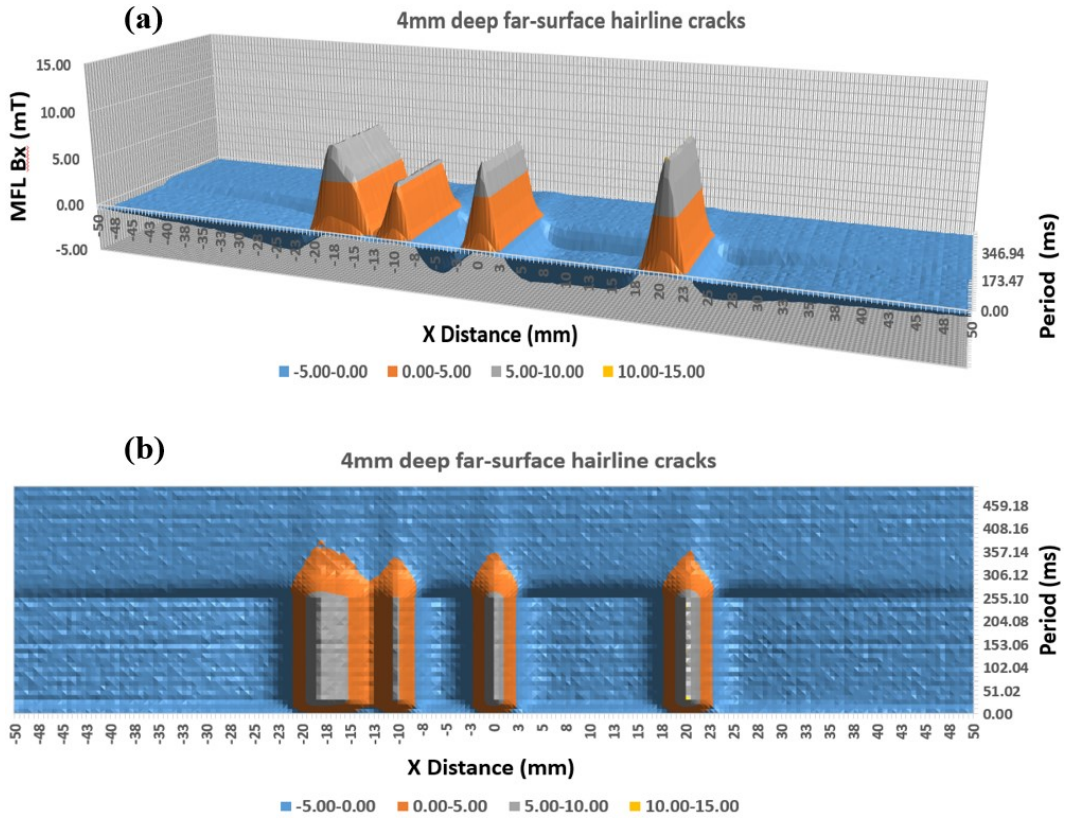

Figure 5.49. Time domain representation - A line scan of the measured differential leakage field distribution ($\Delta \boldsymbol{B_{xb}}$), illustrating the effect of neighbouring hairline cracks on the acquired leakage field amplitude; a) 4mm deep far-surface hairline cracks, b) Top view of the 4mm deep far-surface hairline cracks.

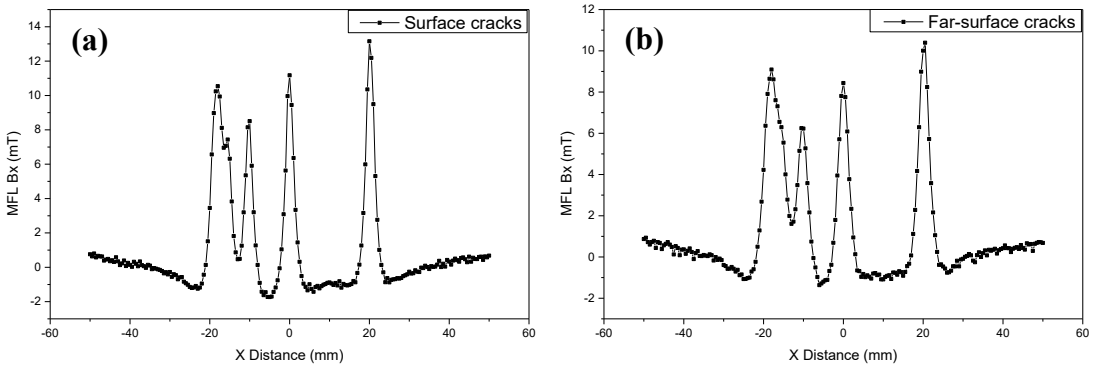

Figure 5.50. The measured differential leakage field amplitude ($\Delta \boldsymbol{B_{xb}}\ at\ t = 153.75$ ms) obtained at the centre of each hairline crack as a function of scanning distance, illustrating the effect of neighbouring hairline cracks on the acquired leakage field amplitude; a) 4 mm deep surface hairline cracks and b) 4 mm deep far-surface hairline cracks.

Therefore, the presence of neighbouring cracks influences the amplitude and distribution pattern of the acquired leakage field from both surface and far-surface hairline cracks. The greatest effect occurs when the existing nearby cracks are located very close to the hairline crack under scrutiny. This is because, there will be an increase in the measured leakage field amplitude or a merging of the leakage fields from all the nearby cracks. Thus, causing a misinterpretation of the true leakage field amplitude, which could result in a misrepresentation of the hairline crack features and parameters.

5.9) Comparison between the DCMFL and PMFL Inspection Results

Table 5.6. A comparison of the main results obtained while using the newly developed DCMFL and PMFL inspection systems (practical experiments).

Parameters	DCMFL Inspection	PMFL Inspection
Excitation parameters	Generated sufficient leakage field to be detected while using a direct excitation current of 4 A.	Generated sufficient leakage field to be detected while using an excitation pulse period of 500 ms with a pulse width of 25 ms or 250 ms.
Detection limit (crack size and location).	Detected a 0.2 mm deep surface and 0.6 mm deep far-surface hairline cracks.	Detected a 0.2 mm deep surface and 0.4 mm deep far-surface hairline cracks.
Detection limit (sensor lift-off).	Maintained a good detection sensitivity up to a lift-off of 5 mm.	Maintained a good detection sensitivity up to a lift-off of 9 mm.
Power consumption (thermal effect).	Maximum heating of 56.8 °C at 60 mins scan time.	Maximum heating of 40.9 °C (PW= 250 ms) and 30.7 °C (PW= 25 ms) at 60 mins scan time.
Percentage Error (repeatability).	0.9 % and 0.23 % error for surface and far-surface measurements respectively.	2.4 % and 1.7 % error for surface and far-surface measurements respectively.

5.10) Feasibility for Implementation of Hairline Crack Detection and Characterization via PMFL Method

The results presented in this chapter via FEM numerical modelling and practical experiments has contributed to the PMFL capabilities for an effective detection and characterization of surface and far-surface hairline cracks. Moreover, with the benefit of an improved magnetic field penetration as a result of the rich frequency components present in the excitation pulse signal, its practicality for an improved characterization and quantification of hairline cracks has been established. According to the simulation and experimental findings, it has been demonstrated that hairline cracks present on the surface and far-surface of ferromagnetic pipeline structures can generate sufficient magnetic field to be detected using the newly developed PMFL system, while operating with an excitation pulse period of 100 ms or 500 ms with a constant duty cycle of 50 % and a pulse width of 25 ms, 50 ms, 100 ms and 250 ms with a constant excitation period of 500 ms

As reported in section 5.4.3, the newly developed PMFL inspection system is able to detect a surface hairline crack with a depth of 0.2 mm, width of 0.2 mm and length of 10 mm, in a 10 mm thick pipeline, with a signal to noise ratio of 0.44 dB. Also, the system is capable of showing an indication of a far-surface hairline crack with a depth of 0.4 mm, width of 0.2 mm and length of 10 mm, located 9.6 mm below the surface of a 10 mm thick pipeline, with a signal to noise ratio of 0.3 dB. The maximum percentage error recorded for the surface and far-surface hairline cracks were 2.4 % and 1.7 % (repeatability) respectively, which shows a high measurement precision of the data collected from the sensor over the inspected area

The well-optimized PMFL inspection system can be effectively used in pipeline industries to detect and characterize various hairline cracks according to their depth sizes, using the acquired leakage field amplitude, distribution pattern and the peak arrival time of the leakage field signals (forward problem), with a reduced energy consumption and thermal effects compared to the traditional MFL techniques. The extraction of hairline crack features and parameters (crack reconstruction) can be achieved through the method of visualization and 3D rapid imaging of the leakage field distribution pattern, using the inverse problem technique. The imaged features

can then be used to evaluate the shape, location and size (length and width) of existing surface and far-surface hairline cracks. The identification and estimation of hairline crack features will be implemented using an image recognition software such as LabVIEW, which allows for real time data of the scan to be viewed and monitored as the inspection progresses. The newly developed PMFL inspection system also has an advantage of a reduced power consumption and thermal effects compared to the traditional MFL testing methods (i.e. 50 % heat reduction compared to the DCMFL system). Thus, making the new system more suitable for inspection of long pipelines with large cross-sectional areas. In addition, the developed PMFL system is able to detect and characterize surface and far-surface hairline cracks at a sensor lift-off of 9 mm, thereby making it very effective and beneficial in applications where large lift-off distances between the sensor and pipe surface is required.

One major drawback for the practical application of the newly developed PMFL inspection system is the inability to separate all the surface hairline cracks inspected from the far-surface hairline cracks, as a result of the overlap in the surface and far-surface leakage field values. Another major drawback is the inability to obtain an approximate size of the hairline crack depth, using just the signal width in the length and width directions. This is attributed to the fact that the leakage field distribution pattern in the length and width directions are almost unaffected by variation in crack depth. Therefore, an alternative method has to be established and used in order to ascertain the corresponding depth size of hairline cracks, as well as to accurately separate the existing surface hairline cracks from the far-surface hairline cracks.

Also, for the practical implementation of the PMFL method for hairline crack detection and characterization, the magnetic sensor array approach could be utilized for a better visualization and imaging of hairline crack features and geometries. The array system provides a greater measurement coverage, which would prevent cracks from being missed, especially hairline cracks. With regards to the visualization and imaging of hairline crack features through the use of magnetic sensor array topology, the commercially available sizes of magnetic sensors (width = 3 mm and above), result in low spatial resolution for the experimental implementation of the PMFL testing [3-6]. High spatial resolution is required in order to accurately detect slight

variations in the hairline crack features so as to utilize the features extracted from the imaged leakage field distribution, for an accurate characterization and quantification. Besides the high price of designing the magnetic sensor array, the implementation of the array technique means that the sensing topology will be rigid, hence, this flexibility limitation of the array design becomes a drawback when testing structures with non-uniform surfaces [5]. Another limitation of the magnetic sensor array configuration is that it can result in electrical interference, which could lead to a distortion and misinterpretation of the resultant leakage field signals, as well as causing a degradation in the signal to noise ratio [5], especially for the feeble magnetic field signals from far-surface hairline cracks. Hence, the visualization and imaging of the magnetic field signals in real time will be unattainable, which could result in a decreased testing efficiency.

5.11) Chapter Summary

The FEM numerical modelling and experimental PMFL inspection techniques for detecting and characterizing surface and far-surface hairline cracks, based on visualization and 3D imaging of the resultant leakage field distribution has been performed, for various hairline cracks located at different depths within a 10 mm thick plate. First, the influence of excitation pulse period variation (see section 5.3.1.1) and pulse width variation (see section 5.3.1.2) on the inspection output were investigated via FEM simulation, using the MagNet software by Infolytica. The model-predictions (transient responses) were supported and validated using practical experimental results (see section 5.4.2.2 and section 5.4.2.3). The results obtained from both approach suggests that the use of longer excitation periods (100 ms and 500 ms) enable for deeper magnetic field penetration within the test sample, which is suitable for the detection and characterization of both surface and far-surface hairline cracks. Also, both the predicted and measurement results showed that narrower pulse widths (5 ms and 10 ms) are more suitable for detecting and characterizing surface hairline cracks, since they are mostly made up of high frequency components, which limits the induced magnetic field around the test sample surface. However, for hairline cracks located further away from the sample surface, wider pulse widths are

preferable, because of the dominance of low frequency components towards the end of the excitation pulse corresponding to both surface and far-surface features.

The PMFL experimental results show that hairline crack quantification can be achieved by studying and extracting the features contained in the imaged leakage field distribution. Also, through the imaging of the resultant leakage fields, various information corresponding to the crack type, shape, size (length and width) position and orientation can be extracted. In addition, the predicted and measured PMFL transient responses, such as; a) amplitude variation in time domain, b) time to peak variation, and c) amplitude analysis in frequency domain, have proven to provide additional useful information for hairline crack discrimination, based on their individual depth sizes as well as their locations within the test specimen. The PMFL sensor was able to detect a 4 mm deep surface hairline crack and a 4 mm deep far-surface hairline crack up to a lift-off distance of 9 mm. Furthermore, the results gathered from the investigation revealed that the presence of neighbouring cracks have a significant influence on the inspection output (affects the leakage field amplitude and distribution pattern). That is; the leakage field amplitude increases with increasing crack spacing and the rate of increase is greater for a shorter crack spacing compared to a longer crack spacing. Also, the leakage field from hairline cracks, which are very close to each other could merge together, leading to difficulties in hairline crack characterization and sizing. The maximum percentage error recorded for the surface and far-surface measurements while using the newly developed PMFL inspection system were 2.4 % and 1.7 % respectively.

Moreover, the newly developed PMFL inspection system produced a maximum heating of 40.9 °C and 30.7 °C at a scan time of 60 mins, while operating with an excitation pulse period of 500 ms with a pulse width of 250 ms and 25 ms respectively. That is; 28 % (PW = 250 ms) and 50 % (PW = 25 ms) heat reduction compared to the DCMFL inspection system (56.8 °C). The advantage of the pulsed method used in this case is a significant reduction in the power consumption and thermal effects for hairline crack detection and characterization, compared with the constant powering of the excitation yoke and coil (DCMFL). Hence, eliminating the need to cool down the excitation coil for longer inspection periods. The newly developed and optimized PMFL inspection system was able to detect as small as a

0.2 mm deep surface hairline crack (2 % surface wall loss) via practical experiments, while using an excitation pulse period of 500 ms and a pulse width of 250 ms. However, the system was not able to detect a 0.2 mm deep far-surface hairline crack (2 % deep far-surface wall losses) located 9.8 mm below the sample surface. Another limitation of the newly developed PMFL measurement tool is the inability to separate all the surface hairline cracks from the far-surface hairline cracks and to provide an approximate depth size of the inspected hairline cracks, using just the imaged leakage field distribution pattern. Therefore, an alternative means to accurately separate surface cracks from far-surface cracks and to visualize or map out the corresponding depth size of hairline cracks has to be established, in order to overcome these limitations.

5.12) References

1) J. Wilson and G. Y. Tian, "Pulsed Electromagnetic Methods for Defect Detection and Characterization". *NDT & E International* 40(4), 275-283 (2007).
2) J. Wilson, M. Kaba and G. Y. Tian, "New Techniques for the Quantification of Defects through Pulsed Magnetic Flux Leakage". School of Electrical, Electronic and Computer Engineering, *Merz Court, University of Newcastle upon Tyne*, Newcastle, NE1 7RU, UK.
3) NVE Corporation, "GMR sensors data book". [Online]. Available at: http://www.cs.cmu.edu/~sensing-sensors/readings/GMR_magnetic_sensor_databook.pdf. [Accessed 3 Sept. 2016].
4) Honeywell International, "1- and 2- axis magnetic sensors". [Online]. Available at: http://www.honeywell.com/sites/servlet/com.merx.npoint.servlets.DocumentServlet?docid=D5169116C-67A8-D99E-0995-FAD409AFC81D. [Accessed 3 Sept. 2016].
5) I. M. Z. Abidin, "Modelling and Experimental Investigation of Eddy Current Distribution for Angular Defect Characterisation". In Electrical, Electronic and Computer Engineering. Volume, *PhD Newcastle upon Tyne: Newcastle University,* (2010).
6) W. Singh et al. "Flexible GMR Sensor Array for Magnetic Flux Leakage Testing of Steel Ropes". *Journal of sensors*, 1-6, (2012).

Chapter 6: Conclusions and Future Work

This chapter will summarize the current investigation and conclusions are made regarding the ability of the techniques used in providing a satisfactory QNDE of hairline cracks present in ferromagnetic steel pipelines. Also, the possible future directions for this work are presented, with respect to the FEM numerical simulations as well as the experimental approach for hairline crack detection and characterization.

6.1) Conclusions

In this research, an axial MFL-type NDE system was developed, based on direct current (DCMFL) and pulsed current (PMFL) techniques, to detect and characterize tangentially oriented hairline cracks in underground pipelines, which are too difficult to be detected using the existing MFL systems [1-5]. This was achieved by adopting the method of visualization and imaging of the resultant leakage field distribution generated by the existing hairline cracks. Useful information such as; the type, orientation, shape and size of various hairline cracks have been extracted using the features embedded in the imaged leakage field distribution, via the FEM numerical simulation approach. The simulation findings were confirmed using experimental measurements. The experimental results were also used to assess the feasibility for implementation of the proposed system as well as its capability to provide useful information necessary for practical use in obtaining vital information about hairline cracks. It is expected that the findings from this research would benefit the oil, gas and petrochemical industries, as well as the NDE community as a whole in the detection and characterization of real-life (natural occurring) hairline cracks.

The major contributions and conclusions of this work are summarised in detail as follows:

6.1.1) 3D FEM Computation of DCMFL and PMFL Investigations on Hairline Cracks

In order to investigate the possibility of detecting and characterizing hairline cracks present in ferromagnetic pipeline structures, the 3D FEM numerical computation approach was employed due to its obvious advantages compared to the analytical approach. The advantages are; it computes a wide range of physics and geometry, improves the accuracy of the approximated solution of a problem, solves non-linear problems, inspects materials with complex defect shapes and inspects materials with non-uniform surfaces. In this project, the expected output from the magnetic field interaction with hairline cracks present in a pipeline structure is predicted, via a series of simulations conducted in the 7.6 MagNet software by Infolytica. Also, the imaging of the resultant leakage field distribution due to the existing hairline cracks has been implemented using both the DCMFL and PMFL techniques. The study and evaluation of the simulation results has assisted in creating a link between the acquired information and the orientation, 3D shape, size (length and width) and location of interacting hairline cracks. Also, the simulation results have helped in solving both the forward and inverse problems as well as assisting in the experimental probe design, experimental setup, pattern identification, crack quantification and reconstruction of hairline cracks for DCMFL and PMFL testing. The details are outlined below:

- Since the magnetization and sensing power are the crucial factors influencing the MFL inspection system reliability, an FEM simulation was performed in order to optimize the experimental parameters, thereby, improving the overall system performance. The optimized parameters included; the yoke shape, yoke parameters (geometry), yoke permeability, yoke clearance from the test sample surface (yoke lift-off), sensor lift-off and the magnetization current. The optimization of these parameters helped in achieving the largest possible sensor signal variation at the hairline crack vicinity, especially for the feeble signals generated by the far-surface hairline cracks.

- The DCMFL and PMFL numerical predictions has provided an understanding of the underlying phenomena controlling the magnetic field distribution within a test sample, as well as the acquired leakage field signatures due to the presence of surface and far-surface hairline cracks. This was identified through the visualization of the simulated graphical results. Crack features were extracted with respect to the change in field profile (i.e. the $\boldsymbol{B_x}$, $\boldsymbol{B_y}$, $\boldsymbol{B_z}$ spread) caused by the variation in the crack geometries and location within the test sample. The extracted features were then critically analyzed and used to obtain useful information regarding the crack shape and size (length and width). The width and length of the surface and far-surface hairline cracks were estimated by analyzing the 3D imaged leakage field distribution pattern (signal width) in the width and length directions respectively.

- For the DCMFL approach, the model predictions were used to provide a quantitative assessment of the various hairline cracks simulated in terms of their orientation, shape, size and location within the test sample. This was achieved by; a) measuring the strength of the axial, radial and tangential components of the leakage fields emerging from both surface and far-surface hairline cracks. b) through an enhanced visualization and rapid 3D imaging of the resultant leakage field distribution. The simulated DCMFL results showed that the magnitude of the leakage field generated by a surface or a far-surface hairline crack is strongly dependent on the ratio of both the crack depth and crack width to the pipe wall thickness.

- Additional means of characterizing the various hairline cracks was provided using the information contained in the PMFL transient responses such as the; a) amplitude variation in time domain, b) time to peak variation and c) amplitude analysis in frequency domain. The simulated PMFL results also showed that the use of longer excitation pulse periods (100 ms and 500 ms) permits for deeper magnetic field penetration inside the pipeline structure, which is suitable for the detection and characterization of both surface and far-surface hairline cracks. However, the use of shorter excitation periods (1 ms, 5 ms, 10 ms and 20 ms) limits the magnetic field to the pipe surface, which is more suitable for the

detection and characterization of surface hairline cracks. Furthermore, the simulation results demonstrated that narrower pulse widths (5 ms and 10 ms) are best suited for the detection and characterization of surface hairline cracks, while wider pulse widths (25 ms, 50 ms, 100 ms and 250 ms) allow for the detection and characterization of both surface and far-surface hairline cracks.

The information needed for the study and analysis of hairline cracks present in ferromagnetic pipeline structures have been successfully identified using 3D FEM numerical simulation of DCMFL and PMFL inspection techniques. The simulated results have helped greatly in accomplishing the aims and objectives of this project. Also, the basis for further work for an efficient QNDE on hairline cracks can be provided using the 3D FEM numerical simulation technique.

6.1.2) Experimental Validation of the Simulated Results

In chapter 4, the experimental findings from the DCMFL inspection showed good agreement with the simulated results (i.e. experimental results were within 10 % of the simulated results), in terms of the detectability, leakage field amplitude obtained and characterization of the various surface and far-surface hairline cracks, with respect to their sizes and locations within the test sample. The simulation and experimental findings showed that the magnitude of the acquired leakage field signal due to the presence of either a surface or far-surface hairline crack is significantly influenced by the ratio of the crack depth and the crack width to the sample thickness. The hairline crack features extracted using the simulation technique have been validated with ferromagnetic low carbon steel plates, with well-defined EDM hairline slots. Vital features (crack signature, orientation, shape, size and location) were extracted through visualization and rapid 3D imaging of the resultant leakage field distribution in the vicinity of various hairline cracks and comparisons were made with the simulated results. The optimized DCMFL inspection system was able to improve the detection sensitivity of the experimental measurement significantly, by detecting as small as a 0.2 mm deep (width = 0.2 mm, length = 10 mm) surface hairline crack and a 0.6 mm deep (width = 0.2 mm, length = 10 mm) far-surface

hairline crack, located 9.4 mm below the surface of a 10 mm thick plate. The maximum percentage error recorded for the surface and far-surface measurements while using the newly developed DCMFL inspection system were 0.9 % and 0.23 % (repeatability) respectively. Also, the DCMFL inspection system was able to maintain good sensitivity for inspecting hairline cracks up to a sensor lift-off of 5 mm, which makes the newly developed system beneficial for applications where a large clearance is required between the sensor and the measurement surface. However, due to the continuous powering of the excitation coil and yoke, the DCMFL inspection system suffered from overheating producing a temperature of 56.8 °C after a 60-minute scan time, thereby, necessitating cooling of the system, especially for longer inspection periods (not suitable for inspecting long pipes). Also, the DCMFL system was unable to separate the surface hairline cracks from the far-surface hairline cracks, due to an overlap in the surface and far-surface leakage field values measured

In chapter 5, the PMFL technique of NDE was carried out on real test samples, with artificially fabricated hairline cracks. The results obtained showed that the effectiveness of detecting and characterizing the various hairline cracks inspected, depends on the particular excitation pulse period and pulse width chosen. Similar to the simulated results, the experimental findings demonstrated an ability to detect and discriminate between all the surface hairline cracks and most of the far-surface hairline cracks investigated, while using a longer excitation period of 100 ms and 500 ms with a 50 % constant duty cycle, as well as a wider pulse width of 25 ms, 50 ms, 100 ms and 250 ms with a constant excitation period of 500 ms. Similar to the DCMFL investigation, the orientation, shape, size (length and width) and location of both surface and far-surface hairline cracks were extracted through visualization and rapid 3D imaging of the resultant leakage field distribution, using the PMFL inspection technique. The optimized PMFL inspection system was able to improve the detection sensitivity of the experimental measurement significantly, by detecting as small as a 0.2 mm deep (width = 0.2 mm, length = 10 mm) surface hairline crack and a 0.4 mm deep (width = 0.2 mm, length = 10 mm) far-surface hairline crack, located 9.6 mm below the surface of a 10 mm thick plate. The maximum percentage error recorded for the surface and far-surface measurements while using the newly developed PMFL inspection system were 2.4 % and 1.7 % (repeatability)

respectively. The PMFL inspection system was able to detect both a 4 mm deep surface hairline crack and a 4 mm deep far-surface hairline crack up to a sensor lift-off of 9 mm. Moreover, the results gathered from the PMFL experimental investigation revealed that the presence of neighbouring cracks have a significant influence on the inspection output. That is, the leakage field amplitude increases with increasing crack spacing and the rate of increase is greater for a shorter crack spacing compared to a longer crack spacing. Also, the experimental findings showed that the leakage fields from hairline cracks that are very close to each other could merge together, leading to difficulties in hairline crack characterization and sizing. The PMFL inspection approach was able to significantly reduce the power consumption and thermal effects by 50 %, compared to the continuous powering (overheating) of the excitation yoke and coil in the DCMFL approach.

A major limitation of the newly developed PMFL inspection system is the inability to accurately separate all the surface hairline cracks inspected from the far-surface hairline cracks, due to the overlap in the surface and far-surface leakage field values. Another limitation of the PMFL inspection system is the inability to provide an approximate depth size of the inspected hairline cracks, using just the imaged leakage field distribution pattern. Therefore, an alternative means to overcome these limitations has to be established.

6.2) Future Work

According to the research findings, the route for further work is presented in order to expand and develop the scope of the research.

6.2.1) Integration and Feature Extraction Techniques

By using the line scan technique across the various hairline cracks, vital features such as the leakage field profile and crack size (width only) were extracted, while using the DCMFL and PMFL inspection methods. Despite the fact that the line scan

technique can provide useful geometrical assessment of the crack, the leakage field distribution data is limited to single dimensional information.

An area scan was conducted and this was able to provide 2D information, using the imaged leakage field distribution at the crack vicinity. Thereby, providing additional information regarding the crack type, shape, orientation, size (both width and length), as well as allowing for easier recognition of the crack using the analyzed data. From the analyzed data, the approximate length and width of the hairline cracks was obtained by analyzing the distribution change of the flux in the length and width directions respectively. However, it was not possible to obtain the depth information of the crack using just the leakage field distribution, since the width of the acquired signals were undisturbed by the variation in crack depth. Therefore, an alternative means to visualize or map out the corresponding depth size of hairline cracks has to be employed in order to overcome this limitation.

This can be achieved by incorporating the active thermography inspection technique with the Digital Image Correlation (DIC) technique, which has been extensively used to monitor the pixel variations via a sequence of image frames [5]. The DIC technique can be used to visualize the heat diffusion within the test specimen, as well as its interaction with the crack geometries. This will provide an initial indication of the nature of the crack within the test specimen. Also, since the heat diffusion in the crack region can be monitored through variations in the pixel values, the heat propagation pattern and direction inside the test specimen could provide a complete geometrical assessment of the crack present, as well as its shape, orientation and location through an area scan analysis.

Also, the Acoustic Emission (AE) NDT technique can be exploited to detect and characterize naturally occurring Stress Corrosion Cracking (SCC) in ferromagnetic pipeline structures. Feature extraction methods such as; specimen elongation measurement, electrochemical noise, digital imaging and acoustic emission interpretation can be utilized to provide a complete geometrical evaluation of naturally occurring cracks, including its orientation and location within the inspected pipeline structure.

6.2.2) Extension of Current Research to Other Areas

Through enhanced visualization and rapid 3D imaging of the leakage field distribution pattern generated by the inspected surface and far-surface hairline cracks, it has been demonstrated in this work that the PMFL technique is an effective means of detecting and characterizing hairline cracks in pipeline structures whilst reducing power consumption and thermal effects. Therefore, the newly developed PMFL inspection system can be employed in the oil, gas, nuclear, energy and petrochemical industries in order to achieve satisfactory pipeline health monitoring, by detecting small cracks, which are initially too insignificant to cause a system breakdown, but can grow into larger cracks over time capable of threatening the pipeline integrity. The PMFL method can also be extended to other related areas such as; the inspection of storage tank floors, rail lines, bridges, aircrafts, etc. for presence of discontinuities.

The FEM numerical simulation technique employing the PMFL approach can be used as a platform to provide the initial results needed to assess such structures and components, as well as to provide an idea about the practicality of achieving the desired outcome.

6.3) References

1) W. Singh, S. Thirunavukkarasu, S. Mahadevan, B.P.C. Rao, C. K. Mukhopadhyay and T. Jayakumar, “Three-Dimensional Finite Element Modelling of Magnetic Flux Leakage Technique for Detection of Defects in Carbon Steel Plates”, *Non Destructive Evaluation Division*, Indira Gandhi Centre for Atomic Research, Kalpakkam-603102, Tamil Nadu, (2010).
2) Y. Tang et al, “Experimental and Finite Element Analysis Study of 3D Magnetic Field Sensing for Pulsed Magnetic Flux Leakage Defect Characterisation”. *Insight - Non-Destructive Testing and Condition Monitoring* 53(9), 497-506, (2011).
3) J. Wilson and G.Y. Tian “Pulsed Electromagnetic Methods for Defect Detection and Characterisation”. NDT&E *International* 40, 275–283, January (2007).
4) A. Sophian, G.Y. Tian, and S. Zairi. “Pulsed Magnetic Flux Leakage Techniques for Crack Detection and Characterisation”. *Sensors and Actuators A: Physical* 125(2), 186-191, (2006).
5) Y. Tang, M. Pan, and F. Chunluo. “Feature Extraction Based on the Principle Component Analysis for Pulsed Magnetic Flux Leakage Testing”. *11th international Conference on Mechatronic science, Electric Engineering and Computer (MEC), IEEE conferences,* 2563-2566, (2011).
6) I. M. Z. Abidin, 2010. "Modelling and experimental investigation of eddy current distribution for angular defect characterisation," in Electrical, Electronic and Computer Engineering. Volume, PhD Newcastle upon Tyne: Newcastle University.

Appendices

Appendices A:

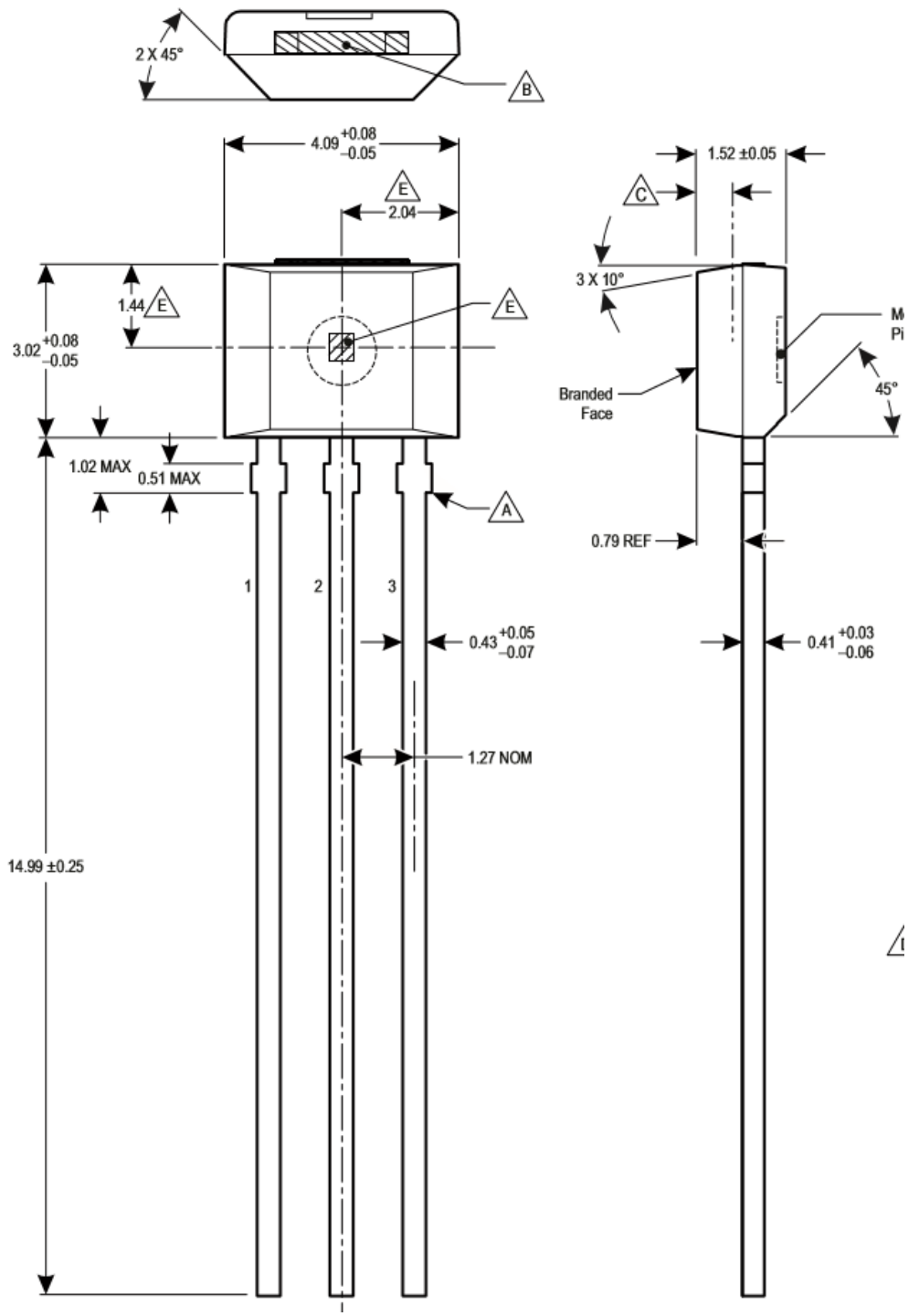

Figure A.1. A schematic diagram of the Ratiometric Hall Effect sensor (A1302KUA-T from Allegro microsystems) used with dimensions.

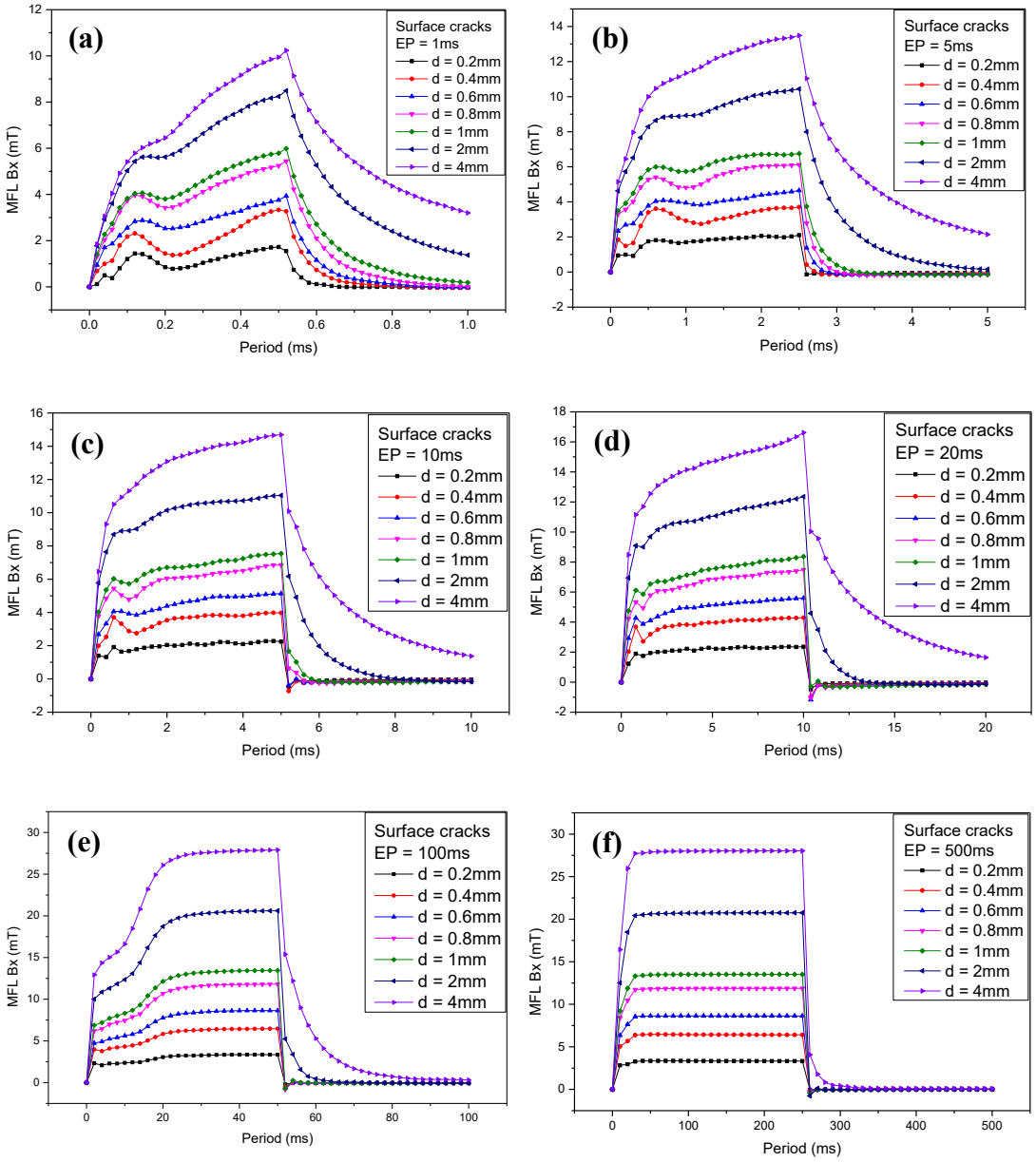

Figure A.2. Time domain representation - The simulated differential leakage field signal ($\Delta \boldsymbol{B_{xb}}$) for surface hairline cracks, with different depth sizes; a) 1 ms excitation period, b) 5 ms excitation period, c) 10 ms excitation period, d) 20 ms excitation period, e) 100 ms excitation period and f) 500 ms excitation period.

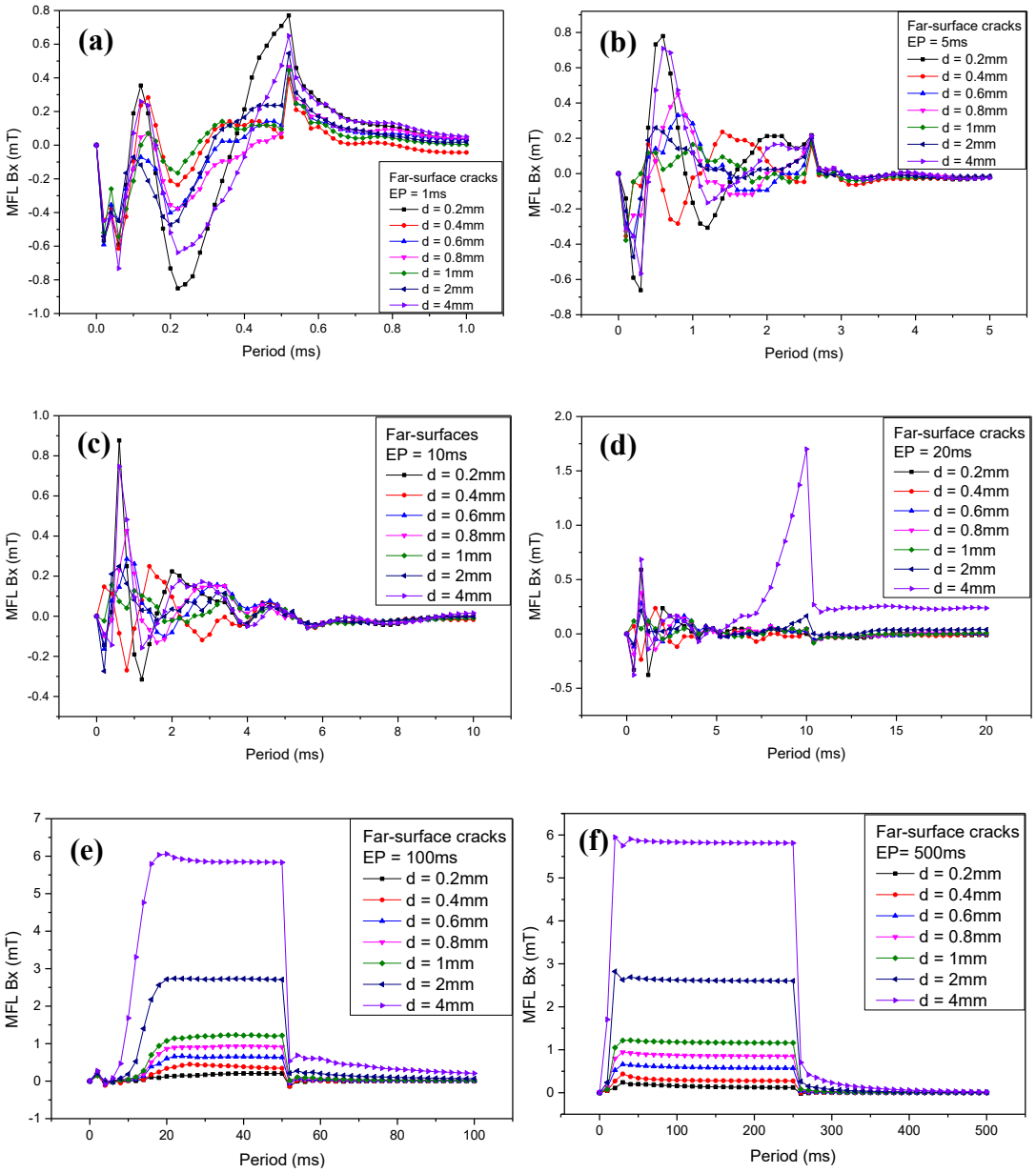

Figure A.3. Time domain representation - The simulated differential leakage field signal ($\Delta \boldsymbol{B_{xb}}$) for far-surface hairline cracks, with different depth sizes; a) 1 ms excitation period, b) 5 ms excitation period, c) 10 ms excitation period, d) 20 ms excitation period, e) 100 ms excitation period and f) 500 ms excitation period.

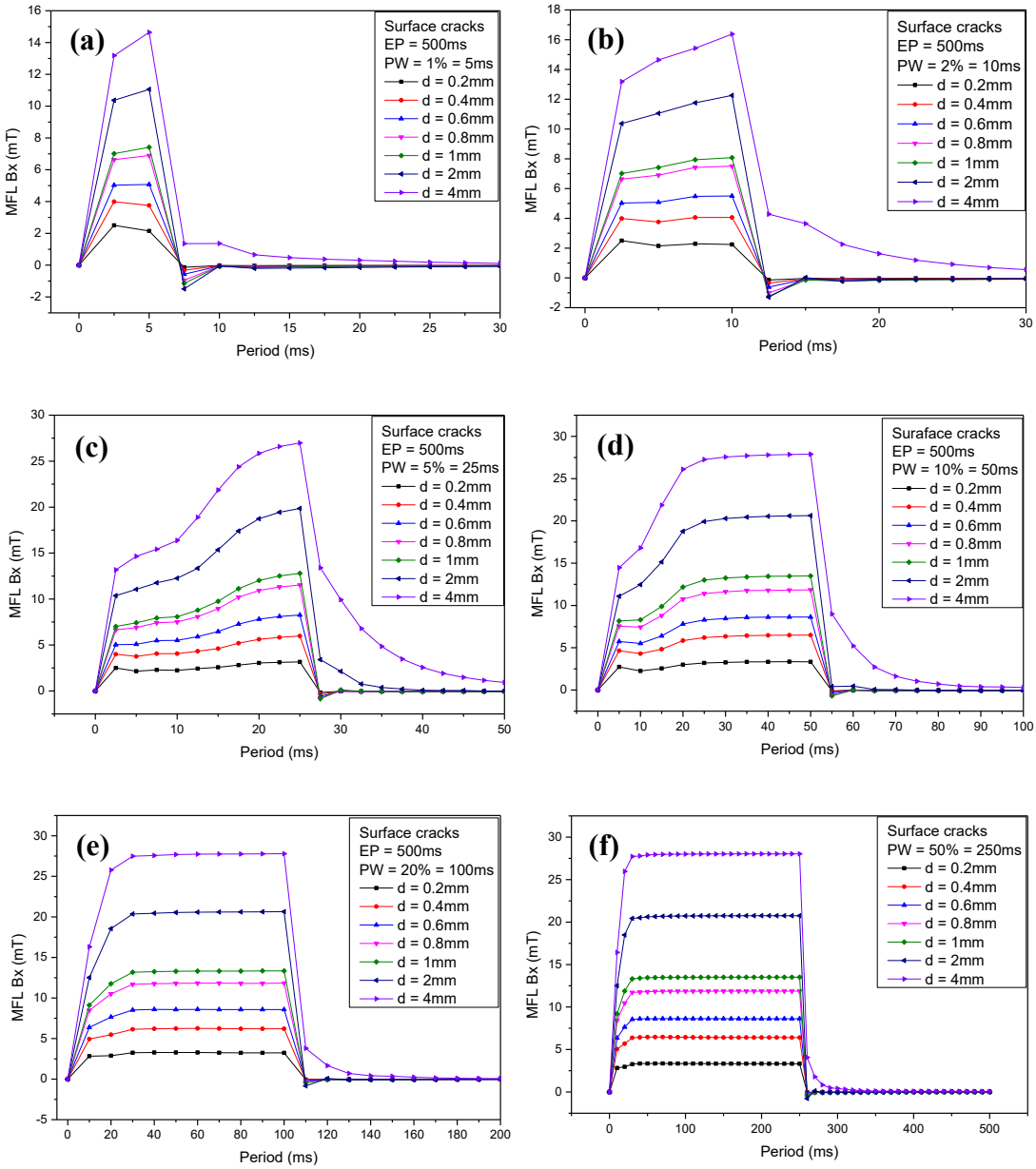

Figure A.4. Time domain representation - The simulated differential leakage field signal ($\Delta \boldsymbol{B_{xb}}$) for surface hairline cracks; a) 5 ms pulse width, b) 10 ms pulse width, c) 25 ms pulse width, d) 50 ms pulse width, e) 100 ms pulse width and f) 250 ms pulse width.

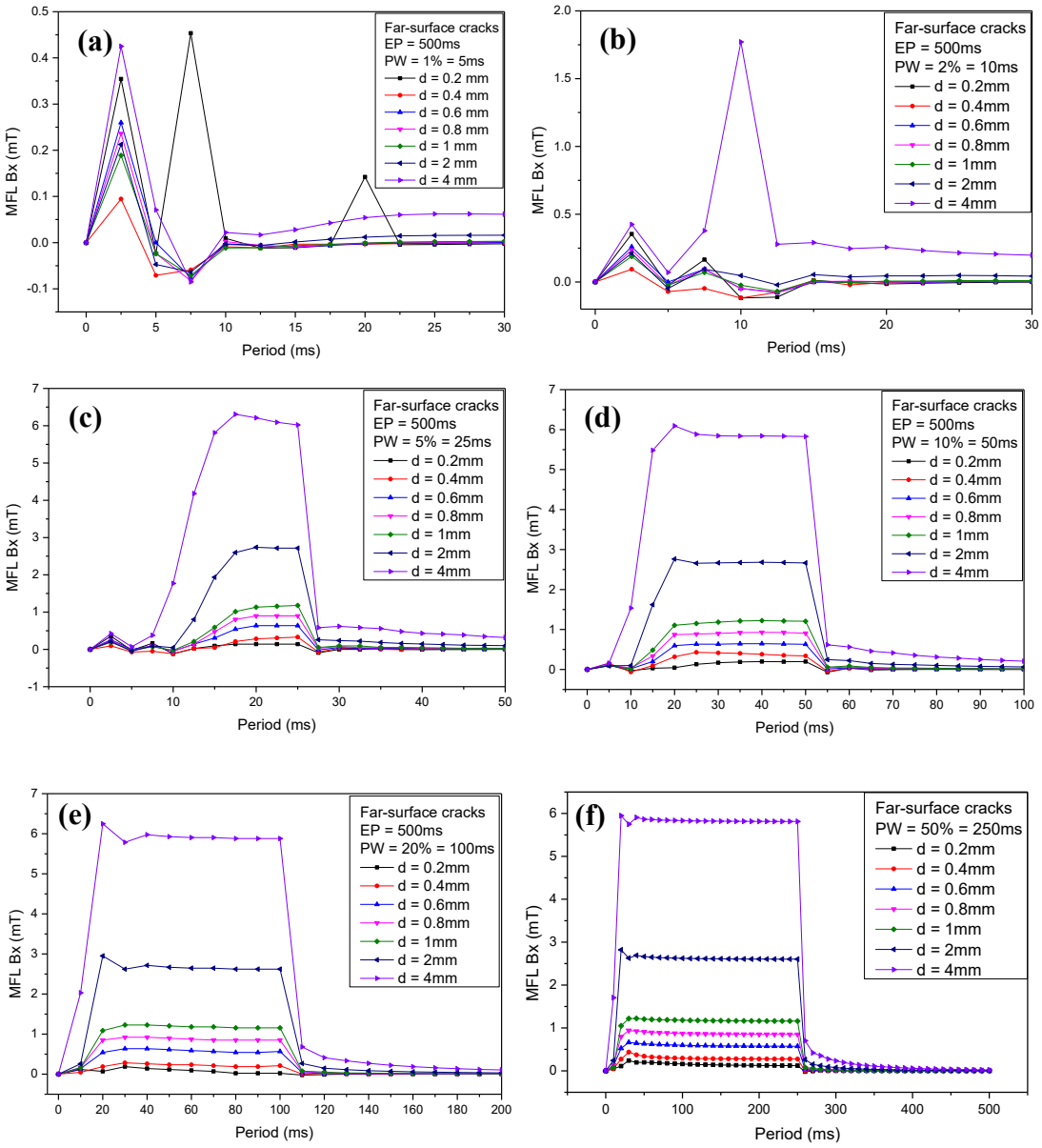

Figure A.5. Time domain representation - The simulated differential leakage field signal ($\Delta \boldsymbol{B_{xb}}$) for far-surface hairline cracks, with different depth sizes; a) 5 ms pulse width, b) 10 ms pulse width, c) 25 ms pulse width, d) 50 ms pulse width, e) 100 ms pulse width and f) 250 ms pulse width.

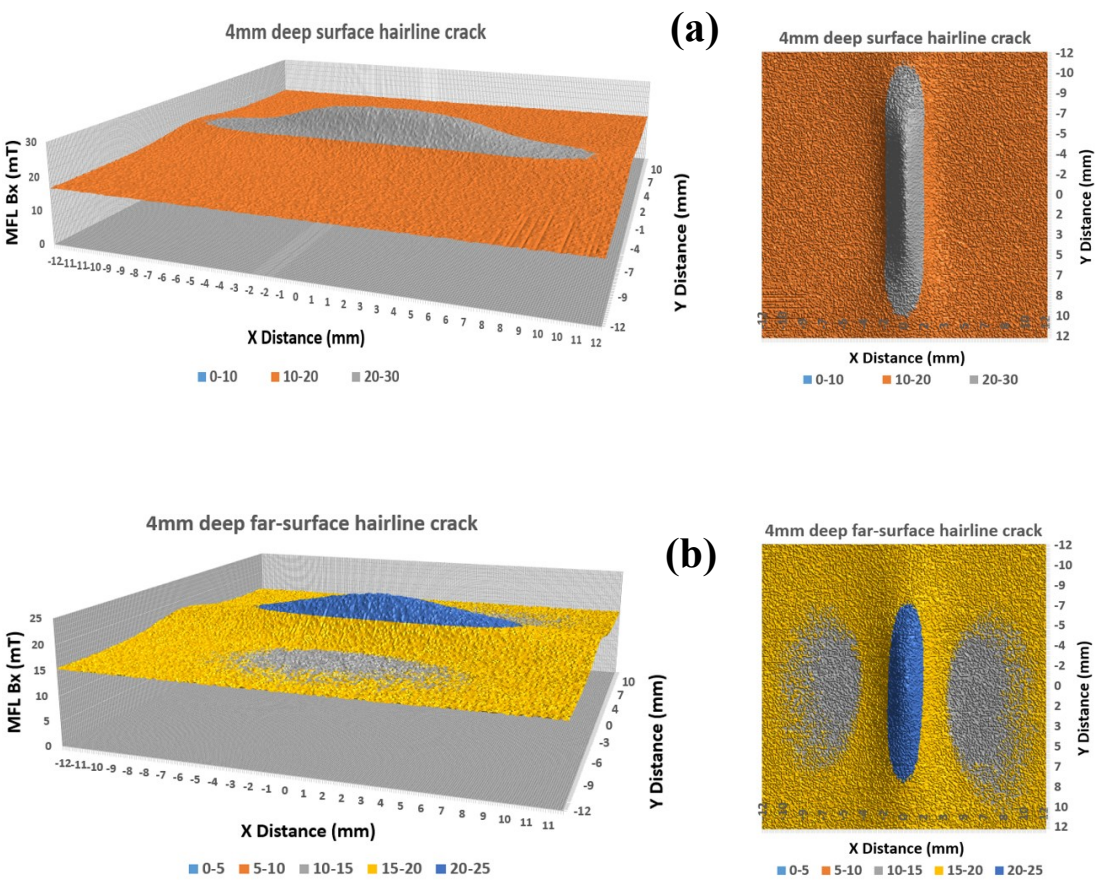

Figure A.6. The measured PMFL crack signal ($\boldsymbol{B_{xb}}$) for; a) a 4mm deep surface hairline crack and b) a 4mm deep far-surface hairline crack.(0.1 mm scan step size; higher spatial resolution).

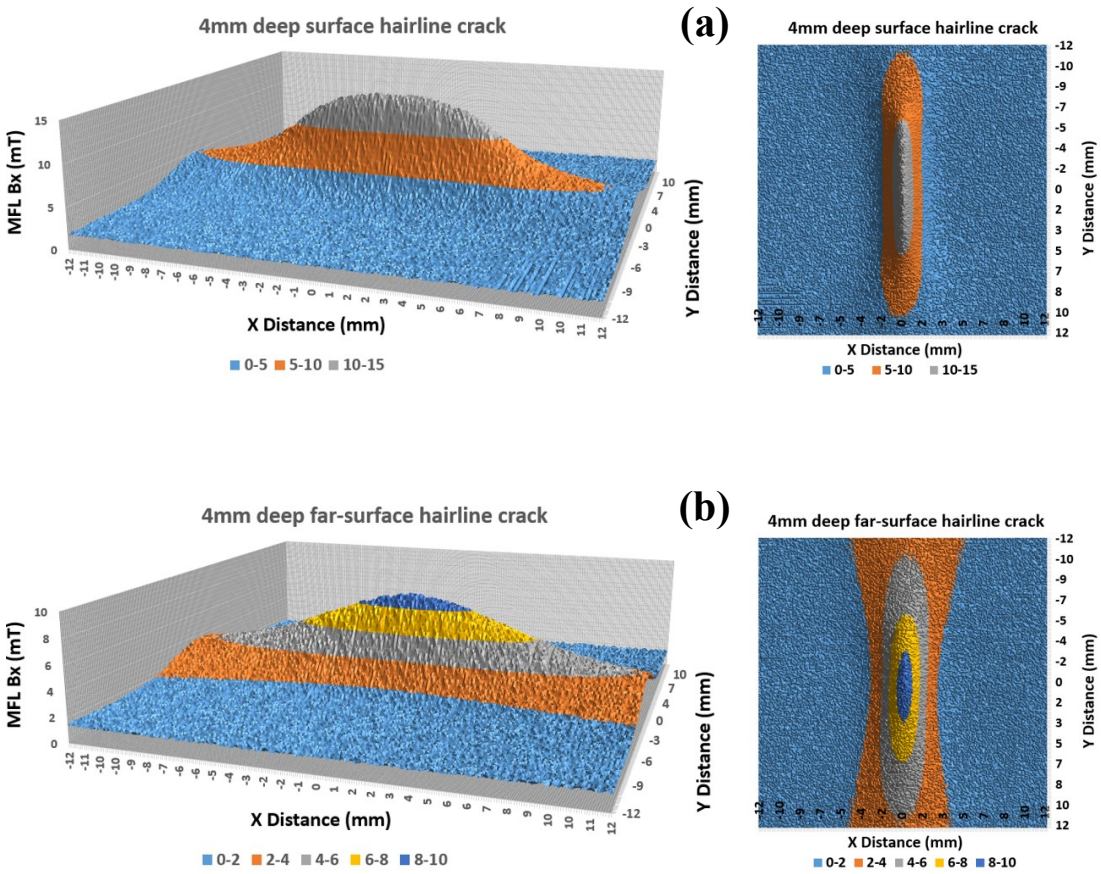

Figure A.7. The measured PMFL differential crack signal ($\Delta \boldsymbol{B_{xb}}$) for; a) a 4mm deep surface hairline crack and b) a 4mm deep far-surface hairline crack.(0.1 mm scan step size; higher spatial resolution).